THÈSE

Pour obtenir le grade de

DOCTEUR DE L'UNIVERSITÉ GRENOBLE ALPES

École doctorale : PHYS - Physique
Spécialité : Physique de la Matière Condensée et du Rayonnement
Unité de recherche : Institut LAUE LANGEVIN

Structure, dynamique et assemblage de la β-caséine comme protéine modèle intrinsèquement désordonnée étudiés par diffusion de neutrons

Structure, dynamics, and assembly of β-casein as a model intrinsically disordered protein investigated by neutron scattering

Présentée par :

Laura MATEO MIÑARRO

Direction de thèse :

Tilo SEYDEL SENIOR SCIENTIST, INSTITUT LAUE- LANGEVIN	Directeur de thèse
Jean-Louis BARRAT PROFESSEUR DES UNIVERSITES, UNIVERSITE GRENOBLE ALPES	Co-directeur de thèse

Rapporteurs :

VICTORIA GARCÍA SAKAI
SENIOR SCIENTIST, ISIS NEUTRON AND MUON SOURCE
ANDREAS STADLER
SENIOR SCIENTIST, RWTH AACHEN UNIVERSITY

Thèse soutenue publiquement le **15 décembre 2025**, devant le jury composé de :

JUDITH PETERS, PROFESSEURE DES UNIVERSITES, UNIVERSITE GRENOBLE ALPES	Présidente
VICTORIA GARCÍA SAKAI, SENIOR SCIENTIST, ISIS NEUTRON AND MUON SOURCE	Rapporteure
ANDREAS STADLER, SENIOR SCIENTIST, RWTH AACHEN UNIVERSITY	Rapporteur
JÖRG PIEPER, PROFESSEUR, TARTU ÜLIKOOL	Examinateur
MARIE PLAZANET, DIRECTRICE DE RECHERCHE, CNRS DELEGATION ALPES	Examinatrice

Preamble

The research work presented in this thesis was carried out within the framework of the IDPXN project, a collaborative effort between the Institut Laue-Langevin (ILL), Grenoble, France, the Université Grenoble Alpes (UGA), France, and the University of Tübingen, Germany. The project is coordinated by Prof. Dr. Frank Schreiber (University of Tübingen) and Dr. Tilo Seydel (ILL), with Prof. Dr. Martin Oettel (University of Tübingen) and Prof. Dr. Jean-Louis Barrat (UGA) as partners.
IDPXN is funded through the German-French collaborative grant DFG-ANR (ANR-21-CE06-0047 / DFG SCHR700/42-1). This PhD project was specifically supported by the ANR.

Contents

List of Figures **v**

List of Tables **ix**

Glossary **xi**

Abstract **1**

Résumé **3**

1 Introduction **5**

2 Theoretical background **9**

2.1 Fundamental aspects of neutron scattering 10

2.1.1 Neutron properties 10

2.1.2 Neutron scattering cross-section and dynamic structure factor . . . 12

2.1.3 Coherent and incoherent neutron scattering 16

2.2 Diffusion in condensed matter systems 19

2.2.1 Brownian motion and Fickian diffusion 19

2.2.2 Anomalous diffusion 20

2.2.3 Self- and collective diffusion 21

2.2.4 Dynamical independence approximation 24

2.3 Neutron Spectroscopy 24

2.3.1 Quasi-elastic neutron scattering (QENS) 24

2.3.2 Elastic incoherent structure factor (EISF) 27

2.3.3 Neutron backscattering spectroscopy (NBS) 29

2.3.4 Neutron spin-echo (NSE) 31

2.4 Small-Angle Neutron Scattering (SANS) 33

3 Biophysical background: β-casein - A review 39

3.1 Proteins 39
3.2 Intrinsically disordered proteins 40
3.3 β-Casein as a model IDP 42
3.4 Structural characterization of β-casein micelles 46
3.5 Neutron spectroscopy studies on β-casein dynamics 54
3.6 Summary 60

4 Materials &methods 63

4.1 Materials 63
4.1.1 β-Casein 63
4.1.2 Solvents 64
4.1.3 Sample preparation 66
4.2 Methods 66
4.2.1 Dynamic light scattering 67
4.2.2 Small-angle neutron scattering (D33) 68
4.2.3 Neutron backscattering spectroscopy (IN16B / BATS) 70
4.2.4 Neutron spin-echo spectroscopy (IN15) 72

5 Structural characterization and collective dynamics of β-casein assemblies 75

5.1 Introduction 75
5.2 Results and discussion 76
5.2.1 Static structure of β-casein assemblies 76
5.2.2 Diffusive dynamics at mesoscopic scales 85
5.2.3 Collective dynamics at microscopic scales 91
5.3 Conclusions 96

6 Apparent non-Fickian diffusion within β-casein assemblies 97

6.1 Introduction 97
6.2 Results and discussion 98
6.2.1 Comparison with a well-folded protein: BSA as a reference system . 98
6.2.2 Molecular dynamics simulations and MDANSE analysis 104

6.2.3 Numerical model of dynamic heterogeneity . . . 110
6.3 Conclusion . . . 116

7 Confined internal dynamics 119
7.1 Introduction . . . 119
7.2 Results and discussions . . . 120
7.3 Conclusions . . . 128

8 Chemical dissociation and free monomer dynamics 129
8.1 Introduction . . . 129
8.2 Results and discussion . . . 130
8.2.1 Structure under chemical dissociation . . . 130
8.2.2 Transition from assembly to free monomer dynamics . . . 135
8.3 Conclusions . . . 141

9 Conclusions and perspectives 143
9.1 Summary and conclusions . . . 143
9.2 Perspectives . . . 146

Résumé détaillé 149

Appendices 153
A Molecular dynamics simulation details . . . 153
B List of experiments at large-scale facilities . . . 155
C Comparison of standard and 3D cross-correlation DLS . . . 159
D Single- vs. double-exponential fitting of DLS correlation functions . . . 163
E Concentration and temperature dependencies of $S(q)$, $D(q)$, and $D(q)S(q)$ . . . 165
F Two-component fits with global Fickian diffusion contributions . . . 167
G Alternative reconstruction of $P(D)$ by direct averaging of synthetic distributions 169
H Radius of gyration distributions of β-casein in water and urea . . . 171

Acknowledgements 173

Bibliography 191

List of Figures

2.1 Scattering geometry in a neutron experiment. 14
2.2 Self and collective dynamics in particle systems. 22
2.3 Elastic, quasi-elastic, and inelastic neutron scattering. 26
2.4 Length and time scales accessible by scattering techniques. 27
2.5 Scheme of IN16B-BATS and distance-time diagram. 30
2.6 Schematic of a neutron spin-echo spectrometer. 32
2.7 Typical setup for small-angle neutron scattering. 34
2.8 q-regimes of the form factor for model particle geometries. 35

3.1 Energy landscapes of ordered versus disordered proteins. 42
3.2 β-casein sequence in one-letter code with residue classes highlighted. 44
3.3 Free energy landscape and block-copolymer-like architecture of β-casein. . 45
3.4 Early schematic representation of a β-casein micelle. 49
3.5 Hydrodynamic radii and mode amplitudes versus temperature. 50
3.6 Cryo-TEM images of β-casein aggregates at different pH and temperatures. 51
3.7 SANS results showing GdmCl-induced micelle-to-monomer transition. . . . 52
3.8 Temperature dependence of micelle dimensions from SANS. 53
3.9 Global and internal dynamic contributions to QENS for caseins and folded proteins. 56
3.10 MSD and β-relaxation of β-casein as a function of temperature. 57

5.1 SANS intensity profiles and core-shell model decomposition. 77
5.2 Comparison of homogeneous sphere and core-shell fits. 79
5.3 Concentration dependence of micelle radii and schematic evolution. 80
5.4 Polydispersity parameter and log-normal size distributions. 81
5.5 Cluster contribution parameters versus concentration. 82

5.6 SANS intensity profiles versus temperature for dilute and concentrated samples. 83
5.7 Temperature dependence of total, core, and shell radii. 84
5.8 Relative width and log-normal size distributions versus temperature. 84
5.9 Integrated cluster weight and power-law exponent versus temperature. . . . 85
5.10 Representative $g^{(2)}(\tau) - 1$ curves with two-exponential fits. 87
5.11 Relaxation rates and mode amplitudes versus q. 88
5.12 DLS hydrodynamic radii and mode amplitudes at 90°. 89
5.13 $g^{(2)}(\tau) - 1$ curves versus temperature for dilute and concentrated samples. 90
5.14 DLS mode amplitudes and hydrodynamic radii versus temperature. 91
5.15 Comparison of single exponential, cumulant, and factorized fits. 92
5.16 Comparison of $D(q)$ from different fitting approaches. 94
5.17 $S(q)$, $D(q)$, and $D(q)S(q)$ at 283 K for 75 mg/mL. 94

6.1 QENS spectra of β-casein and BSA with fitted components. 100
6.2 HWHM versus q^2 for β-casein and BSA. 101
6.3 Diffusion coefficients compared with theoretical monomer and micelle models. 102
6.4 Representative structure of a simulated β-casein aggregate. 104
6.5 Simulated QENS spectrum and q^2-dependence of HWHM. 105
6.6 HWHM from MD simulations for aggregates of varying size. 107
6.7 Water density and backbone mobility profiles in a five-chain aggregate. . . 108
6.8 Synthetic diffusion coefficient distributions and corresponding fits. 112
6.9 Synthetic parameter space and reconstructed $P(D)$ distributions. 115
6.10 Diffusion coefficients and residence times from reconstructed distributions. 115

7.1 $A_0(q)$ and $\Gamma(q)$ comparison for BSA and β-casein 121
7.2 Concentration dependence of fast internal dynamics in β-casein 124
7.3 Comparison of simulated EISF and linewidths for β-casein aggregates . . . 126

8.1 SANS profiles with urea and model fits. 131
8.2 Urea-induced changes in size and aggregation. 132
8.3 Low-q upturn quantification versus urea. 134
8.4 QENS spectrum and linewidth under urea. 137
8.5 D and τ from the slow component QENS fit versus urea. 138
8.6 EISF and linewidths for β-casein at different urea concentrations. 139

8.7 Urea dependence of fast internal dynamics in β-casein 140

C.1 Normalized intensity auto-correlation functions from 2D and 3D DLS. . . . 160
C.2 DLS fit parameters: amplitudes and relaxation rates. 161
D.1 Intensity correlation functions with single- and double-exponential fits. . . 163
E.1 $S(q)$, $D(q)$, and $D(q)S(q)$ at different concentrations and temperatures. . . 166
G.1 $P(D)$ distributions reconstructed by direct averaging of synthetic curves. . 169
H.1 Probability distribution of the radius of gyration for a single β-casein chain in water and in urea. 171

List of Tables

2.1 Neutron scattering cross sections of key biomolecular elements. 18

3.1 Structural studies on β-casein micelles. 47
3.2 Neutron scattering studies on β-casein. 55

6.1 Fitting parameters for β-casein and BSA at different concentrations. 102
6.2 Parameters from $\gamma(q)$ analysis for β-casein aggregates of increasing size. . . 107
6.3 Parameters and statistics of synthetic diffusion coefficient distributions. . . 113

7.1 Comparison of EISF parameters for β-casein, BSA and γ-globulin. 122
7.2 Comparison of dynamical parameters for β-casein, BSA and γ-globulin. . . 123
7.3 Simulated EISF and dynamical parameters for β-casein monomer and aggregate. 126

F.1 Results from the two-component global fit. 168

Glossary

AF4 Asymmetric flow field-flow fractionation. 47, 53

BASIS BAckscattering SIlicon Spectrometer. 55, 57

BATS Backscattering Time-of-Flight Spectrometer. 29, 30, 60, 70, 154

BO Brownian oscillator. 55, 58

BS Backscattering spectroscopy. 25

BSA Bovine serum albumin. 7, 98–102, 116, 119–124, 127, 128, 144, 151

CD Circular dichroism. 43

CMC Critical micelle concentration. 48, 49, 51, 63, 103, 129, 142

COM Center of mass. 99, 108

D33 Massive dynamic q-range small-angle diffractometer. 150

DLS Dynamic light scattering. 7, 46–50, 67, 68, 75, 82, 85–89, 91, 93, 95, 96, 134, 150, 151, 159–161

DNA Deoxyribonucleic acid. 39

dRI Differential refractive index. 53

DWF Debye-Waller factor. 24, 71, 99

EISF Elastic incoherent structure factor. 7, 28, 55, 56, 58, 71, 99, 119, 120, 122, 124–128, 130, 136, 138, 140, 145, 168

FRM-II Forschungsreaktor Munchen II. 54, 56

FTIR Fourier transform infrared spectroscopy. 43

GdmCl Guanidinium chloride. 47, 52, 54

GFP Green fluorescent protein. 57, 58

GROMACS GROningen MAchine for Chemical Simulations. 153, 154

HFBS High Flux Backscattering Spectrometer. 55

HWHM Half-width at half-maximum. 22, 55, 58, 70, 71, 99–101, 105, 107, 111, 112, 114, 119, 126, 137, 138, 140

IDP Intrinsically disordered protein. 1–3, 5, 6, 41–43, 45, 46, 54–56, 60, 97, 149

IDR Intrinsically disordered region. 41

ILL Institut Laue-Langevin. 3, 68, 70, 72, 98, 100

IN15 High resolution spin-echo spectrometer. 150

IN16B Cold neutron high-flux backscattering spectrometer. 29, 30, 60, 72, 100, 122, 150

J-NSE Neutron spin echo spectrometer. 55

LC/MS/MS Liquid chromatography–tandem mass spectrometry. 53

LINCS Linear constraint solver. 153

MALS Multi-angle light scattering. 47, 53

MD Molecular dynamics. 23, 26, 103, 104, 107, 116, 127, 153, 171

MDANSE Molecular Dynamics and Neutron Scattering Experiment. 66, 97, 104, 154

mRNA Messenger ribonucleic acid. 39

MSD Mean squared displacement. 19, 20, 55–57

NBS Neutron backscattering spectroscopy. 6, 7, 9, 40, 55, 58, 143, 145, 148, 150–152

NIST National Institute of Standards and Technology. 55

NMR Nuclear magnetic resonance. 40, 54

NPT Isothermal–isobaric ensemble (constant number of particles, pressure, and temperature). 153, 154

NSE Neutron spin echo. 6, 7, 9, 23, 25, 31–33, 40, 55, 58, 64, 72, 75, 91–96, 143–145, 150, 151, 165

NVT Canonical ensemble (constant number of particles, volume, and temperature). 153, 154

PME Particle–mesh Ewald. 154

QENS Quasi-elastic neutron scattering. 7, 23, 25, 26, 30, 55, 56, 60, 64, 97, 98, 100, 101, 103–105, 116, 119, 122, 130, 137, 139, 141, 142, 144, 146–148, 151

RNA Ribonucleic acid. 39

SANS Small angle neutron scattering. 6, 7, 9, 33, 37, 46–48, 52, 53, 68, 72, 75–77, 80–86, 88–91, 93–96, 129–131, 135, 137, 141–145, 147, 148, 150, 152

SAXS Small angle X-ray scattering. 46–48, 50, 51, 53

SPHERES Backscattering spectrometer. 55

TDP-43 Transactive response DNA binding protein 43 kDa. 42

TEM Transmission electron microscopy. 47, 50, 51

ToF Time-of-flight. 25, 29, 55

TOFTOF Cold neutron time-of-flight spectrometer. 54–56

UGA Université Grenoble Alpes. 3

UV-Vis Ultraviolet-visible. 66

VMD Visual Molecular Dynamics. 104, 154

Abstract

Intrinsically disordered proteins (IDPs) play fundamental roles in biology despite lacking a stable three-dimensional structure. In this thesis, β-casein is employed as a model IDP to investigate how disorder, self-assembly and environment shape protein structure and dynamics across multiple length- and time-scales. We combine advanced neutron scattering techniques with complementary light-scattering measurements and molecular simulations to study β-casein under dilute and crowded conditions, across temperature variations and in the presence of urea, a chemical denaturant. At the mesoscale, β-casein forms self-assembled aggregates already at very low concentrations. Dilute solutions are dominated by soft, highly polydisperse assemblies, whereas concentrated solutions display more defined, less polydisperse aggregates characterized by a compact core and a diffuse outer shell. Temperature narrows the size distribution and slightly compacts the dilute assemblies. Structure and collective dynamics are linked through de Gennes narrowing at the structural correlation peak, consistent with hydrodynamic coupling under crowding. Zooming into the assemblies, we resolve clear deviations from Fickian diffusion. Instead of uniform random motion, β-casein exhibits heterogeneous diffusive behaviors within densely packed aggregates. This high internal density, which we refer to as supercrowding, creates a heterogeneous dynamic environment where chains remain closely associated yet explore different diffusion rates. To capture this behavior, we developed a numerical model based on a distribution of locally Fickian diffusion coefficients, which provides a physical explanation for the apparent non-Fickian response. Such behavior contrasts with well-folded globular proteins and represents a distinctive dynamical signature of disordered assemblies. At shorter timescales, both experiments and simulations reveal a robust internal relaxation on the tens-of-picoseconds range. This mode remains essentially unchanged across concentration, aggregation state, and protein fold, suggesting that it reflects a universal confined process intrinsic to protein dynamics. Finally, the addition

of urea provides a controlled route to dissociate β-casein micelles and probe monomer dynamics. Structural data show a transition between 1 and 4 M urea, where micelles progressively lose their correlation peak and shrink toward effective particle sizes consistent with expanded single chains. Dynamically, the anomalous non-Fickian response of assemblies evolves toward homogeneous Fickian diffusion of free monomers, while internal motions retain their timescale but expand their spatial extent. Urea thus acts not only as a dissociating agent but also as a denaturant, producing swollen monomers distinct from the native state. Altogether, this thesis establishes β-casein as a versatile model for IDPs, providing an integrated view from supramolecular organization to internal dynamics and monomeric behavior. The insights gained reveal how structural plasticity and dynamic heterogeneity manifest as apparent anomalous diffusion across scales, with implications for understanding disordered proteins and other soft condensed matter systems.

Résumé

Les protéines intrinsèquement désordonnées (IDPs) jouent des rôles fondamentaux en biologie malgré l'absence d'une structure tridimensionnelle stable. Dans cette thèse, la β-caséine est utilisée comme protéine modèle afin d'explorer comment le désordre, l'auto-assemblage et l'environnement façonnent la structure et la dynamique protéiques à différentes échelles de temps et d'espace. Nous combinons des techniques avancées de diffusion de neutrons avec des mesures complémentaires de diffusion de la lumière et des simulations moléculaires pour étudier la β-caséine en conditions diluées et encombrées, sous variations de température et en présence d'urée, un dénaturant chimique. À l'échelle mésoscopique, la β-caséine forme des agrégats auto-assemblés dès de très faibles concentrations. Les solutions diluées sont dominées par des assemblages souples et hautement polydisperses, tandis que les solutions concentrées présentent des agrégats plus définis et moins polydisperses, caractérisés par un cœur compact et une enveloppe externe diffuse. L'augmentation de la température resserre la distribution de tailles et compacte légèrement les assemblages dilués. La structure et les dynamiques collectives sont reliées par un effet de rétrécissement de de Gennes au pic de corrélation structurale, en accord avec un couplage hydrodynamique en conditions d'encombrement. En examinant plus finement les assemblages, nous mettons en évidence des déviations nettes par rapport à la diffusion fickienne. Au lieu d'un mouvement aléatoire uniforme, la β-caséine présente des comportements diffusifs hétérogènes au sein d'agrégats denses. Cette forte densité interne, que nous qualifions de super-encombrement, engendre un environnement dynamique hétérogène où les chaînes demeurent étroitement associées tout en explorant différentes vitesses de diffusion. Pour rendre compte de ce phénomène, nous avons développé un modèle numérique basé sur une distribution locale de coefficients de diffusion fickienne, fournissant ainsi une explication physique à la réponse apparemment non fickienne. Un tel comportement contraste avec celui des protéines globulaires bien repliées et constitue

une signature dynamique caractéristique des assemblages désordonnés. À des échelles de temps plus courtes, les expériences et les simulations révèlent une relaxation interne dans la gamme des dizaines de picosecondes. Ce mode reste essentiellement inchangé quelle que soit la concentration, l'état d'agrégation ou le repliement protéique, ce qui suggère qu'il reflète un processus universel de confinement intrinsèque à la dynamique des protéines. Enfin, l'ajout d'urée constitue une voie contrôlée pour dissocier les micelles de β-caséine et sonder la dynamique des monomères. Les données structurales montrent une transition entre 1 et 4 M d'urée, au cours de laquelle les micelles perdent progressivement leur pic de corrélation et se contractent vers des tailles effectives compatibles avec des chaînes monomériques étendues. Du point de vue dynamique, la réponse anormale non fickienne des assemblages évolue vers une diffusion fickienne homogène des monomères libres, tandis que les mouvements internes conservent leur échelle de temps mais s'étendent spatialement. L'urée agit donc à la fois comme agent de dissociation et comme dénaturant, produisant des configurations étendues distinctes de l'état natif. En résumé, cette thèse établit la β-caséine comme un modèle polyvalent de protéine désordonnée, offrant une vision intégrée allant de l'organisation supramoléculaire aux dynamiques internes et au comportement monomérique. Les résultats obtenus révèlent comment la plasticité structurelle et l'hétérogénéité dynamique se manifestent sous forme de diffusion anormale apparente à travers les échelles, avec des implications pour la compréhension des protéines désordonnées et d'autres systèmes de matière molle.

Chapter 1

Introduction

Intrinsically disordered proteins (IDPs) challenge the classical structure-function paradigm by remaining functional without adopting a stable tertiary structure [1–4]. Their flexibility enables binding promiscuity, self-assembly, and adaptability to changing environments, but it also complicates the microscopic understanding of how structure and dynamics emerge from disorder. In this context, characterizing IDPs across the relevant time and length scales remains one of the central challenges in modern biophysics.

Despite major advances in spectroscopy and simulation, a complete picture of IDP dynamics is still elusive. Most experimental techniques probe either local motions or large-scale organization, but rarely connect them. In particular, how disorder and self-assembly jointly shape collective and internal dynamics across scales is still poorly understood. This gap is especially relevant because many IDPs form dynamic assemblies whose physical behavior underlies key biological and technological processes.

In this work, the milk protein β-casein is employed as a model IDP to explore how structural disorder, self-assembly, and environmental factors, such as concentration, temperature, and chemical perturbation, govern structure and dynamics. β-casein is amphiphilic, highly soluble, and known to form soft assemblies whose properties depend sensitively on external conditions. Its intrinsically disordered sequence and transient interactions make it representative of many IDPs, and its assemblies provide an experimentally accessible system to study hierarchical dynamics in solution, which are central to IDP function but remain poorly characterized. While its static structure has been characterized by scattering methods, systematic neutron-based studies of its dynamics in solution have remained scarce as previous experiments could not simultaneously access the full range of

relevant time and length scales. This makes β-casein an ideal benchmark for establishing a multiscale framework of IDP dynamics.

To this end, we combine complementary neutron scattering techniques: small-angle neutron scattering (SANS), neutron spin echo (NSE), and neutron backscattering spectroscopy (NBS) with dynamic light scattering and molecular dynamics simulations. Together, these methods span a broad window of length and, for the case of spectroscopy, time scales, from nanometers to hundreds of nanometers and from picoseconds to hundreds of nanoseconds, linking static correlations, collective diffusion, and internal relaxation within a unified framework. This integrated approach allows us to test how self-crowding, compaction, and chemical dissociation alter the hierarchical dynamics of β-casein assemblies.

The central objectives of this thesis are to (i) elucidate the structural hierarchy of β-casein assemblies and its relation to collective transport, (ii) identify the microscopic origin of the apparent non-Fickian diffusion observed in crowded disordered systems, (iii) characterize the intrinsic fast relaxation underlying local protein flexibility, and (iv) establish how chemical and environmental perturbations modulate both global and internal dynamics.

The thesis is organized as follows.

Chapter 2 lays the theoretical foundations of this work. It introduces the essential principles of neutron scattering and their application to condensed matter systems, emphasizing the link between measurable quantities such as the dynamic structure factor $S(q, \omega)$ and microscopic motion. The chapter also reviews diffusion models ranging from classical Fickian transport to anomalous and heterogeneous regimes, providing the conceptual basis for interpreting quasi-elastic neutron scattering data. Finally, the operating principles and time-length scale windows of the three neutron techniques used in this study: NBS, NSE, and SANS are described, establishing a common framework for the experimental chapters that follow.

Chapter 3 situates the study within a biophysical context by presenting an overview of β-casein as a model IDP. The sequence architecture, amphiphilic character, and self-assembly behavior are discussed as well as their sensitivity to pH, temperature, ionic strength, and denaturants. Previous structural and dynamical investigations are summarized, highlighting that, while the static organization of β-casein micelles has been characterized under various conditions, systematic neutron studies of their internal dy-

namics have remained limited. This motivates the present work as a comprehensive, multi-scale investigation of structure and dynamics across multiple scales.

Chapter 4 details the materials and experimental methods employed. It describes the preparation of β-casein solutions, the different solvents and temperature or chemical conditions explored, and the instrumental setups used for each scattering technique. The data analysis strategies for SANS, NSE, and NBS are introduced, together with supporting measurements from dynamic light scattering (DLS) and molecular dynamics simulations, which provide complementary access to hydrodynamic size distributions and atomistic motions, respectively.

Chapter 5 integrates SANS, DLS, and NSE to establish the structural hierarchy and collective dynamics of β-casein assemblies across concentration and temperature. It identifies two coexisting structural levels: compact micelles and larger cluster-like inhomogeneities, and demonstrates through de Gennes narrowing that static correlations directly determine collective diffusivity, thereby connecting structural compaction and hydrodynamic coupling under crowding.

Chapter 6 focuses on the apparent non-Fickian diffusion observed by QENS and investigates its microscopic origin. By comparing β-casein with a well-folded reference protein (BSA), atomistic molecular dynamics simulations, and a numerical model incorporating spatially distributed local diffusion coefficients, the chapter shows that the anomalous response could arise from dynamic heterogeneity within supercrowded micellar interiors.

Chapter 7 explores the fast internal dynamics of β-casein and BSA, corresponding to localized motions confined to nanometric scales. Analysis of the elastic incoherent structure factor (EISF) and linewidths reveals a robust relaxation mode on the tens-of-picoseconds timescale that persists across concentrations, aggregation states, and folding conditions. These findings identify a confined process that represents an intrinsic, baseline dynamical element of protein flexibility.

Chapter 8 investigates the effect of chemical dissociation using urea to bridge the transition from assemblies to monomers. SANS data reveal a smooth crossover in the 1-4 M range, where micellar correlations fade and particle sizes approach those of expanded single chains. QENS measurements show a corresponding transition from heterogeneous non-Fickian to homogeneous Fickian diffusion, while the fast internal relaxation retains its characteristic timescale but expands spatially. Together, these results establish urea as

both a dissociating and denaturing agent and provide a tunable route to access monomer dynamics at experimentally accessible concentrations.

Finally, Chapter 9 summarizes the main conclusions, distilling the four principal outcomes that emerge from this work: (i) the structural hierarchy governing collective transport, (ii) the microscopic origin of anomalous diffusion, (iii) the robustness of confined internal relaxation, and (iv) the link between chemical control and dynamic remodeling. The chapter also outlines several ongoing and future directions: external crowding, ionic modulation, temperature and pressure effects, that extend the present framework toward more realistic and biologically relevant environments.

Chapter 2

Theoretical background

Neutron scattering techniques offer unique insights into the microscopic structure and dynamics of materials. In this chapter, we introduce the fundamental physical concepts and mathematical formalisms underlying the neutron scattering techniques employed in this work.

Neutron scattering has become a versatile tool to explore both static and dynamic properties of condensed matter systems. Due to their unique interaction mechanisms and deep penetration, thermal and cold neutrons can access length scales ranging from a few Ångströms to hundreds of nanometers, and time scales spanning from picoseconds to hundreds of nanoseconds. These features make neutron techniques particularly suitable for the study of complex fluids, polymers, biological macromolecules, and disordered systems.

This chapter begins with a general introduction to the principles of neutron scattering, including the distinction between coherent and incoherent scattering and the definition of the scattering cross section and the dynamic structure factor. We then focus on the fundamental concepts of diffusion in condensed matter, discussing classical Brownian motion, Fickian diffusion, and deviations from ideal behavior, including anomalous diffusion and jump processes.

Finally, we present the theoretical foundations of the three main experimental techniques employed in this thesis: Neutron backscattering spectroscopy (NBS), Neutron spin echo (NSE), and Small angle neutron scattering (SANS), emphasizing the physical quantities they probe and the time and length scales they access. This theoretical framework provides the necessary context for understanding the experimental results and data analysis presented in the subsequent chapters.

The main sources for this chapter are: *Theory of neutron scattering from condensed matter* by S. W. Lovesey (1984) [5], *Introduction to the Theory of Thermal Neutron Scattering* by G. L. Squires [6], *Neutron Scattering - Fundamentals* by F. Fernandez-Alonso and D. Price [7], and *Quasielastic Neutron Scattering* by M. Bee [8].

2.1 Fundamental aspects of neutron scattering

2.1.1 Neutron properties

Neutrons are electrically neutral subatomic particles that, along with protons, constitute the atomic nucleus. Since their discovery by James Chadwick in 1932, neutrons have been recognized not only as crucial to explaining how atomic nuclei are held together and as active participants in various physical processes, but also as powerful tools used to investigate the behavior of materials at the atomic scale. A free neutron has a rest mass of approximately $m = 1.675 \times 10^{-27}$ kg, slightly greater than that of a proton, and it is unstable outside the nucleus, undergoing beta decay with a mean lifetime of about 880 seconds.

One of the main properties of neutrons is their charge neutrality. Neutrons have a low probability of interaction with matter since they do not interact with the electron cloud and therefore penetrate deeply into matter (about a few centimeters). They interact with atomic nuclei through nuclear forces and are consequently good probes for bulk properties in a non-destructive manner.

The energy and wavelength of neutrons are directly related to their velocity and, consequently, to their temperature. For sufficiently slow neutrons (cold and thermal), the non-relativistic expression applies:

$$E = \frac{1}{2}mv^2 \tag{2.1}$$

where m is the neutron mass and v its velocity. According to de Broglie's relation and the classical expression for kinetic energy, the energy of a free neutron can be expressed directly in terms of its wavelength as:

$$E = \frac{h^2}{2m\lambda^2} \tag{2.2}$$

where k_B is the Boltzmann constant. Neutrons in thermal equilibrium follow the Maxwell-Boltzmann velocity distribution, and their average energy is related to temperature by:

$$E = \frac{3}{2} k_B T \tag{2.3}$$

Based on their energy (or temperature), neutrons are commonly classified as:

- Hot neutrons ($E > 50$ meV, $\lambda < 1$ Å): Higher energies and shorter wavelengths make them suitable for probing high-energy excitations or small structural features.
- Thermal neutrons ($E \approx 25$ meV at ~ 300 K, $\lambda \approx 1.8$ Å): Their wavelength matches typical interatomic distances, making them ideal for neutron diffraction to determine crystal structures.
- Cold neutrons ($E \sim 1 - 10$ meV, $\lambda = 4 - 20$ Å): Longer wavelengths and lower energies are advantageous for studying soft matter, biological systems, and magnetic structures, as well as slow dynamics and low-energy excitations through inelastic neutron scattering.

The ability to tune neutron energy and wavelength allows researchers to select the appropriate neutron spectrum depending on the length or energy scale of interest. As a result, neutrons are widely used not only for diffraction experiments that provide structural information, but also for neutron spectroscopy techniques that probe dynamic processes, including molecular motions in complex condensed matter systems.

Neutrons also carry a magnetic dipole moment, $\mu_N = -1.913\ \mu_B$, which allows them to interact with unpaired electron spins in materials. This magnetic interaction gives rise to magnetic scattering, enabling the investigation of magnetic structures and excitations. However, since this thesis focuses on nuclear interactions and the dynamics of non-magnetic systems, magnetic scattering will not be discussed further.

Finally, neutrons have an intrinsic spin quantum number of $s = \frac{1}{2}$, which classifies them as fermions. This means their spin angular momentum has two allowed projections along any chosen axis, typically $m_s = \pm\frac{1}{2}\hbar$. These discrete spin states enable spin-dependent interactions and allow the spin to be flipped ($-\frac{1}{2} \leftrightarrow +\frac{1}{2}$) through interactions with magnetic fields. This property is fundamental for experiments using polarized neutrons, where controlling and analyzing neutron spin enables detailed investigation of magnetic and nuclear structures.

In a neutron scattering experiment, detectors measure the scattered neutrons to determine how their momentum and energy have changed due to interactions with the sample. The two fundamental quantities derived from such experiments are momentum transfer, described by the scattering vector $\vec{q}$, and energy transfer $\hbar\omega$.
When a neutron with initial wave vector $\vec{k}_i$ and energy E_i is scattered into a final state characterized by wave vector $\vec{k}_f$ and energy E_f, the scattering vector is defined as:

$$\vec{q} = \vec{k}_i - \vec{k}_f \tag{2.4}$$

and represents the momentum transferred to the sample. The magnitude of $\vec{q}$ is related to the spatial resolution of the measurement, typically corresponding to interatomic distances. The energy transfer is given by:

$$\hbar\omega = E_i - E_f = \frac{\hbar^2 k_i^2}{2m} - \frac{\hbar^2 k_f^2}{2m} \tag{2.5}$$

and reflects the amount of energy exchanged between the neutron and the sample. Equations (2.4) and (2.5) can be combined to relate $q = |\vec{q}|$ and $\hbar\omega$ explicitly:

$$q^2 = k_i^2 + k_f^2 - 2k_i k_f \cos\theta = \frac{2m}{\hbar^2}\left(2E_i - \hbar\omega - 2\sqrt{E_i(E_i - \hbar\omega)}\cos\theta\right) \tag{2.6}$$

This shows that the momentum transfer q and the energy transfer $\hbar\omega$ are kinematically related, and this relation imposes constraints on the scattering experiment. As a result, the accessible region in the $(\vec{q}, \omega)$-space is limited and depends on the energy of the incident neutrons and the scattering geometry.
For example, probing excitations involving large energy transfers at moderate momentum transfers typically requires high-energy incident neutrons and small scattering angles, corresponding to scattering geometries oriented in the forward direction. In contrast, accessing excitations characterized by low energy transfer and large momentum transfer requires larger scattering angles and often backward-oriented geometries. These kinematic constraints must be carefully considered when designing an experiment, as they determine which structural or dynamical features of the sample can be effectively investigated with a given instrumental setup.

2.1.2 Neutron scattering cross-section and dynamic structure factor

When a neutron approaches a nucleus, two fundamental types of interactions can occur. In the first case, the neutron is absorbed by the nucleus, forming an excited compound

nucleus. This unstable intermediate state typically decays by emitting gamma rays or alpha particles, a process used in ^{3}He neutron detectors, for example. In certain heavy nuclei, such as uranium, neutron absorption can instead trigger nuclear fission, a reaction essential for the functioning of nuclear reactors. The second possibility is scattering: the neutron interacts with the nucleus without being captured, resulting in a change in its trajectory, energy, and momentum. For thermal neutrons, whose energies are too low to excite the internal structure of the nucleus or its electron cloud, the scattering is governed primarily by interactions with the atomic nuclei undergoing translational or vibrational motion. These nuclear motions involve much lower energy scales and give rise to inelastic scattering processes, in which the neutron can gain or lose energy depending on the dynamics of the system.

When a neutron beam with an incident current I_0 (neutrons per second per square centimeter) strikes a sample, the rate at which interactions occur can be described in terms of the two fundamental neutron-nucleus interaction processes: absorption and scattering. The number of absorption events per unit time and per square centimeter, I_a, and the number of scattering events, I_s, are given by:

$$I_a = I_0 \, \sigma_a \tag{2.7}$$

$$I_s = I_0 \, \sigma_s \tag{2.8}$$

where σ_a and σ_s denote the absorption and scattering cross sections, respectively. These cross sections represent the effective area that a nucleus presents to an incoming neutron for a specific interaction process. They are expressed in units of area, typically in barns, with 1 barn $= 10^{-24}$ cm^2. For reference, Table 2.1 summarizes the relevant neutron scattering cross sections for key biomolecular elements.

At low incident energies, particularly in the thermal and cold neutron range (meV scale), the absorption cross section σ_a exhibits a smooth dependence on the neutron energy. In many cases, it approximately scales with the neutron wavelength, or inversely with its velocity:

$$\sigma_a \propto \lambda \propto \frac{1}{v} \tag{2.9}$$

This behavior reflects the quantum mechanical nature of neutron absorption and is particularly relevant for applications involving neutron moderation and detection.

A quantitative description of neutron scattering requires an understanding of the scattering geometry, which defines how the neutron exchanges momentum and energy with the

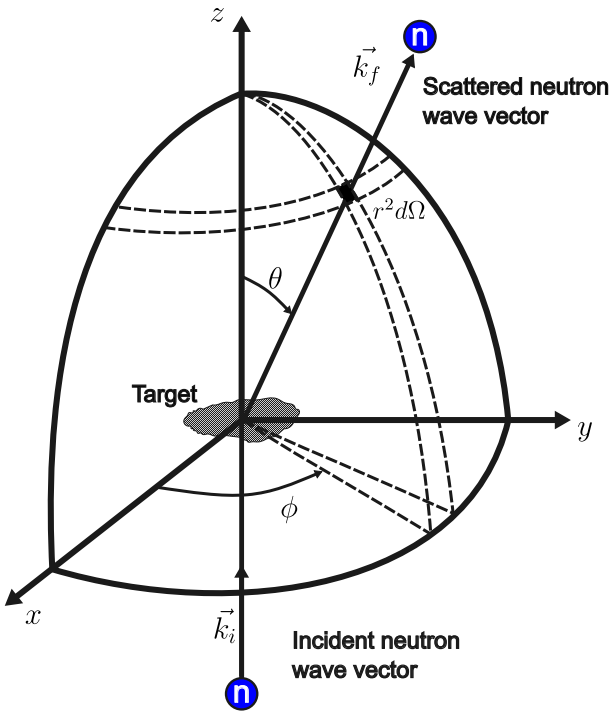

Figure 2.1. Scattering geometry in a neutron experiment. A neutron beam approaches the target sample with its initial wave vector $\vec{k_i}$ aligned along the z-axis. After interacting with the sample, the neutron is scattered forming an angle θ with respect to the z-axis and an azimuthal angle ϕ within the $x-y$ plane. The resulting wave vector is $\vec{k_f}$. The angles θ and ϕ describe the scattering configuration and define the element of solid angle $r^2 d\Omega$. Figure adapted from [5] and rendered with Inkscape.

sample. As illustrated in Figure 2.1, a neutron with incident wave vector $\vec{k_i}$ and energy E_i interacts with the target and is scattered into a final state with wave vector $\vec{k_f}$ and energy E_f. The direction of the scattered neutron is specified by the polar angle θ (with respect to the z-axis) and the azimuthal angle ϕ in the x-y plane. These angles define an infinitesimal element of solid angle given by: $d\Omega = \sin\theta \, d\theta \, d\phi$. The main observable in a scattering experiment is the double differential cross section:

$$\frac{d^2\sigma}{d\Omega \, d\omega} \tag{2.10}$$

which represents the probability per unit incident flux that a neutron with initial energy E_i is scattered into a direction within the solid angle $d\Omega$, transferring an energy $\hbar\omega = E_f - E_i$ to the sample. This quantity has dimensions of area per unit energy per unit solid angle [area^2/(energy $\cdot$ solid angle)].

The total scattering cross section is obtained by integrating over all scattering directions

and energy transfers:

$$\sigma = \int d\Omega \int dE_f \, \frac{d^2\sigma}{d\Omega \, dE_f} \tag{2.11}$$

Experimental evidence indicates that the range of the nuclear interaction is considerably shorter compared to both the wavelength of thermal neutrons and the typical nuclear radius. In this regime, neutron-nucleus scattering can be treated as point-like, and the process becomes isotropic. The interaction is then fully characterized by a single parameter, b, the scattering length, which is independent of the neutron energy. This parameter can be complex, with a real part that may be positive or negative depending on the nature of the interaction. A positive real part corresponds to a repulsive potential, while a negative real part indicates an attractive interaction. The imaginary part of b represents absorption, mainly due to radiative capture of slow neutrons, and is generally small compared to the real part. In general, different atomic species and even different isotopes possess distinct scattering lengths. Additionally, the value of b may depend on the relative orientation between the neutron spin and the nuclear spin.

The incident neutron beam can be represented as a plane wave of the form $\Psi(\vec{r}) \propto e^{i\vec{k_i}\cdot\vec{r}}$, where $\vec{k_i}$ is the wave vector of the incoming neutron. Upon interacting with a single nucleus, the neutron is scattered, and the outgoing wave can be approximated as a spherical wave emanating from the point of interaction. This results in a scattered wave of the form $\Psi_{\text{sc}}(\vec{r}) \propto \frac{e^{ik_f r}}{r}$, where k_f is the magnitude of the scattered wave vector.
In a real sample, the neutron interacts with many nuclei. The total scattered wave is thus the coherent superposition of spherical waves originating from each scattering center. Each nucleus contributes with a phase factor depending on its position $\vec{R}_i$, and an amplitude weighted by its scattering length b_i. Since the nuclei are in constant motion and arranged in various configurations due to thermal and quantum fluctuations, the measured scattering intensity reflects an average over all microscopic states. This averaging leads to the introduction of the dynamic structure factor $S(\vec{q}, \omega)$, defined here in the van Hove formalism, which encodes the spatial and temporal correlations of the nuclei and directly connects to the measured scattering intensity [9]:

$$S(\vec{q}, \omega) = \frac{1}{2\pi\hbar} \sum_{j,k} \overline{b_j b_k^*} \int_{-\infty}^{\infty} dt \, e^{i\omega t} \left\langle e^{-i\vec{q}\cdot\vec{R}_k(0)} e^{i\vec{q}\cdot\vec{R}_j(t)} \right\rangle . \tag{2.12}$$

Here, $\vec{R}_j(t)$ denotes the position operator of the nucleus j at time t, and $\langle \cdots \rangle$ indicates an ensemble average over the quantum and thermal states. Physically, $S(\vec{q}, \omega)$ is also called the response function, since it characterizes spontaneous dynamical fluctuations within the material. Because neutron scattering is a weak perturbation, the sample's response is linear and can be analyzed using perturbation theory. Consequently, the double differential scattering cross-section can be expressed as a measure of the spectrum of these intrinsic fluctuations without disturbing the system:

$$\frac{d^2\sigma}{d\Omega\, dE_f} = \frac{k_f}{k_i} S(\vec{q}, \omega), \tag{2.13}$$

Thus, neutron scattering directly measures $S(\vec{q}, \omega)$, providing detailed insight into the undistorted dynamical properties and correlations of the sample.

2.1.3 Coherent and incoherent neutron scattering

In a neutron scattering experiment, the total measured cross section arises from the interference of waves scattered by all nuclei in the sample. This interference can be constructive or destructive depending on the statistical distribution of scattering lengths b_i across the nuclei. When the scattering lengths are similar or identical, the waves interfere coherently, producing interference patterns that reflect spatial correlations between particles. In contrast, significant fluctuations in b_i disrupt phase relationships and give rise to an additional incoherent scattering contribution.
This leads to two fundamentally different components of the scattering signal:

- Coherent scattering, which originates from the average scattering length, $\langle b_i \rangle$ over all isotopes and nuclear spin states. It provides information about collective behaviors and correlations between different particles.

$$b^{\text{coh}} = \langle b_i \rangle \tag{2.14}$$

- Incoherent scattering, which arises from the variance in the scattering lengths and reflects self-correlations associated with individual particle motion.

$$b^{\text{inc}} = \sqrt{\langle b_i^2 \rangle - \langle b_i \rangle^2} \tag{2.15}$$

Essentially, incoherent scattering focuses on how the position of a single particle changes over time (self-dynamics), whereas coherent scattering looks at how positions of different

particles are correlated as time progresses (collective dynamics). These concepts are discussed in more detail in Section 2.2.3.

When a neutron interacts with a nucleus of spin s, it can form total spin states $S_+ = s + \frac{1}{2}$ and $S_- = s - \frac{1}{2}$, associated with scattering lengths b_+ and b_-, respectively. The multiplicities of these states are $n_+ = 2S_+ + 1 = 2s + 2$ and $n_- = 2S_- + 1 = 2s$. Assuming both spin states occur with equal probability, the coherent and incoherent scattering lengths are given by:

$$b^{\text{coh}} = \frac{1}{n_+ + n_-}[n^+ b^+ + n^- b^-] \tag{2.16}$$

$$b^{\text{inc}} = \frac{1}{2s+1}[(s+1)b^+ + s b^-] \tag{2.17}$$

These expressions allow the evaluation of the so-called bound cross sections for the coherent and incoherent contributions, respectively:

$$\sigma_{\text{coh}} = 4\pi \left(b^{\text{coh}}\right)^2 \tag{2.18}$$

$$\sigma_{\text{inc}} = 4\pi \left(b^{\text{inc}}\right)^2 \tag{2.19}$$

The total scattering cross section is then given by the sum:

$$\sigma = \sigma_{\text{coh}} + \sigma_{\text{inc}}. \tag{2.20}$$

Analogously, the dynamic structure factor $S(\vec{q}, \omega)$ can also be separated into a sum of coherent and incoherent contributions:

$$S(\vec{q}, \omega) = S_{\text{coh}}(\vec{q}, \omega) + S_{\text{inc}}(\vec{q}, \omega) \tag{2.21}$$

$$S_{\text{coh}}(\vec{q}, \omega) = \frac{1}{2\pi\hbar} \sum_{j \neq k} \overline{b_j b_k^*} \int_{-\infty}^{\infty} dt\, e^{i\omega t} \left\langle e^{-i\vec{q}\cdot\vec{R}_k(0)} e^{i\vec{q}\cdot\vec{R}_j(t)} \right\rangle \tag{2.22}$$

$$S_{\text{inc}}(\vec{q}, \omega) = \frac{1}{2\pi\hbar} \sum_{j} (\overline{|b_j|^2} - |\overline{b_j}|^2 \int_{-\infty}^{\infty} dt\, e^{i\omega t} \left\langle e^{-i\vec{q}\cdot\vec{R}_j(0)} e^{i\vec{q}\cdot\vec{R}_j(t)} \right\rangle \tag{2.23}$$

Importantly, by applying successive inverse Fourier transforms to $S_{\text{coh}}(\vec{q}, \omega)$, from ω to t and from $\vec{q}$ to $\vec{r}$, one obtains the time-dependent pair-correlation function, also known as the van Hove function:

$$G_{\text{coh}}(\vec{r}, t) = \frac{1}{(2\pi)^3\hbar} \sum_{j \neq k} \overline{b_j}\, \overline{b_k^*} \int d^3q\, e^{-i\vec{q}\cdot\vec{r}} \left\langle e^{-i\vec{q}\cdot(\vec{R}_k(0) - \vec{R}_j(t))} \right\rangle. \tag{2.24}$$

This function can also be written as

$$G_{\text{coh}}(\vec{r}, t) = \frac{1}{N} \sum_{j \neq k} \int \left\langle \delta\left(\vec{r}' - \vec{R}_j(0)\right) \delta\left(\vec{r}' + \vec{r} - \vec{R}_k(t)\right) \right\rangle d\vec{r}', \tag{2.25}$$

Element	σ_{coh} [b]	σ_{inc} [b]	σ_{tot} [b]	σ_{abs} [b]
Hydrogen	1.7568	80.26	82.02	0.3326
Deuterium	5.592	2.05	7.64	0.000519
Nitrogen	11.01	0.5	11.51	1.9
Oxygen	4.232	0.0008	4.232	0.00019
Carbon	5.551	0.001	5.551	0.0035
Phosphorus	3.307	0.007	1.026	0.172
Aluminum	1.495	0.0082	1.503	0.231
Vanadium	0.0184	5.08	5.1	5.08

Table 2.1. Coherent and incoherent neutron scattering cross sections (σ_{coh}, σ_{inc}), total scattering cross section (σ_{tot}), and absorption cross section (σ_{abs}) for thermal neutrons (2200 m/s, 300 K) of key elements in biomolecules and neutron scattering studies. Cross sections are in barns (1 b = 10^{-24} cm^2). Data sourced from NIST Center for Neutron Research (NCNR)

which represents the probability of finding a particle at position $\vec{r}$ at time t, given that another particle was at the origin at time $t = 0$. Similarly, the van Hove self-correlation function is obtained from $S_{\text{inc}}(\vec{q}, \omega)$:

$$G_{\text{inc}}(\vec{r}, t) = \frac{1}{(2\pi)^3 \hbar} \sum_j \left(\overline{|b_j|^2} - |\overline{b_j}|^2 \right) \int d^3q \, e^{-i\vec{q}\cdot\vec{r}} \left\langle e^{-i\vec{q}\cdot(\vec{R}_j(0) - \vec{R}_j(t))} \right\rangle . \tag{2.26}$$

In real space, this becomes

$$G_{\text{inc}}(\vec{r}, t) = \frac{1}{N} \sum_j \int \left\langle \delta\left(\vec{r}' - \vec{R}_j(0)\right) \, \delta\left(\vec{r}' + \vec{r} - \vec{R}_j(t)\right) \right\rangle \, d\vec{r}', \tag{2.27}$$

which gives the probability of finding the same particle at position $\vec{r}$ at time t, given that it was at the origin at $t = 0$.

A particularly illustrative case is hydrogen, which has nuclear spin $s = 1/2$. The large difference between $b_+ = 10.85$ fm and $b_- = -47.52$ fm leads to a high variance in the scattering lengths, and thus to a large incoherent cross section. However, deuterium, the isotope of hydrogen with nuclear spin s = 1, exhibits quite different scattering properties. Its scattering lengths are more similar in magnitude, resulting in a much smaller incoherent cross section compared to hydrogen. This contrast between hydrogen and deuterium is often exploited in neutron scattering studies of biological samples, which are typically rich

in hydrogen atoms. The implications of this difference will be explored in detail in the following chapters.

2.2 Diffusion in condensed matter systems

The study of diffusion processes in condensed matter systems is fundamental to understanding a wide variety of physical, chemical, and biological phenomena. At the microscopic level, diffusion arises from the stochastic motion of particles driven by thermal fluctuations. This motion, often characterized as a random walk, leads to the net transport of matter over time [10–13].

2.2.1 Brownian motion and Fickian diffusion

In its classical formulation, diffusion is modeled as Brownian motion, where particles undergo uncorrelated, stochastic displacements due to collisions with surrounding molecules. This leads to a Gaussian distribution of particle positions and a linear growth of the mean-square displacement (MSD) with time. When these conditions hold, the process is referred to as Fickian diffusion, characterized by a constant translational diffusion coefficient D and governed at the macroscopic scale by Fick's laws of diffusion.
Fick's first law establishes a linear relationship between the diffusive flux $\vec{J}(\vec{r},t)$ and the concentration gradient $\nabla c(\vec{r},t)$:

$$\vec{J}(\vec{r},t) = -D\,\nabla c(\vec{r},t), \tag{2.28}$$

where $c(\vec{r},t)$ denotes the particle concentration at position $\vec{r}$ and time t, and D is the (scalar) diffusion coefficient. This expression assumes isotropic and homogeneous media and reflects the intuitive idea that particles migrate from regions of high to low concentration. For clarity, Eq. (2.28) concerns the evolution of the collective density field $c(\vec{r},t)$.
Conservation of mass requires that the change in concentration equals the negative divergence of the flux,

$$\frac{\partial c(\vec{r},t)}{\partial t} = -\nabla\cdot\vec{J}(\vec{r},t), \tag{2.29}$$

which, combined with Eq. (2.28), yields Fick's second law:

$$\frac{\partial c(\vec{r},t)}{\partial t} = D\,\nabla^2 c(\vec{r},t), \tag{2.30}$$

where ∇^2 is the Laplacian. For an initial delta distribution, Eq. (2.30) predicts a Gaussian concentration profile that broadens over time:

$$c(\vec{r}, t) = \frac{1}{(4\pi D t)^{d/2}} \exp\left[-\frac{r^2}{4Dt}\right]. \tag{2.31}$$

At the single-particle level, the diffusive behavior is quantified by the mean-square displacement (MSD) of a tagged particle,

$$\langle r^2(t)\rangle = \left\langle |\vec{r}(t) - \vec{r}(0)|^2 \right\rangle = 2d\, D_{\text{self}}\, t, \tag{2.32}$$

which in three dimensions reduces to $\langle r^2(t)\rangle = 6D_{\text{self}}t$. This linear scaling is the hallmark of Fickian (normal) diffusion when displacements are uncorrelated beyond a characteristic relaxation time. In ideal dilute systems D_{self} and the collective diffusivity D coincide, whereas in interacting or heterogeneous media they may differ.

2.2.2 Anomalous diffusion

In many systems of interest, especially those with structural heterogeneity, interactions, or constraints, deviations from Fickian behavior emerge [14]. These are collectively referred to as anomalous diffusion, characterized by a non-linear time dependence of the MSD:

$$\langle r^2(t)\rangle \sim t^{\alpha}, \tag{2.33}$$

with $\alpha \neq 1$. When $\alpha < 1$, the system exhibits subdiffusion, typically due to obstacles, binding events, viscoelastic damping, or confinement. In contrast, $\alpha > 1$ indicates superdiffusion, which can arise in systems with long-range correlations, active driving, or persistent motion.

Among the different ways anomalous diffusion can manifest, jump diffusion occupies a historically central role. Broadly speaking, this term denotes transport processes where motion proceeds through intermittent episodes of localization and displacement rather than by continuous Brownian trajectories. The concept has appeared in several forms depending on the underlying physical picture and the system studied. In solid-state diffusion, for example, the models of Chudley-Elliott [15] and Hall-Ross [16] describe atoms performing discrete jumps between equivalent lattice sites, leading to characteristic quasi-elastic broadening patterns in the scattering spectra. In contrast, the heuristic model proposed by Singwi and Sjölander [17] was developed for molecular motion in liquid water,

where particles undergo localized vibrations within transient cages and intermittently perform jumps to neighboring regions.

Within the Singwi-Sjölander framework, a particle remains confined for an average residence time τ before performing a random jump of characteristic length l. The resulting quasi-elastic linewidth follows

$$\Gamma(q) = \frac{Dq^2}{1 + Dq^2\tau}, \tag{2.34}$$

where $D = l^2/(6\tau)$ is the long-time diffusion coefficient. This simple expression interpolates between the localized limit ($q^2 D\tau \gg 1$) and the continuous diffusive regime ($q^2 D\tau \ll 1$), offering a unified description of the crossover between restricted and free motion. Because of its analytical simplicity and physical transparency, the Singwi-Sjölander model remains widely used as a convenient representation of intermittent dynamics observed in quasi-elastic neutron scattering.

In this thesis, the Singwi-Sjölander formalism is adopted in an even broader and more phenomenological sense. Rather than implying literal molecular jumps, it serves as a conceptual framework to describe diffusion processes governed by dynamic heterogeneity. From this perspective, the model provides a useful bridge between heterogeneous relaxation and apparent deviations from Fickian behavior, offering a deeper physical interpretation of complex diffusive dynamics beyond the conventional jump-diffusion picture.

2.2.3 Self- and collective diffusion

As introduced earlier in the discussion of coherent and incoherent scattering, particle diffusion in many-body systems can be decomposed into self and collective components, described respectively by the self part $G_{\mathrm{inc}}(\vec{r}, t)$ and the distinct part $G_{\mathrm{coh}}(\vec{r}, t)$ of the van Hove correlation function.

Figure 2.2 schematically illustrates these concepts by showing a system of randomly distributed particles evolving over a time interval from t_0 (light gray) to $t_0 + \Delta t$ (dark gray). The self dynamics track the trajectory of an individual particle, correlating its position at t_0 with its position at later times. In contrast, the collective dynamics reflect correlations between the initial position of a particle and the overall spatial arrangement of all particles as the system evolves. This visualization provides an intuitive complement to the formal definitions given by the van Hove functions.

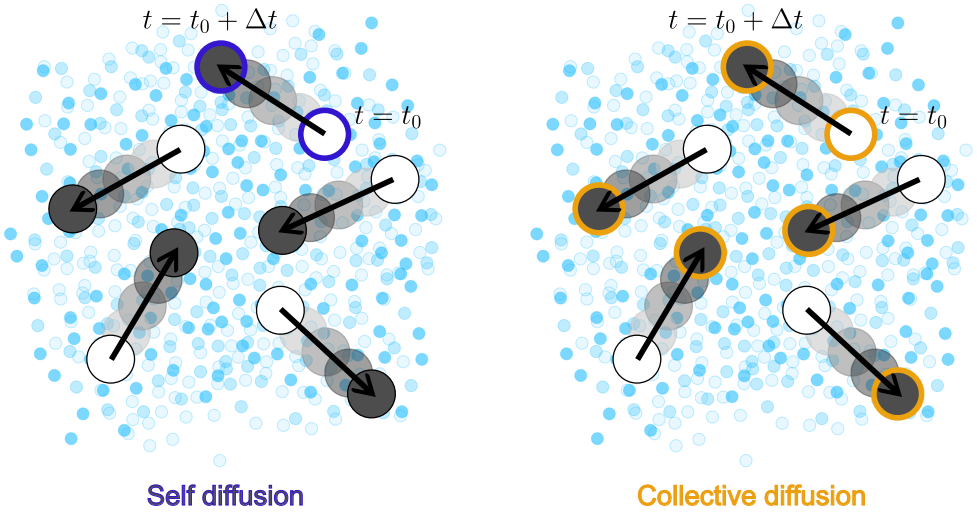

Figure 2.2. Representation of self and collective dynamics in a system of randomly distributed particles, visualized across a time interval from $t = t_0$ (white) to $t = t_0 + \Delta t$ (dark gray), with intermediate configurations shown in between. Self dynamics describes how the trajectory of an individual particle evolves over time by correlating its position at t_0 with its position at later times (highlighted in blue). Collective dynamics, on the other hand, involves correlations between the initial position of a particle and the overall spatial arrangement of all particles at subsequent times (highlighted in orange). Figure adapted from [18] and rendered with Inkscape.

For an ideal diffusive process, the self part of the van Hove function is isotropic and Gaussian:

$$G_{\text{inc}}(\vec{r}, t) = \frac{1}{(4\pi D t)^{3/2}} \exp\left(-\frac{r^2}{4Dt}\right), \tag{2.35}$$

where D is the diffusion coefficient. Fourier transforming G_{inc} in space yields the incoherent intermediate scattering function:

$$I_{\text{inc}}(\vec{q}, t) = \exp\left(-Dq^2 t\right). \tag{2.36}$$

Subsequent temporal Fourier transformation produces the dynamic structure factor:

$$S_{\text{inc}}(\vec{q}, \omega) = \frac{1}{\pi} \frac{\Gamma(q)}{\omega^2 + \Gamma(q)^2}, \tag{2.37}$$

where the half-width at half-maximum (HWHM) is

$$\Gamma(q) = Dq^2. \tag{2.38}$$

This Lorentzian shape reflects the exponential decay of the self-intermediate scattering function and is fundamental for extracting diffusion coefficients in quasi-elastic neutron

scattering (QENS) experiments. In concentrated suspensions of (approximately) spherical colloids, Eq. (2.38) remains valid for the incoherent contribution in the asymptotic short- and long-time regimes, provided that D is interpreted as the corresponding effective self-diffusion coefficient, that is, $\Gamma(q) = D_s^{\text{short}} q^2$ for $t \ll t_\alpha$ and $\Gamma(q) = D_s^{\text{long}} q^2$ for $t \gg t_\alpha$, with crowding and hydrodynamic interactions renormalizing D but not the q^2 scaling.

The distinction between self and collective diffusion is crucial, as they probe different physical aspects: self-diffusion pertains to individual particle trajectories governed mainly by thermal motion, whereas collective diffusion encompasses many-body correlations influenced by interactions and structural organization. In dense or structured media, the coherent intermediate scattering function $I_{\text{coh}}(\vec{q}, t)$ typically exhibits slower decay than $I_{\text{inc}}(\vec{q}, t)$, signaling effects such as caging, hydrodynamic coupling, or emergent order; more generally, near maxima of the static structure factor $S(q)$ the decay of I_{coh} is further slowed (de Gennes narrowing).

Deviations from ideal Fickian diffusion often arise in both self and collective dynamics, manifested as non-Gaussian displacement distributions or slow relaxation processes. These deviations indicate underlying complexity in particle motion, including heterogeneity, crowding effects, and structural constraints.

In addition to experimental methods, molecular dynamics (MD) simulations offer a microscopic perspective by explicitly resolving the trajectories of individual particles. From MD trajectories, both the self part $G_{\text{inc}}(\vec{r}, t)$ and the distinct part $G_{\text{coh}}(\vec{r}, t)$ of the van Hove correlation function can be directly computed. This enables quantitative comparison with QENS and NSE measurements and facilitates a detailed exploration of the underlying diffusion mechanisms. The high temporal and spatial resolution of MD is particularly valuable for investigating systems where confinement, complex geometries, or hierarchical structures strongly influence both self and collective dynamics.

In many-particle systems such as colloidal suspensions, polymer networks, or crowded biological environments, the motion of individual particles is strongly influenced by the presence of neighboring entities [19]. This crowding effect reduces the available free volume and introduces hydrodynamic and steric interactions that slow down diffusion and lead to heterogeneous dynamics. As a consequence, the effective diffusion coefficient becomes concentration-dependent, and deviations from simple Fickian behavior may arise, often manifesting as subdiffusive motion or anomalously slow relaxation. Understanding

crowding is therefore essential for describing transport processes in dense soft-matter and biological systems.

2.2.4 Dynamical independence approximation

In many complex condensed matter systems, the overall atomic or molecular dynamics results from the superposition of several distinct types of motion, such as translational diffusion, rotational reorientations, and vibrational fluctuations. These motions often occur on different time and length scales and can be weakly coupled or dynamically independent.

When the coupling between these motions is negligible, the total intermediate scattering function can be approximated as the product of the individual contributions:

$$I(\vec{q},t) = I_{\text{trans}}(\vec{q},t) \cdot I_{\text{rot}}(\vec{q},t) \cdot I_{\text{vib}}(\vec{q},t), \tag{2.39}$$

where I_{trans}, I_{rot}, and I_{vib} correspond to translational, rotational, and vibrational components, respectively.

Accordingly, the dynamic structure factor in the frequency domain is given by the convolution of these separate contributions:

$$S(\vec{q},\omega) = S_{\text{trans}}(\vec{q},\omega) \otimes S_{\text{rot}}(\vec{q},\omega) \otimes S_{\text{vib}}(\vec{q},\omega). \tag{2.40}$$

Within the quasi-elastic region, vibrational motions typically contribute as an elastic term, often approximated by a Debye-Waller factor (DWF), denoted as $\beta(\vec{q})$, which modulates the elastic intensity.

2.3 Neutron Spectroscopy

2.3.1 Quasi-elastic neutron scattering (QENS)

Neutron scattering experiments are generally classified according to the energy exchange between the incident neutron and the sample. When there is no measurable energy transfer (or when it falls below the resolution of the instrument) the process is termed elastic scattering. In this case, the scattered intensity ideally forms a delta function centered at zero energy transfer reflecting truly static components; in practice, very slow components

whose energy exchange with the neutron is smaller than the instrument's resolution also contribute to this peak, appearing effectively indistinguishable from a true delta function. Conversely, when the scattered neutron undergoes a well-defined energy exchange with the sample, associated with the excitation or relaxation of elementary modes, the process is known as inelastic scattering. These excitations appear as distinct peaks at specific energy transfers in the measured spectrum. QENS occupies an intermediate regime characterized by small but measurable energy exchanges, typically in the microelectronvolt to millielectronvolt range. Instead of distinct peaks, QENS manifests as a broadening around the elastic line in the dynamic structure factor $S(\vec{q},\omega)$. This broadening reflects diffusive or overdamped motions occurring on timescales accessible to the experiment. The three types of scattering processes are illustrated in Figure 2.3.

As introduced in Eq. (2.21), the dynamic structure factor $S(\vec{q},\omega)$ can be decomposed into coherent and incoherent components, which respectively describe correlated and self-correlated motions within the sample. In QENS experiments, the measured $S(\vec{q},\omega)$ arises from the sum of all scattering contributions, whose relative weights depend on the isotopic composition and interaction strengths. Most commonly, QENS is used to follow self dynamics, taking advantage of the strong neutron–hydrogen interaction, while coherent contributions may also play a role in some cases. QENS spectrometers are generally categorized as: (i) direct-geometry time-of-flight (ToF); (ii) indirect-geometry time-of-flight, commonly implemented as backscattering time-of-flight (BS-ToF); and (iii) indirect-geometry without ToF (backscattering (BS)). All cover a similar q-range (0.2-2 Å^{-1}) but differ in energy resolution and accessible time windows: BS offers the highest resolution ($\sim 1\,\mu$eV) but limited time range, while BS-ToF and ToF spectrometers provide greater flexibility and broader dynamic coverage, particularly for faster processes. Given the broad range of dynamical timescales in soft matter, it is often necessary to combine data from different spectrometers to capture the full spectrum of motions. The specific instruments employed in this thesis will be discussed in detail in a later chapter.

NSE spectroscopy is also considered a QENS technique, as it probes quasi-elastic processes, but it operates on a fundamentally different principle by directly measuring the intermediate scattering function $I(q,t)$ in the time domain. Because of this conceptual difference, NSE is discussed separately in the following section. QENS is particularly well suited for probing dynamical processes on picosecond to nanosecond timescales and over length scales of a few to several tens of angstroms, as illustrated in Figure 2.4, compa-

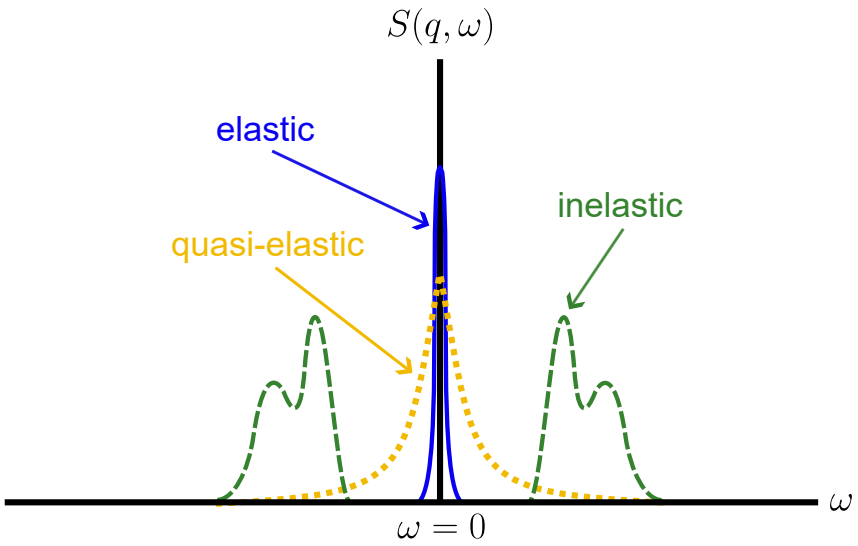

Figure 2.3. Sketch of the scattering function of elastic, quasi-elastic and in neutron scattering, in the absence of so-called detailed-balance effeincts. Elastic scattering appears as a sharp peak at $\omega = 0$, QENS results in a broader peak also centered at $\omega = 0$, while inelastic scattering is characterized by peaks at $\omega \neq 0$. Figure adapted from [20] and rendered with Inkscape.

rable to typical intermolecular and intramolecular distances. It is especially sensitive to self-dynamics and local motions, making it highly suitable for the study of hydrogenous materials. From the spectral broadening, quantitative information such as diffusion coefficients and relaxation times can be extracted, as well as the geometry of the underlying motions [8]. The technique captures a wide range of dynamics, including localized rotations [21], segmental relaxations [22], reorientations [23], and translational diffusion [24]. Importantly, the specific types of motion that contribute to the QENS signal depend not only on the system under investigation, but also on the instrumental resolution.

Furthermore, the temporal and spatial scales probed by QENS closely align with those accessible via molecular dynamics (MD) simulations, enabling direct comparison. This complementarity allows QENS to validate computational models and benefits from simulation insights to interpret experimental data [26–28]. Combining QENS with other complementary experimental techniques is becoming common practice for a comprehensive understanding of molecular dynamics [29].

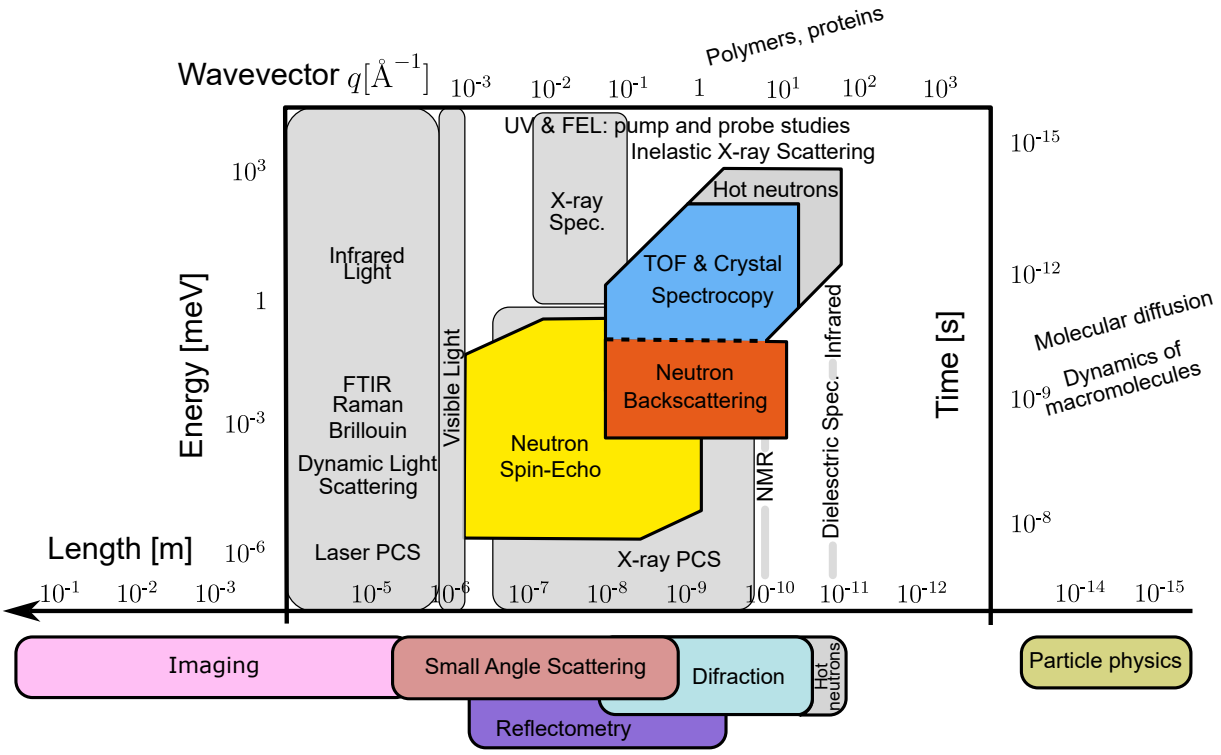

Figure 2.4. The diagram maps the range of length scales (bottom axis) and time scales (right axis) accessible by various scattering techniques, as determined by the energy (left axis) and wavevector q (top axis) involved in the measurement. Static scattering methods appear in the lower region. Representative examples of biological or soft matter systems, along with phenomena occurring at corresponding spatial and temporal scales, are also indicated. The dashed line indicates that the techniques are not completely separate and may be related. The figure represents a simplified and conceptual sketch. Figure adapted from [25] and rendered with Inkscape.

2.3.2 Elastic incoherent structure factor (EISF)

When analyzing the self part of the time-dependent pair correlation function, $G_{\text{inc}}(\vec{r}, t)$, in the limit $t \to \infty$, two regimes can be distinguished depending on the nature of the motion. For particles undergoing unrestricted diffusion, $G_{\text{inc}}(\vec{r}, t)$ decays to zero at long times, as the particle can explore all space. In contrast, when motion is confined within a finite volume, the function approaches a non-zero asymptote:

$$G_{\text{inc}}(\vec{r}, t) = G_{\text{inc}}(\vec{r}, \infty) + G'_{\text{inc}}(\vec{r}, t), \tag{2.41}$$

with $G'_{\mathrm{inc}}(\vec{r}, t \to \infty) = 0$. This distinction is reflected in the incoherent scattering function, which in the case of confined motion can be expressed as a sum of two contributions:

$$S_{\mathrm{inc}}(\vec{q}, \omega) = S^{\mathrm{el}}_{\mathrm{inc}}(\vec{q})\, \delta(\omega) + S^{\mathrm{in}}_{\mathrm{inc}}(\vec{q}, \omega) \tag{2.42}$$

The elastic term $S^{\mathrm{el}}_{\mathrm{inc}}(\vec{q})$ contains information about spatial confinement and the geometry of motion and is commonly referred to as the Elastic incoherent structure factor (EISF). If both the total scattering function $S_{\mathrm{inc}}(\vec{q}, \omega)$ and the inelastic component due to unbound diffusion $S^{\mathrm{in}}_{\mathrm{inc}}(\vec{q}, \omega)$ are normalized, Eq. (2.42) can be expressed as:

$$S_{\mathrm{inc}}(\vec{q}, \omega) = A_0(\vec{q})\, \delta(\omega) + [1 - A_0(\vec{q})]\, S^{\mathrm{in}}_{\mathrm{inc}}(\vec{q}, \omega), \tag{2.43}$$

where $A_0(\vec{q}) \equiv S^{\mathrm{el}}_{\mathrm{inc}}(\vec{q})$ represents the elastic incoherent structure factor (EISF) in this normalized formulation. Within this context, $A_0(\vec{q})$ corresponds to the relative elastic weight in the total scattering function. Strictly speaking, this equality holds only when the total scattering is normalized; otherwise, $A_0(\vec{q})$ is commonly treated as an effective or empirical EISF parameter, obtained directly from spectral fitting rather than from explicit integration of elastic and inelastic intensities.

More generally, the EISF is defined as

$$\mathrm{EISF} = \frac{I_{\mathrm{el}}}{I_{\mathrm{el}} + I_{\mathrm{inel}}}, \tag{2.44}$$

which coincides with $A_0(\vec{q})$ when the spectra are normalized such that $\int_{-\infty}^{\infty} S_{\mathrm{inc}}(\vec{q}, \omega)\, d\omega = 1$. Analytical expressions for $A_0(\vec{q})$ exist for various geometries of confined motion (e.g., rotational diffusion on a sphere, localized hopping, diffusion within a sphere), providing a powerful means to extract structural and dynamical information from experimental data [30–32].

It is important to note that the experimental determination of the EISF depends on the resolution of the spectrometer used. Due to the finite energy resolution of neutron instruments, only motion that appears static over the instrument's observation time $t_{\mathrm{obs}} \propto 1/\Delta E$ will contribute to the elastic signal. Therefore, measurements performed on different instruments with varying resolutions may yield different EISF values for the same sample, reflecting the timescale sensitivity of the technique.

2.3.3 Neutron backscattering spectroscopy (NBS)

Backscattering spectrometers are indirect-geometry instruments optimized to achieve the highest possible energy resolution in neutron spectroscopy. Their hallmark is the use of monochromator and/or analyser crystals operated in near-backscattering geometry with scattering angles close to 180°. The benefit of this geometry follows from the differential form of Bragg's law (i.e., the Gaussian error on the wavelength definition):

$$n\lambda = 2d\sin\theta \quad \Rightarrow \quad (\Delta\lambda)^2 = (2\,\Delta d\sin\theta)^2 + (2d\cos\theta\,\Delta\theta)^2. \tag{2.45}$$

At $\theta = 90°$ the angular term vanishes and the wavelength spread depends only on crystal imperfections (Δd). Consequently, backscattering instruments can reach sub-μeV resolution, resolving dynamical processes on timescales of tens to hundreds of picoseconds.

As a concrete example, we describe the operation of the IN16B backscattering spectrometer in inverted neutron time-of-flight (BATS) mode, which serves as the reference instrument for this work (see Fig. 2.5). Backscattering spectrometers can be conceptually divided into two parts: the primary spectrometer, which defines the incident neutron energy, and the secondary spectrometer, which analyzes the scattered neutrons.

In the primary spectrometer, neutrons from the source are first pulsed by a system of choppers, establishing the time structure necessary for ToF determination of the incident energy. A velocity selector subsequently transmits only a narrow wavelength band centered on the desired value, thereby restricting the distribution of incident velocities. In BATS mode, the temporal width of the pulses and hence the effective incident wavelength band at the sample is set by the chopper-sample distance and rotation speed, and is ideally matched to the transmission range of the velocity selector [33, 35]. Finally, a background chopper suppresses noise and avoids overlap between consecutive pulses, ensuring a clean incident beam.

In the secondary spectrometer, after neutrons scatter from the sample, only those with the selected final energy are reflected by analyzer crystals operating in near-backscattering geometry. These neutrons are then collected by detectors placed around and behind the sample. The energy transfer is thus obtained from the difference between the well-defined final energy and the incident energy deduced from the ToF measurement. The bottom panel of Fig. 2.5 shows a distance-time diagram that tracks neutron packets from the source to the detectors while color-coding their energy.

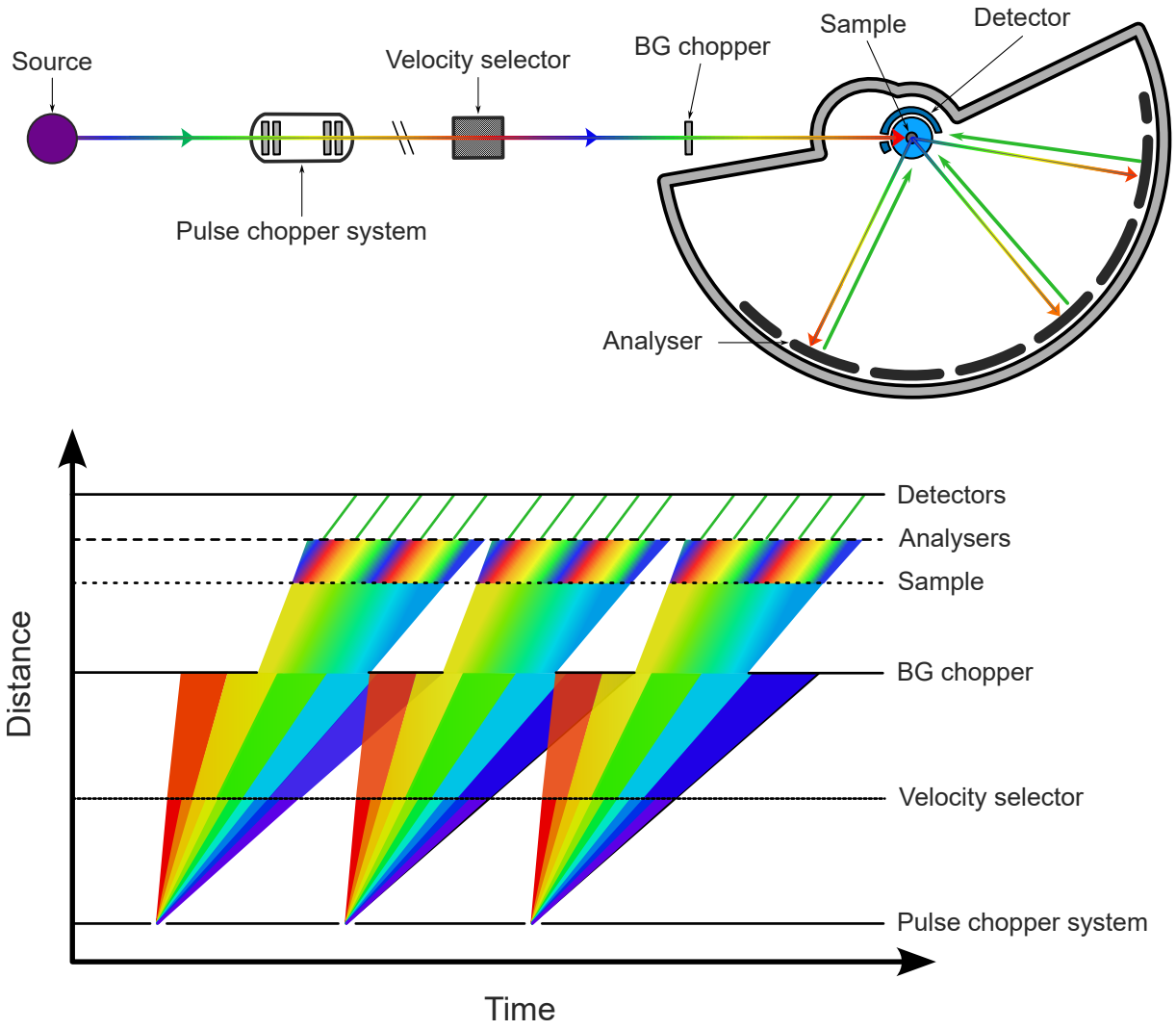

Figure 2.5. Top: schematic layout of the IN16B backscattering spectrometer in BATS mode. **Bottom**: distance-time diagram showing how neutron energy evolves across the instrument. In both panels, energy is color-coded from red (higher) to blue (lower). Figure adapted from [33, 34] and rendered with Inkscape.

The pulse shape and duration are crucial parameters for this type of instrument. Shorter pulses provide a more precise determination of the neutron time-of-flight, thereby improving the energy resolution; however, this comes at the expense of the accessible dynamic range, since shorter pulses restrict the usable time frame between pulses and thus the spread of measurable energies. The BATS mode of IN16B is designed to optimize this trade-off, enabling sub-μeV energy resolution while maintaining a suitable energy window for QENS experiments.

2.3.4 Neutron spin-echo (NSE)

While some high resolution spectroscopy techniques like backscattering and time-of-flight provide direct access to $S(q,\omega)$, Neutron spin-echo (NSE) offers an alternative approach that directly measures the intermediate scattering function $I(q,t)$ in the time domain. Rather than determining the energy transfer $\hbar\omega$ from the difference of initial and final neutron energies, NSE uses the neutron spin as a phase-sensitive probe to track minute changes in velocity, effectively acting as an internal clock for each neutron.

The principle of NSE is based on Larmor precession: a polarized neutron beam is subjected to controlled magnetic fields before and after the scattering event. When traversing a magnetic field of strength B, the neutron spin precesses around the field direction with a Larmor frequency $\omega_L = -\gamma_L B$, where $\gamma_L = 2.916\,\mathrm{kHz/Oe}$ is the neutron gyromagnetic ratio commonly referred to as the Larmor constant. The total accumulated precession angle is proportional to the flight time of the neutron through the field, which in turn is determined by the velocity of the neutron. Thus, any change in neutron velocity due to scattering translates into a change in spin phase.

In a typical NSE setup, the polarized neutrons first pass through a $\pi/2$ flipper, which tips their spins into the transverse plane relative to a guide field. They then enter the first magnetic precession region (length l_1, field B_1), where the spins accumulate a phase

$$\phi_1 = -\gamma_L \frac{B_1 l_1}{v_1}. \tag{2.46}$$

After interacting with the sample, the scattered neutrons pass through a π-flipper, which inverts the accumulated phase, and enter a second precession region (length l_2, field B_2) where they accumulate a further phase

$$\phi_2 = -\gamma_L \frac{B_2 l_2}{v_2}, \tag{2.47}$$

The total spin-echo signal depends on the difference $\phi = \phi_1 - \phi_2$, which vanishes in the case of purely elastic scattering with identical precession fields and paths.

When the neutron experiences a small energy change $\hbar\omega$ due to inelastic scattering, the resulting shift in velocity causes a residual phase difference between the two arms. This phase difference leads to a reduction in the measured polarization of the neutron beam, which encodes information about the distribution of energy transfers $S(q,\omega)$. Importantly, the spin-echo polarization $P(t)$ is the normalized cosine transform of the dynamic

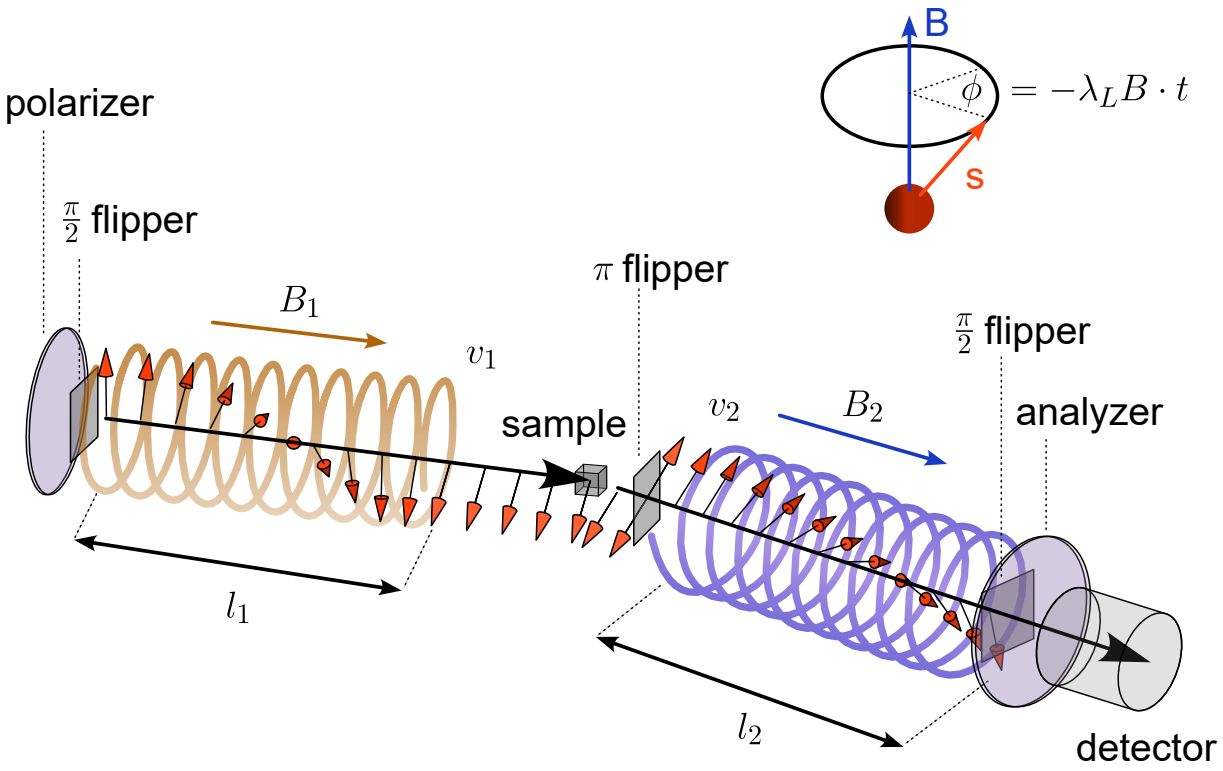

Figure 2.6. Schematic of a spin-echo spectrometer, showing the primary (yellow) and secondary (purple) sections. A neutron beam enters from the left with velocity v_1 and is polarized by a mirror, aligning spins along the magnetic field B_1 (black arrow in the middle of the yellow solenoid). Passing through a $\pi/2$ spin-flipper, spins rotate perpendicular to B_1 (first red arrow). Neutrons then undergo Larmor precession over length l_1, acquiring a phase $\varphi_1 = -\gamma_L B_1 l_1 / v_1$ (illustrated in the top right inset). After scattering on the sample (grey cube), velocity changes to v_2 and spins are inverted by a π-flipper, preserving the component along the field. The beam then enters the secondary solenoid (purple), precessing around field B_2 over distance l_2. A final $\pi/2$ flip realigns spins before analysis and detection on the right. Figure adapted from [36] and rendered with Inkscape.

structure factor,

$$P(t) = \frac{\int_{-\infty}^{\infty} S(q,\omega)\, \cos(\omega t)\, d\omega}{\int_{-\infty}^{\infty} S(q,\omega)\, d\omega} \equiv \frac{I(q,t)}{I(q,0)}. \tag{2.48}$$

where t is the spin-echo (Fourier) time determined by the instrument configuration. NSE thus, directly measures the normalized intermediate scattering function $I(q,t)/I(q,0)$, bypassing the need for a Fourier transform from energy space and allowing access to dynamical processes on nanosecond to sub-microsecond time scales (Figure 2.4).

In real experiments, corrections are needed to account for changes in the neutron polarization due to spin-incoherent scattering processes. For an incoherently scattering system, the polarization loss is characterized by a prefactor $P_S = -\frac{1}{3}P_0$, where P_0 is the polarization of the incoming neutron beam. The total measured NSE signal is then given by

$$\frac{I(q,t)}{I(q,0)} = \frac{S_{\mathrm{coh}}(q,t) - \frac{1}{3}S_{\mathrm{inc}}(q,t)}{S_{\mathrm{coh}}(q,0) - \frac{1}{3}S_{\mathrm{inc}}(q,0)}. \tag{2.49}$$

Experimentally, the scattering vector q is varied by rotating the detector around the sample, while the Fourier time t is tuned by adjusting the incident neutron wavelength and the strength of the precession fields. For a given wavelength, a range of t values can be probed by fine-tuning the symmetry of the magnetic fields in the precession arms. Measurements are typically acquired in groups (echo groups) corresponding to different t-values, from which the full time-dependence of $I(q,t)$ is reconstructed.

NSE is particularly well suited for studying slow and collective motions in soft matter and biological systems, such as diffusion, segmental dynamics, and conformational fluctuations. In the context of this thesis, NSE provides access to the time-resolved dynamics of proteins in solution at different concentrations, complementing the spatial structural information obtained from SANS.

2.4 Small-Angle Neutron Scattering (SANS)

Small angle neutron scattering (SANS) is a powerful technique used to probe the structural organization of materials at nanometer to micrometer length scales. By measuring the intensity of neutrons scattered at small angles, typically below a few degrees, SANS provides access to information about the size, shape, and spatial correlations of scattering entities in a sample. It is particularly well-suited for investigating soft matter, polymers, biological macromolecules, and porous materials, where relevant structures span from 1 to several hundred nanometers (Figure 2.4).

SANS is classified as a scattering technique, in which the angular distribution of scattered intensity is measured without resolving energy changes. In practice, the signal is dominated by elastic scattering, providing information on the static structure of the sample.

The working principle of a SANS instrument is illustrated in Figure 2.7.

The scattering intensity $I(q)$ recorded in a SANS experiment depends on the magnitude

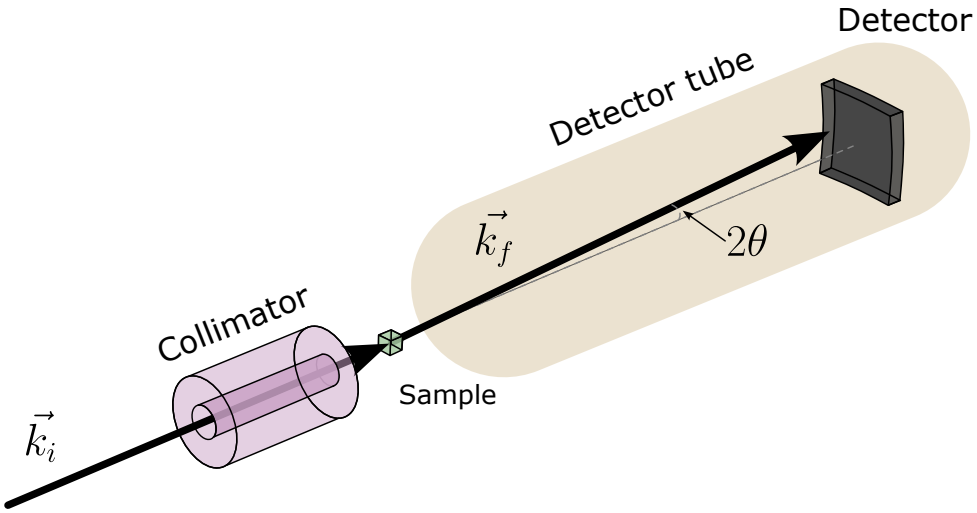

Figure 2.7. Schematic representation of a typical ng setup. Figure adapted from [36] and rendered with Inkscape.

of the scattering vector, defined as

$$q = \frac{4\pi \sin\theta}{\lambda}, \tag{2.50}$$

where θ is half the scattering angle and λ is the incident neutron wavelength. This expression is directly related to Bragg's law, which states that constructive interference occurs when

$$\lambda = 2d \sin\theta, \tag{2.51}$$

where d is the characteristic distance between scattering planes or structural features. In reciprocal space, combining Eq. (2.50) and Eq. (2.51) leads to the relation

$$q = \frac{2\pi}{d}, \tag{2.52}$$

indicating that small scattering angles (low q values) correspond to large real-space distances. In the low-q regime, where $q \ll \pi/d$, the scattering experiment does not resolve individual atoms. Instead, scattering arises from the interference of neutron waves scattered by regions of characteristic size $l \approx \pi/q$. In this limit, the discrete summation over atomic scattering centers can be approximated by a continuous spatial integral over fluctuations in the scattering length density (SLD). The local SLD $\rho(\vec{r})$ varies throughout the sample due to the presence of different particles embedded in a solvent matrix, and its spatial average over the illuminated volume is denoted by $\langle\rho\rangle$. The scattering-relevant quantity is then the deviation from this average, defined as

$$\delta\rho(\vec{r}) = \rho(\vec{r}) - \langle\rho\rangle. \tag{2.53}$$

Using this definition, the coherent part of the differential scattering cross section can be expressed as

$$\left(\frac{d\sigma}{d\Omega}\right)_{\text{coh}} = \frac{1}{N}\left|\int_V \delta\rho(\vec{r})\, e^{i\vec{q}\cdot\vec{r}}\, d\vec{r}\right|^2, \tag{2.54}$$

where the integral is performed over the sample volume V and N is the number of scattering centers. This coherent term captures spatial correlations in the SLD fluctuations, while incoherent scattering appears as an isotropic flat background.

Considering the case of N_p identical particles with homogeneous scattering length density (SLD) ρ_p, embedded in a solvent of SLD ρ_s, the contrast between the particles and the solvent is defined as

$$\Delta\rho = \rho_p - \rho_s. \tag{2.55}$$

Each particle occupies a volume V_p, and the particles are positioned at distinct locations $\vec{R}_j$ within the sample. In this model, the SLD fluctuation $\delta\rho(\vec{r})$ is nonzero only inside the particles and zero elsewhere. The coherent part of the differential scattering cross section can then be expressed as

$$\left(\frac{d\sigma}{d\Omega}\right)_{\text{coh}} = \Delta\rho^2 \left|\sum_{j=1}^{N_p} \int_{V_p} e^{i\vec{q}\cdot(\vec{r}+\vec{R}_j)}\, d\vec{r}\right|^2. \tag{2.56}$$

Since all particles are assumed to be identical in shape and composition, we factorize

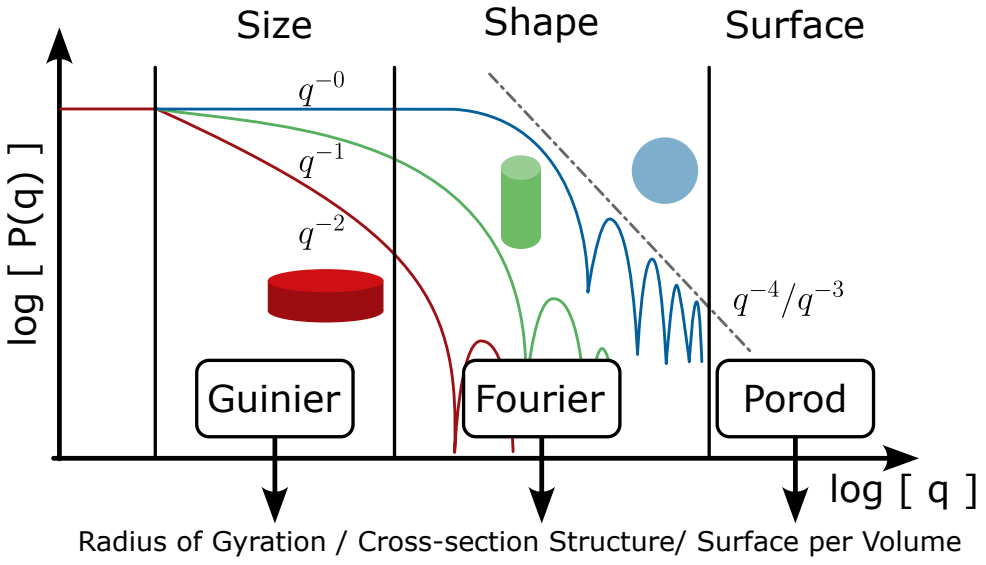

Figure 2.8. Characteristic q-regimes of the form factor for model particle geometries. Figure adapted from [37]

the scattering amplitude into a single-particle contribution and a term describing their spatial arrangement. The integral inside the sum,

$$F(\vec{q}) = \int_{V_p} e^{i\vec{q}\cdot\vec{r}}\, d\vec{r}, \tag{2.57}$$

is known as the form factor amplitude, representing the Fourier transform of the scattering length density of a single particle. Physically, $F(\vec{q})$ encodes information about the shape, size, and internal structure of an individual scatterer. The experimentally measurable counterpart of this quantity is the form factor, defined as the normalized squared magnitude of this amplitude,

$$P(\vec{q}) = \frac{1}{V_p^2} \left|F(\vec{q})\right|^2 = \frac{1}{V_p^2} \left| \int_{V_p} e^{i\vec{q}\cdot\vec{r}}\, d\vec{r} \right|^2 . \tag{2.58}$$

Here, $F(\vec{q})$ is the theoretical scattering amplitude of an isolated particle, while $P(\vec{q})$ is the experimental form factor obtained from measurements. The form factor describes how the scattering intensity varies as a function of the scattering vector $\vec{q}$ due to the geometry and internal structure of isolated particles. In the following, we consider the powder average; therefore, we replace the vector $\vec{q}$ with its magnitude q.

Figure 2.8 illustrates the different regimes of the form factor and the types of structural information that can be obtained from each analysis: Guinier, Fourier, and Porod. The Guinier approximation, valid in the low-q limit, allows estimation of the overall size of scattering entities through the radius of gyration, assuming a particular shape such as sphere, cylinder, or disk. A Fourier transformation of the form factor $P(q)$, known as the pair distribution function, provides a histogram of distances within the scattering domains, which can be used to identify the particle shape based on characteristic features in the curves. At high q values, the Porod regime reveals information about the surface-to-volume ratio and the nature of interfaces within the sample.

Up to this point, the discussion has assumed sufficiently low particle concentrations such that correlations between particle positions can be neglected. Under these dilute conditions, the scattering intensity depends solely on the form factor describing isolated particles. However, in many practical systems, such as the concentrated protein solutions studied in this thesis, the spatial arrangement and interactions between particles play a crucial role in determining the scattering behavior.

To account for these inter-particle correlations, the sample can be conceptually divided into N_p cells, each containing exactly one particle located at position $\vec{R}_j$. This subdivision allows us to describe the scattering from the entire system as arising not only from

the individual particle shape and internal structure but also from their relative spatial distribution. Incorporating these positional correlations leads to the introduction of the structure factor, which captures how particles are organized within the sample and how their mutual interference affects the scattering pattern.

$$S(q) = \frac{1}{N_p} \left\langle \sum_{j=1}^{N_p} \sum_{k=1}^{N_p} e^{i\vec{q}\cdot(\vec{R}_j - \vec{R}_k)} \right\rangle, \tag{2.59}$$

where the brackets denote an ensemble average over particle configurations. This factor accounts for interference effects arising from the relative positions of particles and encodes information on particle interactions, ordering, and crowding.

Combining form and structure factors, the total coherent scattering intensity is given by

$$I(q) = N_p \cdot \Delta\rho^2 \cdot V_p^2 \cdot P(q) \cdot S(q). \tag{2.60}$$

Introducing the volume fraction of scatterers,

$$\phi = \frac{N_p V_p}{V}, \tag{2.61}$$

where V is the total sample volume, the expression can be rewritten as

$$I(q) = \phi \cdot \Delta\rho^2 \cdot V_p^2 \cdot P(q) \cdot S(q) + B, \tag{2.62}$$

with B accounting for incoherent and instrumental background.

This separation between form and structure factors is fundamental in SANS analysis: $P(q)$ characterizes individual particle morphology, while $S(q)$ reflects collective effects arising from particle interactions and spatial correlations.

Chapter 3

Biophysical background: β-casein - A review

3.1 Proteins

Proteins are essential macromolecules for life that perform a wide range of functions in all living organisms. These versatile biomolecules are involved in nearly every biological process, including catalyzing chemical reactions, regulating gene expression, transporting molecules, and forming cellular structures. Their biological relevance has made them a central focus of numerous scientific disciplines, not only in biology and medicine, but also in chemical engineering, colloid science, and nanotechnology. When defective or dysregulated, proteins can cause significant cellular dysfunction and contribute to the onset of various diseases [38–41].

At their core, proteins are linear polymers composed of amino acids linked together by peptide bonds. In nature, there are 20 standard amino acids, each with unique physicochemical properties such as charge, polarity, size, and hydrogen bonding capacity. The sequence of amino acids, also known as the primary structure, is genetically encoded and synthesized through the process of translation. Ribosomes read messenger RNA (mRNA) transcripts derived from DNA and assemble polypeptide chains by binding amino acids through peptide bonds in a precise order dictated by the genetic code. Following synthesis, proteins typically fold into specific three-dimensional conformations driven by a variety of non-covalent interactions, including hydrogen bonding, hydrophobic effects, electrostatic interactions, and van der Waals forces. Protein structure is classically described in hierar-

chical levels: the primary structure (sequence), secondary structures (local conformational patterns such as α-helices and β-sheets), tertiary structure (overall 3D fold of a single chain), and quaternary structure (assembly of multiple subunits). This folded structure is typically compact, particularly in the case of globular proteins, and spans just a few nanometers in size.

While classical structural biology has traditionally focused on folded protein conformations, it is now well recognized that biological activity often depends critically on internal and global dynamics. Proteins fluctuate across a wide range of timescales and length scales, from rapid picosecond-scale methyl group rotations to nanosecond backbone motions and slower domain rearrangements. In solution, these internal fluctuations coexist with the translational and rotational diffusion of the center of mass, modulating how proteins explore space, form interactions, and participate in complex reaction networks [42, 43].

These dynamical modes are strongly influenced by the surrounding physicochemical environment. Parameters such as hydration level, ionic strength, pH, temperature, and presence of other macromolecules can alter both internal and global motions. In vivo, cells are densely packed with biomacromolecules, leading to volume exclusion and crowding effects that significantly reduce diffusion coefficients and may modulate conformational flexibility [44–46]. Consequently, studying proteins under dilute, idealized conditions often fails to capture functionally relevant behavior.

Neutron scattering techniques such as NBS and NSE, described in the previous chapter, provide detailed information on protein dynamics across picosecond to nanosecond timescales and nanometer length scales [47–50]. These methods reveal how protein motions, from internal fluctuations to global diffusion, are modulated by factors including hydration, temperature, solvent composition, and crowding [20, 51].

3.2 Intrinsically disordered proteins

For many decades, molecular biology, biochemistry, and protein biophysics have been dominated by the assumption that functional proteins possess unique, stable three-dimensional structures. This view was largely supported by numerous protein structures solved by X-ray crystallography and NMR spectroscopy, which depicted proteins as relatively rigid

molecules with fixed atomic positions fluctuating only slightly around their equilibrium conformations.

According to this classical structure-function paradigm, a specific amino acid sequence encodes a stable three-dimensional fold essential for biological activity. However, recent research has revealed that a significant portion of proteins defies this model [52,53]. Many proteins either lack stable tertiary structures entirely or contain intrinsically disordered regions (IDRs) that do not adopt a fixed conformation under physiological conditions [2]. When disorder is predominant, these proteins are referred to as intrinsically disordered proteins (IDPs), a term that has also historically been described as natively unfolded or intrinsically unstructured [54]. In this work, we use the term IDP broadly to refer to both fully disordered proteins and those containing significant disordered regions. The distinction between folded and IDPs becomes especially clear when considering their conformational ensembles. Folded proteins typically fluctuate around a well-defined native conformation that corresponds to a deep and narrow global energy minimum (Figure 3.1, left). These thermally accessible states are structurally similar, reflecting a stable and compact fold. By contrast, IDPs sample a much broader and more diverse ensemble of conformations. Their energy landscapes are relatively flat, populated by multiple shallow local minima separated by low barriers, often comparable to thermal fluctuations (k_BT). This topography facilitates rapid transitions between distinct conformational states, resulting in a highly dynamic and heterogeneous ensemble (Figure 3.1, right). Rather than representing a limitation, this structural flexibility enables IDPs to perform a wide range of biological functions.

This lack of stable tertiary structure arises from their distinctive sequence properties. IDPs are typically enriched in polar and charged residues, such as glutamic acid, lysine, and serine, while being depleted in hydrophobic amino acids that normally drive protein folding through hydrophobic collapse [56]. Additionally, the presence of disorder-promoting residues like glycine and proline disrupts the formation of stable secondary structures [57]. As a result, IDPs display low sequence complexity, low hydrophobicity, and high net charge characteristics that together prevent the formation of a compact, folded conformation.

Although they lack a stable structure, IDPs are functionally versatile and participate in essential cellular processes such as cellular signaling, regulation, and molecular recognition [58]. Their intrinsic flexibility enables them to interact with multiple partners, often

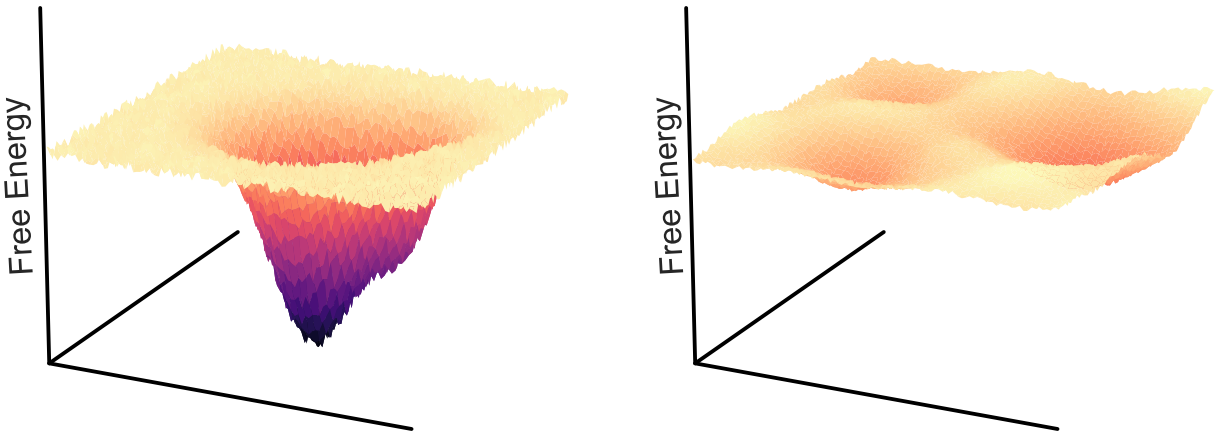

Figure 3.1. Schematic of an energy landscape for an ordered protein (**left**) and a disordered protein (**right**). Ordered proteins have a dominant, deep energy minimum corresponding to a stable native conformation. Disordered proteins exhibit shallow and multiple local minima that enable conformational diversity. The two unlabeled axes denote generic configurational coordinates. Figure generated with Matplotlib [55].

undergoing disorder-to-order transitions upon binding [59]. Moreover, many IDPs exhibit an intrinsic capacity for self-assembly, driven by weak, transient interactions that allow them to form dynamic, higher-order structures without the need for a well-defined folded state [60,61]. Their flexible architecture and multivalent binding capacity also allow them to act as disordered scaffolds capable of transiently binding, storing, or neutralizing small ligands and signaling molecules [62].

However, the same features that confer functional versatility through self-assembly can also predispose IDPs to pathological aggregation. When the finely tuned balance between dynamic interactions and structural disorder is perturbed, IDPs can misassemble into toxic oligomers or fibrillar aggregates. This process is central to the pathogenesis of several neurodegenerative diseases, including Alzheimer's, Parkinson's, and amyotrophic lateral sclerosis, where disordered proteins such as tau, α-synuclein, and TDP-43 are known to misfold and accumulate abnormally [63–65]. Likewise, the malfunction of self-assembling disordered domains in key regulatory proteins, such as p53 or c-Myc, has been linked to cancer [66].

3.3 β-Casein as a model IDP

Identifying an appropriate model system is a critical step in the study of IDPs, especially when aiming to explore their behavior under diverse yet controlled experimental conditions. For this work, we selected β-casein, one of the major milk proteins, as a representative IDP due to a combination of structural, functional, and practical advantages. β-casein is a medium-sized protein (209 residues, approximately 25 kDa) and is part of the broader casein family, which includes α_{s1}-, α_{s2}-, and κ-casein. Unlike many IDPs that remain monomeric in solution, β-casein spontaneously self-associates via hydrophobic interactions to form micelle-like aggregates. These oligomeric structures are dynamic, reversible, and remain soluble, typically comprising tens of monomers. Although commonly referred to as micelles, they differ structurally from classical surfactant micelles. Their formation is highly sensitive to environmental parameters such as pH, temperature, ionic strength, concentration, and protein purity [67–69]. Throughout this work, we use the terms micelles, aggregates, and assemblies to refer to these self-assembled structures. We retain the term micelle to align with its dominant usage in the casein literature, while also employing the more general assembly and, in the context of simulations that address small clusters of monomers, aggregate. Unless otherwise stated, no mechanistic or morphological distinction is intended by this terminology.

In its monomeric state, β-casein exhibits several hallmarks of intrinsically disordered proteins, including a net negative charge, uneven charge distribution, and lack of a stable tertiary structure under physiological conditions. Early spectroscopic studies using circular dichroism (CD), FTIR, and Raman spectroscopy reported low levels of regular secondary structure [70–72]. These findings have been corroborated by recent computational work, including all-atom simulations, which reveal a broad ensemble of conformations that interconvert dynamically rather than folding into a unique structure [73].

However, the notion that disorder correlates with low hydrophobicity does not apply here. β-casein contains a substantial number of hydrophobic residues, particularly in its C-terminal domain, which plays a central role in its ability to self-associate [74]. The sequence displays a modular chemical organization: the N-terminal segment (residues 1-40) is hydrophilic and carries most of the negative charge; the central region (residues 41-135) is moderately hydrophobic; and the C-terminal tail (residues 136-209) is distinctly hydrophobic [75]. This distribution imparts amphiphilic character and underlies

the capacity of the protein to remain soluble while forming reversible aggregates. This organization is visually summarized in Figure 3.2, which maps the sequence according to residue charge and hydrophobicity. This sequence segmentation is also reflected in

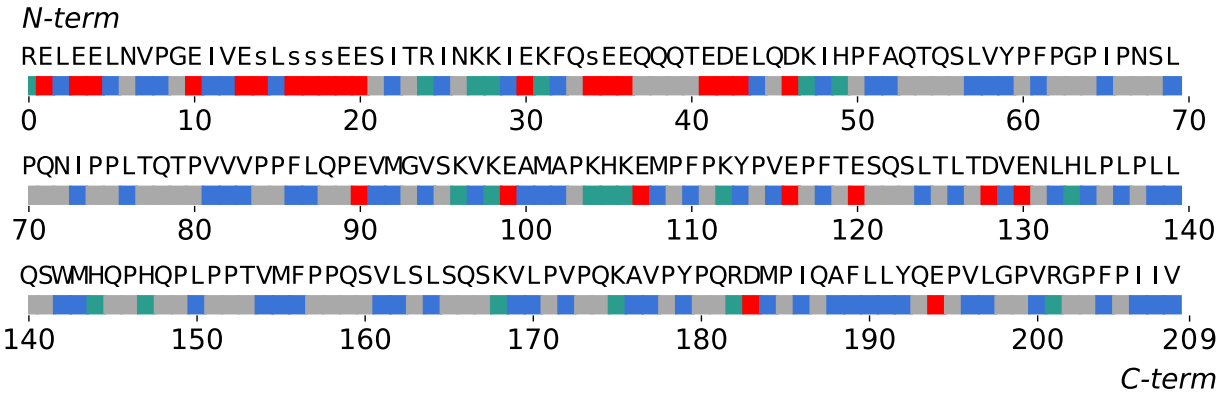

Figure 3.2. One-letter code representation of the β-casein sequence. Basic (positively charged) residues are shown in green, acidic (negatively charged) residues in red, hydrophobic residues in blue, and polar uncharged residues in gray. The N-terminal and C-terminal are indicated on the left and right ends of the sequence, respectively. UniProtKB entry name CASB_BOVIN and accession number P02666. Figure generated with Matplotlib [55].

enhanced-sampling molecular simulations, which reveal a complex free energy landscape with three major conformational basins: compact, intermediate, and extended [73]. These conformers differ in global dimensions such as radius of gyration and solvent-accessible surface area, as well as in their local segmental behavior. The N-terminal region remains swollen across all conformational classes, the C-terminal region remains consistently compact, and the central segment exhibits class-dependent variation in expansion (Figure 3.3). Upon self-assembly, the conformational preferences and dynamic properties of β-casein can change significantly. The aggregation process, primarily driven by interactions involving the hydrophobic C-terminal domain, may stabilize certain transient structural elements or reduce conformational heterogeneity. In this work, we focus on the structure and dynamics of β-casein in its aggregated state. A detailed discussion of the structure of these aggregates and the environmental factors that modulate them is presented in later sections.

More broadly, studying proteins in their aggregated states is crucial for understanding both functional assemblies and pathological processes. While the focus of this thesis

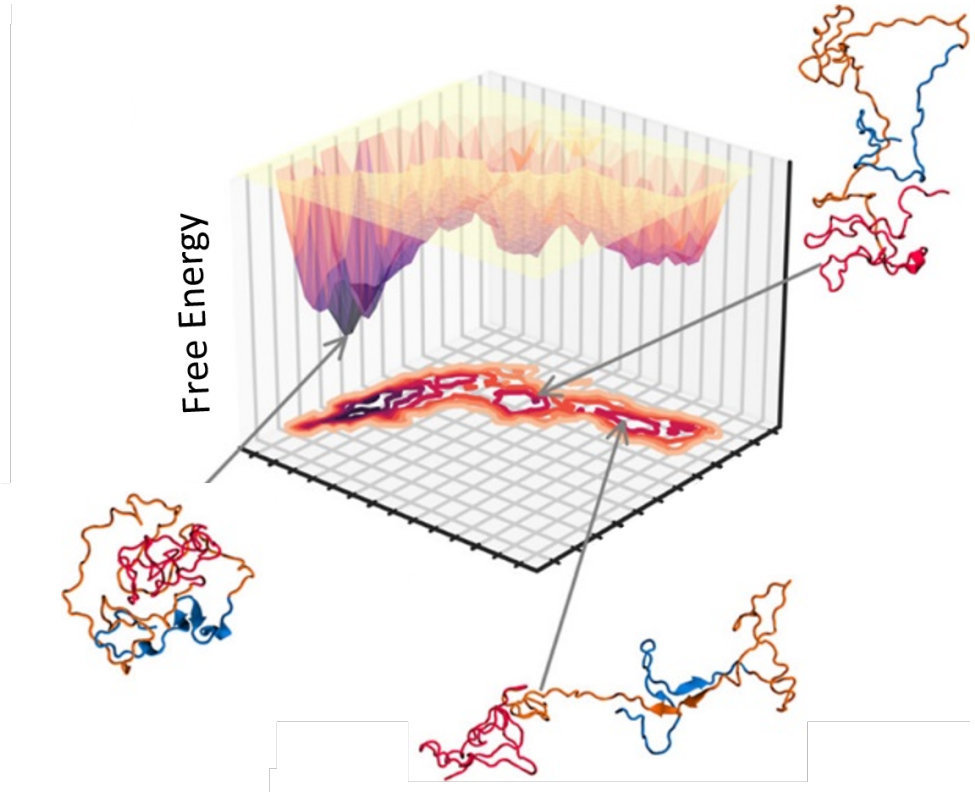

Figure 3.3. Free energy landscape illustrating the conformational heterogeneity of β-casein. A pronounced global minimum is accompanied by two shallow basins, with arrows indicating representative structures sampled from each region. Colored segments highlight the block-copolymer-like architecture of β-casein: the hydrophilic N-terminal region (residues 1-40) is shown in blue; the moderately hydrophobic middle region (residues 41-135) in orange; and the highly hydrophobic C-terminal region (residues 136-209) in red. The two unlabeled axes denote generic configurational coordinates. Figure from [73].

is not on pathological aggregation, it is worth noting that β-casein has been shown to form amyloid-like fibrils under specific conditions [76]. This highlights the relevance of β-casein not only as a model for reversible self-assembly, but also as a system with potential connections to the broader field of protein aggregation and misfolding diseases.

Beyond its biological interest, β-casein offers numerous practical advantages for experimental studies. It is commercially available in large quantities and high purity, enabling reproducible experiments under a wide range of solution conditions. Its solubility in water, non-toxic nature, and chemical modifiability make it particularly well-suited for methods requiring large sample volumes, such as neutron spectroscopy.

Altogether, β-casein provides a robust and versatile model system for investigating the interplay between intrinsic disorder, self-assembly, and environmental responsiveness in IDPs. Its relevance spans fundamental biophysics as well as applications in food science, pharmaceuticals, and biomaterials.

3.4 Structural characterization of β-casein micelles

One of the distinguishing features of β-casein as a model IDP is its ability to self-assemble into micelle-like structures under physiologically relevant conditions. Unlike the casein micelles found in whole milk which consist of multiple casein types (α_{s1}, α_{s2}, β, and κ) and are stabilized by colloidal calcium phosphate [77], micelles formed from isolated β-casein arise through a distinct mechanism. In the absence of calcium phosphate nanoclusters or other caseins, β-casein self-associates into soft, dynamic aggregates driven primarily by hydrophobic interactions, particularly involving its C-terminal domain.

The structural properties of these micelles, such as their size, shape, internal organization, and aggregation number, have been extensively investigated using a wide array of scattering and imaging techniques. Small angle neutron scattering (SANS), small angle X-ray scattering (SAXS), and dynamic light scattering (DLS) have been particularly valuable in resolving the self-assembled structures formed by β-casein under various solution conditions. These studies have revealed that micelle formation is highly sensitive to temperature, pH, ionic strength, and protein concentration, and that the resulting aggregates are often polydisperse, both in size and in internal density.

In this section, we summarize key findings from structural studies of β-casein micelles, with an emphasis on the reported radii of gyration (R_g), the hydrodynamic radii (R_h), the aggregation numbers and proposed structural models. Particular attention is paid to the diversity of experimental conditions used in the studies and to the challenges of comparing the results obtained under different buffer compositions, temperatures, and concentrations (see Table 3.1).

Table 3.1. Summary of structural studies on β-casein micelles.

Reference	**Techniques**	**Buffer / pH**	**Concentration (mg/mL)**	**T (°C)**	R_g **(nm)**	R_h **(nm)**	N_{agg}	**Model / Observations**
Thurn et al. (1987) [78]	DLS, SANS	Na-phosphate, pH 6.7	DLS: 0.5-8, SANS: 1-6	DLS: 10-40, SANS: 15	13.5	13.2-16.6 (with T)	-	Star-branched architecture; dense core with polymer-like arms.
Kajiwara et al. (1988) [79]	SAXS	Na-phosphate, pH 6.7	5-50	5, 15, 25	69-86.1 (concentration and T)	77.8-102.2 (concentration and T)	-	Ellipsoidal; becomes more spherical with increasing T; $R_g/R_h \approx 0.8$.
Leclerc et al. (1997) [67]	SANS	Na-phosphate + NaCl, pH 7	1.25-10	4.5-70	4.5-11.5	-	-	Core-corona; core density 0.4-0.9 g/cm^3, very diffuse corona.
Leclerc et al. (1998) [80]	SANS	Na-phosphate + NaCl, pH 7	1.25-10	5-73	13.5	-	5-72	Core-corona with random chains; aggregation number increases with T and concentration.
de Kruif et al. (2002) [81]	DLS	Na-phosphate, pH 6.5	0.5-40	4.5-35	-	12 (fast mode)	-	Bimodal decay; "slow mode" due to polydispersity, not large particles.
Moitzi et al. (2008) [82]	SAXS, cryo-TEM	Water or lactic acid/HCl; pH 6.7 or 2.6	10-40	4-60	-	-	2-$\sim$150	pH 2.6: disc-like aggregates; pH 6.7: T-driven transition from planar to spherical micelles.
Aschi et al. (2009) [83]	SANS	20 mM imidazole, pH 7	7.5	10-70	$\sim$6-13	-	$\sim$20-80	Core-corona; R_g and N_{agg} increase with T; GdmCl causes micelle dissociation.
Cragnell et al. (2017) [69]	SAXS, osmometry, AF4-MALS	Tris, pH 8.5, 60 mM ionic strength	0.25-14	20	2-10	-	dimers-$\sim$200	Broad size distribution; ellipsoids; N_{agg} from dimers to $\sim$200 proteins.

One of the first structural studies of isolated β-casein micelles was reported by Thurn et al. [78], who combined SANS and DLS to characterize their size and shape in solution. Measurements were carried out at pH 6.7 in sodium phosphate buffer under moderate ionic strength. They obtained a radius of gyration of 13.5 nm and hydrodynamic radii between 13.2 and 16.6 nm, depending on temperature. From these data they also estimated the molecular weight and internal density of the micelles. Analysis of the scattering profiles suggested deviations from a simple spherical geometry, leading the authors to propose a "star-branched" model consisting of a dense central core with 36 polymer-like arms. The ratio R_g/R_h varied between values characteristic of star polymers and those of hard spheres.

Kajiwara et al. [79] extended this work using SAXS to investigate a wider concentration range (5-50 mg/mL) and three temperatures (5, 15, and 25 °C). Experiments were conducted at pH 6.7 in sodium phosphate buffer, matching the conditions of the earlier SANS/DLS work. Fourier transformation of the scattering intensity yielded an asymmetric pair-distance distribution function, indicating a deviation from spherical symmetry. The data were best described by an ellipsoidal model, with the shape becoming more spherical as temperature increased. R_g showed little variation with concentration in this range, although the authors noted previous reports of R_g increasing and molecular weight decreasing at concentrations below 2 mg/mL. From the ellipsoidal fits, they calculated R_h values and corresponding R_g/R_h ratios (around 0.8), consistent with micelles having a hard core surrounded by a thin, soft surface layer. As the temperature increased, the micelles exhibited a greater degree of polymerization and gradually adopted a more spherical geometry.

In one of the most detailed early SANS characterizations of isolated β-casein micelles, Leclerc et al. [67] examined samples in Na-phosphate buffer containing NaCl at pH 7. A key observation was that the Guinier-derived R_g strongly depended on the q-range selected for analysis. For the low q regime ($qR_g < 1$), R_g increased markedly as concentration decreased (from 115 Å at 1.23 mg/mL to 45 Å at 10 mg/mL) which the authors attributed to attractive interparticle interactions occurring near the critical micelle concentration (CMC). In contrast, for the intermediate q range ($1 < qR_g < 2$), R_g remained nearly constant across all concentrations (71.5±1.1 Å)which indicates that repulsive interactions dominate at this structural scale. To rationalize the data, the authors proposed a core-corona model, with a relatively dense inner region surrounded by a more diffuse outer

layer. Notably, even the core was less dense (0.4-0.9 g/cm^3) than a typical globular protein (1.35 g/cm^3), while the corona density was substantially lower (0.025-0.14 g/cm^3). The external radius ($\sim 130 \pm 10$ Å) was almost independent of concentration and temperature up to 70 °C, whereas the core radius increased from 45 Å to 70 Å over the same range. These results led the authors to conclude that attractive interactions, particularly near the CMC, are central to micelle formation, and that β-casein micelles interact as soft spheres.

In a subsequent, more concise follow-up study [80], Leclerc and co-workers refined their structural model to improve the fits at higher q by replacing the constant density corona with a shell containing ideal random chains. Within this framework, they reported that the aggregation number increased dramatically (from about 5 to 72) with both concentration and temperature, despite the micelles retaining an almost constant external radius. This was one of the first studies to include a schematic representation of a β-casein micelle (Figure 3.4), illustrating the dense core surrounded by a polymeric corona.

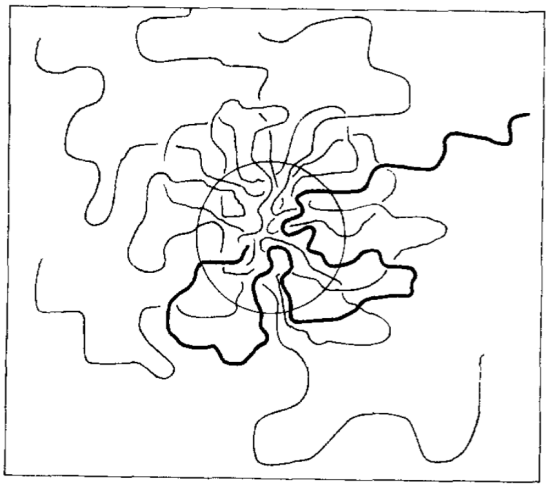

Figure 3.4. One of the earliest schematic representations of a β-casein micelle. The thick solid line traces a single β-casein chain within the aggregate. The example corresponds to an aggregation number of 6, representative of micelles formed at ~ 2.5 mg/mL and 4.5 °C in Na-phosphate buffer (pH 7) with NaCl. Figure from [80].

Continuing the investigation of micellization dynamics, de Kruif et al. [81] used DLS in Na-phosphate buffer at pH 6.5 to explore concentrations ranging from 0.5 to 40 mg/mL. In their introduction, they discussed the micellization transition concept, describing the coexistence of monomers and micelles and how their relative populations shift with con-

centration and temperature as summarized in Figure 3.5. Analysis of the intensity autocorrelation functions required a bimodal fit, revealing two diffusive modes. The faster mode corresponded to particles with $R_h \approx 12$ nm, while the slower mode yielded apparent sizes of 60-100 nm. Both radii were largely invariant with temperature and concentration. However, the relative amplitudes A_1 and A_2 changed systematically: the fraction of the slow mode decreased with increasing temperature. The authors attributed the fast mode to β-casein micelles and argued that the slow mode did not correspond to genuinely larger particles, since such objects would scatter light much more strongly and their amplitude would increase rather than decrease. Instead, they associated this contribution with polydispersity in the diffusion coefficients. This polydispersity diminished with temperature, indicating a reduction in long-range correlations as micellization progressed. The number of micelles increased with temperature despite their constant size, and at higher protein concentrations the slow mode decayed more slowly, suggesting stronger interparticle interactions.

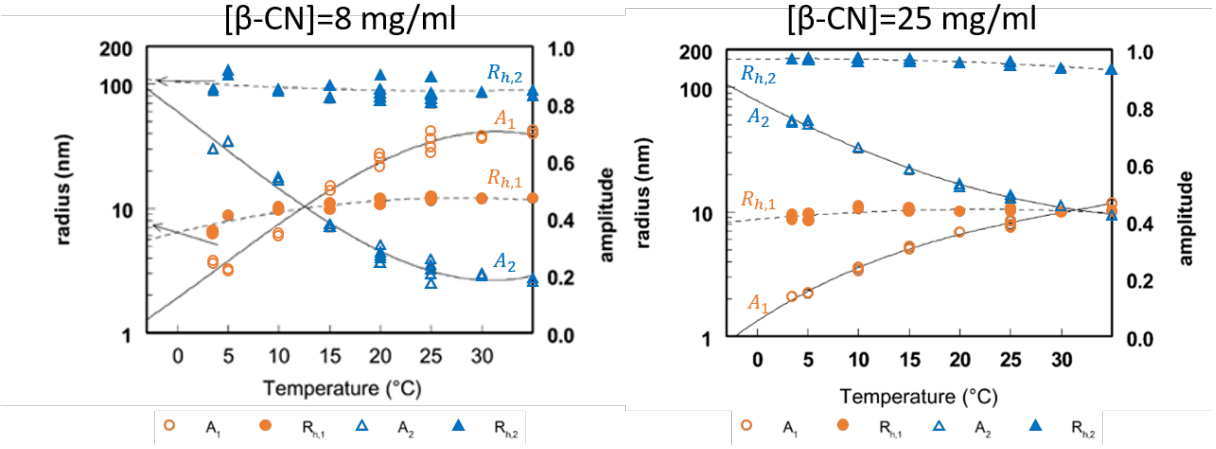

Figure 3.5. Apparent hydrodynamic radii ($R_{h,1}$ and $R_{h,2}$, left axis) and relative amplitudes (A_1 and A_2, right axis) as a function of temperature for β-casein in Na-phosphate buffer ($I \approx 0.1$) obtained from DLS measurements. Left: 8 mg/mL; right: 25 mg/mL. The "large particles" associated with the slow mode have not been attributed a direct physical meaning but reflect a relaxation process linked to polydispersity in diffusion (see main text for details). Figure adapted from [81].

Building on studies focused on temperature and ionic effects, Moitzi et al. [82] examined the influence of pH on β-casein self-assembly using SAXS and cryo-TEM. Solutions at pH 6.7 were prepared in distilled water at concentrations between 10 and 40 mg/mL,

while samples at pH 2.6 were obtained by acidification with lactic acid or HCl. At low pH, SAXS profiles indicated disc-like aggregates, a morphology confirmed by cryo-TEM images (Figure 3.6, top row), with dimensions of approximately 3-4 nm in thickness and 20-25 nm in lateral extension. The authors determined that at pH 2.6 the CMC was ~ 5 mg/mL at 4 °C, based on a constant aggregation number of 2 above this concentration. Increasing the temperature led to a rise in aggregation number and a decrease in CMC to 0.25-1 mg/mL.

At neutral pH, SAXS measurements and cryo-TEM images (Figure 3.6, bottom row) consistently showed a temperature-driven morphological transition, from extended planar structures at low temperatures (10 °C), to oblate micelles at intermediate temperatures (25 °C), and finally to compact spheres at around 60 °C. At low temperatures, only monomers were detected, and the aggregation number increased with heating. The authors concluded that both pH and temperature modulate the balance between electrostatic repulsion and hydrophobic attraction, thereby controlling not only the extent of aggregation but also the geometry of the micelles. They proposed that near the isoelectric point (low pH), reduced charge repulsion allows chains to collapse into thin, anisotropic aggregates, whereas at neutral pH, thermal energy is required to overcome repulsive forces and drive the system toward compact, spherical assemblies.

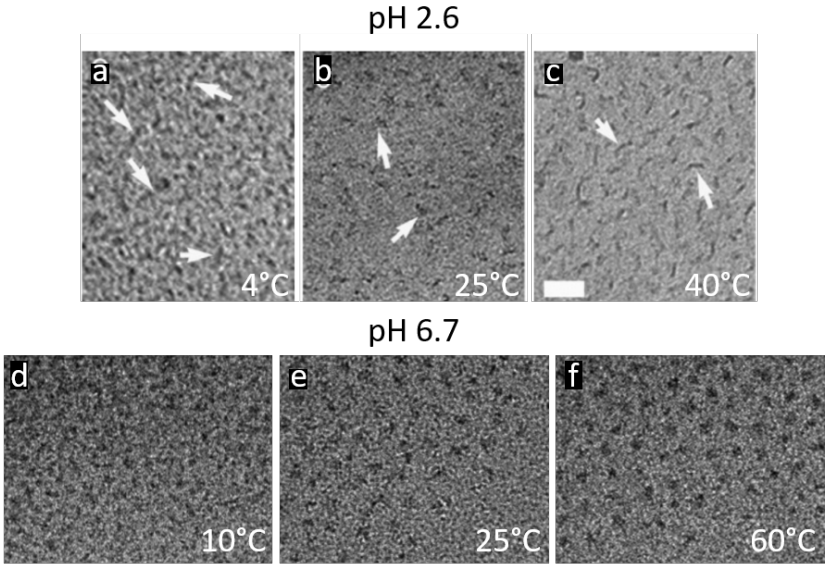

Figure 3.6. Cryo-TEM images of β-casein aggregates at different pH and temperatures. Top row: pH 2.6 at 4 °C (a), 25 °C (b), and 40 °C (c). Bottom row: pH 6.7 at 10 °C (d), 25 °C (e), and 60 °C (f). Figure adapted from [82].

In order to assess how chemical denaturation affects micelle structure, Aschi et al. [83] investigated β-casein at 7.5 mg/mL in 20 mM imidazole buffer (pH 7) using SANS, varying both temperature and guanidinium chloride (GdmCl) concentration. Like urea [84], GdmCl is known to disrupt hydrophobic interactions and dissociate casein micelles. For GdmCl-free samples, the scattering profiles were consistent with spherical micelles comprising a dense core surrounded by a diffuse corona, in agreement with previous SANS studies [67].

When GdmCl was added, both the aggregation number and R_g decreased until only monomers remained in solution. Above a certain GdmCl threshold, SANS profiles showed a sharp drop in the scattering intensity (Figure 3.7, left), indicating the sudden disappearance of aggregates and a marked reduction in interparticle interactions. This change was accompanied by decreases in R_g and aggregation number (Figure 3.7, right), consistent with a shift of the solvent quality that weakens hydrophobic association of the C-terminal domains. Although no detailed structural model was provided for the high-GdmCl regime, the scattering resembled that of synthetic polymer chains.

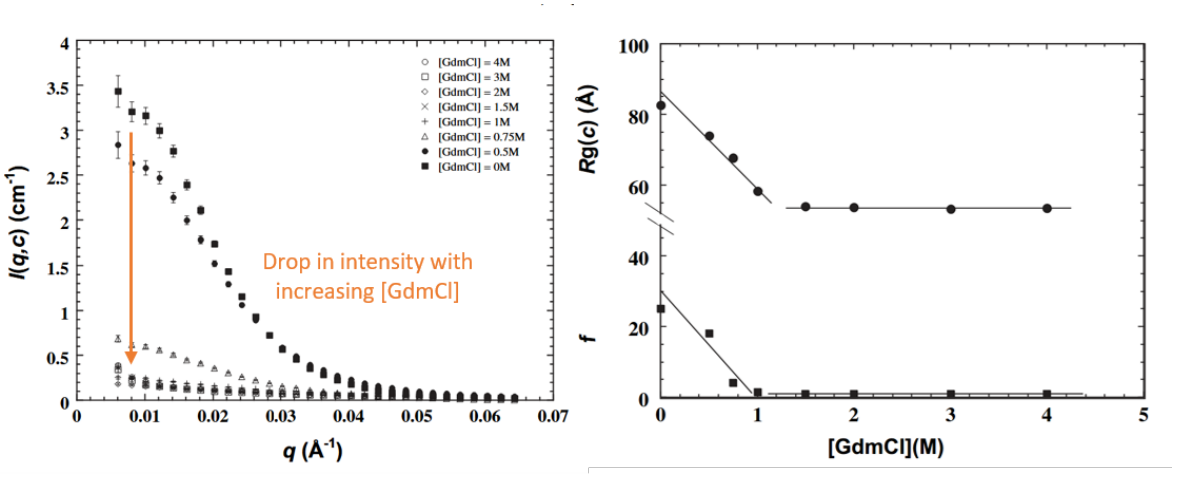

Figure 3.7. Effect of GdmCl on β-casein micelles at 7.5 mg/mL in 20 mM imidazole buffer (pH 7) from SANS measurements. **Left:** Scattering intensity profiles showing a sharp decrease once the GdmCl concentration exceeds a threshold, indicating the disappearance of aggregates and reduced interparticle interactions. **Right:** Radius of gyration (R_g) and aggregation number as a function of GdmCl concentration, illustrating the transition from micellar aggregates to monomers. Figure adapted from [83].

They also assessed the temperature dependence of micellization in the absence of GdmCl, finding that both R_g and the aggregation number increased upon heating (Figure 3.8,

left). Within the core-corona framework, the analysis indicated that both the core and corona radii exhibited a slight expansion with temperature (Figure 3.8, right).

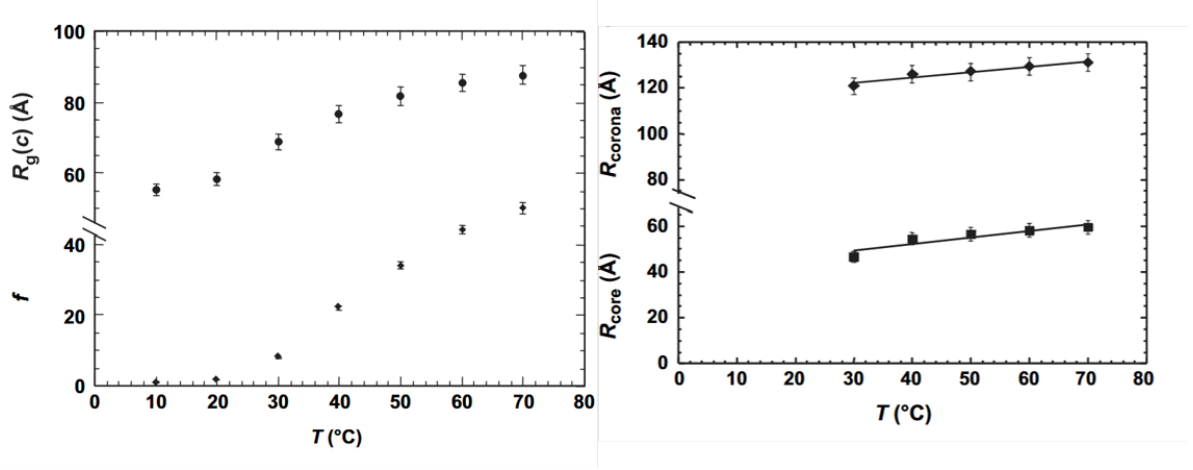

Figure 3.8. Temperature dependence of β-casein micelle dimensions from SANS measurements at 7.5 mg/mL in 20 mM imidazole buffer (pH 7). **Left**: Variation of R_g and aggregation number with increasing temperature. **Right**: Corresponding changes in the core radius and corona thickness within the core-corona model. Figure from [83].

Finally, addressing the question of polydispersity in β-casein assemblies, Cragnell et al. [69] studied bovine protein in Tris buffer at pH 8.5 (60 mM ionic strength) over a concentration range of 0.25-14 mg/mL. They combined SAXS, osmometry, and asymmetrical flow field-flow fractionation (AF4) coupled to MALS and dRI detection. LC/MS/MS analysis confirmed that the commercial protein was not pure, containing mainly β-casein (51%) along with α_{S1}-, α_{S2}-, and κ-casein, plus minor milk proteins.

SAXS data indicated that micelles could be modeled as ellipsoids with radii of approximately 7 nm and 20 nm (for 13 mg/mL), and aggregation numbers between 10 and 40 depending on concentration. Osmometry on the same systems yielded much lower apparent aggregation numbers, closer to dimers, likely reflecting a bias toward detecting the smaller micelles in the polydisperse mixture.

AF4-MALS provided direct evidence for a broad size distribution, with molecular weights spanning nearly three orders of magnitude and R_g values from 20 to 100 nm. Two main populations were evident: a small-size fraction eluting at $\sim$2 min, and a larger-size fraction eluting between 5 and 15 min. The largest assemblies detected corresponded to $\sim$200 proteins, although it was not possible to distinguish between single large micelles and clusters of smaller ones. Overall, the study demonstrated that β-casein forms an equilibrium

distribution of micelles and/or micelle clusters with substantial polydispersity, rather than a monodisperse population.
Across the studies reviewed, a variety of structural models, including ellipsoids, spheres, core-corona architectures, and core-shell geometries with polymeric chains, have been applied to describe β-casein micelles. The reported behavior with changing concentration and temperature ranges from nearly monodisperse micelles whose size remains essentially constant to highly polydisperse systems spanning orders of magnitude in molecular weight and radius. In addition to these intrinsic variations, experimental work has explored a wide range of solution conditions, including pH shifts, the presence of denaturants such as GdmCl, and differences in buffer composition and ionic strength. Taken together, these findings highlight that β-casein aggregates can adopt markedly different structural states depending on the environment, and that direct structural characterization is essential to accurately describe the system under the specific conditions studied.

3.5 Neutron spectroscopy studies on β-casein dynamics

Neutron spectroscopy techniques have played a central role in characterizing the internal and global dynamics of β-casein. These methods offer direct access to atomic-scale motions over picosecond to nanosecond timescales, making them especially valuable for studying IDPs, whose flexibility and structural heterogeneity challenge structure-based approaches such as crystallography or even conventional NMR.
In this section, we review key neutron scattering studies on β-casein, highlighting how different experimental approaches disentangle global and internal components of motion, characterize relevant dynamical processes, and compare β-casein to both folded proteins and other IDPs. Table 3.2 summarizes the techniques, resolutions, sample states, and key findings from each study.

One of the earliest neutron scattering studies to systematically compare the dynamics of intrinsically disordered and well-folded proteins was conducted by Gaspar et al. [85], using the TOFTOF spectrometer at FRM-II. The study investigated α-, β-, and κ-casein as representative IDPs and compared them to three well-folded globular proteins: myoglobin, lysozyme, and concanavalin A.

Table 3.2. Comparison of neutron scattering studies on β-casein.

Study	**Main technique**	**Instrument/ Resolution**	**Sample state**	**Global diffusion**	**Internal motions**	**Key findings**
Gaspar et al. (2008) [85]	ToF	TOFTOF /30 μeV $\rightarrow$ 22 ps	Solution ($\sim$100 mg/mL)	HWHM vs q^2 linear fit $D = 3.8 \pm 0.2$ Å^2/ ns	HWHM, EISF	IDPs show finite offset in HWHM at low q, suggestive of an extra dynamical contribution.
Dhindsa et al. (2014) [86]	NBS	HFBS/ 0.8 μeV	Dry/Hydrated powder	Assumed negligible	MSD, EISF, τ_β	Hydrated sample shows transitions at 100 K (methyl) and 225 K (backbone); 320 K unfolding signature. Dry sample lacks second transition.
Perticaroli et al. (2014) [87]	NBS	BASIS/ 3.5 μeV	Dry/Hydrated powder	Assumed negligible	Boson peak susceptibility, EISF	Calcium binding increases rigidity; methyl/local motions remain. Flexibility lies between globular proteins and extended biomolecules.
Nakagawa et al. (2021) [88]	NSE, NBS	J-NSE, SPHERES/ 0.67 μeV	Solution $\sim$83 mg/mL	Assumed Fickian; D extracted (NSE) and fixed (NBS)	Two modes: τ_1 (NSE), τ_2 (NBS), BOmodel	Micelle formation does not affect internal dynamics. Slow mode requires bulk water; fast mode is solvent-decoupled.

In solution, the authors separated the QENS signal into two distinct components: global and internal dynamics. The global motion, associated with center-of-mass diffusion of the protein (or of the entire assembly in the case of caseins), revealed a clear difference between disordered and folded proteins. For the folded proteins, the HWHM of the global component of the quasi-elastic broadening scaled linearly with q^2 and extrapolated to zero at low q, as expected for Fickian diffusion. In contrast, IDPs such as β-casein exhibited a finite offset at low q (Fig. 3.9, left), suggesting the presence of additional unresolved dynamic contributions. The authors associated this behavior with slow internal or collective motions that fall outside the accessible time window of the instrument, and recommended further studies using higher-resolution techniques such as NBS or NSE. The internal dynamics were also analyzed. While the HWHM values were similar between protein types, the EISF differed significantly. For IDPs, the EISF decayed more strongly with increasing q, indicating a greater degree of internal flexibility (Fig. 3.9, right).

Dhindsa et al. [86] investigated the temperature-dependent internal dynamics of β -casein in dry and hydrated states using NBS on the high-flux spectrometer HFBS at NIST.

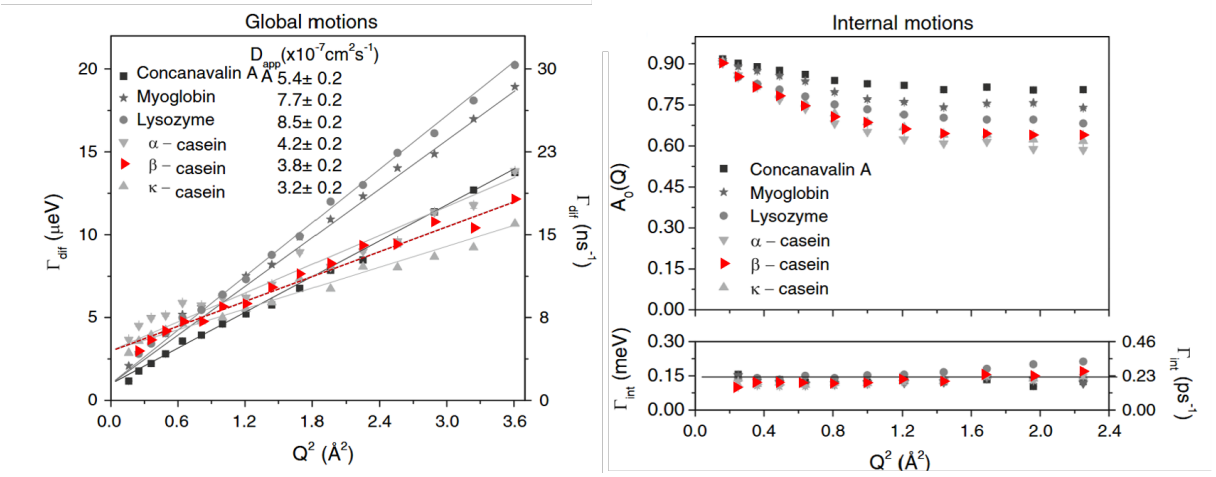

Figure 3.9. Global (left) and internal (right) dynamic contributions to the QENS signal for caseins (IDPs) and well-folded proteins , measured on the FRM-II TOFTOF spectrometer (energy resolution 30 μeV). Figure adapted from [85].

Because the protein was studied in dry and hydrated powders, only internal motions could be probed. The data were analyzed in both energy and time domains. In the energy domain, the spectra were fitted using a single Lorentzian function with an EISF. In parallel, the MSD was calculated from the elastic intensity as a function of temperature. In the time domain, the Fourier-transformed intermediate scattering functions were fitted using a model derived from the mode coupling theory, with the β-relaxation time, τ_β, as a key fit parameter.

The MSD revealed distinct dynamical regimes. In both dry and hydrated samples, a low-temperature onset around 100 K was observed and attributed to the rotations of the methyl groups. However, only the hydrated sample exhibited a second transition near 225 K, corresponding to the well-known dynamic transition associated with the activation of backbone fluctuations and hydration-dependent side-chain mobility. The absence of this transition in the dry state supports the conclusion that the flexibility of hydrophilic residues in β-casein is critically dependent on the presence of hydration water. These features are clearly visible in the MSD data, shown in Fig. 3.10, where the transitions are marked with arrows.

The analysis of the EISF further corroborated these findings: a marked increase in atomic displacement amplitudes was observed in the hydrated sample, consistent with greater internal mobility. Moreover, both the parameters derived from the EISF and the time-domain analysis revealed a third transition around 320 K, which the authors associated

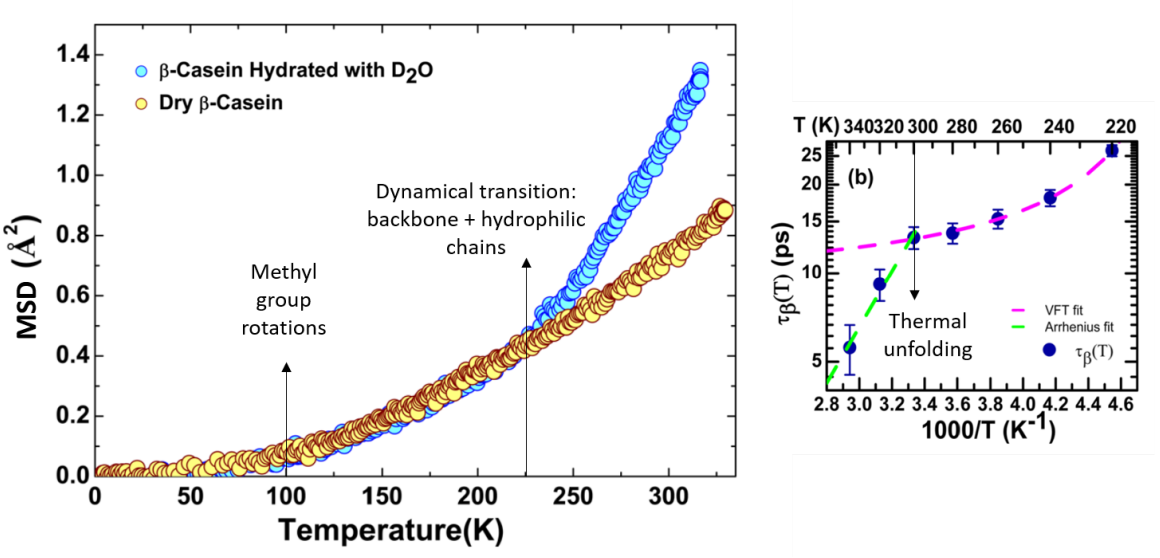

Figure 3.10. Left: MSD of dry and hydrated β-casein as a function of temperature, showing two distinct onsets in the hydrated state (arrows). Right: Arrhenius plot of the β-relaxation time, τ_β, derived from the time-domain analysis. The deviation near 320 K is associated with partial thermal unfolding. Figure adapted from [86].

with partial thermal unfolding of the protein. This transition was characterized by a reduction in the volume of diffusion, suggesting a collapse of the hydrogen bond network and a reduction in the protein flexibility. This high-temperature transition is also reflected in the temperature dependence of τ_β (Fig.3.10, right), where a deviation from Arrhenius behavior becomes apparent.

Perticaroli et al. [87] investigated the internal dynamics of β-casein in both its calcium-bound and unbound states, comparing its behavior to that of green fluorescent protein (GFP), a well-folded globular protein. Using neutron scattering on the BASIS spectrometer and dynamic light scattering, they derived the dynamic susceptibility from the dynamic structure factor, applying Bose population factors for neutron data and intensity correlations for light scattering. Their analysis focused on the boson peak, a feature reflecting low-frequency vibrational modes associated with local rigidity, and how it is modulated by hydration, temperature, and calcium binding.

In its unbound state, β-casein showed high internal flexibility, consistent with its disordered nature and functional role in calcium binding and transport. Upon calcium coordination, the protein exhibited increased rigidity and partial folding but still remained

more flexible than GFP. Interestingly, despite these structural differences, β-casein and GFP showed comparable fast dynamics on short timescales.

To further characterize local motions, the authors analyzed the EISF, which they fitted using a model combining three-site jump rotations of methyl groups with localized diffusion inside a sphere. From this analysis, they noted that the ratio of hydrophobic to total residues in β-casein (0.4) is higher than in typical globular proteins. Accordingly, the amplitude and nature of local motions placed β-casein between folded proteins and fully extended biomolecules in terms of flexibility.

Finally, they identified 6.75 mM as the minimum Ca^{2+} concentration required to saturate the binding capacity of β-casein, based on prior work by Müller-Buschbaum et al. [89].

Nakagawa et al. [88] extended the investigation of β-casein dynamics by employing high-resolution neutron scattering techniques, NSE and NBS, to probe nanosecond and sub-nanosecond timescales, respectively. This dual approach enabled a detailed characterization of internal motions in β-casein micelles in solution, surpassing the temporal resolution of previous studies.

Using NSE, the authors identified a slow internal relaxation process ($\tau_1 \sim 1$ ns) superimposed on the global diffusion of the micelle. This internal mode emerged at higher q-values ($q > 0.7$ nm^{-1}), corresponding to spatial scales of 10 nm. The global diffusion coefficient showed no q-dependence. The relaxation was modeled using a Brownian oscillator (BO) framework, yielding a dynamic amplitude $A_1(q)$ and a spring constant of approximately $K \approx 0.04$ N/m. The relaxation time scaled with solvent viscosity, indicating that this slow mode is strongly coupled to bulk water and thus absent in dry powders.

In the NBS analysis, the authors did not fit the HWHM as a function of q^2, but instead assumed Fickian diffusion and fixed the diffusion coefficient D to the value extracted independently from NSE data. This constraint improved the separation of global and internal contributions, allowing for the identification of a second, faster internal mode.

This faster relaxation process ($\tau_2 \sim 100$ ps) was associated with localized motions of smaller amplitude ($\langle u^2 \rangle \sim 0.01$ nm^2), also modeled with the Brownian oscillator. The extracted spring constant for this mode was $K \approx 0.4$ N/m, comparable to values reported for hydrated globular proteins. Notably, the parameters of this fast mode were nearly identical in hydrated powders and in solution, suggesting that these motions are largely solvent-independent and likely arise from intrinsic side-chain or local backbone dynamics.

The study concluded that micelle formation does not significantly alter the nanosecond internal dynamics of β-casein. This stands in contrast to globular proteins, where folding and unfolding typically lead to substantial dynamical changes due to differences in atomic packing and hydration. In β-casein, the slower internal motion appears to be an intrinsic feature of the disordered state, requiring the presence of bulk water and disappearing in hydrated powders. This behavior aligns with the notion that casein micelles retain considerable hydration internally.

In summary, neutron spectroscopy studies have shown that β-casein exhibits multiple dynamic components that can be separated across different timescales. Two main internal modes have been identified: a fast, localized motion on the 100 ps scale that is largely independent of hydration, and a slower nanosecond-scale relaxation that only appears in the presence of bulk water. These findings highlight the role of hydration in enabling larger-amplitude internal dynamics. However, global motions have not been explored in detail since the initial work by Gaspar et al. [85], who observed a finite offset in the q^2-dependence of the quasielastic linewidths. Similarly, the effect of macromolecular crowding has not been systematically studied, and while some reports identify a thermal transition around 320 K, its reversibility remains uncharacterized. Moreover, all existing solution studies have focused on β-casein in its aggregated micellar form; the internal and global dynamics of monomeric β-casein under dissociating conditions such as in the presence of urea have not yet been addressed. These open questions form the basis of the present thesis.

In summary, neutron spectroscopy studies have shown that β-casein exhibits multiple dynamic components that can be separated across different timescales. Two main internal modes have been identified: a fast, localized motion on the $\sim$100 ps scale that is largely independent of hydration, and a slower nanosecond-scale relaxation that only appears in the presence of bulk water. These findings highlight the role of hydration in enabling larger-amplitude internal dynamics. However, global motions have not been explored in detail since the initial work by Gaspar et al. [85], who observed a finite offset in the q^2-dependence of the quasi-elastic linewidths. Similarly, the effect of macromolecular crowding has not been systematically studied, and while some reports identify a thermal transition around 320 K, its reversibility remains uncharacterized. Moreover, all existing solution studies have focused on β-casein in its aggregated micellar form; the internal and global dynamics of monomeric β-casein under dissociating conditions (e.g., in the

presence of urea) have not yet been addressed. Earlier studies were constrained by the instrumentation available at the time, resulting in limited q-ω coverage and limited statistical precision. Recent advances in QENS instrumentation, such as the increased flux and expanded dynamic range available on instruments like IN16B operating in BATS mode, now allow high energy resolution together with access to broader energy transfer windows within a single experiment. This capability enables the collection of larger and more systematic data sets across relevant state points and contrast conditions, which previously required measurements on different instruments optimized either for resolution or for flux.

3.6 Summary

Intrinsically disordered proteins challenge the traditional structure-function paradigm in biology by lacking a single, stable fold yet remaining central to essential biological processes. Their structural flexibility allows them to engage in diverse and often multivalent interactions, adapt to changing environments, and form dynamic assemblies. These same properties, however, can predispose them to misfolding and pathological aggregation. Understanding IDPs is therefore key not only for uncovering fundamental principles of protein behavior but also for addressing their roles in health, disease, and biotechnological applications. Because their conformational ensembles and dynamics are highly sensitive to temperature, hydration, ionic strength, and crowding, studying them requires methods that capture atomic motions over nanometer and nanosecond scales, such as neutron spectroscopy.

β-casein exemplifies these principles. It is amphiphilic, with clearly defined hydrophilic and hydrophobic blocks, and is able to self-associate into micelle-like aggregates that remain soluble and dynamic. Spectroscopy and simulations reveal it as an IDP with a heterogeneous conformational landscape, while its hydrophobic C-terminal domain plays a key role in aggregation. Its ready availability, high solubility, and compatibility with neutron-based methods make it an ideal system for controlled biophysical studies with well-controlled and tunable parameters.

Structural studies reveal β-casein micelles as soft, polydisperse assemblies whose size, shape, and aggregation number are highly sensitive to pH, temperature, ionic strength, and the presence of denaturants. Models ranging from ellipsoids to core-corona architectures capture their diverse morphologies, while scattering and imaging techniques confirm

their structural adaptability. Together, these observations establish β-casein as a model system for exploring the interplay between intrinsic disorder, self-assembly, and environmental responsiveness, providing a strong foundation for the experimental work presented in the following chapters.

Neutron spectroscopy investigations of β-casein have revealed a clear separation between internal and global dynamical modes. The internal motions, which have been the main focus of experimental work, span a wide range of relaxation timescales, from fast localized motions that are largely independent of hydration to slower, larger-scale relaxations that depend strongly on the presence of bulk water. These features distinguish β-casein from globular proteins, whose folding states tend to cause more pronounced dynamical changes. In contrast, the global dynamics of the micellar assemblies remain largely unexplored, and current evidence suggests that micelle formation does not significantly suppress the intrinsic flexibility of the disordered chains.

Chapter 4

Materials & methods

4.1 Materials

4.1.1 β-Casein

Bovine β-casein (BioUltra, ≥98% purity; Sigma-Aldrich / Merck KGaA, Darmstadt, Germany; Prod. C6905) was obtained as lyophilized powder and used as supplied. According to the certificate of analysis, the product contains at least 75% total protein by the Biuret method, of which ≥98% is β-casein, corresponding to a minimum overall content of 73.5% β-casein in the material. Protein identity and purity were independently confirmed by mass spectrometry.

Many of the structural and functional properties of β-casein are discussed in detail in Chapter 3; here we briefly summarize the most relevant aspects for the present study. It is a medium-sized protein composed of 209 amino acids with an average molecular weight of 23 988 Da, determined by mass spectrometry and consistent with the value calculated from its sequence (Fig. 3.2) using the ExPASy ProtParam molecular weight calculator (UniProtKB entry name CASB_BOVIN and accession number P02666). Its amphiphilic sequence organization promotes reversible self-association into micelle-like aggregates above a critical micellar concentration (CMC) in the range of 1-5 mg/mL, depending on pH, ionic strength, and temperature [83,84]. These assemblies are typically polydisperse and remain soluble over a broad range of conditions [69]. For concentration determination, an extinction coefficient of $\varepsilon_{278} = 11500\ \mathrm{M^{-1}\ cm^{-1}}$ was used (equivalent to $E^{1\,\mathrm{cm}}_{1\%} = 4.79$ for $M_\mathrm{w} = 23\,988$ Da) [69].

4.1.2 Solvents

Water (H_2O) and heavy water (D_2O)

Water is one of the most fundamental molecules in biology, serving as the medium for most biochemical reactions, dissolving biomolecules, and mediating essential interactions such as protein hydration and diffusion.

In neutron experiments it is standard practice to replace H_2O with heavy water (D_2O) as the solvent. D_2O is the isotopically substituted form of water in which the hydrogen atoms (^1H) are replaced by deuterium (^2H). This substitution is advantageous because deuterium has a much lower incoherent neutron scattering cross-section than hydrogen, which reduces background and enables contrast-variation protocols in SANS, QENS, and NSE (see Chapter 2). As a solvent, D_2O differs from H_2O in physicochemical properties; at 25 °C it is denser (1.105 vs. 0.997 $g\,cm^{-3}$), more viscous (1.25 vs. 0.89 mPa s), and has higher boiling and freezing points (101.4/3.8 vs. 100/0 °C). The acidity scale is shifted in D_2O; with glass electrodes calibrated in H_2O we use the practical correction $pD \approx pH_{reading} + 0.4$ and formulate buffers to a target pD. These differences are accounted for during buffer preparation and when interpreting diffusion-related measurements.

Note, however, that the isotopic composition of the solvent can influence protein behavior. For intrinsically disordered proteins such as β-casein, replacing H_2O with D_2O may alter hydration, conformational flexibility, self-assembly, and phase behavior. A systematic investigation of such isotope effects is beyond the scope of this work; this remark is included solely to emphasize that comparisons with literature data obtained in H_2O should be made with caution. In this work, all buffers and protein solutions were prepared in D_2O (≥99.9 atom % D, Sigma-Aldrich / Merck KGaA, Darmstadt, Germany) unless otherwise stated.

Sodium phosphate buffer

The use of a buffer system in protein studies is essential to maintain a controlled pH, ensuring reproducible structural and dynamic properties of the samples. For β-casein, the pH plays a critical role in solubility and micelle formation [90]. Deviations from the optimal range can promote aggregation or precipitation, compromising both sample stability and the reliability of scattering experiments.

In this work, a 25 mM sodium phosphate buffer in D_2O at pD 7.3 was employed. Phosphate buffer is among the most commonly used media in β-casein studies, as it provides stable capacity close to neutrality, avoids specific interactions with the protein, and is chemically simple and transparent to spectroscopic and neutron techniques. The chosen acidity falls within the natural pH window of bovine milk, thereby mimicking realistic conditions as closely as possible. Moreover, the use of this buffer and pH facilitates comparison with previous reports on β-casein solubility and aggregation behavior, where phosphate systems were systematically applied (see Chapter 3).
The buffer was prepared from sodium phosphate monobasic (MW 119.98 g mol^{-1}, Sigma-Aldrich / Merck KGaA, Darmstadt, Germany) and sodium phosphate dibasic (MW 141.96 g/mol, Sigma-Aldrich / Merck KGaA) dissolved in D_2O (≥99.9 atom% D, Sigma-Aldrich / Merck KGaA). The relative amounts of acid and base were calculated from the Henderson-Hasselbalch relation with $pK_a = 7.21$, adjusted to the target pD with 1 M NaOD or 1 M DCl, completed to final volume with D_2O, and filtered through 0.22 μm regenerated-cellulose membranes prior to use.

Urea

Urea is one of the most widely used protein denaturants. At sufficiently high concentrations, it destabilizes noncovalent interactions by disrupting the hydrogen-bonding network of water and weakening hydrophobic interactions [91,92]. In addition, urea can interact directly with both polar and nonpolar side chains, thereby reducing the cooperative forces that stabilize folded conformations or supramolecular assemblies. For β-casein, whose micellization is largely driven by hydrophobic interactions of the C-terminal domain, the presence of urea diminishes this driving force and promotes solvation of the protein chains, leading to micelle dissociation and the release of monomeric protein [84].
For neutron experiments, we employed deuterated urea, $CO(ND_2)_2$ (MW 64.08 g mol^{-1}, CDN Isotopes, Cat. D-0391), dissolved in sodium phosphate buffer prepared in D_2O. The deuterated form minimizes proton incoherent background while preserving the chaotropic effect. This solvent system was applied in Chapter 8 to probe the transition from assembled β-casein micelles to free monomers and to study the dynamics of the dissociated state.

4.1.3 Sample preparation

Samples were prepared by dissolving lyophilized β-casein in 25 mM sodium phosphate buffer prepared in D_2O (pD 7.3) without agitation at 5 °C. Solutions were allowed to hydrate and equilibrate for 24 h. Immediately before the measurements, samples were transferred to the appropriate sample holders and equilibrated at the desired measurement temperature; when required, solutions were passed through 0.22 µm regenerated-cellulose filters prior to loading.

When measurements at different protein concentrations were required, we typically prepared a concentrated stock solution and then diluted aliquots with the same buffer to the target values. This approach was used especially for low concentrations ($< 10\,\mathrm{mg\,mL^{-1}}$), as weighing larger masses reduces relative errors compared with weighing very small amounts of protein. In contrast, high-concentration samples ($\geq 25\,\mathrm{mg\,mL^{-1}}$) were usually prepared individually by direct dissolution to ensure accurate composition and reproducible self-assembly.

The final concentration of each sample was determined by UV-Vis spectroscopy using a dilution series for each protein solution on a Jasco V-630 spectrophotometer (Tokyo, JP). For each dilution step, absorbance spectra were collected and the peak absorbance at 280 nm was plotted against the reciprocal dilution factor. The resulting datasets were fitted with the Beer-Lambert law,

$$A = \varepsilon_{278}\, c\, \ell, \tag{4.3}$$

where ℓ is the optical path length of the cuvette and ε_{280} the sample extinction coefficient at 278 nm (see Section 4.1.1). In practice, the nominal concentrations and the UV-Vis-determined values agreed within $\lesssim 5\%$ in most cases; therefore, for clarity and consistency we report nominal concentrations throughout the thesis.

4.2 Methods

This section describes only the experimental methods employed in this work. The molecular dynamics simulations and associated MDANSE analyses were performed by Dr. Saikat Chakraborty, postdoctoral researcher on this project. A concise description of these simulations is provided in Appendix A, where full methodological details can be found. For

completeness, a chronological list of all large-scale facility experiments in which the author participated (highlighting those directly related to this thesis) is provided in Appendix B.

4.2.1 Dynamic light scattering

Dynamic light scattering (DLS) is a photon correlation technique that probes temporal fluctuations of scattered light intensity to access the dynamics of particles in solution. The decay of the intensity autocorrelation function reflects the translational diffusion of the scatterers, from which their hydrodynamic radius can be determined via the Stokes-Einstein relation. Due to its sensitivity to particle size and aggregation state, DLS is widely used to characterize proteins and colloids in aqueous solution.

DLS experiments were carried out on a commercial setup (LS Instruments AG, Fribourg, Switzerland) equipped for both two-dimensional (2D) and three-dimensional (3D) cross-correlation measurements. A laser with a wavelength of 660 nm was used as the light source, and scattering angles in the range 30-150° were explored. This corresponds to a scattering vector range of approximately $q \approx 0.006$–$0.025\,\mathrm{nm}^{-1}$, probing length scales on the order of 250–1000 nm and dynamics typically in the microsecond to second time window. Each measurement lasted 240 s, with the sample temperature controlled by a circulating water bath to within $\pm\,0.3\,^{\circ}\mathrm{C}$.

The normalized intensity autocorrelation functions $g_2(q,\tau)$ were recorded and used directly for analysis. To quantify the relaxation modes, the correlation functions were fitted with a biexponential model of the form

$$g_2(\tau) - 1 = A_1 \exp(-2\Gamma_{\mathrm{fast}}\tau) + A_2 \exp(-2\Gamma_{\mathrm{slow}}\tau), \tag{4.1}$$

where A_1 and A_2 are the amplitudes of the fast and slow modes, respectively, and Γ_{fast} and Γ_{slow} their corresponding relaxation rates. Hydrodynamic radii were subsequently obtained from the decay rates via the Stokes-Einstein relation, using the viscosity of D_2O at the measurement temperature.

To exclude the possibility of multiple scattering, complementary measurements were performed in 3D cross-correlation mode, which suppresses contributions from multiply scattered light. The resulting $g_2(\tau)$ functions were almost indistinguishable from those obtained with standard 2D measurements at all concentrations (Appendix C), confirming that the observed slow mode is intrinsic to the system. In this work we therefore report 2D

DLS data, as the 3D configuration is known to suffer from reduced correlation intercepts due to cross-talk between beams.

4.2.2 Small-angle neutron scattering (D33)

Small-angle neutron scattering (SANS) experiments were performed on the D33 instrument at the Institut Laue-Langevin (ILL), Grenoble, France. Samples were filled into 1 mm path-length flat quartz cuvettes (Hellma Analytics, Müllheim, Germany), sealed with Parafilm®, and mounted on a copper holder for thermal stability. The accessible momentum-transfer range was $q = 0.0115\text{-}0.44$ Å^{-1}. Quartz was chosen because it produces minimal scattering at the low q values probed in SANS, avoiding the small-angle scattering that would arise from aluminum cells due to alloy grain structure.

Raw data were saved in NeXus format and reduced with the ILL Graphical Reduction and Analysis SANS Program (GRASP; MATLAB™-based), following the standard pipeline. Corrections included empty-cell scattering, transmission (from attenuated-beam measurements), and electronic background determined with a $^{10}B_4C$ absorber. Absolute intensity calibration (in cm^{-1}) was obtained from attenuated direct-beam measurements under identical instrument settings.

Solvent scattering was subtracted from the sample-plus-solvent data accounting for the solvent volume fraction in the loaded cell. On an absolute, transmission-corrected scale this reads

$$I_{\text{protein}}(q) = I_{\text{sample}}(q) - \phi_{\text{solv}}\, I_{\text{solv}}(q), \tag{4.2}$$

where ϕ_{solv} is the solvent volume fraction defined in Eq. (4.10).

Data analysis was carried out with Python scripts specifically developed for this study. We fitted the SANS intensity with the minimal piecewise model of Eq. (5.1), using a fixed crossover at $q^* = 8.5 \times 10^{-2}$ Å^{-1}. In the low-q regime, $Cq^{-m} + B$ accounts phenomenologically for large-scale clustering. In the high-q regime, the data were modeled as $I(q) = A\,P(q)\,S(q) + B$ with $P(0) = 1$, choosing $P(q)$ and (when required) $S(q)$ from the following standard kernels.

For *homogeneous spheres* of radius R, the scattering amplitude and normalized form factor are

$$F_{\mathrm{sp}}(q;R) = 3\,\frac{\sin(qR) - qR\cos(qR)}{(qR)^3}, \tag{4.3a}$$

$$P_{\mathrm{sp}}(q;R) = \Big|F_{\mathrm{sp}}(q;R)\Big|^2. \tag{4.3b}$$

For *core-shell spheres* with core radius R_c, shell thickness t, and relative contrast $\beta = \Delta\rho_{\mathrm{shell}}/\Delta\rho_{\mathrm{core}}$,

$$F_{\mathrm{cs}}(q;R_c,t,\beta) = F_{\mathrm{sp}}(q;R_c)\,R_c^3 + \beta\Big[F_{\mathrm{sp}}(q;R_c+t)\,(R_c+t)^3 - F_{\mathrm{sp}}(q;R_c)\,R_c^3\Big], \tag{4.4a}$$

$$P_{\mathrm{cs}}(q;R_c,t,\beta) = \frac{\Big|F_{\mathrm{cs}}(q;R_c,t,\beta)\Big|^2}{\Big|F_{\mathrm{cs}}(0;R_c,t,\beta)\Big|^2}. \tag{4.4b}$$

For *Gaussian coils* (Debye form) with radius of gyration R_g,

$$P_{\mathrm{coil}}(q;R_g) = \frac{2\left[e^{-(qR_g)^2} - 1 + (qR_g)^2\right]}{(qR_g)^4}. \tag{4.5a}$$

Size polydispersity (sphere radius, core radius, or R_g) was incorporated by averaging $P(q)$ over lognormal distributions and renormalizing to enforce $P(0) = 1$. A log-normal distribution was chosen because it ensures that all particle sizes are strictly positive and captures the right-skewed shape of particle-size distributions in self-assembled systems. It also provides a stable parametrization equivalent to a Schulz-Zimm distribution for moderate dispersities. The distribution is defined as

$$f(R) \propto [R\,s\,\sqrt{2\pi}]^{-1}\exp[-(\ln R - \mu)^2/(2s^2)], \tag{4.6}$$

with mean radius $\langle R\rangle = e^{\mu+s^2/2}$ and relative polydispersity $\rho = \sigma_R/\langle R\rangle = \sqrt{e^{s^2}-1}$, where σ_R is the standard deviation of R. The parameter ρ is reported as obtained from the fits.

Inter-assembly correlations at higher concentrations were captured by a *hard-sphere structure factor* $S_{\mathrm{HS}}(q;R_{\mathrm{HS}},\phi)$ in the Percus-Yevick approximation (Ashcroft-Lekner closed form), parameterized by an effective hard-sphere radius R_{HS} and the volume fraction ϕ. In the dilute limit ($c < 10$ mg/mL) we set $S(q) = 1$; otherwise, $S(q) = S_{\mathrm{HS}}(q;R_{\mathrm{HS}},\phi)$ was fitted jointly with the chosen $P(q)$.

4.2.3 Neutron backscattering spectroscopy (IN16B / BATS)

Neutron backscattering measurements were performed on the cold-neutron spectrometer IN16B at the Institut Laue-Langevin (ILL), Grenoble, France, in the inverted time-of-flight (BATS) configuration with Si(111) analyzer crystals [33, 93, 94]. In this mode, the instrument provides a Gaussian energy resolution of approximately 1.75 μeV (HWHM) and an accessible dynamic range of ± 150 μeV. The Si(111) analyzers set the elastic wavelength to $\lambda = 6.271$ Å ($E_f = 2.08$ meV), and the accessible momentum transfer spans from 0.2 to 1.9 Å^{-1}.

Samples were loaded into cylindrical aluminum sample holders with an outer diameter of 15 mm and a wall spacing of 0.3 mm between the inner and outer cylinders, sealed with indium wire, and mounted in a standard Orange cryofurnace for temperature control during the data acquisition. The use of aluminum minimizes background scattering and ensures good thermal contact with the helium exchange gas in the cryofurnace. The narrow gap in the sample holder results in total scattering of less than 10% for all samples, making the probability of multiple scattering negligible. For background correction, both the empty cell and the cell filled with solvent alone were measured under identical conditions.

High-concentration protein samples ($\geq$50 mg/mL) were measured for at least 4 h each, while lower-concentration samples ($<$50 mg/mL) were measured for a minimum of 6 h in order to obtain sufficient statistics. The instrumental resolution function, $R(\omega)$, was determined by measuring a thin vanadium foil inside the same sample holder. Vanadium is used as a resolution standard because it scatters neutrons almost entirely incoherently, producing a purely elastic response independent of q and ω.

Raw data were processed to the dynamic structure factor $S(q, \omega)$ using the Mantid software framework [95], applying standard reductions including monitor normalization and detector-efficiency corrections.

Because the empty-cell statistics were insufficient and small differences existed between the container used for the solvent and that used for the samples, we did not subtract the empty-cell signal directly. Instead, we treated the container explicitly as an elastic contribution $\propto \delta(\omega)$ within the model. The fitting workflow proceeded in two steps:

(i) Solvent fit. The D_2O buffer spectrum was first fitted with a single-Lorentzian model for the solvent dynamics plus an elastic container term, both convolved with the measured

resolution,

$$S_{\mathrm{solv}}(q,\omega) = R(\omega) \otimes \Big[\beta_{\mathrm{D_2O}}\, \mathcal{L}(\gamma_{\mathrm{D_2O}},\omega) + A_{\mathrm{c}}\, \delta(\omega) + B \Big], \tag{4.7}$$

where $\mathcal{L}(\Gamma,\omega) = \dfrac{1}{\pi}\dfrac{\Gamma}{\Gamma^2+\omega^2}$ is a unit-area Lorentzian with half-width at half-maximum (HWHM) Γ, $\beta_{\mathrm{D_2O}}$ and $\gamma_{\mathrm{D_2O}}$ are the solvent amplitude and HWHM, A_{c} is the container amplitude, and B is a constant flat background. Parameters $\{\gamma_{\mathrm{D_2O}}, \beta_{\mathrm{D_2O}}, A_{\mathrm{c}}, B\}$ were determined from these independent solvent measurements.

(ii) Sample fit. For protein samples, the total model comprised the sample's quasi-elastic signal, the solvent contribution rescaled by the solvent volume fraction ϕ_{solv} in the loaded cell, and the elastic container term, all convolved with the resolution function, $R(\omega)$:

$$S(q,\omega) \;=\; R(\omega) \otimes \Big[S_{\mathrm{sample}}(q,\omega) \;+\; \phi_{\mathrm{solv}}\, S_{\mathrm{solv}}(q,\omega) \;+\; S_{\mathrm{cont}}(q,\omega) \Big]. \tag{4.8}$$

Expanding the right-hand side gives

$$\begin{aligned} S(q,\omega) = R(\omega) \otimes \Big\{ & \underbrace{\beta\, \mathcal{L}(\gamma,\omega) \otimes \Big[A_0(q)\, \delta(\omega) + \big(1 - A_0(q)\big)\, \mathcal{L}(\Gamma,\omega) \Big]}_{\text{sample signal (free)}} \\ & + \quad \underbrace{\phi_{\mathrm{solv}} \Big[\beta_{\mathrm{D_2O}}\, \mathcal{L}(\gamma_{\mathrm{D_2O}},\omega) + B \Big]}_{\text{solvent rescaled by volume fraction (fixed)}} \quad + \quad \underbrace{A_{\mathrm{c}}\, \delta(\omega)}_{\text{container (fixed)}} \Big\}. \end{aligned} \tag{4.9}$$

In the fits, the parameters $\beta, A_0(q), \gamma, \Gamma$ describing the sample signal were optimized, while the solvent and container terms remained fixed. Here, β is the Debye-Waller factor (DWF), $A_0(q)$ the elastic incoherent structure factor (EISF), and γ/Γ denote the HWHM of the slow/fast components, respectively. In these fits, the solvent and container terms inherited their shapes and amplitudes from Eq. (4.7); only the overall solvent amplitude was rescaled by the solvent volume fraction,

$$\phi_{\mathrm{solv}} \;=\; 1 \;-\; \frac{c}{1000}\,\nu, \tag{4.10}$$

where c is the protein concentration in mg/mL (so $c/1000$ is in mL/g and ν is the specific volume of β-casein ($\nu = 0.746$ mL/g). Thus $(c/1000)\nu$ is the protein volume fraction, and ϕ_{solv} is the remaining solvent fraction (assuming volume additivity).

Further details of the analysis strategy and parameter interpretation are provided in Chapter 6.

4.2.4 Neutron spin-echo spectroscopy (IN15)

Neutron spin-echo (NSE) measurements were performed on the high-resolution spin-echo spectrometer IN15 at the Institut Laue-Langevin (ILL), Grenoble, France [96]. Experiments were carried out at four incident wavelengths, λ = 6, 8, 10, and 17 Å, with corresponding angular positions of 9°, 6°, 4°, and 3.5°, respectively. This configuration provided access to Fourier times up to 1000 ns and to a q-range of 0.017-0.18 Å^{-1}.

Polarization was achieved with Fe-Co-Si supermirror polarizers on Si substrates, while the analyzer was a Fe-Co supermirror. Detectors were positioned 4.6 m downstream from the sample and consisted of a 32×32 pixel array (1 cm^2 per pixel) filled with ^{3}He at 1 bar and CF_4 at 0.3 bar. Further technical details of IN16B can be found in Refs. [96–98] and on the instrument website.

Samples were loaded in flat quartz cells (40 × 30 mm, internal thickness 2 mm; Aireka Scientific Co., Ltd., Hong Kong), closed with plastic caps and sealed with Parafilm® (Merck/MilliporeSigma) to minimize evaporation. Quartz was used, as in the SANS experiments, to minimize unwanted scattering at the low q values accessed in NSE. Quartz was used, as in the SANS experiments, to minimize unwanted scattering at the low q values accessed in NSE. A graphite sample and pure buffer were measured as references for resolution and background, respectively. Measurements were carried out in a temperature-controlled sample changer. A full acquisition cycle, covering the four wavelength configurations, required approximately 4 h per sample and temperature.

Raw data were reduced using the standard NSE routines implemented in Igor Pro [99], including resolution correction and subtraction of the buffer background.

NSE data were processed and analyzed using custom Python scripts developed in-house. Several fitting models were compared systematically, as discussed in detail in Chapter 5. For consistency and quantitative comparison, we adopted the cumulant analysis as the primary description of the intermediate scattering function. In this framework, the normalized intermediate scattering function is expressed as

$$\frac{I(q,t)}{I(q,0)} \;=\; A(q)\,\exp\!\Big[-\Gamma(q)\,t \;+\; \tfrac{1}{2}\,\mu_2(q)\,t^2\Big]\,, \tag{4.11}$$

where $A(q)$ is the q-dependent amplitude, $\Gamma(q)$ is the first cumulant, and $\mu_2(q)$ the second cumulant. From this expression, the normalized second cumulant is defined as

$$k_2(q) \;=\; \frac{\mu_2(q)}{\Gamma^2(q)}. \tag{4.12}$$

The first cumulant $\Gamma(q)$ reflects the average relaxation rate of the system, while $k_2(q)$ quantifies deviations from a single-exponential decay. This approach provides a robust characterization of the q-dependent dynamics and served as the basis for the subsequent analysis presented in Chapter 5.

Chapter 5

Structural characterization and collective dynamics of β-casein assemblies

5.1 Introduction

This chapter integrates small-angle neutron scattering (SANS), dynamic light scattering (DLS), and neutron spin-echo (NSE) to map how β-casein assemblies organize and relax across concentration and temperature. Our objective is to identify the relevant structural levels and the associated diffusive modes and to relate them within a common q-window. SANS is used to quantify the static architecture of the assemblies via a minimal piecewise description that separates the form-factor contribution (micelles) from a low-q excess (cluster-like inhomogeneities), with explicit treatment of polydispersity. DLS then probes mesoscopic time scales and resolves the intensity autocorrelation into two exponentials, providing fast and slow diffusive modes; 3D cross-correlation data are employed to rule out multiple scattering. Finally, NSE accesses short-time collective dynamics at the same q values as SANS, allowing a direct comparison between structure and relaxation and a test of de Gennes narrowing through the joint analysis of $D(q)$ and $S(q)$. The chapter is organized accordingly: static structure (SANS), diffusive dynamics at optical q (DLS), and short-time collective dynamics in the SANS window (NSE).

5.2 Results and discussion

5.2.1 Static structure of β-casein assemblies

To characterize the static organization of β-casein assemblies, we performed SANS measurements over a wide range of concentrations and temperatures. The left panel of Figure 5.1 shows representative scattering curves together with their total fits (Eq. 5.1), highlighting the progressive changes that occur with increasing concentration. At low concentrations, the profiles display the smooth decay characteristic of finite-sized particles [100]. In this regime, the data can be described by form factors such as homogeneous spheres or core-shell geometries, motivated by previous studies on β-casein assemblies discussed in Chapter 3. Polydispersity must be included to account for the broadening of the scattering features, reflecting the fact that the assemblies are not monodisperse but instead exhibit a distribution of sizes [69].

Beyond the contribution of the assemblies, all datasets exhibit a pronounced upturn at low q, corresponding to structural inhomogeneities on length scales much larger than the average radius of the assemblies. This excess scattering cannot be reproduced by the form factor alone and is therefore modeled as an additional term associated with larger, transient clusters of assemblies. Most samples follow the expected trend, although at 2 mg/mL a notably higher low-q scattering is observed. The observation of this low-q excess is consistent with the slow diffusive mode independently detected by dynamic light scattering (see Section 5.2.2). To avoid confusion, in the following we will refer to this large-scale contribution as clusters, thereby distinguishing it from the micelles themselves, which are elsewhere in the text also referred to as assemblies or aggregates.

At higher concentrations, the scattering profiles undergo a qualitative change: a distinct correlation peak emerges at intermediate q, reflecting short-range order due to micelle-micelle interactions. This feature requires the inclusion of a hard-sphere structure factor in the analysis. We analyze the SANS intensity with a minimal piecewise model,

$$I(q) = \begin{cases} C\,q^{-m} + B, & q < q^*, \\ A\,P(q)\,S(q) + B, & q > q^*, \end{cases} \tag{5.1}$$

where C and m describe the low-q cluster contribution, A is the assembly amplitude (with $P(0) = 1$), B is a q-independent background, and q^* denotes the crossover wavevector,

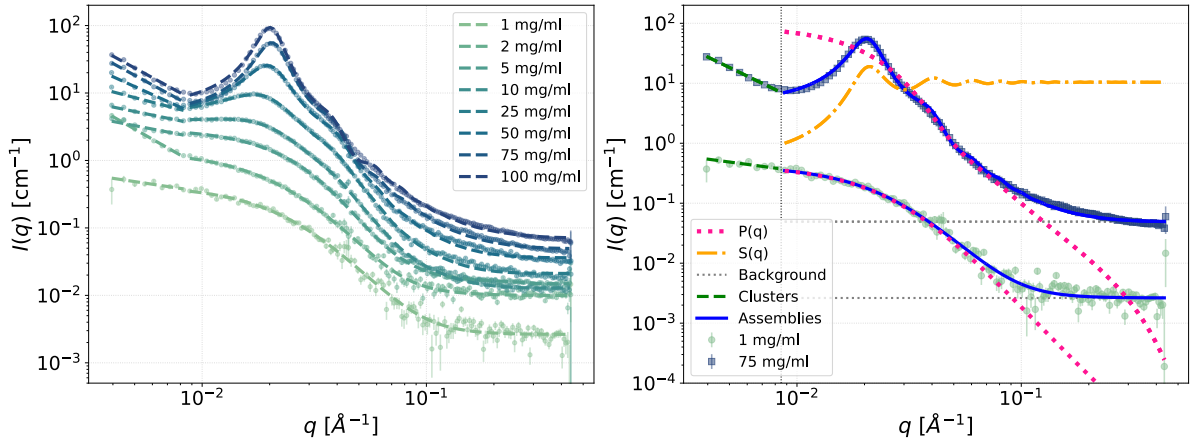

Figure 5.1. Left: SANS intensity profiles of β-casein assemblies at increasing concentrations, together with their fits using the piecewise model of Eq. 5.1 with a core-shell form factor. Symbols show the experimental data, while dashed lines indicate the corresponding fits. **Right:** Detailed decomposition of the fit for one dilute (1 mg/mL) and one concentrated (75 mg/mL) sample. The form factor of the assemblies (core-shell model including polydispersity of the total radius) is shown in pink, the fitted assembly contribution in blue, the low-q cluster term in green, the hard-sphere structure factor in orange (concentrated case), and the incoherent background in gray. The vertical dotted line marks the crossover wavevector q^* separating the cluster- and assembly-dominated regimes.

fixed to $q^* = 8.5 \cdot 10^{-3}\,\text{Å}^{-1}$ for all samples. For dilute samples ($c < 10$ mg/mL), we set $S(q) = 1$, while at higher concentrations we include inter-assembly correlations via the aforementioned hard-sphere structure factor $S(q)$. The form factor $P(q)$ corresponds to either a homogeneous sphere or a core-shell geometry, with polydispersity accounted for in the outer (or core) radius, more details of the fitting can be found in Chapter 4. We note that the model can alternatively be formulated as a weighted sum of the two contributions (clusters and assemblies) without fixing a sharp crossover at q^*. In practice, however, this approach leads to less stable fits due to the increased number of free parameters. Importantly, the results obtained with both strategies are qualitatively similar, and therefore, to improve the robustness of the analysis, we adopted the piecewise description with a fixed q^* throughout all the samples.

The right panel of Figure 5.1 shows the detailed decomposition for one dilute and one concentrated sample. In both cases, the form factor of the β-casein assemblies (including

polydispersity) is shown in pink as a reference. The assembly fit used for the intermediate- and high-q region is plotted in blue, while the cluster contribution describing the low-q upturn is plotted in green. For the concentrated sample, an additional hard-sphere structure factor is overlaid in orange to account for the correlation peak at intermediate q. A constant incoherent background is shown in gray for both samples. The vertical dotted line marks the crossover wavevector q^* used to separate the cluster and assembly regimes. Note that we do not plot a single total fit curve, because the model is defined piecewise as the sum of the blue (assemblies) and green (clusters) contributions on their respective q-ranges.

In addition to the piecewise description introduced above, we examined the choice of form factor used to describe the assemblies. Figure 5.2 compares the fits obtained with a simple homogeneous sphere model and with a core-shell geometry, shown for representative dilute (left panel) and concentrated (right panel) samples. At low concentrations, both models reproduce the experimental data equally well, and the resulting fits are nearly indistinguishable. In this regime, the additional parameters introduced in the core-shell model (e.g. core radius and shell thickness) do not significantly improve the description and instead lead to larger uncertainties in the fitted values, reflecting reduced stability of the fit.

At higher concentrations, however, clear differences between the two models emerge. In particular, the homogeneous sphere form factor systematically fails to capture the high-q region, whereas the core-shell model provides an improved description of the data. This suggests that with increasing concentration, the distinction between the protein-rich core and the more hydrated shell becomes increasingly relevant, and the simplified sphere approximation is no longer adequate. For consistency across all concentrations, we therefore base our main analysis on the core-shell model. Nevertheless, for dilute samples we also report the results obtained with the simpler sphere model, as its reduced parameter set yields more robust fits in this regime. At high concentrations, only the core-shell model is retained, as it is the only one capable of reproducing the full q-range of the experimental profiles.

The upper left panel of Figure 5.3 summarizes the variation in overall assembly size with concentration. In the dilute regime, the fitted radii show no clear trend. This partly reflects the limited stability of the models when applied to such weak scattering, but may also indicate that at very low concentrations the assemblies themselves are less compact

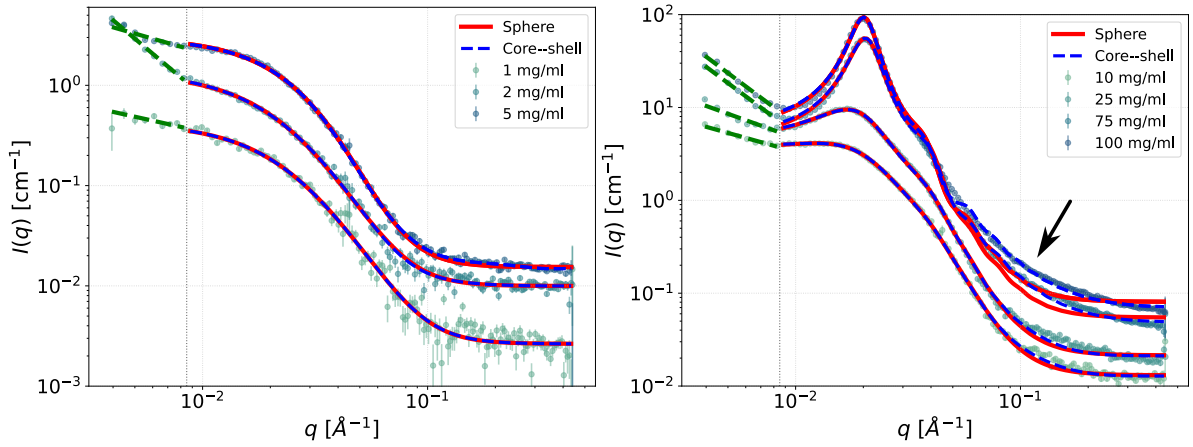

Figure 5.2. Left: Comparison of homogeneous sphere and core-shell form factors for a dilute sample (1 mg/mL). Both models reproduce the data equally well, yielding nearly indistinguishable fits. **Right:** Same comparison for a concentrated sample (75 mg/mL). In this case, the homogeneous sphere model fails to capture the high-q regime, while the core-shell geometry provides a significantly improved description of the data. The arrow highlights the q-range where the discrepancy between the two models is most pronounced.

and more heterogeneous, with a softer and more diffuse architecture that is intrinsically harder to represent with simple geometric form factors. In this regime, both the sphere and the core-shell fits are included: although they reproduce the data equally well, they yield somewhat different size estimates and trends, highlighting the difficulty of extracting reliable structural parameters under dilute conditions. The right panel of Figure 5.3 separates the core and shell contributions obtained from the core-shell model. At low concentrations, the fits typically return a dominant core radius with a vanishingly small shell thickness, suggesting that the assemblies are not compact enough to generate a measurable contrast between the protein-rich core and the outer layer, making the distinction between these two contributions effectively unresolved. In the concentrated regime, a clearer behavior emerges: the total radius increases only slightly with concentration, remaining confined to a narrow range of $\sim$ 9.5-11 nm. Within this stable size, the core radius shows a modest increase while the shell thickness decreases correspondingly, consistent with a progressive compaction of the assemblies. The hypothesized structural evolution is summarized schematically in the bottom panel of Figure 5.3.

Polydispersity is accounted for only in the form factor $P(q)$, by averaging it over a log-normal size distribution of radii characterized by the relative width parameter ρ obtained

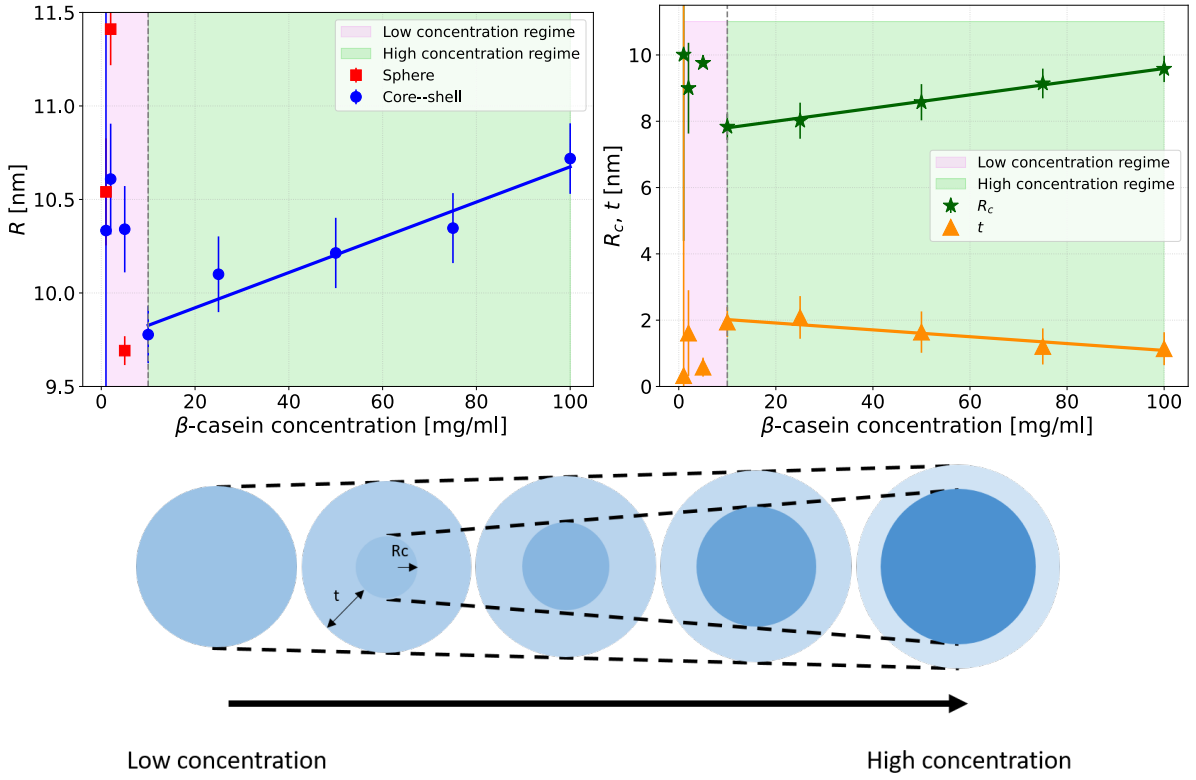

Figure 5.3. Top left: Total radius (R) of the β-casein assemblies as a function of concentration, obtained from SANS fits with both the homogeneous sphere and core-shell models. **Top right:** Decomposition of the total radius into core radius (R_c) and shell thickness (t) (core-shell model only), from SANS analysis. Shaded backgrounds distinguish the dilute and concentrated regimes; solid lines are guides for the eye. **Bottom:** Schematic illustration of the hypothetical structural evolution inferred from the fits. With increasing concentration, the assemblies retain an approximately constant overall size, while the protein-rich core (darker shading) becomes denser and larger and the outer shell (lighter shading) progressively thinner.

from the fits (see Chapter 4 for details). The behavior of ρ follows a trend closely resembling that of the radius. As shown in Figure 5.4, ρ does not exhibit a clear dependence in the dilute regime, where the fits are less stable and the assemblies themselves may be more heterogeneous. In contrast, at higher concentrations a systematic decrease of ρ is observed, indicating that the assemblies become more uniform in size as crowding increases. The right panel of Figure 5.4 illustrates this effect by displaying the corresponding log-normal size distributions: with increasing concentration, the distributions shift toward

slightly larger radii while simultaneously narrowing, consistent with an increase of the average radius and a reduction in polydispersity.

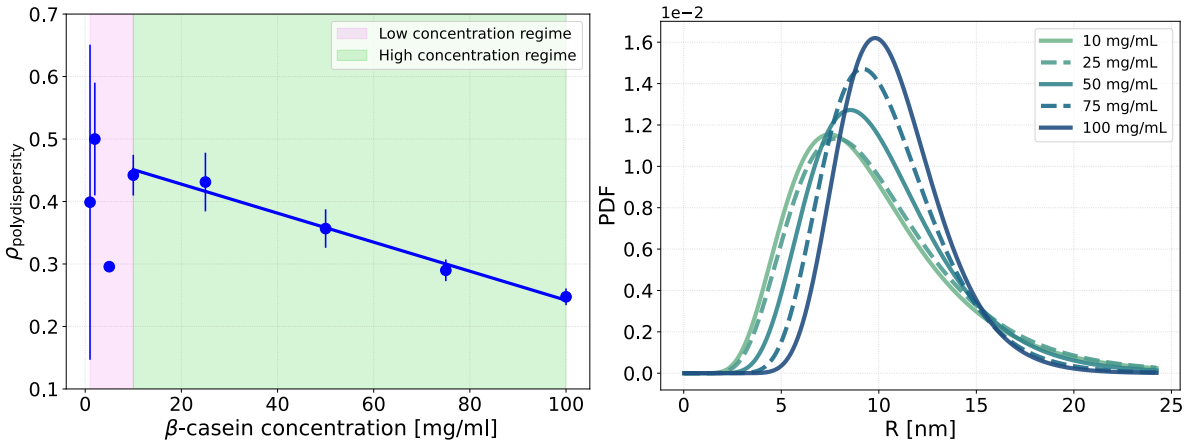

Figure 5.4. Left: Polydispersity parameter ρ obtained from log-normal SANS fits as a function of concentration. Shaded backgrounds distinguish the dilute and concentrated regimes; solid lines are guides for the eye. **Right:** Corresponding log-normal size distributions for concentrated samples.

To complete the characterization of the large-scale contribution, we quantified the cluster term by its integrated scattering weight rather than by the bare prefactor C. Specifically, starting from the low-q power law in Eq. 5.1, we define the integrated scattering weight

$$W_{\mathrm{cl}} \equiv \int_{q_{\min}}^{q^*} C\, q^{-m}\, dq = \frac{C}{1-m}\left[(q^*)^{1-m} - (q_{\min})^{1-m}\right], \tag{5.2}$$

with $q_{\min} = 0.004$ Å^{-1} the lowest measured q and $q^* = 8.5 \times 10^{-3}$ Å^{-1} the crossover separating cluster- and assembly-dominated regimes. By construction, W_{cl} provides a scale-integrated measure of the total static intensity associated with large-scale inhomogeneities within the experimental window, avoiding the ambiguity that arises from the mutual coupling of C and m.

Figure 5.5 (left) shows that W_{cl} increases with concentration, indicating that the absolute scattering contribution of the cluster contribution becomes stronger under crowding. In parallel, the power-law exponent m (right) increases non-linearly from ∼0.7 in dilute samples to ∼1.8 at high concentration. Such values are consistent with mass-fractal-like scattering, where m reflects an effective fractal dimension of the inhomogeneities [101]. The point at 2 mg/mL deviates significantly from the main trend, plausibly due to experimental artifacts such as occasional dust contamination. Altogether, these results suggest

a crossover from tenuous, diffuse clusters at low concentration to denser, more compact inhomogeneities at high concentration, consistent with the slow diffusive mode gaining prominence in DLS (Section 5.2.2).

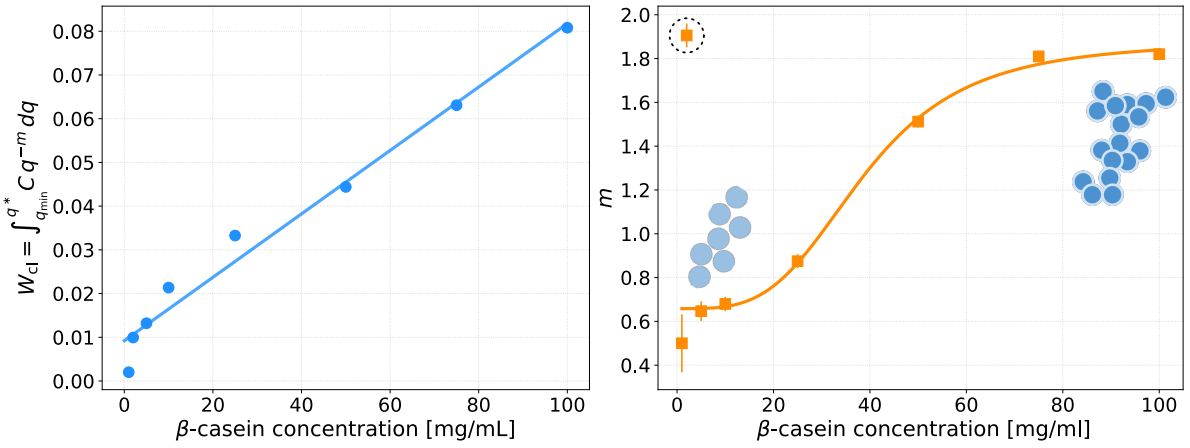

Figure 5.5. Concentration dependence of the parameters describing the cluster contribution to the SANS intensity. **Left:** Integrated scattering weight of the cluster contribution, $W_{\mathrm{cl}} = \int_{q_{\min}}^{q^*} C q^{-m}\, dq$, with $q_{\min} = 0.004$ Å^{-1} and $q^* = 8.5 \times 10^{-3}$ Å^{-1}. **Right:** Power-law exponent m versus concentration. Solid lines are guides to the eye; the dashed circle marks an outlier sample. The sketches illustrate a qualitative evolution from loose to compact inhomogeneities as m increases; they do not imply a specific micellar/cluster morphology.

Now that we have examined in detail all relevant parameters extracted from the concentration series, including the low-q cluster contribution, the overall assembly radius, the internal partitioning into core and shell, and the degree of polydispersity, a coherent picture emerges for the structural organization of β-casein. At low concentrations, the assemblies display a rather diffuse character: the low-q signal indicates highly heterogeneous clusters, while the fitted radii and even the choice of form factor remain unstable and do not follow a consistent trend. This reflects the intrinsically soft, heterogeneous nature of the assemblies in the dilute regime. In contrast, at higher concentrations the results become much more robust and systematic. The overall size of the assemblies increases slightly, while the internal structure evolves in a clear manner: the protein-rich core becomes progressively denser and slightly larger, the hydrated shell correspondingly thinner, and the polydispersity decreases. Together with the suppression of the low-q cluster contribution and the emergence of a correlation peak, this concentrated regime reveals assemblies that

are structurally more compact and uniform, embedded in a crowded environment where micelle-micelle interactions dominate. Having identified these two distinct regimes we next investigate how temperature modulates the structural organization. To this end, we selected one representative concentration from each regime, 1 mg/mL and 75 mg/mL, and analyzed their SANS profiles as a function of temperature using the same piecewise description of Eq. 5.1 and the form factor choice established above (homogeneous sphere at 1 mg/mL, core-shell at 75 mg/mL). As shown in Figure 5.6, the model reproduces the systematic evolution of the scattering upon heating at both concentrations.

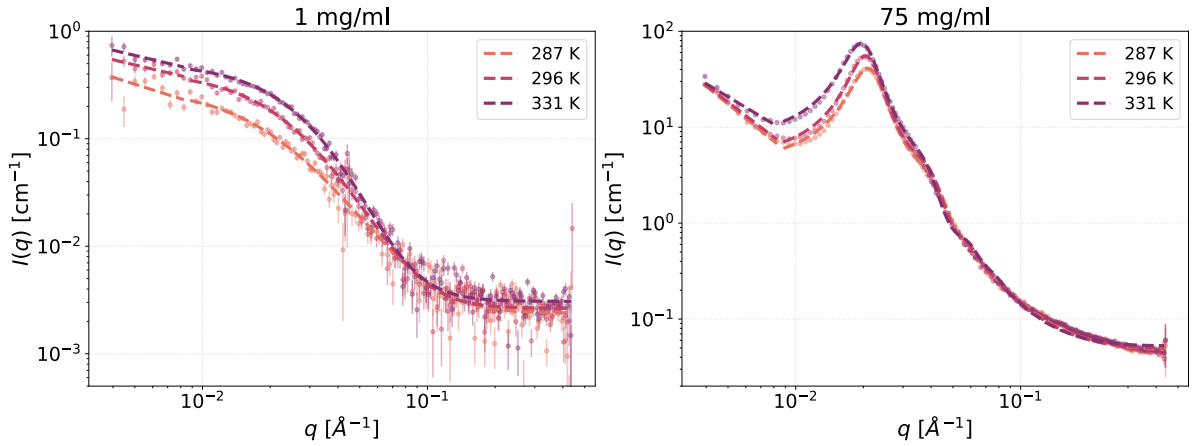

Figure 5.6. SANS intensity profiles versus temperature at: **Left:** 1 mg/mL fitted with a homogeneous sphere form factor. **Right:** 75 mg/mL fitted with a core-shell form factor. Symbols denote experimental data; dashed lines are fits using the piecewise model of Eq. 5.1. The same crossover wavevector $q^* = 8.5 \times 10^{-3}$ Å^{-1} is used as in the concentration series.

Heating impacts the two regimes differently (Figure 5.7). In dilute conditions (1 mg/mL), the total radius decreases with temperature, consistent with a mild compaction of the assemblies. Under crowding (75 mg/mL), the total radius instead increases slightly; both core radius R_c and shell thickness t grow weakly, suggesting a subtle swelling of the core-shell architecture. In both cases, the changes are modest in absolute terms, yet systematic across the measured range.

Temperature also narrows the size distributions at both concentrations (Figure 5.8). The log-normal relative width ρ decreases with T, and the corresponding distributions become sharper, shifting in the same direction as the mean radius (towards smaller radii at

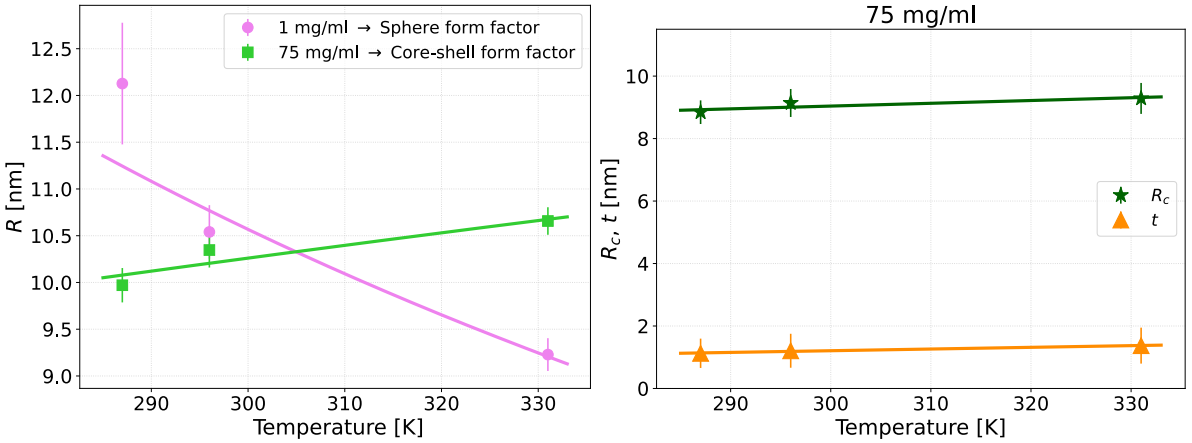

Figure 5.7. Left: Total radius as a function of temperature for 1 mg/mL (sphere) and 75 mg/mL (core-shell), from SANS analysis. **Right:** Decomposition of the 75 mg/mL fits into core radius R_c and shell thickness t. Solid lines are guides for the eye.

1 mg/mL and slightly larger at 75 mg/mL). This points to a temperature-driven homogenization of the assembly sizes irrespective of concentration.

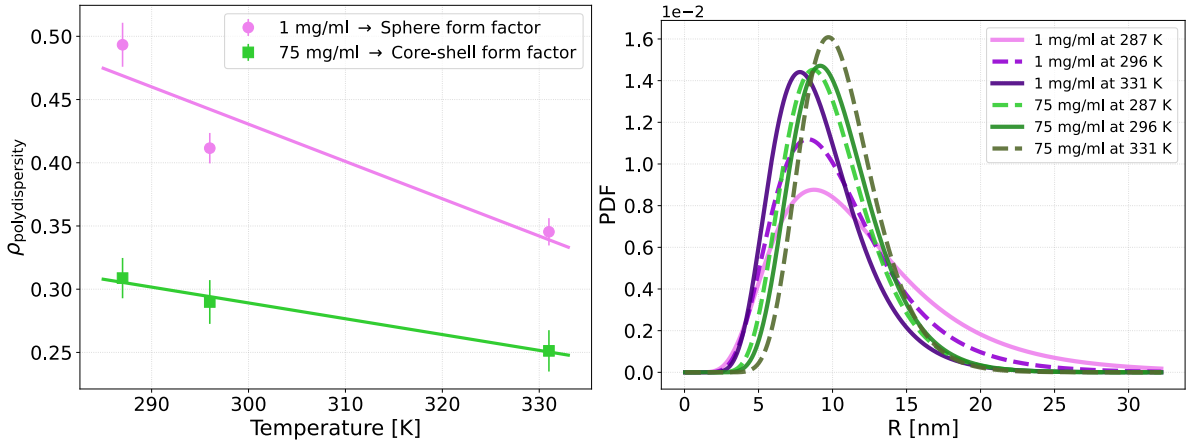

Figure 5.8. Left: Relative width ρ of the log-normal size distribution, obtained from SANS fits, as a function of temperature for 1 mg/mL and 75 mg/mL. **Right:** Corresponding log-normal size distributions at selected temperatures. Solid lines are guides for the eye.

Finally, the cluster contribution in absolute terms increases with temperature (Fig. 5.9). For both concentrations, W_{cl} increases with T, indicating that large-scale inhomogeneities gain scattering power upon heating. At the same time, the power-law exponent m decreases with temperature, from ~ 1.9 to ~ 1.4 at 75 mg/mL, and from ~ 0.7 to ~ 0.45

at 1 mg/mL, consistent with a shift toward more tenuous, diffuse structures (lower effective fractal dimension) at higher T. We will return to this trend when discussing the temperature dependence of the DLS modes.

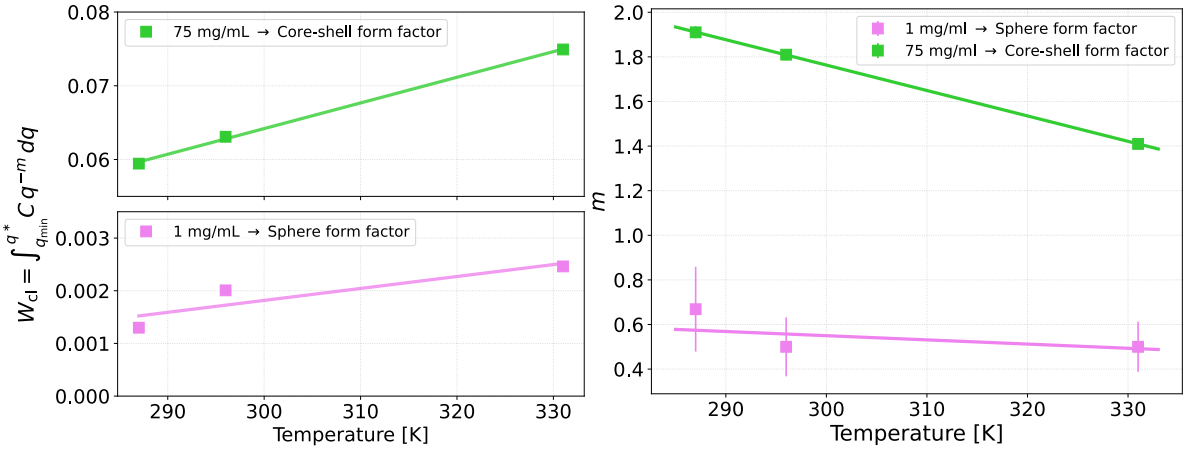

Figure 5.9. Left: Integrated cluster weight W_{cl} as a function of temperature, from SANS analysis. Errors were not propagated through the integral. **Right:** Power-law exponent m versus temperature. Solid lines are guides for the eye.

In summary, the SANS results delineate two clear regimes: in the dilute limit, the profiles reflect soft, diffuse assemblies with heterogeneous low-q features and structural parameters that lack robust trends; at high concentration, the behavior becomes systematic, with a correlation peak, a clearer core-shell partitioning, and reduced polydispersity. Temperature scans at 1 and 75 mg/mL reveal common signatures such as a narrowing of size distributions and a reshaping of the low-q excess, together with regime-specific responses including opposite trends in the characteristic radius. With this static landscape established across concentration and temperature, the next step is to determine how these structures relax in time and how the relevant length scales couple to dynamics.

5.2.2 Diffusive dynamics at mesoscopic scales

While the SANS measurements described above provide detailed insight into the static organization of β-casein assemblies across concentration, they do not directly probe the dynamics of these structures. To complement the static picture, we performed DLS experiments over a similar range of concentrations and temperatures. By recording the scattered intensity at different detection angles (converted into scattering vectors q as

described in Chapter 2, Eq. 2.50), DLS probes the temporal fluctuations of scattered light and thereby provides access to the collective relaxation modes of the system on mesoscopic length scales.

Representative intensity correlation functions $g^{(2)}(\tau)$ are shown in Figure 5.10 for the full concentration series. At all conditions, the correlation functions exhibit a two-step relaxation, with a fast decay at short lag times and a slower decay at longer lag times. For concentrated samples the two steps are clearly visible by eye, while for dilute samples the second decay is much less pronounced. However, single-exponential fits do not reproduce properly the data, and two exponential functions are consistently required (Appendix D). To capture this behavior, following De Kruif and co-workers [81] we fit the intensity correlation functions with a sum of two exponential functions:

$$g^{(2)}(\tau) - 1 = A_1 \exp(-2\Gamma_{\text{fast}}\,\tau) + A_2 \exp(-2\Gamma_{\text{slow}}\,\tau)\,, \tag{5.3}$$

where A_1 and A_2 are empirical amplitudes of the fast and slow modes, and Γ_{fast} and Γ_{slow} are their relaxation rates. This is an effective two mode parameterization rather than the exact expansion of the Siegert relation $g^{(2)} = 1 + \beta\,|g^{(1)}|^2$, which would include a cross term if $g^{(1)}$ contained two exponential functions. In practice, the fitted amplitudes absorb that contribution together with the coherence factor β, and the model robustly describes the observed two step relaxation.

Within this framework, two distinct diffusive processes are resolved. The fast relaxation mode is present across all concentrations, with rates scaling as $\Gamma_{\text{fast}} \propto q^2$, consistent with the center-of-mass diffusion of individual β-casein micelles. The slow relaxation also follows a q^2 scaling but with a diffusion coefficient about two orders of magnitude smaller, reflecting much slower dynamics that we associate with clusters.

It should be noted that in the literature the slow relaxation has sometimes been attributed to artifacts, such as polydispersity effects or multiple scattering, rather than to a genuine collective mode, as mentioned in Chapter 3. In our case, we assign the slow process to the transient formation of clusters, consistent with the excess low-q scattering observed in SANS. To exclude the possibility of multiple scattering, we performed 3D cross-correlation DLS measurements, which suppress the contribution of multiply scattered light. The resulting correlation functions were practically indistinguishable from those obtained with standard DLS at all concentrations (Appendix C), confirming that the observed slow mode reflects intrinsic sample dynamics rather than an optical artifact.

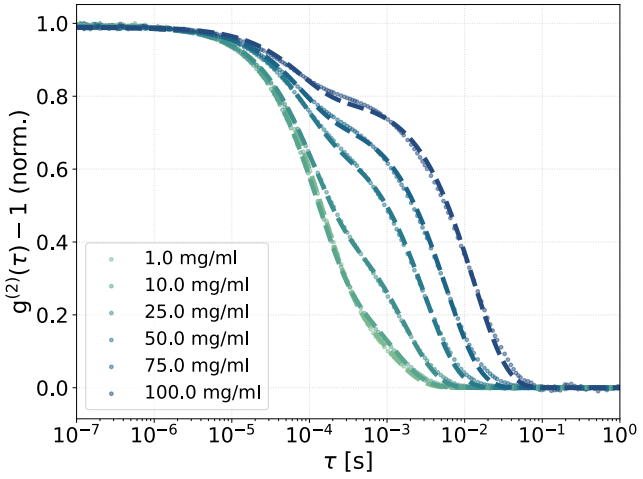

Figure 5.10. Representative DLS intensity autocorrelation functions $g^{(2)}(\tau)-1$ measured at a scattering angle of 90° for increasing concentrations, together with two-exponential fits (Eq. 5.3). Symbols show experimental data; dashed lines indicate the corresponding fits. Error bars denote 1σ confidence bounds of the fits.

A representative analysis of the q-dependence is shown in Figure 5.11. The left panel reports Γ_{fast} (top) and Γ_{slow} (bottom) versus q^2, demonstrating the diffusive nature of both processes with distinct diffusion coefficients. The right panel shows the corresponding amplitudes A_1 and A_2 as a function of q for an intermediate concentration (10 mg/mL). At small q the slow mode dominates, consistent with its origin in large-scale inhomogeneities, while at higher q the fast mode becomes more prominent, reflecting micelle-scale dynamics. From the angle-resolved data, diffusion coefficients were obtained by linear fits of Γ versus q^2 according to $\Gamma = D\,q^2$ (using the full q-range to extract D_{fast} and D_{slow}). The corresponding hydrodynamic radii were then computed from the Stokes-Einstein relation,

$$D = \frac{k_B T}{6\pi\eta R_h}, \tag{5.4}$$

with η the solvent viscosity at the experimental temperature. We report R_h under the standard perfect-stick (no-slip) convention corresponding to the 6π prefactor. Alternative interfacial boundary conditions would rescale R_h by a constant factor (for instance, perfect slip replaces 6π by 4π) but do not affect the qualitative trends. Figure 5.12 summarizes the concentration dependence of $R_{h,1}$ and $R_{h,2}$ (from the full q-range) together with the mode amplitudes A_1 and A_2 evaluated at a fixed scattering angle of 90°. Because the two radii differ by roughly two orders of magnitude, the y-axis (right) is shown on a

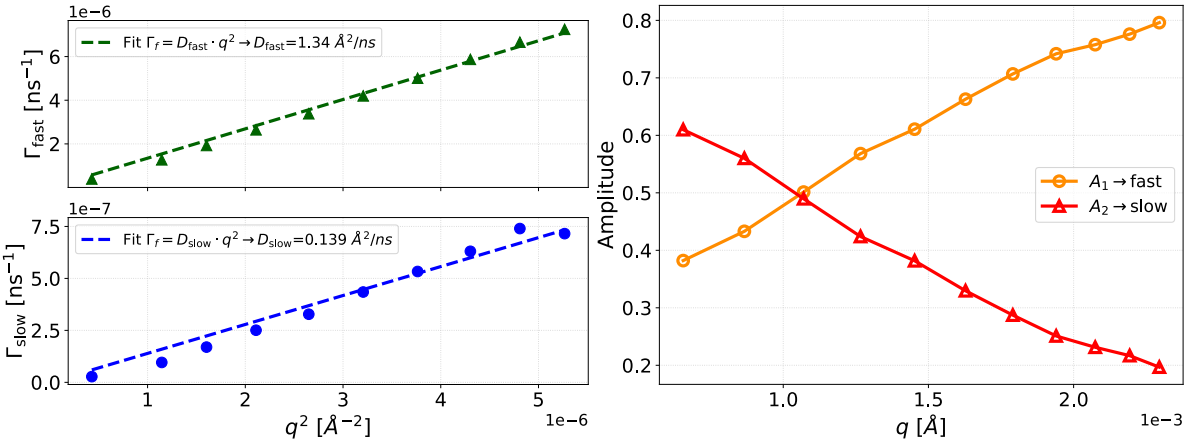

Figure 5.11. Left: DLS relaxation rates Γ_{fast} (top) and Γ_{slow} (bottom) versus q^2 for 10 mg/mL; symbols denote experimental values and dashed lines are linear fits to $\Gamma = D\,q^2$ (slopes yield D_{fast} and D_{slow}, see legend). **Right:** Corresponding mode amplitudes A_1 (fast) and A_2 (slow) versus q; solid lines are guides for the eye.

logarithmic scale. Over the measured concentration range, $R_{h,1}$ decreases from $\sim$ 17 to $\sim$ 10 nm, whereas $R_{h,2}$ increases from $\sim$ 130 to $\sim$ 1700 nm (i.e., up to $\sim$ 1.7 μm).

The hydrodynamic radius of the fast mode, $R_{h,1}$, decreases monotonically with concentration. At the lowest concentrations the micelles behave as soft, highly hydrated objects: the SANS data are well described by a homogeneous-sphere form factor, indicating that any internal contrast between a core and a corona is negligible, yet the strong hydration increases hydrodynamic drag and yields a larger apparent $R_{h,1}$ in DLS. Upon increasing concentration, dehydration and compaction reduce this softness and the associated drag, bringing $R_{h,1}$ into agreement with the $\sim$ 10 nm structural radius obtained from SANS at high concentration. In contrast, $R_{h,2}$ increases with concentration, indicating that the slow mode increasingly reflects collective, cluster-dominated rearrangements with a larger effective hydrodynamic length scale under crowding.

At the selected q, the amplitudes evolve oppositely with concentration: A_1 decreases while A_2 increases. This redistribution of spectral weight is consistent with the static trends from SANS once the q window is considered: DLS probes much lower q than SANS, and $A_i(q)$ reflect both the static scattering weight and the mode coupling. As concentration rises, the assemblies compactify (denser core, thinner hydrated shell) and polydispersity decreases, which diminishes the single-assembly contrast at the DLS length scale and reduces the relative weight of the fast (micellar) mode. Concurrently, SANS shows the

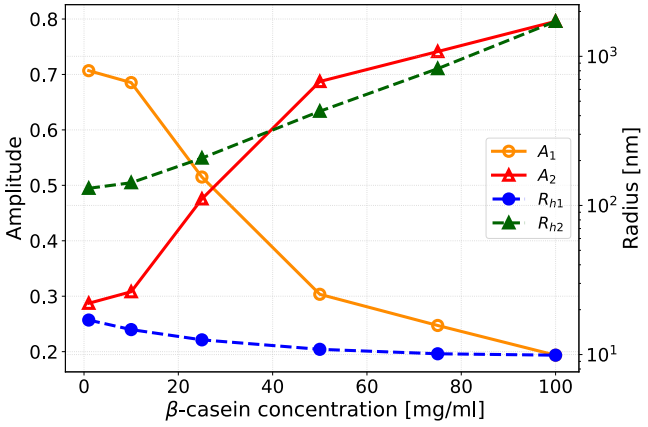

Figure 5.12. Hydrodynamic radii $R_{h,1}$ (fast) and $R_{h,2}$ (slow), obtained from the fitted relaxation rates via the Stokes-Einstein relation (logarithmic scale), together with the mode amplitudes A_1 and A_2 at a fixed scattering angle of 90°. All lines are guides for the eye.

build-up of interparticle correlations (emergence of a correlation peak) and denser cluster-like inhomogeneities (increase of the low-q exponent), so large-scale density fluctuations become slower and more persistent; their dynamical signature can therefore grow at the DLS q, enhancing the slow-mode amplitude A_2. Note that, at fixed q, the DLS amplitudes depend on both the static scattering $\propto P(q)S(q)$ (i.e. the SANS intensity $I(q)$ up to constants and background) and the mode structure; thus the increase of A_2 with concentration is consistent with the growth of the integrated low-q cluster weight W_{cl} (Eq. 5.2) observed in SANS, as the slow mode becomes longer-lived and more spatially correlated in crowded conditions.

Having now identified in DLS two distinct dynamical contributions (a fast, micellar mode and a much slower mode linked to large-scale heterogeneities) in direct correspondence with the two structural levels resolved by SANS (individual assemblies at intermediate to high q and cluster-like excess at low q), we next examine how temperature reshapes these dynamics in the dilute and crowded regimes. To this end, we selected 1 mg/mL and 75 mg/mL as representative concentrations and performed angle-resolved DLS as a function of temperature, analyzing $g^{(2)}(\tau)$ with the same two-exponential model to extract $\Gamma_{\mathrm{fast}}(q,T)$, $\Gamma_{\mathrm{slow}}(q,T)$ and the corresponding amplitudes.

Guided by the SANS temperature analysis at 1 and 75 mg/mL, we ask how those structural changes are reflected in the dynamics. As shown in Figure 5.13, the two-step character of $g^{(2)}(\tau)$ is preserved at both concentrations while the decays shift to shorter lag times upon heating.

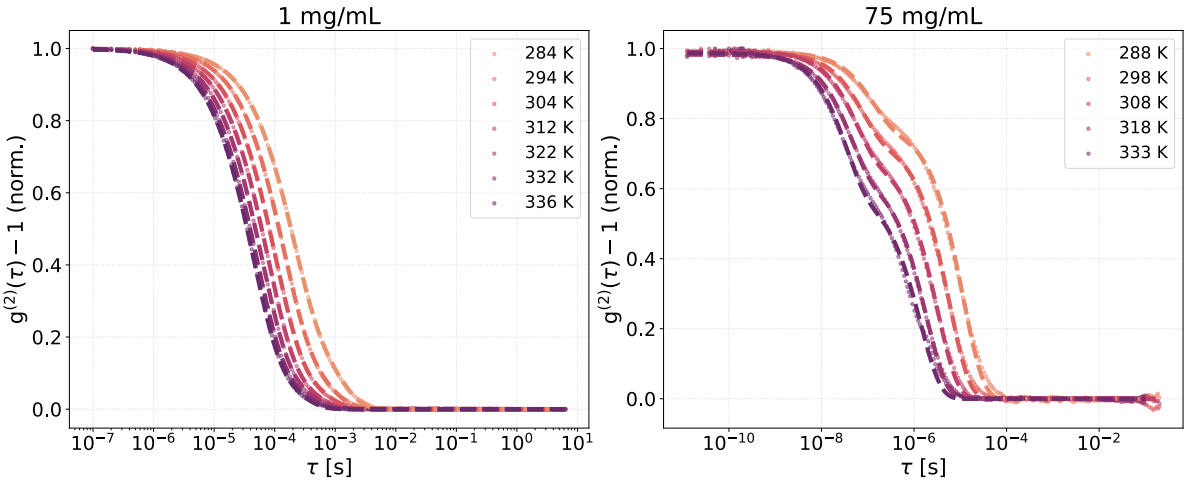

Figure 5.13. Representative $g^{(2)}(\tau) - 1$ curves at a scattering angle of 90° for 1 mg/mL (left) and 75 mg/mL (right), shown for increasing temperature. Symbols denote experimental data; dashed lines are fits with the two-exponential model of Eq. 5.3.

A quantitative summary is given in Figure 5.14. For both concentrations, the hydrodynamic radii extracted from the fitted rates decrease with temperature for the two modes ($R_{h,1}$ and $R_{h,2}$), even though SANS reports opposite trends in the geometric size: at 1 mg/mL the total radius decreases with T, whereas at 75 mg/mL it increases slightly. This is expected because R_h is an effective hydrodynamic length set by friction, hydration and long-range coupling, not only by the geometric size. Heating reduces the solvent viscosity and weakens hydration layers; together with the SANS observation of narrower size distributions and a reduction of the low-q exponent m (clusters becoming more tenuous), this leads to a decrease in hydrodynamic drag for both the micellar and the cluster-related modes and, consequently, to smaller $R_{h,1}$ and $R_{h,2}$.

The amplitudes evolve in the opposite direction: A_1 increases with temperature while A_2 decreases, for both concentrations and at fixed scattering angle. In the dilute sample the fast mode is dominant across the entire temperature range; in the crowded sample the slow mode remains larger, although the gap narrows as temperature rises. This behavior is consistent with the SANS trends once one considers what each observable weights. SANS

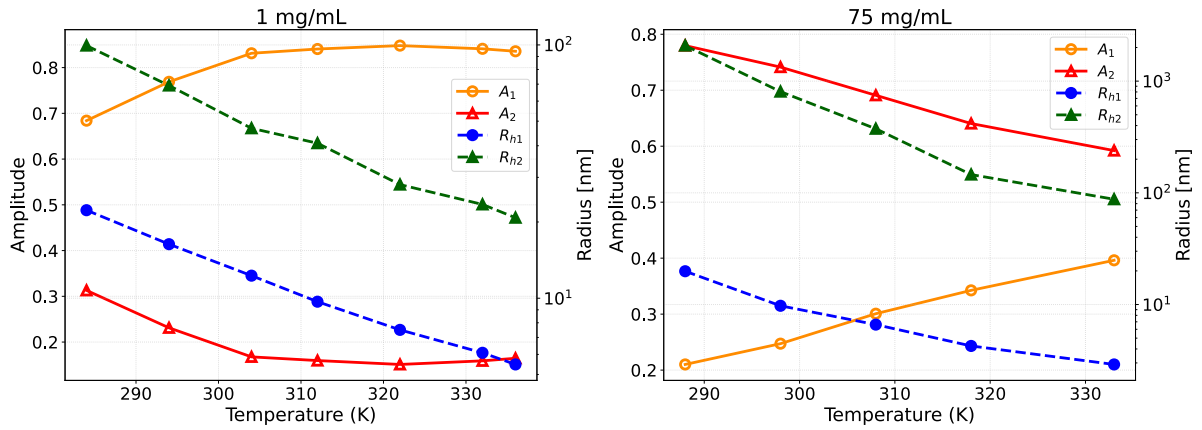

Figure 5.14. Mode amplitudes A_1 (fast) and A_2 (slow) at 90° and the corresponding hydrodynamic radii $R_{h,1}$ and $R_{h,2}$ (from $\Gamma = Dq^2$ and Stokes-Einstein with $\eta(T)$) for 1 mg/mL (left) and 75 mg/mL (right). R_h is plotted on a logarithmic axis to accommodate its dynamic range; lines are guides for the eye.

shows that the cluster term gains static weight with T (increase of W_{cl}) while becoming more tenuous (decrease of m). At the optical q probed here, DLS amplitudes reflect both the static scattering weight $\propto P(q)S(q)$ (i.e. the SANS intensity $I(q)$ up to constants and background) and the mode structure; heating reduces the hydrodynamic extent and lifetime of the slow rearrangements ($R_{h,2}$ decreases), which weakens their contribution at fixed q, whereas micelle-scale fluctuations gain relative weight (increase of A_1). These trends are robust whether one considers raw rates or viscosity-normalized diffusivities.

DLS has been instrumental in resolving two diffusive modes and in clarifying how their weights and hydrodynamic length scales evolve with concentration and temperature. However, the optical q-range of DLS lies orders of magnitude below that of SANS, so the two techniques probe largely distinct length scales. To investigate the dynamics in the same reciprocal-space window that defines the SANS structure, we now turn to NSE, which measures time correlations in the same wavevector range as SANS and enables a direct, like-for-like comparison between static structure and dynamics.

5.2.3 Collective dynamics at microscopic scales

To probe dynamics in the same reciprocal-space window that defines the SANS structure, we performed NSE on two concentrated samples (75 and 100 mg/mL) at three temperatures closely matching the SANS conditions. The normalized intermediate scattering

functions $I(q,t)/I(q,0)$ were measured at several q values by combining three instrument configurations (see Chapter 4 for details). Figure 5.15 provides an overview of the dataset and fitting strategy for the 75 mg/mL sample at 283 K: the left panel displays the full set of $I(q,t)/I(q,0)$ curves together with second-order cumulant fits, while the right panel compares the three fitting schemes described below at three representative values of q.

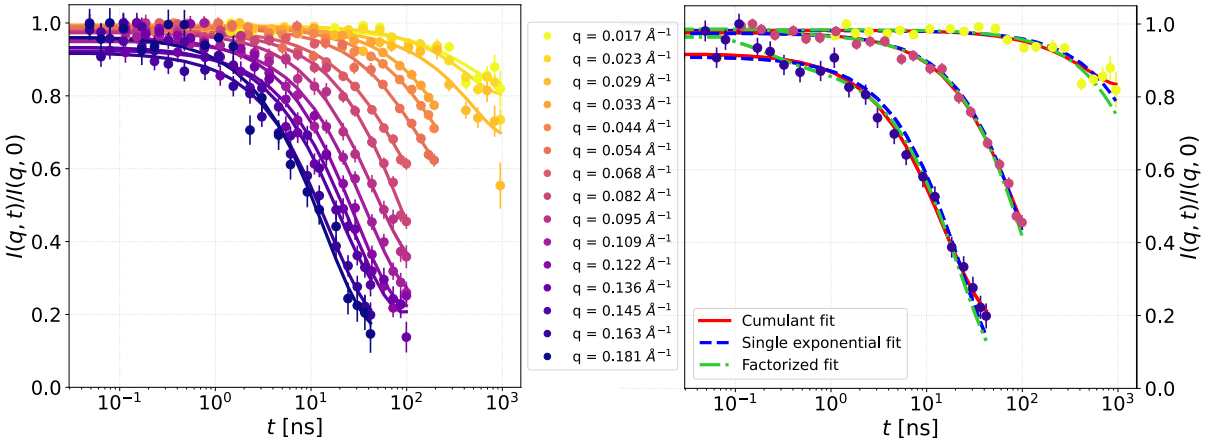

Figure 5.15. Left: NSE intermediate scattering functions $I(q,t)/I(q,0)$ for all measured q values for the 75 mg/mL sample at 283 K with second-order cumulant fits (solid lines). **Right:** Three representative q values (0.017, 0.082 and 0.163 Å^{-1}) fitted with a single exponential (blue), a second-order cumulant (red), and the factorized model $I_c = I_1 \exp[-q^2 Dt/2]$ (green). The central legend is shared between both panels.

We benchmarked three descriptions of $I(q,t)/I(q,0)$: (i) a single-exponential decay,

$$\frac{I(q,t)}{I(q,0)} \;=\; A(q)\,\exp\Big[-\Gamma(q)\,t\Big], \tag{5.5}$$

(ii) a second-order cumulant expansion,

$$\frac{I(q,t)}{I(q,0)} \;\approx\; A(q)\,\exp\Big(-\Gamma(q)\,t+\tfrac{1}{2}\,\mu_2(q)\,t^2\Big), \tag{5.6}$$

which yields the first cumulant $\Gamma(q)$ and the normalized second cumulant $k_2(q)$ defined as $k_2(q) = \mu_2(q)/\Gamma^2(q)$, and (iii) a factorized model that separates translational diffusion from a weak internal or extrinsic relaxation, motivated by earlier NSE analyses (see Chapter 3, [88]),

$$\frac{I(q,t)}{I(q,0)} \;=\; I_1(q,t)\,\exp\Big[-\Gamma(q)\,t\Big], \tag{5.7}$$

$$I_1(q,t) \;=\; 1-A_1(q)+A_1(q)\,\exp\Big(-\frac{t}{t_1}\Big). \tag{5.8}$$

In the first two cases, $A(q)$ is a weighting prefactor that accounts for the experimental contrast at $t = 0$ (instrument resolution, residual background, and any unresolved ultrafast process); in practice it is close to unity and only weakly dependent on q and temperature. In the factorized model, $A_1(q)$ quantifies the weight of an additional weak relaxation with time t_1, while the translational part is captured by the diffusive factor $\exp[-\Gamma(q)\,t]$ (with $\Gamma(q) = q^2 D(q)$ for pure translational diffusion).

A single exponential already captures the decays reasonably well, but adding the second cumulant produces a small and systematic improvement, most visible at long Fourier times, which is consistent with the finite polydispersity established by SANS (nonzero k_2). In contrast, at short Fourier times, the factorized model reproduces the initial curvature more faithfully because the additional weak-relaxation term $I_1(q,t) = 1 - A_1(q) + A_1(q)\exp[-t/t_1]$ accounts for extra short-time dynamics. The factorized model is, in principle, more complete because it allows for a weak additional relaxation. In practice, a direct global fit is numerically unstable. To stabilize it we adopted a two-step protocol: for each q we determined an optimal lower-time cutoff $t_{\min}(q)$ by scanning $t_{\min}$ and selecting the value that maximized the fit quality of the long-time single-exponential sector. Because the dataset spans three instrument configurations, the optimal $t_{\min}$ varies with q. We then first fitted the long time window $t \geq t_{\min}(q)$ to determine the diffusive part, and later fitted the full curve while holding $\Gamma(q)$ fixed. Under this procedure, the resulting $D(q) = \Gamma(q)/q^2$ is very similar to the single-exponential and cumulant estimates, and the q-trends are nearly identical (Figure 5.16), although the curves do not strictly overlap within the experimental uncertainties.

Since our focus here is the collective dynamics of the assemblies rather than short-time internal modes, we adopt the cumulant analysis as the primary description. It is model-agnostic, it uses the full time window without a q-dependent $t_{\min}$, it is numerically robust, and it quantifies weak non-exponentiality through k_2 in line with the SANS-derived polydispersity.

On the absolute scale, the diffusion coefficients extracted from NSE are of the same order as those previously reported for β-casein assemblies [88] and comparable to the fast DLS mode, which supports assigning the NSE decay to the diffusion of the assemblies. Unlike Nakagawa et al. [88], who found an approximately q independent D, our data show a shallow minimum at low-intermediate q followed by a slight increase. We attribute this difference to the extended Fourier-time window and improved statistics in our measure-

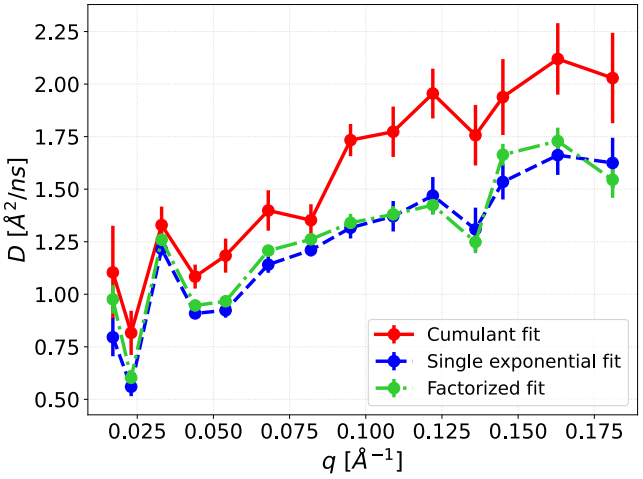

Figure 5.16. Comparison of $D(q) = \Gamma(q)/q^2$ from NSE analysis using a single exponential (blue), a second-order cumulant analysis (red), and the factorized model (green) for 75 mg/mL at 283 K. All lines are guides for the eye.

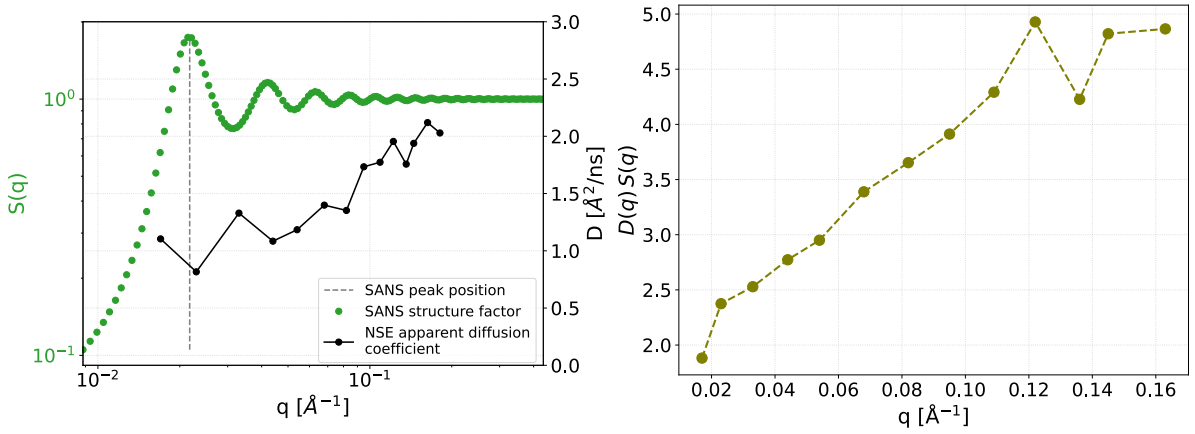

Figure 5.17. Left: $S(q)$ (left axis) and $D(q)$ (right axis) for the 75 mg/mL sample at 283 K; the vertical dashed line marks the SANS peak position q_p, where $D(q)$ shows a minimum (de Gennes narrowing [102]). Right: product $D(q)S(q)$ for the same sample, emphasizing the hydrodynamic contribution in the picture of Eq. 5.9; $D(q)S(q)$ increases nearly linearly with q across the accessible range. Lines are guides for the eye.

ments, which allow us to resolve a weak q dependence. When $D(q)$ is plotted together with the SANS structure factor $S(q)$, the minimum of $D(q)$ coincides with the SANS correlation peak (Figure 5.17, right panel), consistent with de Gennes narrowing: density modes at wave vectors with strong static correlations (large $S(q)$) relax more slowly. In

the short-time regime this relation reads

$$D(q) = \frac{D_0\, H(q)}{S(q)}\,, \tag{5.9}$$

where D_0 is the single-particle (infinite-dilution) diffusivity and $H(q)$ is the hydrodynamic function that quantifies how many-body hydrodynamic interactions modulate the decay of a density fluctuation of wavelength $2\pi/q$ (with $H = 1$ for particles without hydrodynamic interactions).

In our system a unique D_0 cannot be specified, because the micelles compact and change internal architecture with concentration; the infinite-dilution diffusivity of the same hydrodynamic entity present at 75 mg/mL is therefore not accessible. Instead, we examine the product $D(q)S(q)$, which is proportional to $H(q)$ up to the constant D_0. For 75 mg/mL at 283 K, $D(q)S(q)$ is not constant but increases nearly linearly with q (Figure 5.17, left panel). This indicates a non-constant hydrodynamic function and thus appreciable many-body hydrodynamic coupling even at a modest volume fraction ($\phi \approx 0.05$) [103]. We do not pursue a quantitative model for $H(q)$ here; the combination of a clear minimum of $D(q)$ at the $S(q)$ peak and a rising $D(q)S(q)$ across our q-window already establishes the structure-dynamics link relevant to this study.

Concentration and temperature dependencies within the NSE window are modest and do not alter the q-shape. Increasing concentration from 75 to 100 mg/mL produces an almost uniform downward shift of $D(q)$ at all q, while the minimum at q_p and the subsequent increase with q are preserved. Heating accelerates the dynamics indicating that temperature primarily rescales the overall rate. In both cases the product $D(q)S(q)$ retains its near-linear increase with q, confirming that de Gennes narrowing and the non-constant hydrodynamic response are robust across these variations (see Appendix E).

In summary, NSE in the SANS q-window resolves a single dominant collective relaxation that is robustly captured by a cumulant analysis. The resulting $D(q)$ displays a clear minimum at the SANS correlation peak and increases toward higher q, consistent with de Gennes narrowing. The product $D(q)S(q)$ rises nearly linearly across the accessible q-range, indicating a non-constant hydrodynamic function and appreciable many-body hydrodynamic coupling. The absolute magnitude of $D(q)$ is comparable to the fast DLS mode and to previous reports on related β-casein systems, supporting its assignment to micellar motion.

5.3 Conclusions

Across structure and dynamics, a coherent picture emerges for the β-casein assemblies. SANS establishes the static landscape across concentration and temperature and reveals two coexisting structural levels. At low concentration the profiles are dominated by soft, diffuse assemblies with a heterogeneous low-q excess, and fitted parameters show weak or unstable trends. At high concentration the behavior becomes systematic: a correlation peak emerges, a clearer core-shell partitioning is resolved, and polydispersity decreases. The pronounced low-q upturn, captured by a power-law term, reflects large-scale, cluster-like fluctuations. Temperature narrows the size distributions in both regimes; it slightly shrinks dilute assemblies, while under crowding both core and shell grow weakly. The cluster term gains weight and becomes more tenuous as temperature rises.

DLS complements this picture by resolving two diffusive modes whose weights and time scales evolve with concentration and temperature. The fast mode scales as q^2 and yields hydrodynamic radii of tens of nanometers, consistent with micellar center-of-mass diffusion; its effective radius decreases with concentration and temperature, in line with SANS-inferred compaction and shell thinning. The slow mode, roughly two orders of magnitude slower, gains amplitude with concentration and reflects cluster-level rearrangements; its hydrodynamic length grows with crowding and decreases with temperature, indicating thermal weakening and shortening of large-scale inhomogeneities. At fixed q, spectral weight shifts from the fast to the slow mode with increasing concentration and reverses with increasing temperature, mirroring the SANS trends.

NSE measurements performed in this work close the loop at the same q values as SANS by linking structure to short-time collective dynamics. The collective diffusivity $D(q)$ shows de Gennes narrowing with a minimum at the SANS peak and a rise toward higher q, while the increase of $D(q)S(q)$ across the window signals a non-constant hydrodynamic function, as expected from many-body coupling in crowded soft assemblies. Together, SANS, DLS, and NSE provide a coherent, multiscale account in which micellar compaction and cluster formation set both static correlations and the hierarchy of dynamical processes. This framework motivates neutron backscattering to access shorter time scales at comparable q, connecting mesoscale transport with single-particle spectral response.

Chapter 6

Apparent non-Fickian diffusion within β-casein assemblies

6.1 Introduction

This chapter presents a quasi-elastic neutron scattering (QENS) study of the dynamic behavior of β-casein in solution. The investigation was originally aimed at comparing the dynamics of the intrinsically disordered protein (IDP) β-casein with those of well-folded globular proteins. The data were analyzed using the same colloidal diffusion model commonly applied to well-folded proteins, which separates the scattering signal into contributions from global and internal motions. Typically, the global component corresponds to the center-of-mass diffusion of the protein or assembly, whereas the internal component accounts for localized dynamics within the molecule or aggregate.

However, the global motion shows a clear deviation from classical Fickian diffusion, a phenomenon previously observed in supercrowded systems, polymer melts, and various simple and complex fluids [104–108]. Importantly, this global diffusion behavior cannot be simply attributed to isolated monomers or whole micelles in solution.

To complement the experimental data, simulated QENS spectra were generated using MDANSE software, based on fully atomistic molecular dynamics trajectories of the protein. These simulated spectra closely reproduce the experimental results and, when analyzed with the same fitting procedure, reveal the same deviation from classical diffusion. This provides strong evidence that the observed deviation arises from protein aggregation. Furthermore, the atomistic simulations reveal dynamic heterogeneity within the assem-

blies.

Building on this, we developed a numerical model demonstrating that dynamic heterogeneity alone can produce deviations from Fickian diffusion, which can be effectively described by a Singwi-Sjölander jump diffusion model without explicitly assuming discrete jump events. Therefore, fitting the data with a jump diffusion model does not necessarily imply the presence of actual jumps but rather reflects the underlying heterogeneity of the system.

Together, these findings suggest that, at the timescales and length scales accessed in this study, β-casein assemblies exist in an intermediate dynamical regime where neither simple monomeric diffusion nor rigid aggregate models fully describe the behavior. At these scales, the observed dynamics correspond primarily to the interior of the micelles, where diffusion is spatially heterogeneous. This supercrowding-induced heterogeneity within micelles leads to anomalous diffusion, providing new insights into the complex dynamics of intrinsically disordered protein assemblies.

6.2 Results and discussion

6.2.1 Comparison with a well-folded protein: BSA as a reference system

To establish a reliable reference for interpreting the dynamics of β-casein, we compared it with bovine serum albumin (BSA), a well-folded globular protein whose dynamics have been extensively characterized using QENS [109–111]. In particular, BSA has served as a reference system in studies that examine the effects of crowding and temperature on protein motion [24, 110–112]. Here, we present previously unpublished QENS data on BSA, acquired under identical experimental conditions (ILL experiment 9-13-952) and using the same instrumental setup as for β-casein. Importantly, both datasets were analyzed using the exact same Python fitting routine to ensure consistency and allow for direct comparison.

Both BSA and many other globular proteins are commonly described using a two-component diffusion model to capture their complex dynamical behavior [20, 24, 45, 47]. This phenomenological model accounts for the coexistence of global translational motion and internal localized dynamics, which typically occur on distinct timescales. The model

generally includes a slow component associated with the diffusion of the center-of-mass (COM) of the protein and a fast component related to internal motions such as side-chain fluctuations or domain vibrations.

The measured scattering spectra were analyzed using a modified version of this two-component model. In this framework, the dynamic structure factor is expressed as:

$$S(q,\omega) = \mathcal{R} \otimes \Big\{ \beta\, \mathcal{L}_s(\gamma,\omega) \otimes \Big[A_0(q)\, \delta(\omega) + (1 - A_0(q))\, \mathcal{L}_f(\Gamma,\omega) \Big] + S_{\text{solvent}}(q,\omega) + S_{\text{container}}(q,\omega) \Big\}, \tag{6.1}$$

where $\mathcal{R}$ is the instrumental resolution function and $\otimes$ denotes convolution. The function $\mathcal{L}_s(\gamma,\omega)$ is a Lorentzian with half-width at half-maximum (HWHM) γ, describing the slow component, typically attributed to the translational diffusion of the particle's center-of-mass. The fast component, $\mathcal{L}_f(\Gamma,\omega)$, with HWHM Γ, represents localized internal motions. The scalars $A_0(q)$ and β are the elastic incoherent structure factor (EISF) and the Debye-Waller factor (DWF), respectively. The model includes fixed contributions from the solvent and the sample container. The solvent signal is modeled as:

$$S_{\text{solvent}}(q,\omega) = \beta_{D_2O} \mathcal{L}(\gamma_{D_2O},\omega) + \mathrm{B}_{D_2O}, \tag{6.2}$$

where β_{D_2O} is the amplitude of the quasi-elastic component, γ_{D_2O} its corresponding HWHM (reflecting the diffusion of the solvent), and B_{D_2O} an energy-independent background term. These parameters were obtained from independent measurements of the pure solvent under identical instrumental conditions and were kept fixed during the analysis of the protein samples. The container contribution, $S_{\text{container}}(q,\omega)$, arises from scattering by the sample holder, is assumed to be static, and is modeled as an elastic delta function in energy, $\delta(\omega)$, with amplitude $C_{\text{ctr}}(q)$. Although this background cannot be subtracted directly, $C_{\text{ctr}}(q)$ is determined from the solvent-only measurements and held fixed in the global fits. These modifications—particularly the explicit container term—are necessary due to non-negligible differences in scattering among the containers used. Treating the container signal in this way, rather than subtracting it, does not affect the extracted dynamical parameters but markedly improves the quality and stability of the fits. The full fitting procedure and details of the parameter optimization are described in Chapter 4.

Figure 6.1 shows representative spectra for both β-casein and BSA at $q = 1.48$ Å^{-1} and $T = 280$ K, alongside their respective model fits and component contributions. In both

cases, the fits closely reproduce the experimental spectra, validating the applicability of the model.

To evaluate the nature of the global motion, we focus on the dependence of the half-

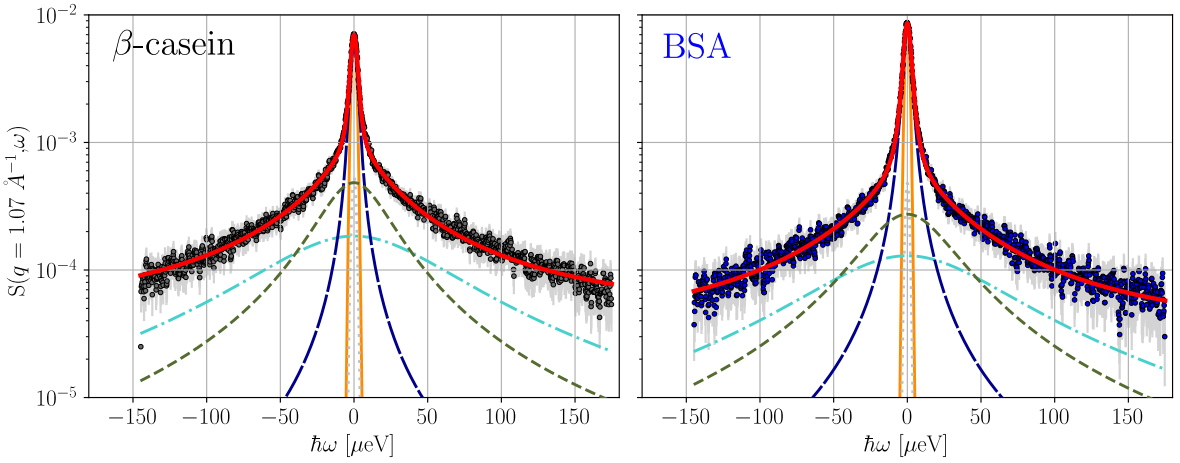

Figure 6.1. Left: Experimental QENS spectrum of β-casein at 100 mg/mL (gray symbols). **Right**: Experimental QENS spectrum of BSA at 150 mg/mL (blue symbols). Both spectra were recorded on IN16B (ILL experiments 9-13-1046 and 9-13-952, respectively) at $T = 280\,\text{K}$ and $q = 1.07\,\text{Å}^{-1}$. The solid red lines show the total fits obtained using the model described in Eq. 6.1. Dashed lines represent the individual dynamic components: long-dashed dark blue for the slow component and short-dashed dark green for the fast one. The dotted gray line, solid orange line, and dash-dotted cyan line correspond to the resolution function, container, and solvent contributions, respectively.

width at half-maximum (HWHM), denoted γ, of the slowest Lorentzian component as a function of q^2. In the case of BSA (Figure 6.2, right), the dependence of $\gamma(q^2)$ exhibits a clear linear behavior consistent with Fickian diffusion, described by $\gamma = Dq^2$, where D is the apparent self-diffusion coefficient. The term "apparent" reflects the effective hydrodynamic size of the protein, including any hydration layer that diffuses along with it [24, 113]. This proportional relationship indicates that the slowest component of the scattering signal is dominated by the center-of-mass motion of the BSA molecules. Using the Stokes-Einstein equation:

$$D = \frac{k_\text{B}T}{6\pi\eta R_H}\ , \tag{6.3}$$

the fitted diffusion coefficient $D = 2.8 \pm 0.02\ \text{Å}^2/\text{ns}$ yields a hydrodynamic radius $R_H = 4.06\,\text{nm}$, well within the experimentally reported range for BSA in solution [114].

In contrast, the data for β-casein (Figure 6.2, left) deviate significantly from linearity.

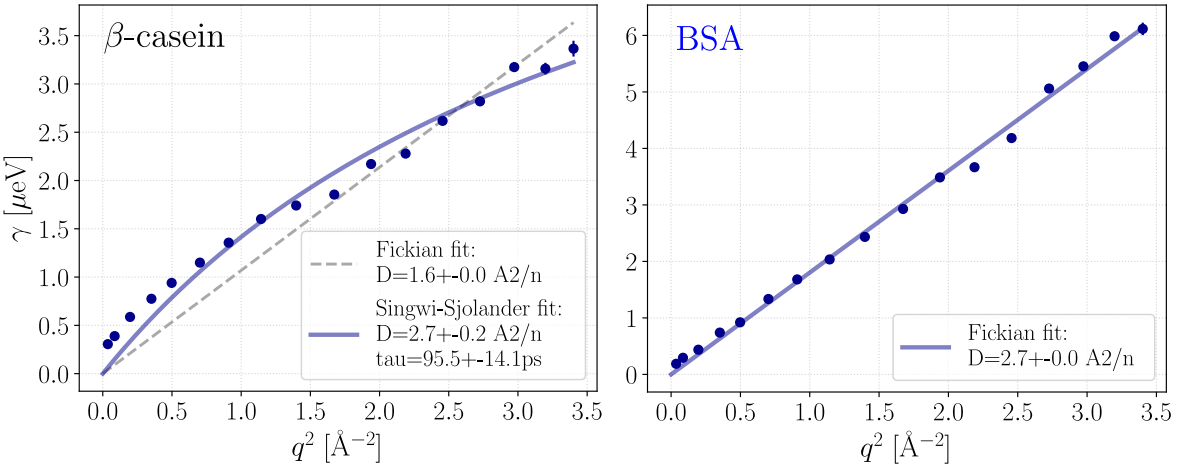

Figure 6.2. Fitted γ (HWHM) versus q^2 for β-casein (**left**) and BSA (**right**) from experimental QENS analysis. Solid lines show the best-fit model in each case, while dashed lines indicate alternative fitting approaches (see legend).

Instead, the observed q-dependence of γ is better described by the Singwi-Sjölander jump diffusion model:

$$\gamma = \frac{Dq^2}{1 + Dq^2\tau} \ , \tag{6.4}$$

which introduces a residence time τ and accounts for restricted motion in complex environments. The diffusion coefficient extracted from this model has an average value of $D = 2.9$ Å^2/ns, as shown in the right panel of Figure 6.3. Unlike the case of BSA, interpreting this value in terms of a well-defined hydrodynamic radius is nontrivial due to the heterogeneous and dynamic nature of the β-casein assemblies. The fitted parameters for different concentrations of β-casein, as well as for the dilute BSA sample, are summarized in Table 6.1.

To gain further insight, we revisit the colloidal framework and estimate the effective length scales associated with the fitted diffusion coefficients. While β-casein exists as a monomer at very low concentrations, it spontaneously forms micelles in aqueous solution, especially above the critical micelle concentration. Reported hydrodynamic radii for these micelles typically range from 8 to 15 nm [84]. On the other hand, atomistic simulations of isolated β-casein chains suggest monomer radii of approximately 2 nm.

Using the diffusion coefficients predicted by Eq. 6.3, we find that the experimentally fitted D values fall between those expected for free monomer diffusion ($D_{\text{monomer}} \approx 7.9$ Å^2/ns)

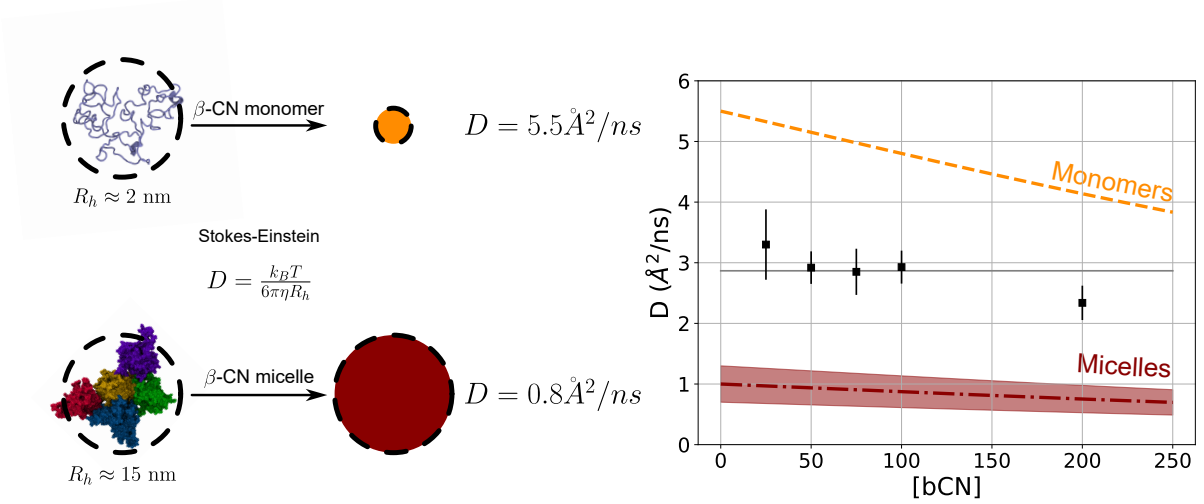

Figure 6.3. Left: Schematic illustration of a β-casein single monomer (top) and a micelle (bottom), as conceptualized within the colloidal diffusion framework. **Right**: Apparent diffusion coefficients D from the fits using Eq 6.4 are plotted as a function of protein concentration (black symbols). Dashed lines represent the theoretical translational diffusion for monomers (orange) and micelles (red) modeled as rigid (Eq. 6.5).

and micelle diffusion ($D_{\text{micelle}} \approx 0.76$ Å^2/ns), suggesting a more complex picture.
To improve this comparison, we apply a correction for hydrodynamic interactions in crowded suspensions based on a hard-sphere model. The effective diffusion coefficient at volume fraction ϕ is given by

$$D_s(\phi) = \frac{D_0}{1 + L(\phi)} \tag{6.5}$$

Table 6.1. Fitting parameters for different concentrations of β-casein and for BSA].

Protein	Concentration (mg/ml)	Fitting Model	D (Å^2/ns)	τ (ps)
BSA	150	Fickian diffusion (Eq. 6.3)	2.8 ± 0.02	–
	25		3.3 ± 0.6	112 ± 23
	50		$2,9 \pm 0.2$	132 ± 14
β-casein	75	Jump diffusion (Eq. 6.4)	2.9 ± 0.4	140 ± 21
	100		2.9 ± 0.3	136 ± 14
	200		2.3 ± 0.3	183 ± 23

where D_0 is the diffusion coefficient at infinite dilution, calculated using the Stokes-Einstein equation (Eq. 6.3), and $L(\phi)$ is a nonlinear function of ϕ accounting for multi-body hydrodynamic interactions [115]. This correction reduces the diffusion coefficient as concentration increases, producing the dashed lines in Figure 6.3 (right) for monomers and micelles modeled as rigid spheres.

These observations raise the question of what kind of dynamical process is being accessed, and what causes the deviation from Fickian behavior observed in the β-casein data. One possible explanation is the coexistence of freely diffusing monomers and micellar aggregates, which could lead to an apparent average diffusion coefficient. However, we rule out this possibility for several reasons.

First, given the limited time resolution of the instrument, we do not expect to access the dynamics of whole micelles. Due to their large size and slow motion, they appear essentially static within the probed time window. Second, in previous QENS studies involving mixtures of two proteins with distinct hydrodynamic radii, the resulting spectra exhibited a weighted average of the two diffusion processes; however, the overall q^2 dependence remained Fickian [116]. This contrasts with the non-Fickian signature observed here. Third, as detailed in Appendix F, we attempted a two-component fit assuming separate populations of monomers and micelles. These fits yielded unphysical parameters: one of the diffusion coefficients was unrealistically large, and the extracted fraction of each population suggested that only a single dynamic process is present.

In a*D*ition, given the very low critical micelle concentration (CMC) of β-casein, we expect that monomers strongly favor aggregation due to dominant hydrophobic interactions. As a result, the population of free monomers in solution is likely too small to be experimentally detectable. Moreover, the coherent signal from the micelles is expected to overshadow any contribution from monomers, further limiting their observability in the measured spectra. Together, these results suggest that the observed dynamics arise not from the coexistence of discrete populations, but from internal dynamics within heterogeneous micellar assemblies. We hypothesize that the deviation from Fickian behavior is a signature of dynamical heterogeneity inside the micelles, potentially due to structural polydispersity or internal flexibility of the casein chains.

To further investigate the microscopic origin of this anomalous diffusion, we performed molecular dynamics (MD) simulations of β-casein assemblies, which are presented and discussed in the following section.

6.2.2 Molecular dynamics simulations and MDANSE analysis

All-atom molecular dynamics (MD) simulations[1] were employed to investigate the microscopic origin of the non-Fickian dynamics observed experimentally. By constructing aggregates of β-casein chains ranging from $N = 1$ to 5, we aimed to capture the early stages of micellization in a controlled, fully solvated environment. The resulting structures remained stable throughout the simulations and exhibited characteristics consistent with the expected compact and hydrated nature of micelles (Fig. 6.4).

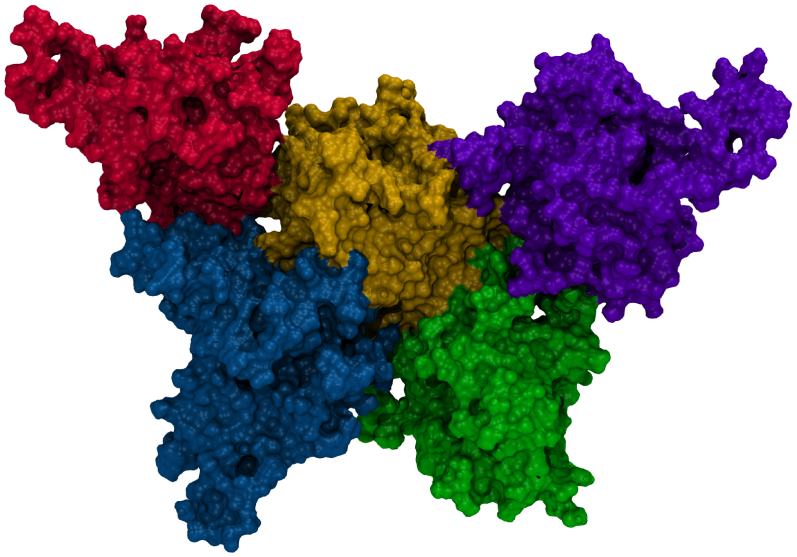

Figure 6.4. Representative structure of a five-chain β-casein aggregate obtained from MD simulations. Each chain is shown in a different color using a surf representation. Water molecules are omitted for clarity. Figure rendered using VMD [117]

We computed simulated QENS spectra from the MD trajectories using the *MDANSE* software package. Figure 6.5 displays representative results for an $N = 5$ aggregate: the simulated QENS spectrum (left) shows a clear quasi-elastic broadening, with both the profile and width comparable to the experimental spectrum shown in Fig. 6.1 (left).

[1]Simulations and MDANSE calculations were performed by Dr. Saikat Chakraborty, postdoctoral researcher on this project. Data analysis was carried out by the author; the physical interpretation was developed jointly. Full simulation details are provided in Appendix A.

To fit the simulated $S(q,\omega)$, we employed the same model used in the experimental data analysis (Eq. 6.1), excluding contributions from the solvent and sample container, which are absent in the simulation. Notably, two Lorentzian components are again required to accurately capture the relaxation dynamics: a narrow component reflecting slower motions, and a broader one corresponding to fast internal dynamics—reproducing the two-timescale structure observed experimentally.

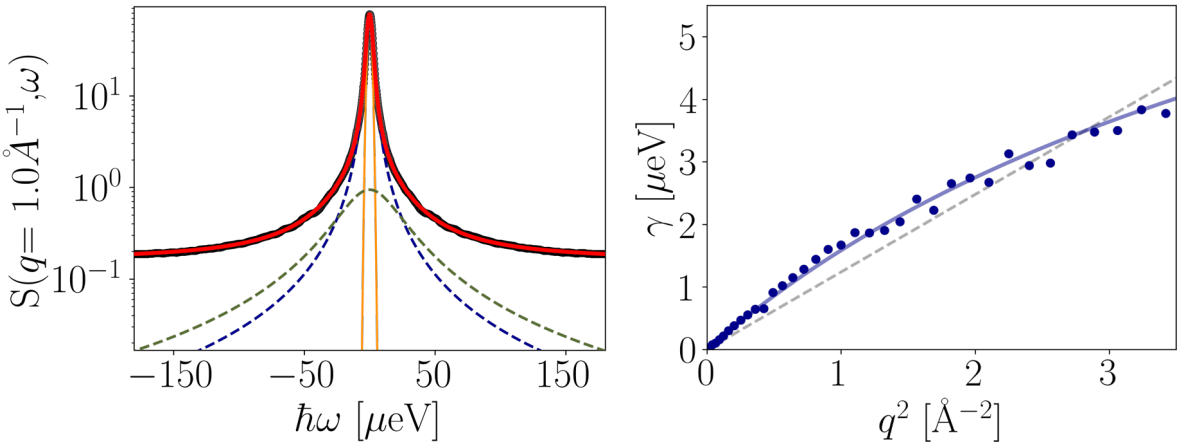

Figure 6.5. Left: Simulated QENS spectrum for an aggregate of five protein chains at $q = 1\,\text{Å}^{-1}$ and $T = 280$ K. Dashed lines represent global (blue) and internal (green) contributions. The solid orange line corresponds to the resolution function, and the solid red line shows the total fit. **Right:** HWHM, $\gamma(q)$, of the narrow component plotted as a function of q^2. The grey dashed line shows a fit assuming Fickian diffusion (Eq. 2.38), while the blue solid line corresponds to the jump diffusion fit (Eq. 6.4).

The extracted HWHM of the narrow component, $\gamma(q)$, is plotted in Fig. 6.5 (right). As observed in the experimental results (Fig. 6.2, left), $\gamma(q)$ clearly deviates from the linear q^2 dependence expected for Fickian diffusion (grey dashed line). Instead, the data is well described by the jump diffusion model of Singwi and Sjölander (Eq. 6.4), confirming that the anomalous diffusion behavior also emerges in relatively small aggregates composed of only a few chains.

Interestingly, similar deviations from Fickian diffusion have been reported in other complex fluids, such as deep eutectic solvents, where the observed non-Fickian behavior has been attributed to cage-like clustering dynamics [108]. In those systems, jump diffusion arises from the transient formation and dissolution of spatially heterogeneous clusters of varying sizes and lifetimes. The characteristic jump time τ is interpreted as the average

residence time of a particle within a given cluster before hopping to another. A similar approach could, in principle, be applied to the β-casein aggregates. However, our molecular dynamics simulations do not support this interpretation: once aggregates form, individual protein chains remain stably associated throughout the entire microsecond-long trajectory, and no inter-aggregate hopping events are observed. Despite this, the simulated $\gamma(q)$ spectra are still well described by the Singwi-Sjölander equation (Eq. 6.4), which effectively captures the observed deviation from Fickian diffusion. In our case, the parameters D and τ do not correspond to classical translational diffusion and hopping between states, but instead reflect an apparent diffusion coefficient and the degree of internal dynamical heterogeneity within the aggregate. Their specific interpretation in this context will be discussed in detail in the following sections.

To systematically investigate the origin of this deviation, we performed simulations of aggregates with an increasing number of chains (Fig. 6.6). For a single β-casein chain (green), $\gamma(q)$ follows the expected Fickian behavior, in excellent agreement with Eq. 2.38. In this regime, the dynamics are dominated by the translational motion of the entire molecule, i.e., center-of-mass diffusion, which effectively masks any underlying internal heterogeneity. As shown in Table 6.2, the diffusion coefficient obtained for the single-chain case matches exactly the value expected in the infinite dilution limit for monomers, as illustrated in Figure 6.3. However, as soon as a second chain is introduced, the concept of a single center-of-mass motion becomes ambiguous due to the loss of symmetry and the emergence of interchain constraints.

A potential explanation for this change in dynamics lies in the altered hydration environment that arises upon aggregation. As illustrated in Figure 6.7 (right), the spatial profile of water density in a five-chain aggregate reveals a non-uniform distribution: water density decreases progressively toward the center-of-mass, indicating that inner regions are less hydrated than the periphery. In contrast to a single, fully solvated chain—where hydrodynamic interactions with the surrounding water are well defined—aggregation causes portions of the protein surface to become buried at inter-chain interfaces, reducing their direct exposure to solvent. This disrupts the formation of a clear hydration shell and leads to local variations in water accessibility. Moreover, due to the intrinsic flexibility and dynamic disorder of β-casein, the spatial arrangement of water fluctuates across the aggregate, further modulating the local dynamical behavior of the chains.

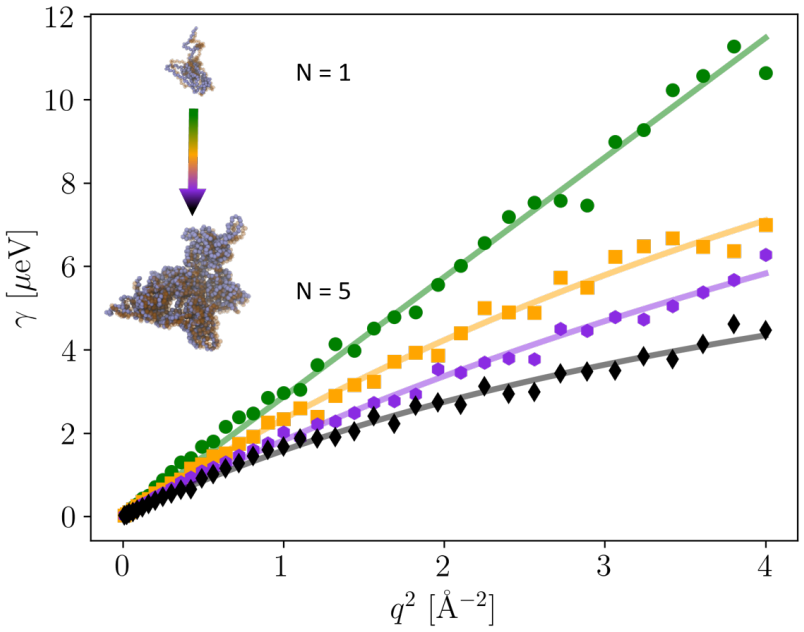

Figure 6.6. q-dependence of the HWHM, $\gamma(q)$, of the Lorentzian corresponding to the slow contribution from MD simulations for different protein chain aggregates (single chain in green, circular symbols; $N = 2$ in orange, square symbols; $N = 3$ in violet, hexagonal symbols; and $N = 5$ in black, diamond symbols). Solid lines in matching colors represent fits using Eq. 2.38 for the single chain, and Eq. 6.4 for $N = 2$, $N = 3$, and $N = 5$. The inset provides a schematic representation of the transition from a single chain to a five-chain aggregate, illustrating the systems analyzed.

To directly probe the connection between hydration and dynamics, we computed the mobility of each backbone atom, defined as the distance traveled over a fixed 1 ns window. The results, presented in Figure 6.7 (left), reveal a pronounced spatial heterogeneity.

Table 6.2. Fitting parameters obtained from $\gamma(q)$ analysis for aggregates with increasing number of β-casein chains.

Number of chains	HWHM fitting model	D (Å^2/ns)	τ (ps)
1	Fickian diffusion (Eq. 2.38)	5.42	–
2	Jump diffusion (Eq. 6.4)	3.97	29
3		3.03	30
5		2.83	63

Atoms located inside, where water access is limited, exhibit significantly reduced mobility compared to those on the surface of the aggregate. These findings support the notion that reduced solvent exposure imposes local dynamic constraints, and that the overall motion reflects a superposition of spatially heterogeneous environments and diffusion rates. As a result, the dynamics can no longer be captured by a single diffusion coefficient but instead emerge from partially independent, non-uniform contributions across the system. Consequently, $\gamma(q)$ deviates from linearity and is better described by Eq. 6.4.

We believe that the coupling between restricted hydration and dynamic variability ob-

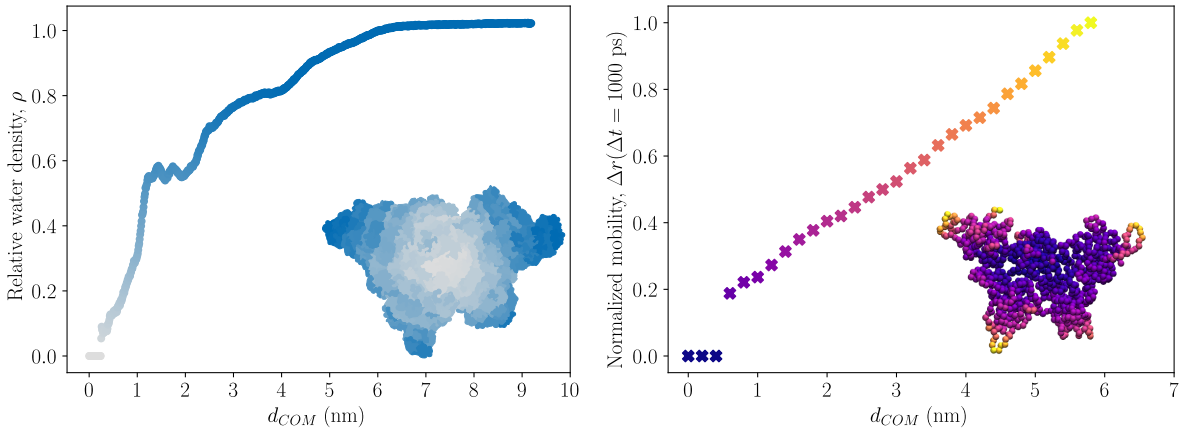

Figure 6.7. Left: Radial profile of the relative water density, ρ, within a β-casein aggregate composed of five chains. The main plot shows the average water density as a function of the distance from the aggregate's center-of-mass. The density is normalized, with $\rho = 0$ indicating complete water exclusion and $\rho = 1$ corresponding to the bulk water density outside the aggregate. The curve is color-coded using a custom gray-to-blue gradient for visual clarity. The inset displays a schematic of the aggregate structure, color-coded by local relative water density using the same gradient for consistency. **Right:** Radial profile of the normalized mobility of backbone Cα atoms within the same β-casein aggregate. Mobility is defined as the average displacement (Δr) over a 1000 ps interval and is normalized by the maximum value observed across all atoms in the aggregate. The curve is color-coded using the plasma colormap for enhanced contrast. The inset shows a schematic of the aggregate in which each Cα atom is colored according to its individual Δr value, using the same colormap. Note that values near the center-of-mass ($r \approx 0$) are affected by uncertainties in the COM definition.

served in β-casein aggregates can be extended to other highly crowded systems, such as

the cellular interior and concentrated protein solutions. In both of these environments, deviations from Fickian diffusion have already been reported for the slow dynamic component, reflecting a similar underlying dynamic heterogeneity [104,105]. Motivated by these findings, in the following section we develop a numerical model to test the effect of summing over particles with heterogeneous diffusion coefficients. This approach allows us to assess how microscopic dynamical heterogeneity gives rise to the macroscopic non-Fickian behavior observed in $\gamma(q)$.

6.2.3 Numerical model of dynamic heterogeneity

To investigate the origin of the non-Fickian behavior observed in $\gamma(q)$, we developed a numerical model that explicitly incorporates microscopic dynamic heterogeneity. This approach is motivated by the spatial variation in mobility observed in our simulations of β-casein aggregates, where different regions of the system, such as the interior and surface experience varying degrees of solvent exposure and local constraints.

Instead of assuming a single uniform diffusion coefficient, we consider a population of particles where each diffuses with a distinct coefficient D, sampled from a predefined distribution $P(D)$. To allow flexible control over the shape of the diffusion coefficient distribution using a minimal number of parameters, we employ a double-exponential function with tunable asymmetry centered at a mean value $\mu$and characterized by distinct decay rates on either side. This function provides a general framework that can reproduce a wide range of asymmetric distributions without assuming a specific underlying microscopic origin. The distribution is defined as follows:

$$P(D) = \begin{cases} A \cdot \dfrac{D}{\mu} \exp\left(-\dfrac{\mu - D}{\lambda_1}\right), & D < \mu \\ A \cdot \exp\left(-\dfrac{D - \mu}{\lambda_2}\right), & D \geq \mu \end{cases} \tag{6.6}$$

Here, λ_1 and λ_2 are decay lengths controlling the spread to the left and right of the peak, respectively, and A is a normalization constant. The prefactor D/μ ensures that the distribution smoothly vanishes as $D \to 0$, avoiding contributions from immobile particles. To simplify the numerical evaluation of the model, we discretize the distribution $P(D)$ over a set of N diffusion coefficients $\{D_i\}$, sampled on a logarithmic grid to ensure accurate representation across multiple orders of magnitude. This logarithmic spacing ensures that all diffusion components are properly captured, even when their associated weights are small. The corresponding weights are computed by normalizing the values of the distribution:

$$w_i = \frac{P(D_i)}{\sum_{j=1}^{N} P(D_j)} \tag{6.7}$$

Each subpopulation is assumed to undergo local Fickian diffusion characterized by its own diffusion coefficient D_i. Under this assumption, the corresponding linewidth is given by $\Gamma_i = D_i q^2$, and the associated contribution to the dynamic structure factor takes the Lorentzian form:

$$S_{D_i}(q, \omega) = \frac{1}{\pi} \cdot \frac{\Gamma_i}{\omega^2 + \Gamma_i^2} = \frac{1}{\pi} \cdot \frac{D_i q^2}{\omega^2 + (D_i q^2)^2} \tag{6.8}$$

To obtain the total model scattering signal, we sum all contributions and then convolve the result with a Gaussian resolution function $\mathcal{R}(\omega)$:

$$S_{\text{model}}^{\text{numerical}}(q,\omega) = \mathcal{R}(\omega) \otimes \sum_{i=1}^{N} w_i \left[S_{D_i}(q,\omega)\right] \tag{6.9}$$

where the resolution function is defined as:

$$\mathcal{R}(\omega) = \frac{1}{\sqrt{2\pi}\sigma} \exp\left(-\frac{\omega^2}{2\sigma^2}\right) \tag{6.10}$$

and σ corresponds to the instrumental energy resolution, and its value is taken directly from the experimental measurements to ensure that the simulated signal closely reflects realistic experimental conditions.

For each q value, the convoluted scattering function $S_{\text{model}}^{\text{numerical}}(q,\omega)$ is fitted to a single Lorentzian function, also convoluted with the resolution $\mathcal{R}(\omega)$, to extract an effective HWHM $\Gamma(q)$. This fitted width represents the apparent dynamics that would be observed experimentally if the system were assumed to exhibit uniform diffusion.

The fitting function is given by

$$S_{\text{fit}}(q,\omega) = \mathcal{R} \otimes \left[\frac{1}{\pi} \frac{\Gamma(q)}{\omega^2 + \Gamma(q)^2}\right] \tag{6.11}$$

Building on this model for the distribution of diffusion coefficients, Figure 6.8 (left) shows several example distributions obtained by tuning the parameters of $P(D)$. The blue curve corresponds to a narrow distribution, indicating low heterogeneity, while the yellow curve represents a broader distribution with a wider range of dynamic environments.

For each case, we compute the apparent HWHM $\Gamma(q)$ using the numerical procedure described above. The results are shown in Figure 6.8 (right). As heterogeneity increases, with the distribution of diffusion coefficients broadening, the behavior of $\Gamma(q)$ progressively deviates from the linear dependence expected for simple Fickian diffusion. This deviation indicates that, although the microscopic dynamics remain locally Fickian, their superposition produces non-Fickian features at the macroscopic level.

Interestingly, despite the presence of many distinct Lorentzian components, each associated with a different local diffusion coefficient, the total signal can still be well approximated by a single effective Lorentzian. This is shown in the inset of Figure 6.8 (left). Although the system exhibits dynamic heterogeneity, its overall behavior can be effectively captured by a simple effective model.

Given that fitting the data with a large number of Lorentzian components is infeasible

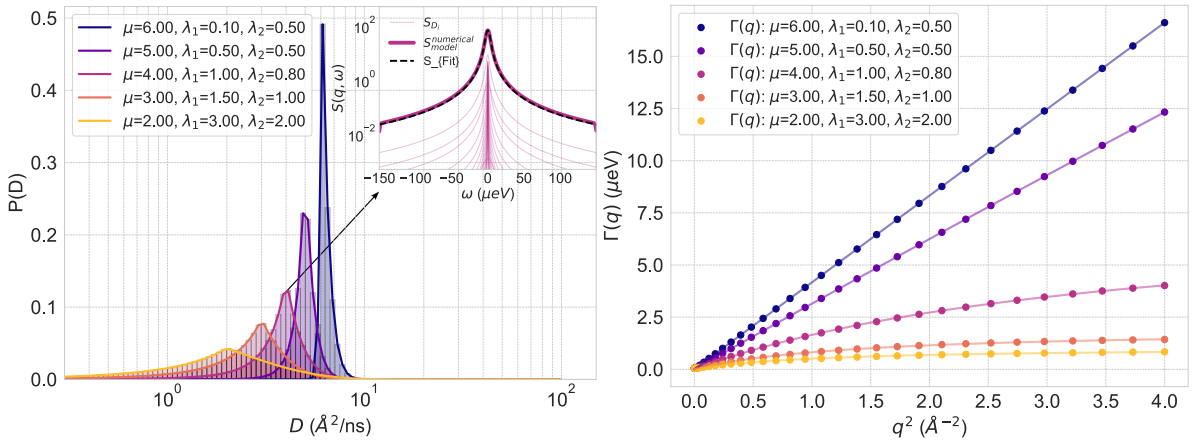

Figure 6.8. Left: Diffusion coefficient distributions $P(D)$ generated using the non-symmetric parametric function described in Eq. 6.6, with varying shape parameters. The inset shows a representative example of the numerically constructed scattering function $S^{\text{numerical}}_{\text{model}}(q,\omega)$ for $q = 1.04\,\text{Å}^{-1}$, obtained by summing weighted Lorentzian components (shown as thin lines) and convolving the result with the instrumental resolution function. The overall signal is fitted using Eq. 6.11. **Right:** Fitted HWHM values $\Gamma(q)$ shown for each distribution using matching colors. Solid lines correspond to fits based on Eq. 6.4.

due to the excessive number of free parameters, we instead characterize the heterogeneity through the dependence of the HWHM $\Gamma(q)$ on q^2. For this purpose, we apply the Singwi and Sjölander jump diffusion model, which provides an excellent fit to the data with only two free parameters. Originally formulated to describe intermittent jump processes, this phenomenological model successfully captures the observed deviations from Fickian diffusion in the present system. In this context, the fitted parameters D and τ should not be interpreted literally as a diffusion coefficient between jumps and a residence time,but instead as effective parameters that reflect key aspects of the underlying distribution $P(D)$, providing a concise description of the heterogeneity of the system. To better understand the interpretation of these parameters, we summarize in Table 6.3 the fitted values of D and τ for each synthetic distribution, along with statistical properties such as the mean and standard deviation of $P(D)$. We observe that the fitted diffusion coefficient D closely matches the mean of the distribution in all cases. On the other hand, the parameter τ exhibits a strong correlation with the standard deviation of the distribution. This suggests that τ effectively captures the degree of dispersity within the system. In this framework, τ

can be interpreted not as a residence time, but as a phenomenological measure of dynamic heterogeneity.

Table 6.3. Fitted parameters and statistical properties of the diffusion coefficient distributions $P(D)$ for five synthetic cases.

$P(D)$ plot	μ	λ_1	λ_2	Fitted D (Å^2/ns)	Mean D (Å^2/ns)	Std. Dev. (Å^2/ns)	Fitted τ (ps)
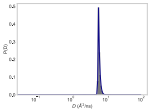	6	0.10	0.5	6.37	6.34 ± 0.01	0.5	0.2
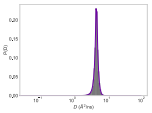	5	0.5	0.5	4.81	4.95 ± 0.01	0.7	1.4
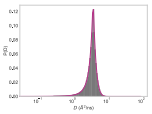	4	1.0	0.8	3.19	3.74 ± 0.02	1.1	85
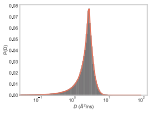	3	1.5	1.0	2.14	2.67 ± 0.03	1.2	340
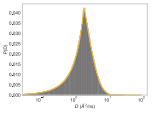	2	3.0	2.0	1.52	2.12 ± 0.1	1.5	629

Having established that dynamic heterogeneity can lead to apparent deviations from Fickian diffusion, we next explore the possibility of reconstructing the underlying distribution of diffusion coefficients $P(D)$ from experimental observations of the fitted parameters D and τ. The key idea is to exploit the relationship between these effective parameters and the statistical properties of $P(D)$, as demonstrated in the previous section.

As a first step, we construct a parametric map that relates the shape of the distribution $P(D)$, defined by the parameters μ, λ_1 and λ_2, to the corresponding values of the fitted parameters D and τ obtained using the Singwi-Sjölander formula (Eq. 6.4). This map is generated by systematically evaluating the fitted D and τ values for a large number of synthetic distributions covering a wide range of the parameter space. Specifically, we sample the distribution parameters in the ranges: $\mu \in [0.5, 4.0]$, $\lambda_1 \in [0.1, 1.5]$, and $\lambda_2 \in [0.5, 10.0]$. These intervals were selected on the basis of prior analysis that demonstrates that they yield distributions that are capable of reproducing the features observed

in the experimental data.

For each set of parameters (μ,λ_1,λ_2), we compute the corresponding distribution $P(D)$, evaluate its statistical properties (mean and standard deviation), and determine the resulting HWHM $\Gamma(q)$ by fitting the calculated total scattering function $S^{\text{numerical}}_{\text{model}}(q,\omega)$. The outcome is a dense map that links each triplet (μ,λ_1,λ_2) to a unique pair (D,τ), providing a forward model from distribution shape to effective parameters.

To infer the distribution underlying the experimental data, we compare the experimentally determined values of D and τ with those in the synthetic map. For each experimental data point, we identify all synthetic distributions whose fitted D and τ values fall within the confidence interval of the experimental measurements. Two approaches can then be used to reconstruct $P(D)$: one consists of averaging the parameters $(\mu, \lambda_1, \lambda_2)$ and defining a single analytical distribution, while the other directly averages the corresponding synthetic $P(D)$ curves. We adopt the first method because it provides a clear, interpretable parametric form that succinctly captures the main features of the distribution, making it easier to compare and analyze across different experimental conditions. Results from the second approach are presented in Appendix G, showing similar mean, standard deviation, and peak position. The results of this reconstruction procedure are shown in Figure 6.9. In the left panel, each blue dot represents a point in the synthetic parameter map corresponding to a particular triplet (μ,λ_1,λ_2), while colored stars indicate the locations of the experimental data in the (D,τ) space. Each color corresponds to a different concentration, allowing for a direct visual comparison across samples. The rectangular area surrounding each experimental point denotes the confidence interval obtained from the fitting of the experimental data. In the right panel, we present the reconstructed distributions $P(D)$ obtained for each experimental case using the above-mentioned averaging procedure.

Finally, we evaluated the accuracy of the reconstructed distributions by comparing their diffusion coefficient D and relaxation time τ with the experimental values. As described earlier, these quantities were obtained by computing the scattering function $S^{\text{numerical}}_{\text{model}}$, extracting the HWHM, and fitting the dispersion using the Singwi-Sjölander jump diffusion model. The comparison, shown in Figure 6.10, reveals that the reconstructed values closely match the experimental ones, usually falling within the corresponding confidence intervals. This agreement supports the validity of the numerical model and indicates that the reconstruction procedure captures the essential dynamical features of the system.

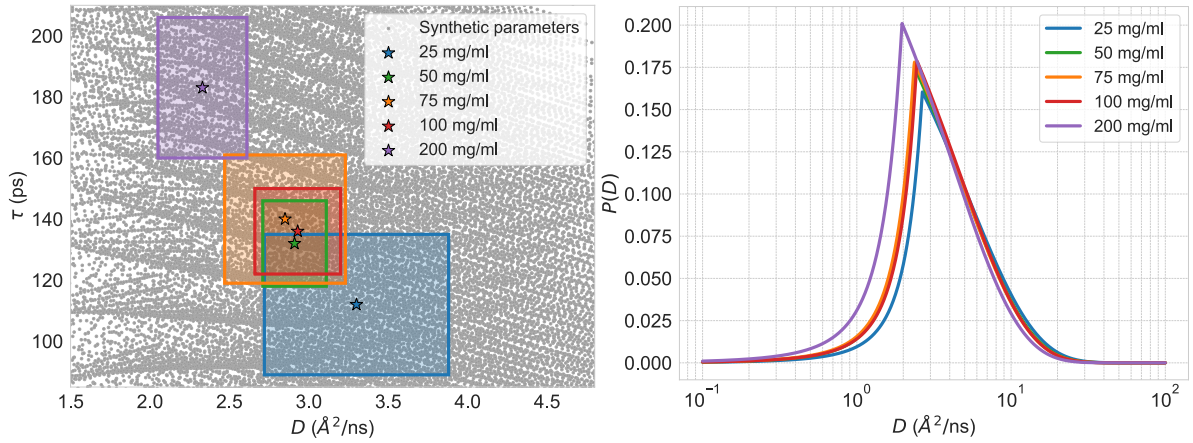

Figure 6.9. Left: Synthetic parameter space showing the distribution of generated diffusion models, where each gray dot corresponds to a specific combination of shape parameters $(\mu, \lambda_1, \lambda_2)$. Colored stars indicate the experimental measurements in the (D, τ) space, with each color representing a different concentration. Rectangular shaded regions denote the confidence intervals derived from the experimental fits. **Right:** Reconstructed diffusion coefficient distributions $P(D)$ for each concentration, computed using the average parameters of the synthetic models falling within the corresponding confidence regions.

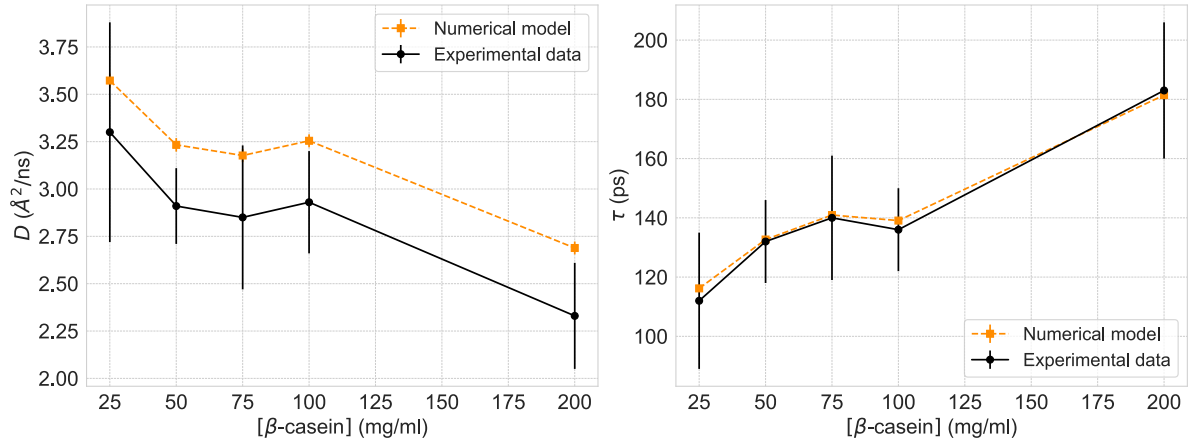

Figure 6.10. Left: Diffusion coefficients D from the reconstructed distributions (orange squares) compared to experimental values (black circles) at various β-casein concentrations. **Right:** Corresponding τ values from both reconstruction and experiments.

6.3 Conclusion

This chapter presented a detailed study of the dynamics of β-casein in solution using QENS, supported by MD simulations and comprehensive computational analysis. The key picture that emerges is one of global diffusion of individual monomers within densely packed yet fluid-like aggregates or assemblies. Unlike well-folded globular proteins such as BSA, which exhibit classical Fickian diffusion, β-casein shows clear deviations from this behavior. Instead, its dynamics are better described by the Singwi-Sjölander jump diffusion model.

Colloidal calculations suggest that these anomalies cannot be simply explained by the presence of free monomers or micelles in solution. Rather, they seem to arise from the internal motions within the aggregates themselves. These β-casein assemblies can be understood as supercrowded systems, where protein chains are packed so closely that their movement becomes limited. This creates a confined and dynamically heterogeneous environment which, combined with the exclusion of water from their interior, accounts for the observed deviations from classical diffusion.

Molecular dynamics simulations provided critical insight into this behavior. Within the small aggregates, protein chains remain closely associated without clear translational jumps between sites. Instead, they exhibit varying degrees of mobility throughout the aggregates. This heterogeneous mobility creates a dynamic environment where local diffusion rates differ, producing the anomalous diffusion patterns observed in the QENS experiments.

To capture this behavior, we developed a numerical model incorporating a distribution of locally Fickian diffusion coefficients rather than assuming a single uniform value. While the model can be fitted using an apparent single effective contribution, it still leads to deviations from classical Fickian diffusion at the macroscopic level, as manifested in the dependence of the spectral linewidth on the momentum transfer. This strongly supports the idea that local mobility heterogeneity is a plausible physical origin of the observed anomalous diffusion. While this appears to be the dominant mechanism, future studies may explore whether additional factors contribute to the observed behavior.

Overall, β-casein exists in a supercrowded state where densely packed chains constrain each other's motion and modulate the local solvent environment. This supercrowding is a key driver of both the anomalous diffusion and the internal dynamic heterogeneity.

Notably, this behavior is not unique to β-casein but is representative of a broader class of biological and soft matter systems, including polymer melts, intracellular environments, and other protein assemblies.

This work lays the groundwork for future investigations aimed at unraveling the functional implications of such complex dynamics in living cells and soft condensed matter systems.

Chapter 7

Confined internal dynamics

7.1 Introduction

This chapter presents a QENS analysis of the fast internal dynamics of β-casein and BSA, focusing on the localized motions that complement the global diffusion discussed in the previous chapter. Within the standard two-component framework, the scattering signal is decomposed into a slow contribution associated with global translational diffusion and a fast contribution reflecting internal relaxations confined to finite length scales (Eq. 6.1). Whereas the global component was shown to deviate from classical Fickian diffusion due to heterogeneity within micellar aggregates, the present analysis addresses the localized dynamics encoded in the EISF and the HWHM of the fast Lorentzian.

The EISF provides direct information on the spatial confinement of protons immobile on the experimental timescale, while the linewidth $\Gamma(q)$ captures the characteristic timescales of local relaxations, such as side-chain fluctuations or restricted backbone motions. Together, these quantities offer complementary geometrical and dynamical perspectives on protein internal dynamics. By comparing β-casein with the well-folded globular protein BSA, we aim to determine whether the fast internal component depends on protein fold or aggregation state. In addition, the concentration dependence of β-casein is systematically investigated to test the impact of crowding on its internal dynamics. Finally, the experimental results are complemented by molecular dynamics simulations of β-casein aggregates, providing a direct link between neutron scattering observables and atomistic trajectories.

7.2 Results and discussions

To parameterize the EISF, several analytical models have been developed in the context of confined diffusion [8, 31]. For proteins, two limiting cases are most relevant: diffusion within a confining sphere and jump diffusion between a finite number of sites [47]. For β-casein, the experimental data are best captured by a mixed model that includes both contributions: a three-site jump term associated with methyl group rotations, and a confined-diffusion term in a sphere of radius R,

$$A_0(q) = p + (1-p)\left[\Phi\, A_{\text{3-site}}(q) + (1-\Phi)\, A_{\text{sphere}}(q,R)\right], \tag{7.1}$$

where p denotes the immobile fraction, Φ the relative weight of methyl rotations,

$$A_{\text{3-site}}(q) = \tfrac{1}{3}\left[\,1 + 2J_0(qa_M)\,\right], \tag{7.2}$$

with $a_M \approx 1.715$ Å the average H-H distance in a methyl group, and

$$A_{\text{sphere}}(q,R) = \left[\frac{3\, j_1(qR)}{qR}\right]^2 \tag{7.3}$$

the confined diffusion in a sphere of radius R. Here J_0 denotes the Bessel function of the first kind (order 0), and j_1 the spherical Bessel function (order 1), with $j_1(x) = [\sin x - x\cos x]/x^2$. This model reproduces the experimental $A_0(q)$ of β-casein significantly better than either component alone, consistent with the large fraction of hydrogens bound in methyl groups and the need for an additional effective confinement to describe other localized motions. For BSA, by contrast, the EISF is adequately described by a single confined-diffusion term in a sphere, without the need for an explicit three-site contribution (Eq. 7.1 with $\Phi = 0$). This does not imply the absence of methyl rotations in BSA, which are universally present in proteins, but rather that their contribution cannot be resolved under the present conditions. To assess whether this difference could originate from chemical composition, we counted methyl-bearing residues (Ala, Thr, Met, Val, Ile, and Leu) in the mature sequences. For β-casein (209 residues), this yields 121 methyl groups (363 methyl protons), while for BSA (583 residues) the corresponding number is roughly 300 methyl groups (about 900 methyl protons). In relative terms, methyl hydrogen atoms represent a comparable fraction of the total incoherent scattering signal in both proteins ($\approx 20\%$ of H_{tot}).

The different visibility of methyl rotations in the EISF cannot therefore be attributed

to the methyl content alone. Instead, it reflects the distinct structural environments: in β-casein, the disordered and solvent-permeated matrix provides sufficient free volume for these groups to rotate within the experimental time window. The fitted value $\Phi \approx 0.54$ for β-casein exceeds the stoichiometric fraction of methyl protons, indicating that Φ acts as an effective parameter – it captures the spectral weight of all fast localized relaxations, including side-chain and local backbone motions, projected onto the three-site jump geometry on the nanosecond timescale. In BSA, the compact globular fold and higher immobile fraction ($p \approx 0.7$) likely shift or mask these contributions, rendering an explicit three-site term statistically unnecessary for a satisfactory fit. Furthermore, the limited statistics in the empty cryostat measurement for BSA introduces systematic uncertainties that can obscure weak dynamical components, including methyl rotations.

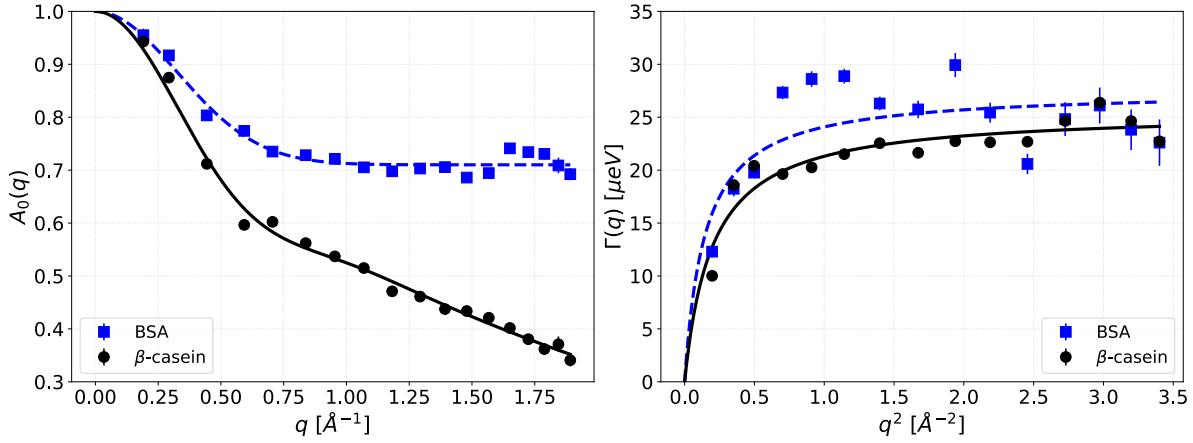

Figure 7.1. Left: Elastic incoherent structure factor $A_0(q)$ for β-casein (blue) and BSA (grey), fitted with Eq. 7.1 ($\Phi = 0$ for BSA). **Right**: Half-width at half-maximum $\Gamma(q)$ of the fast Lorentzian, fitted with the jump-diffusion model, Eq. 7.4.

The fitted confinement radii R for BSA and for the confined fraction of β-casein are of similar magnitude, while the immobile fractions differ markedly, with $p \approx 0.7$ for BSA and $p \approx 0.2$ for β-casein. The corresponding $A_0(q)$ as a function of q for both proteins is shown in Fig. 7.1 (left panel), where the difference in the elastic fraction is clearly visible. A direct comparison of the fitted parameters for BSA, β-casein, and γ-globulin (the latter taken from the literature) is summarized in Table 7.1. The lower immobile fraction in β-casein can be rationalized by the distinct structural context of the assemblies: their more open and solvent-permeated interior enhances local mobility compared to the compact globular fold of BSA. In addition, the explicit inclusion of methyl rotations in the β-

casein model redistributes spectral weight between components, reducing p. Since p is highly sensitive to the fitting model, the energy window, and the treatment of background contributions, these differences should not be over-interpreted. Indeed, QENS studies of γ-globulin have employed the same EISF models and obtained parameters remarkably similar to those of β-casein [45], underscoring that absolute values of p and R must be interpreted with caution and that only relative comparisons within a consistent framework are meaningful. Nevertheless, the concordance of the fitted confinement radii and of the overall parameter ranges across these proteins strongly suggests that the same underlying dynamical process is being accessed in all cases.

Protein	p	R (Å)	Φ
β-casein	0.19 ± 0.01	5.22 ± 0.2	0.54 ± 0.02
BSA	0.71 ± 0.02	4.7 ± 0.2	-
γ-globulin	0.28 ± 0.02	6.7 ± 0.3	0.55 ± 0.02

Table 7.1. Fitted parameters of the EISF for β-casein, BSA, and γ-globulin. Here p denotes the immobile fraction, R the confinement radius, and Φ the relative weight of methyl group rotations. Values for γ-globulin are taken from Ref. [45], where they were found to remain essentially unchanged across concentrations from ∼10 to 500 mg/mL.

The linewidth $\Gamma(q)$ of the fast Lorentzian provides the dynamical counterpart to the geometrical information encoded in the EISF. Rotational motions of methyl groups take place on timescales of about 10^{-10} s, corresponding to broadenings near 100 μeV, and therefore appear essentially flat within the IN16B energy window. The $\Gamma(q)$ observed here thus arises from localized internal motions within the protein on the tens-of-picoseconds timescale. Its q-dependence can be conveniently described by the Singwi-Sjölander expression,

$$\Gamma(q) = \frac{D_f q^2}{1 + D_f q^2 \tau_f}, \tag{7.4}$$

which interpolates between a quadratic increase at low q and a plateau set by the residence time τ_f. The Singwi-Sjölander form provides a physically motivated description of confined local motions in proteins, capturing both the initial q^2-dependence at small q and the high-q plateau corresponding to the residence time τ_f. A simple horizontal line could approximate the relaxation at high q, but it would neglect the initial slope, which encodes information about the effective local diffusivity D_f. This functional form has been suc-

cessfully applied to a variety of globular and disordered proteins [45, 118–120], enabling consistent comparisons across systems and providing additional insight beyond a purely empirical constant. This expression should not be interpreted as evidence that protons undergo literal jumps between discrete sites. Instead, it serves as a coarse-grained representation of the complex dynamics within a rugged energy landscape. In this framework, the crossover from q^2-diffusion to a q-independent plateau reflects how local fluctuations, initially resembling free diffusion at very short scales, eventually become restricted by the steric and energetic barriers of the protein's internal architecture. By accounting for this transition, the model captures the essential physics of confined relaxations without the need for an explicit, multi-parameter potential form, thus providing a robust framework for comparing the internal flexibility of proteins as structurally diverse as β-casein and BSA. Within the heterogeneous framework established in the previous chapter, this behavior can also be rationalized: apparent jump-like signatures do not arise from discrete events, but from the coexistence of dynamical processes with different timescales and spatial extents. For the slow component, the same mathematical form (Eq. 7.4) was shown to emerge as an effective description of heterogeneous global diffusion within the assemblies. For the fast component, by contrast, it reflects the local potential landscape of the protein interior, where energetic barriers confine the accessible motions. Thus, although the same expression provides a consistent parametrization across dynamical regimes, its physical interpretation depends on the scale of motion being probed.

Protein	D_f (Å^2/ns)	τ_f (ps)
β-casein	$\sim$ 180	25.8 ± 0.8
BSA	$\sim$ 220	24 ± 1
γ-globulin	$\sim$ 150	20-40

Table 7.2. Fitted dynamical parameters of the fast Lorentzian component for β-casein, BSA, and γ-globulin. Here D_f is the effective diffusion coefficient and τ_f the associated residence time, as obtained from the jump-diffusion model in Eq. 7.4. Values for γ-globulin are taken from Ref. [45], where τ_f was found to increase monotonically with concentration but remained within the 20-40 ps range.

In both β-casein and BSA, the fitted linewidths fall in the 20-25 μeV range, corresponding to relaxation times of ∼25-30 ps, consistent with previous reports for γ-globulin and other

globular proteins. This similarity is clearly seen in Fig. 7.1 (right panel), where the q^2-dependence of Γ for both proteins follows nearly identical trends. A direct comparison of the fitted parameters D_f and τ_f for β-casein, BSA, and γ-globulin is summarized in Table 7.2, highlighting the consistency of relaxation times across proteins of very different structural classes.

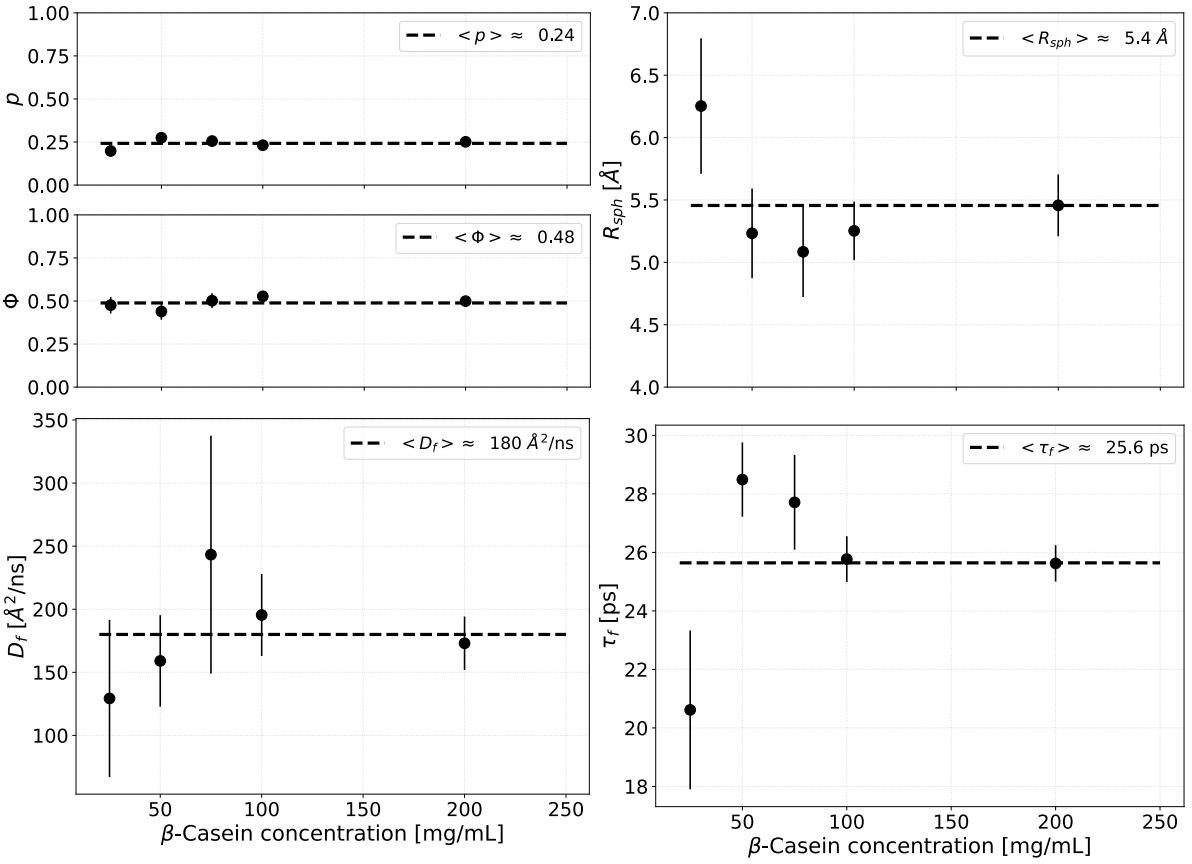

Figure 7.2. Concentration dependence of the fitted parameters describing the fast internal dynamics of β-casein. **Top left**: Immobile fraction p (upper) and methyl fraction Φ (lower). **Top right**: Confinement radius R extracted from the EISF fits. **Bottom left**: Effective diffusion coefficient D_f obtained from the jump-diffusion model, Eq. 7.4. **Bottom right**: Corresponding residence time τ_f. Dashed lines mark the average values, which are also indicated in the legend of each plot.

The concentration dependence of the parameters describing the fast process in β-casein is summarized in Fig. 7.2, which compiles the fitted parameters p, Φ, R, and τ_f across all measured concentrations. Within uncertainties, the variations are small and show no systematic trend, indicating that the fast internal dynamics are essentially insensitive to

crowding. A concentration dependence of the fast internal dynamics could, in principle, be expected for β-casein, since this protein forms micellar assemblies whose internal organization evolves with concentration. At low concentrations, the assemblies are relatively loose and solvent-permeated, whereas at higher concentrations they develop a denser core and a more structured architecture (see Chapter 5. Such structural changes could, in principle, modify the local environment experienced by protein segments and side chains, and thus influence the amplitude or timescale of their internal motions, including methyl rotations. The absence of a systematic evolution in p, Φ, R, or τ_f indicates that, within the experimental time window, these local dynamics remain largely unchanged despite the global reorganization of the assemblies. This contrasts with the slow component discussed in the previous chapter, where the effective diffusion coefficient decreased slightly with concentration while the residence time increased (see Table 6.1). The stability of the fast contribution supports its assignment to localized side-chain and backbone segment motions that remain largely unaffected by the global assembly state. However, the fast component contributes mainly in the spectral region where background and solvent effects have the greatest impact, which limits the robustness of the extracted parameters. These factors inflate uncertainties and may obscure subtle systematic effects. The only notable deviation is found for the most dilute sample (25 mg/mL), but this case is also the most challenging experimentally, since at such a low concentration the signal approaches the detection limits of the instrument. In general, the lack of any monotonic evolution with concentration is a robust result and the characteristic relaxation time of ∼25-30 ps remains consistent across all conditions.

A complementary perspective is provided by molecular dynamics simulations of β-casein aggregates containing between one and five chains, analyzed with the same two-component framework as the experiments (Eq. 6.1). To highlight the role of aggregation, we focus here on the two limiting cases: a single chain in solution ($N = 1$) and a small aggregate of five chains ($N = 5$). The corresponding $A_0(q)$ and $\Gamma(q)$ are shown in Fig. 7.3. Notably, in both cases the EISF is well described using only the confined-diffusion model in a sphere (Eq. 7.1 with $\Phi = 0$), i.e., without requiring an explicit three-site jump contribution. The fitted parameters for $N = 1$ and $N = 5$ are summarized in Table 7.3.
The immobile fraction p remains essentially unchanged between the monomer and the five-chain aggregate, with values around 0.37 ± 0.03 in both cases (Table 7.3). This indicates

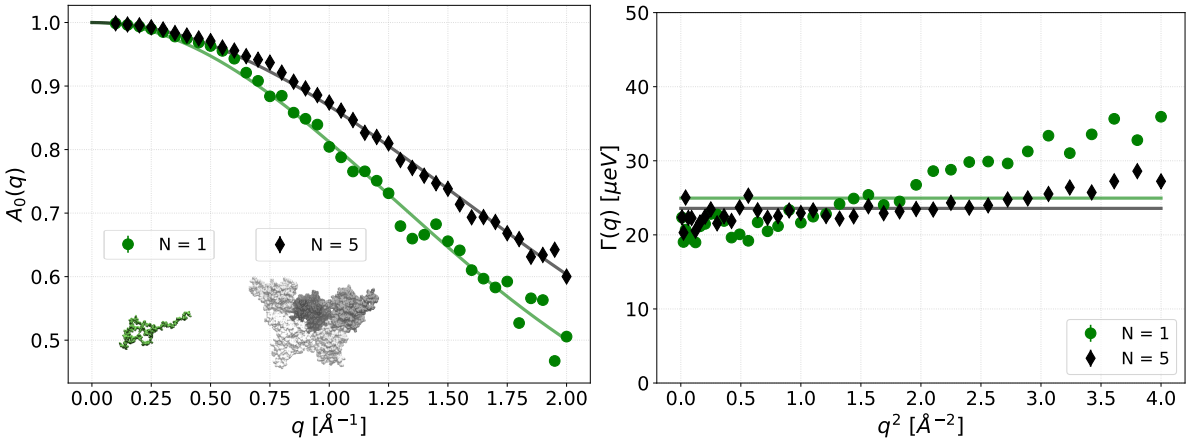

Figure 7.3. Left: Elastic incoherent structure factor $A_0(q)$ for a β-casein monomer (green) and a five-chain aggregate (black), fitted with the confined-diffusion model in a sphere (Eq. 7.1 with $\Phi = 0$). Insets show representative configurations of the monomer and the aggregate. **Right**: Half-width at half-maximum $\Gamma(q)$ of the fast Lorentzian for the same systems, where the lines indicate the average linewidths.

System	p	R (Å)	$\langle\Gamma\rangle$ (μeV)	$\tau \approx 1/\langle\Gamma\rangle$ (ps)
Monomer ($N = 1$)	0.37 ± 0.03	1.31 ± 0.05	~ 25	~ 26
Five-chain aggregate ($N = 5$)	0.37 ± 0.03	1.07 ± 0.03	~ 24	~ 28

Table 7.3. Fitted EISF and dynamical parameters from simulations for a β-casein monomer ($N = 1$) and a five-chain aggregate ($N = 5$). Here p is the immobile fraction, R the confinement radius from the single-sphere model (Eq. 7.1 with $\Phi = 0$), and $\langle\Gamma\rangle$ the average HWHM of the fast Lorentzian. The characteristic time is estimated as $\tau \approx 1/\langle\Gamma\rangle$.

that aggregation does not significantly alter the balance between mobile and immobile fractions at the timescales probed, although finite-size effects and limited sampling in the simulations could still mask subtle differences. The confinement radii R obtained from the fits are consistently smaller than the experimental values (∼5 Å), with $R = 1.31 \pm 0.05$ Å for the monomer and $R = 1.07 \pm 0.03$ Å for the five-chain aggregate. This modest reduction of ∼20% suggests a slight tightening of the effective cage upon aggregation. The overall discrepancy with respect to experiment most likely reflects methodological differences rather than a genuine geometric mismatch: in simulations the absence of q-dependent resolution broadening produces a steeper low-q curvature of $A_0(q)$, biasing the fitted radius downward, while differences in incoherent contrast (e.g. reduced hydration contributions)

and the omission of ultrafast processes such as methyl rotations further lower the apparent confinement scale.

The linewidths show little dependence on aggregation. For both $N = 1$ and $N = 5$, $\Gamma(q)$ remains nearly flat or only weakly q-dependent, with average values around 25 μeV. This corresponds to relaxation times of ∼25-30 ps, in close agreement with the experimental results for both β-casein and BSA. The persistence of this characteristic timescale even in the monomer demonstrates that the fast contribution is an intrinsic property of the protein and does not rely on micelle formation.

Several important methodological differences must be kept in mind when comparing experiment and simulation. First, the MD integration time step is $\Delta t = 2$ fs, but configurations are saved only every $\sim$ 10 ps for analysis. Motions faster than this output stride, such as methyl rotations, are therefore not resolved and do not contribute explicitly to the calculated spectra. As a result, the simulated $A_0(q)$ captures only a subset of the processes contributing experimentally. This is reflected in the fitting: while in simulations a single confined-diffusion model suffices to describe the curvature of $A_0(q)$, in experiments an additional explicit three-site jump term is required. Consequently, the simulated confinement radii R are systematically smaller than the experimental ones.

Second, resolution is treated differently. Experimental spectra are convolved with a q-dependent resolution function, which affects both $A_0(q)$ and $\Gamma(q)$, particularly at low q. In simulations, by contrast, Fourier transforms of correlation functions are typically evaluated without convolution, corresponding to an infinitely sharp, q-independent resolution. This absence of resolution broadening alters the apparent shape of the EISF and the q-dependence of Γ, making direct comparison difficult. Additional experimental factors further complicate matters: container and solvent scattering, imperfect background subtraction, and beam divergence. The latter, constant in the scattering angle θ, translates into a relatively stronger broadening at low q, reducing the experimental sensitivity to the confinement geometry. Such effects likely contribute to the apparent jump-like curvature of experimental $\Gamma(q)$, whereas simulated linewidths remain flat or only weakly q-dependent.

Third, incoherent contrast differs between the two approaches. Experiments weight all hydrogens in the protein and solvent, including the hydration shell, whereas simulations often include only protein hydrogens. This difference inevitably modifies $A_0(q)$ and shifts the balance between the fitted components. Together with finite-size effects and sampling

limitations, these methodological differences explain the mismatch between the simulated and experimental EISF parameters and prevent a direct quantitative comparison of p, Φ, or R.

Despite these limitations, the agreement in dynamical signatures is robust. Both the experiment and the simulation consistently produce line widths in the 20-25,μeV range. This holds for all systems: experimental β-casein and BSA, as well as simulated aggregates from $N = 1$ to $N = 5$. In simulations, even the isolated monomer displays the same relaxation, demonstrating that the fast component is intrinsic to the protein and independent of micelle formation. The comparison between $N = 1$ and $N = 5$ further shows that aggregation has only a minor effect on internal dynamics: both the immobile fraction p and the characteristic relaxation timescale remain essentially unchanged.

7.3 Conclusions

The analysis of the fast component in β-casein and BSA establishes a coherent picture of confined internal dynamics on the tens-of-picoseconds timescale. Both experiments and simulations consistently reveal linewidths in the 20-25 μeV range, corresponding to relaxation times of ∼25-30 ps, irrespective of protein fold, crowding, or aggregation state. While the geometrical signature in the EISF differs between experiment and simulation due to methodological limitations, contrast effects, and the treatment of ultra-fast processes, the dynamical signature in $\Gamma(q)$ is essentially identical across all systems. Within the heterogeneous framework developed in this work, the apparent jump-diffusion like behavior observed experimentally arises as an effective description of overlapping local processes, whereas simulations emphasize its nearly q-independent character once resolution and methyl contributions are excluded. Taken together, these results point to a robust and universal fast relaxation mode that is best understood as the natural outcome of spatial and temporal heterogeneity in confined internal protein dynamics.

Chapter 8

Chemical dissociation and free monomer dynamics

8.1 Introduction

This chapter describes an investigation intended at determining whether the deviations from Fickian diffusion reported previously originate from constraints within assemblies or from properties inherent to intrinsically disordered chains.

The analysis addresses three objectives. First, establish whether urea disrupts micelles across the explored range and whether the resulting scattering signatures align with polymer-like coils, in terms of compatible sizes, absence of interparticle correlations, and an apparent aggregation number close to unity Second, quantify how the slow, global component of the dynamics evolves under chemical dissociation, testing the replacement of the heterogeneous, non-Fickian response associated with the micellar interior by homogeneous center-of-mass diffusion characteristic of free monomers at high urea concentration. Third, assess whether urea provides a viable route to probe the dynamics of free monomers at concentrations compatible with neutron scattering experiments despite the low CMC of β-casein, that is, whether aggregation can be suppressed at high concentration without substantially altering the monomer as commonly reported for well-folded proteins [92].

SANS is employed to quantify the structural response across a range of urea concentrations. The analysis tracks changes in micellar size and apparent aggregation number, and evaluates the persistence of the low-q excess scattering associated with mesoscale inhomogeneities. Particular attention is given to the regime where the correlation peak fades

while a residual low-q upturn remains, indicating large-scale fluctuations that survive micelle dissociation.

QENS complements the structural data by resolving the dynamic response under the same chemical perturbation. Within the two-component framework introduced in Chapter 6, the slow component reflects an effective global diffusion that deviates from Fickian behavior in the assembly regime and approaches linear scaling (Dq^2) as monomers dominate. The fast contribution encodes localized internal relaxations through the EISF and the associated linewidth, enabling an assessment of whether urea-induced chain swelling alters the geometry or timescales of these motions.

The combined SANS-QENS analysis maps the micelle-to-monomer transition under chemical control, establishing whether anomalous global diffusion is suppressed upon dissociation and whether internal dynamics remain largely unchanged or reflect an expanded local configurational space.

8.2 Results and discussion

8.2.1 Structure under chemical dissociation

To investigate the effect of micelle dissociation, we performed SANS measurements in the presence of urea. As representative cases, we selected two concentrations of β-casein, 1 mg/mL and 75 mg/mL, corresponding to the dilute and concentrated regimes previously identified and discussed in Chapter 5. These two conditions capture the essential features of the system: at low concentration the scattering profiles reflect isolated assemblies, whereas at high concentration a pronounced correlation peak emerges due to micelle-micelle interactions.

The analysis of the SANS data was carried out using the same minimal piecewise model introduced in Eq. 5.1. At low concentration (1 mg/mL), the scattering profiles are well captured by a simple spherical form factor, consistent with isolated micelles and negligible interparticle correlations. By contrast, at high concentration (75 mg/mL), the analysis requires a more complex description combining a core-shell form factor with a hard-sphere structure factor, reflecting the emergence of pronounced correlations between neighboring micelles. Upon addition of urea, the scattering curves undergo qualitative changes that reflect the progressive disassembly of the micelles. At high urea concentrations, where

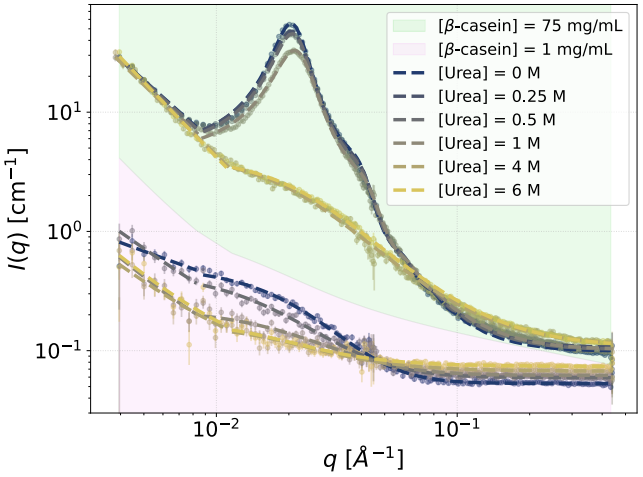

Figure 8.1. Representative SANS intensity profiles of β-casein at 1 mg/mL (pink background) and 75 mg/mL (green background) in the presence of increasing urea concentrations. Symbols show the experimental data; dashed lines denote fits with the piecewise model of Eq. 5.1, using a sphere form factor at 1 mg/mL and a core-shell form factor combined with a hard-sphere structure factor at 75 mg/mL (for [urea] $\leq$ 1 M), and a Gaussian-coil form factor for [urea] $>$ 1 M.

micelles are assumed to be absent, both concentrations were instead analyzed using a Gaussian coil form factor without structure factor, consistent with scattering from expanded monomers in solution.

The low-q upturn observed in all datasets was modeled with the same cluster contribution as in Chapter 5. Overall, this contribution appears to be only weakly affected by the addition of urea. The main change is a shift of the crossover wavevector q^* from 0.085 Å^{-1} in the micellar regime (low urea) to 0.115 Å^{-1} in the fully dissociated state (high urea), indicating a modification in the characteristic length scale of the large-scale inhomogeneities.

Figure 8.1 shows the fitted SANS intensity profiles for the two representative concentrations. At 75 mg/mL (green background), a clear reduction in the correlation peak is observed with increasing urea concentration, until it eventually disappears. The available datasets correspond to 0, 0.25, 0.5, 1, 4 and 6 M urea. The most pronounced drop of the peak intensity occurs between 1 and 4 M, whereas in the case of guanidinium chloride, the transition was already visible between 0 and 1 M (not shown here, see [83]). For this

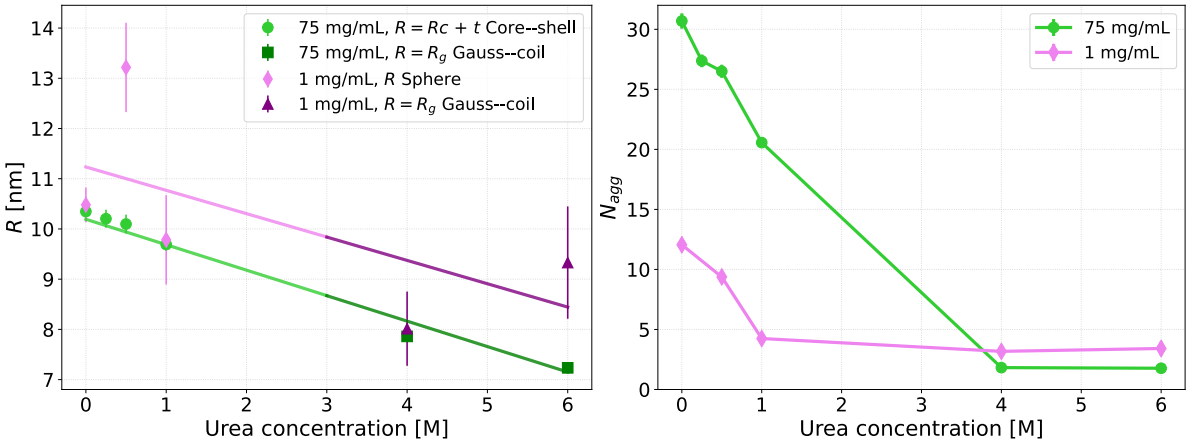

Figure 8.2. Left: Effective size versus urea concentration for 1 mg/mL and 75 mg/mL. For [urea] $\leq$ 1 M, the plotted size is the sphere radius (1 mg/mL) or the total core+shell radius (75 mg/mL); for [urea] $>$ 1 M, both concentrations are analyzed as Gaussian coils and the plotted size is the radius of gyration R_g. A change in color and marker denotes the change of model; lines are guides to the eye. **Right:** Apparent aggregation number $N_{\mathrm{agg}}^{\mathrm{app}}$ computed from the apparent forward intensity of the particle branch, $I_0^{\mathrm{app}} \approx A$ (cluster upturn excluded; see Eq. 5.1 and text). Error bars reflect the propagated statistical uncertainty of A.

reason, we prioritized a finer sampling at low urea concentrations, while the intermediate region (1-4 M) remains less well covered experimentally.

For the dilute samples (1 mg/mL, pink background), the changes are more subtle. A systematic decrease of the overall scattering intensity is observed with increasing urea concentration, reflecting the progressive reduction of the micellar assemblies. At high q, the intensity increases with urea content, indicating a larger contribution from the incoherent background of the solvent. Finally, despite the complete dissolution of the micelles at high urea, the low-q upturn remains present. This feature is likely related to persistent large-scale density fluctuations or transient clustering of monomers in solution.

Figure 8.2 (left) compiles the effective size as a function of urea concentration for the two representative samples. For [urea] $\leq$ 1 M we report the fitted particle radius (the sphere radius at 1 mg/mL, and the total core+shell radius at 75 mg/mL) whereas for [urea] $>$ 1 M we switch to the Gaussian-coil description and plot the radius of gyration R_g. At 75 mg/mL, increasing urea drives a systematic reduction of the fitted radius, which at the highest concentrations approaches $\sim$ 7 nm, consistent with the largest monomer

dimensions reported for β-casein under denaturing conditions. This supports the view that urea does not merely dissociate the micelles but also swells the monomers, in line with single-chain simulations in which isolated chains remain relatively compact in water ($R_g \sim 2$ nm) but can expand up to ~ 7 nm in urea (see Appendix H and [121]). By contrast, at 1 mg/mL, the response to urea is non-monotonic: the fitted radii display scatter and occasional increases at intermediate concentrations, consistent with transient swelling before disassembly. This behavior likely reflects the marginal stability of micelles at such low concentration and the reduced structural contrast, together with the larger incoherent background at high q in urea, which enhances parameter cross-talk and renders the fits less robust.

To quantify this interpretation we estimate the aggregation number, shown in the right panel of Figure 8.2. Because all datasets exhibit a low-q upturn, the total intensity extrapolated to $q \to 0$ would be dominated by the cluster contribution in the piecewise model of Eq. 5.1 and would not represent the micelle/coil forward scattering. For aggregation analysis we therefore use the apparent forward intensity of the micelle/coil contribution, defined as

$$I_0^{\mathrm{app}} \equiv \lim_{q\to 0} A\, P(q)\, S(q) \approx A, \tag{8.1}$$

where A is the fitted amplitude of the micelle/coil branch in Eq. 5.1 and $P(0) = 1$. In other words, we always take $I_0^{\mathrm{app}} \approx A$ and exclude the low-q power-law term from the forward intensity. At 1 mg/mL one has $S(q) \equiv 1$, so $I_0^{\mathrm{app}} = A$ exactly. At 75 mg/mL in the micellar regime, hard-sphere correlations imply $S(0) < 1$; not correcting for $S(0)$ makes I_0^{app} an underestimate of the true forward intensity, but it keeps the procedure uniform across conditions. In the high-urea monomeric regime (Gaussian coil), we also assume negligible interparticle correlations and set $S(q) \equiv 1$ (hence $S(0) = 1$), so that $I_0^{\mathrm{app}} = A$ also in this regime.

From I_0^{app} we compute an apparent molecular weight and aggregation number via

$$M_w^{\mathrm{app}} = \frac{I_0^{\mathrm{app}}\, N_A\, d^2}{c\,(\Delta\rho)^2}, \qquad N_{\mathrm{agg}}^{\mathrm{app}} = \frac{M_w^{\mathrm{app}}}{M_w^{\mathrm{mono}}}, \tag{8.2}$$

where N_A is Avogadro's number, d the protein mass density, c the protein mass concentration and $\Delta\rho$ the protein-solvent SLD contrast. Here M_w^{mono} denotes the molecular weight of a single β-casein chain (taken as $M_w^{\mathrm{mono}} = 25{,}366$ g mol^{-1} in our analysis; see Chapter 4).

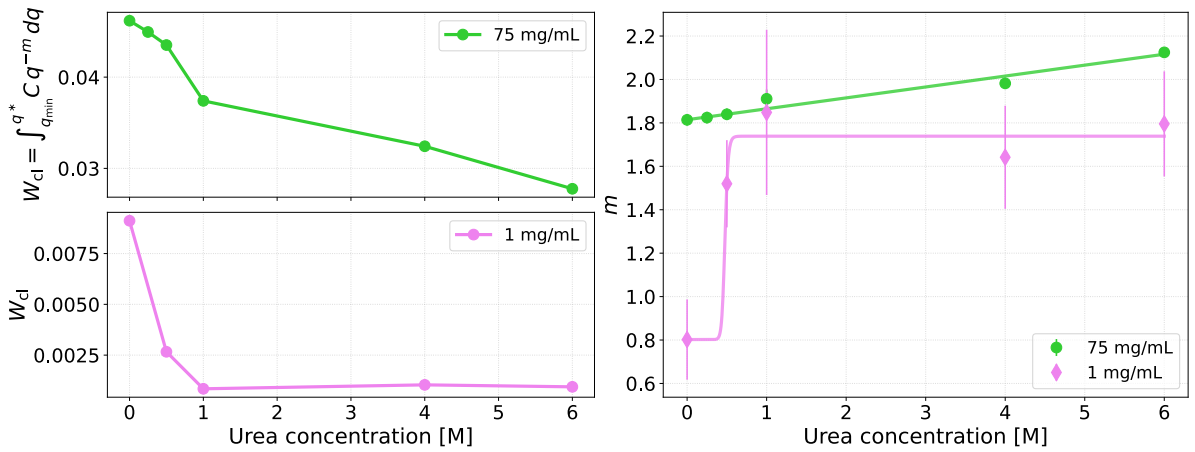

Figure 8.3. Left: Integrated low-q weight $W_{\mathrm{cl}} = \int_{q_{\min}}^{q^*} C q^{-m}\, dq$ computed with a fixed $q^* = 0.085$ Å^{-1} to enable direct comparison across conditions. **Right:** Exponent m as a function of urea concentration. Colors/symbols distinguish concentrations; lines are guides to the eye.

We emphasize that $N_{\mathrm{agg}}^{\mathrm{app}}$ underestimates the absolute value at 75 mg/mL in the micellar regime (since $S(0) < 1$), nevertheless, these effects do not alter the main conclusion: the apparent aggregation number decreases robustly with urea and approaches values close to unity at high urea, consistent with micelle disassembly into monomers.

We then address the low-q upturn. Based on our initial interpretation (Chapter 5), this contribution was associated with large-scale density fluctuations or transient clustering of micelles, in line with the slow diffusive mode observed by DLS. If this were the dominant origin, one would expect the upturn to vanish as urea dissolves the micelles. Instead, it persists across the full urea range and appears only weakly affected by urea addition. Within the piecewise description of Eq. 5.1, we retain the same power-law term $I_{\mathrm{cl}}(q) = Cq^{-m}$ for all samples and we quantify its magnitude by the integrated weight up to a fixed crossover $q^* = 0.085$ Å^{-1} so that all conditions can be compared on the same q window. Figure 8.3 (left) shows that $W_{\mathrm{cl}} = \int_{q_{\min}}^{q^*} C q^{-m}\, dq$ decreases with urea at both concentrations: at 75 mg/mL it decays gradually over the full range, whereas at 1 mg/mL it drops sharply by ∼1 M and then remains essentially constant at higher urea. The persistence of a nonzero W_{cl} even when the correlation peak disappears indicates that the upturn is not tied to micelle-micelle order; rather, it reflects mesoscale concentration fluctuations of proteins in solution or weak, transient clustering of monomers that survive the micelle-to-monomer transition.

The exponent m shows clear, concentration dependent trends (Fig. 8.3, right). At 75 mg/mL, m increases monotonically from ∼1.8 to ∼2.1, indicating a progressive steepening of the low-q decay and, in real space, correlations that extend over a shorter range. At 1 mg/mL, m rises quickly from ∼0.8 to ∼1.8 by about 1 M urea and then remains approximately constant. In scattering terms, these changes are consistent with a shift from very tenuous, slowly varying inhomogeneities at low urea (shallow slopes) to fluctuations with an effective fractal dimension close to 2 at higher urea. Together with the decrease of W_{cl}, the increase of m shows that urea reduces the overall magnitude of the large-scale heterogeneity and shifts it toward steeper correlations of shorter range. This occurs abruptly in the dilute sample and more gradually in the concentrated one. For consistency with the aggregation analysis, we keep the same cluster term across conditions and exclude it from forward-intensity estimates ($I_0^{\mathrm{app}} = A$), so that micellar parameters are not biased by the large-scale contribution.

In summary, SANS shows that urea disassembles the micelles and drives the system toward a monomer dominated state. The fitted sizes decrease and, at high urea, approach ∼ 7 nm, consistent with expanded monomers; the apparent aggregation number falls toward unity; and at 75 mg/mL the correlation peak fades and disappears. The low-q contribution persists but its integrated weight W_{cl} decreases while the exponent m increases, indicating a reduction in the overall strength of large scale heterogeneity and a shift toward correlations of shorter range. Taken together, these structural signatures indicate that the system is now dominated by free monomers. This motivates a direct examination of their dynamics, asking whether translational motion becomes Fickian with diffusion coefficients close to those of isolated chains, and whether the internal mobility of the protein changes in the urea-expanded state.

8.2.2 Transition from assembly to free monomer dynamics

Chemical dissociation by urea provides a direct route to follow how the dynamic response changes as the system moves from an assembly-dominated state toward a monomer-dominated regime. Among the two concentrations highlighted in the structural analysis (1 and 75 mg/mL), only the 75 mg/mL sample offers sufficient quasi-elastic signal within the accessible q and energy windows. To remain consistent with the concentration series, all spectra are analyzed with the same two-contribution model (Eq. 6.1). In the case of

β-casein in normal buffer, the slow Lorentzian captures an effective, heterogeneous diffusion within the micellar assemblies manifested as a deviation from Fickian behavior and well described by the Singwi-Sjölander form (Chapter 6). Within this phenomenological framework, the fitted D approximates the average of an underlying distribution of diffusivities, while τ is related with the dispersity and thus quantifies dynamic heterogeneity. The fast Lorentzian captures localized internal relaxations confined to nanometric length scales; in our framework it is constrained jointly by the EISF (modeled as a mixture of three-site methyl rotations and diffusion within a sphere) and by the associated linewidth $\Gamma(q)$. The $\Gamma(q)$ data are also conveniently parameterized by the Singwi-Sjölander form as an effective description of motion in a rugged local energy landscape, and they fall in the 20-25 μeV range ($\sim$25-30 ps) with only weak q-dependence; these timescales are largely insensitive to crowding. A representative quasi-elastic spectrum at 75 mg/mL and 4 M urea, together with the fitted components, is shown in Fig. 8.4 (left). Following the same order as in the structural analysis, we first examine the slow contribution through the linewidths $\gamma(q)$, and its dependence on q^2. As displayed in Fig. 8.4 (right), increasing urea turns the curved $\gamma(q^2)$ traces into a straight line: at low and intermediate urea the data follow the Singwi-Sjölander form

$$\gamma(q) \;=\; \frac{D\,q^2}{1 + D\,q^2\,\tau}, \tag{8.3}$$

whereas at 4 M a linear law $\gamma = D\,q^2$ is recovered, consistent with Fickian diffusion. The corresponding parameters are compiled in Fig. 8.5. The diffusion coefficient D rises with urea and shows a clear step between 0.5 and 1 M, while the relaxation time τ decreases steadily and becomes negligible only at 4 M. Read together, these trends point to a transition from heterogeneous dynamics within assemblies to dynamics dominated by free monomers. The sharp increase in D suggests that, beyond a certain urea level, a large fraction of assemblies undergo disassembly. Yet τ remains clearly finite at 1 M, indicating marked heterogeneity at that stage. Two microscopic scenarios are therefore compatible with the combination of a larger D and a finite τ: (i) coexistence of freely diffusing monomers with a residual population of small aggregates, or (ii) a single, polydisperse population of assemblies that progressively shrink while retaining spatially heterogeneous motion. Looking at the structural data for the same condition (75 mg/mL, 1 M urea) we observe that the correlation peak is still present and the fits require a hard-sphere structure factor (Fig. 8.1); the fitted size remains compatible with micellar

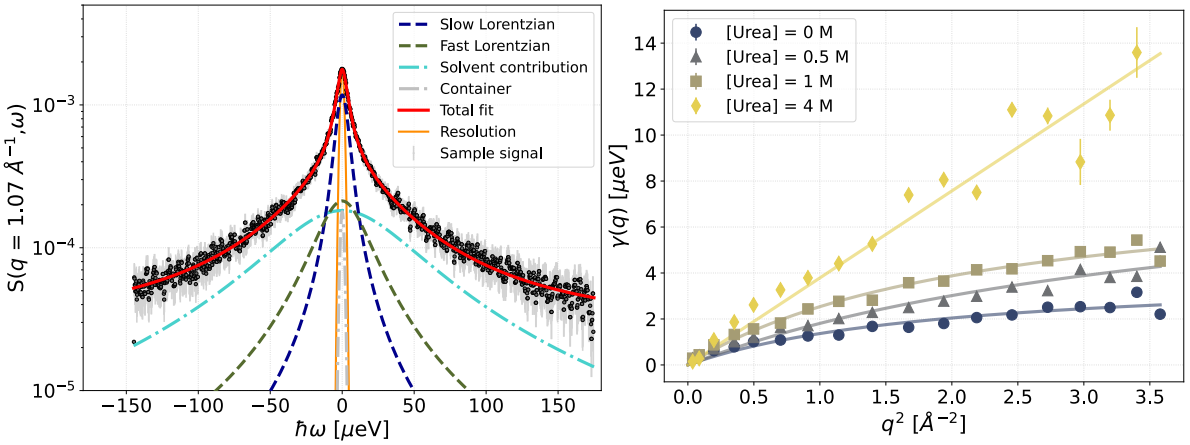

Figure 8.4. Left: Representative quasi-elastic spectrum of β-casein at 75 mg/mL and 4 M urea (symbols) together with the total fit from Eq. 6.1 (red solid line). The different contributions are identified in the legend. **Right:** q^2-dependence of the HWHM of the slow component, $\gamma(q)$. Datasets with [urea] < 4 M are described by the Singwi-Sjölander form $\gamma = Dq^2/(1 + Dq^2\tau)$ (Eq. 8.3), whereas the 4 M dataset follows the linear-in-q^2 Fickian law $\gamma = Dq^2$. Solid lines are fits; symbols are data with uncertainties.

assemblies rather than isolated monomers, and the apparent aggregation number is above unity (Fig. 8.2). Although one polydisperse population fits the data, coexistence remains plausible: monomers and small aggregates with overlapping sizes produce nearly indistinguishable curves in our q range. From the dynamical side, the slow Singwi-Sjölander term in our analysis is an effective representation of a distribution of diffusion coefficients; the fitted pair (D, τ) therefore captures the mean and spread of this distribution rather than resolving distinct species. In particular, if small aggregates and monomers have overlapping or similar diffusion coefficients, they do not produce separate spectral peaks but jointly broaden the effective $P(D)$, yielding an apparent non-Fickian response (finite τ). Only at 4 M, where $\tau \approx 0$ and $\gamma(q^2)$ becomes linear, does the dynamics approach homogeneous Fickian diffusion consistent with free monomers. With the data and effective models used here we therefore cannot distinguish unambiguously between coexistence and continuous shrinking; nonetheless, both SANS and QENS are consistent with a urea-driven crossover toward a monomer-dominated regime by 4 M. To characterize the transition more reliably, additional measurements with denser sampling between 1 and 4 M (where our data indicate the crossover occurs) will be required.

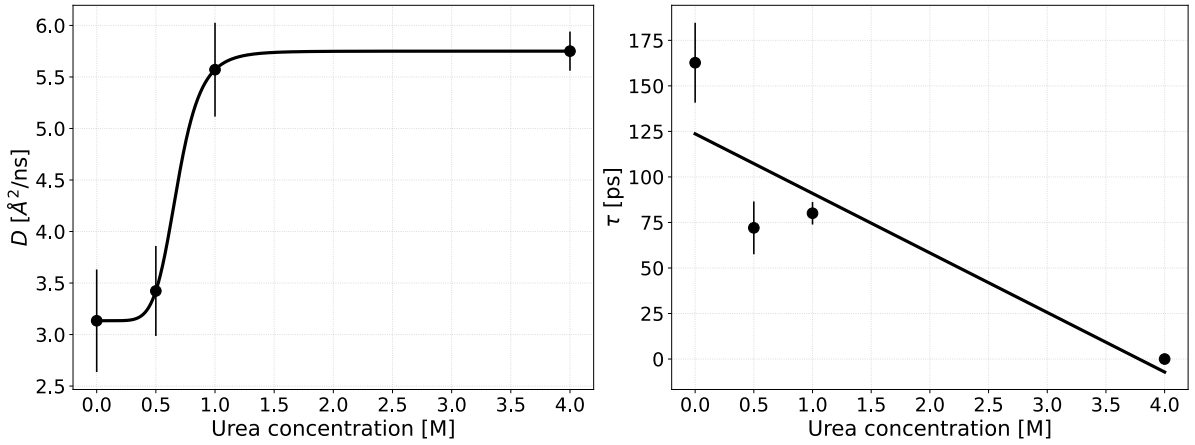

Figure 8.5. Left: Diffusion coefficient D of the slow component at 75 mg/mL as a function of urea concentration. **Right:** Relaxation time τ from the Singwi-Sjölander fits versus urea. Error bars indicate propagated fit uncertainties. Solid lines serve as guides to the eye.

Having established that micellar assemblies dissociate between 1 and 4 M urea, we next examine the fast contribution associated with internal motions. In Chapter 7 we showed that this contribution is largely insensitive to crowding and reflects motions intrinsic to the monomer. The EISF, $A_0(q)$, is captured by a mixture of three-site methyl rotations and localized diffusion within a nanometric cage, while the corresponding linewidth, $\Gamma(q)$, is only weakly dependent on q and lies in the 20-30 μeV range (tens of picoseconds). The question here is whether chemical dissociation by urea modifies these local processes.
To remain fully consistent with Chapter 7, we analyze the EISF and the fast HWHM in exactly the same way and over the same q-intervals. The EISF is fitted with

$$A_0(q) \;=\; p \;+\; (1-p)\left[\,\Phi\, A_{\text{3-site}}(q) \;+\; \Big(1-\Phi\Big)\, A_{\text{sphere}}(q,R)\right], \tag{8.4}$$

where p is the immobile fraction within the instrumental window, Φ the fraction of mobile sites executing three-site methyl rotations, and $A_{\text{sphere}}(q,R)$ describes localized diffusion within a sphere of radius R (Eq. 7.3). The fast linewidth is parameterized with the same effective jump-diffusion form used before,

$$\Gamma(q) \;=\; \frac{D_{\text{f}}\, q^2}{1 + D_{\text{f}}\, q^2\, \tau_{\text{f}}}, \tag{8.5}$$

which provides a compact description of confined local relaxations in a rugged energy landscape. Representative $A_0(q)$ and $\Gamma(q)$ datasets with their fits are shown in Fig. 8.6

(left and right, respectively), and the urea-dependence of the extracted parameters is summarized in Fig. 8.7.

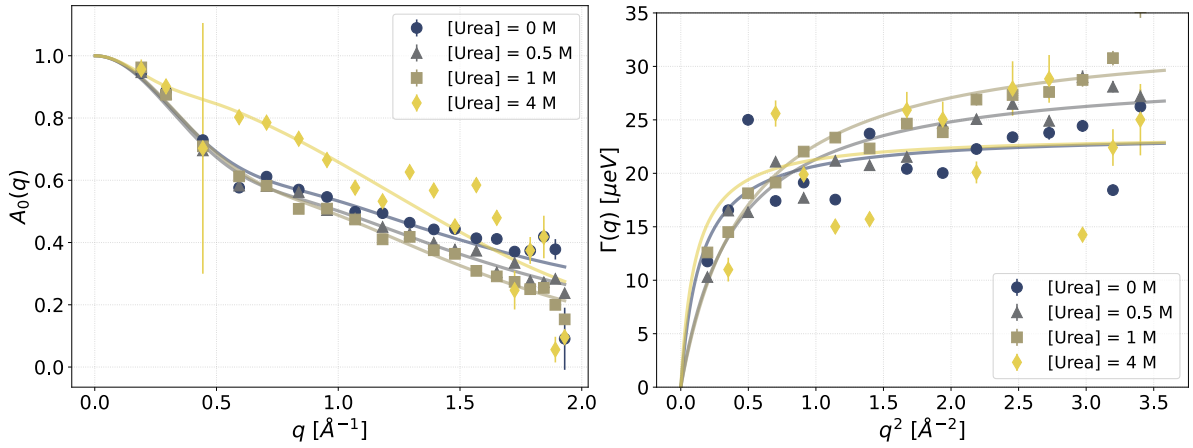

Figure 8.6. Left: Elastic incoherent structure factor $A_0(q)$ for β-casein at various urea concentrations; solid lines are fits using Eq. 8.4. **Right:** Corresponding half-width at half-maximum $\Gamma(q)$ of the fast Lorentzian for the same conditions; solid lines are fits according to Eq. 8.5.

Across the full urea series, the immobile fraction decreases sharply with urea ($p : 0.17 \rightarrow 0.02$ between 0 and 1 M) and approaches zero at 4 M. In parallel, the methyl fraction exhibits only a modest increase up to 1 M ($\Phi : 0.60 \rightarrow 0.68$), then shows a pronounced jump at 4 M, where best-fit values approach $\Phi \approx 0.90$. The localization radius remains essentially constant up to 1 M ($R \approx 5.5$ Å), while at 4 M it appears to increase substantially, with best-fit values around $R \sim 10$ Å. Importantly, the uncertainties on both R and p at 4 M are very large (error bars comparable to the observed changes). The reliable conclusion is that R increases and p decreases markedly at high urea, while their precise values remain uncertain. Taken together, these trends suggest a simple physical picture. As urea progressively weakens inter-assembly interactions and ultimately dissolves the aggregates, a larger fraction of hydrogen sites becomes mobile within the QENS window (reflected in the rise of Φ and decrease of p), and the accessible local volume explored by these sites expands (increase of R). This scenario is consistent with structural results showing that urea not only dissociates micelles but also swells the monomer [121], thereby relaxing local constraints and enlarging the configurational space available to internal rearrangements. By contrast, the characteristic timescale of the internal motions remains comparatively stable. The fast HWHM stays within the same $\sim$ 20-30 μeV band across q throughout

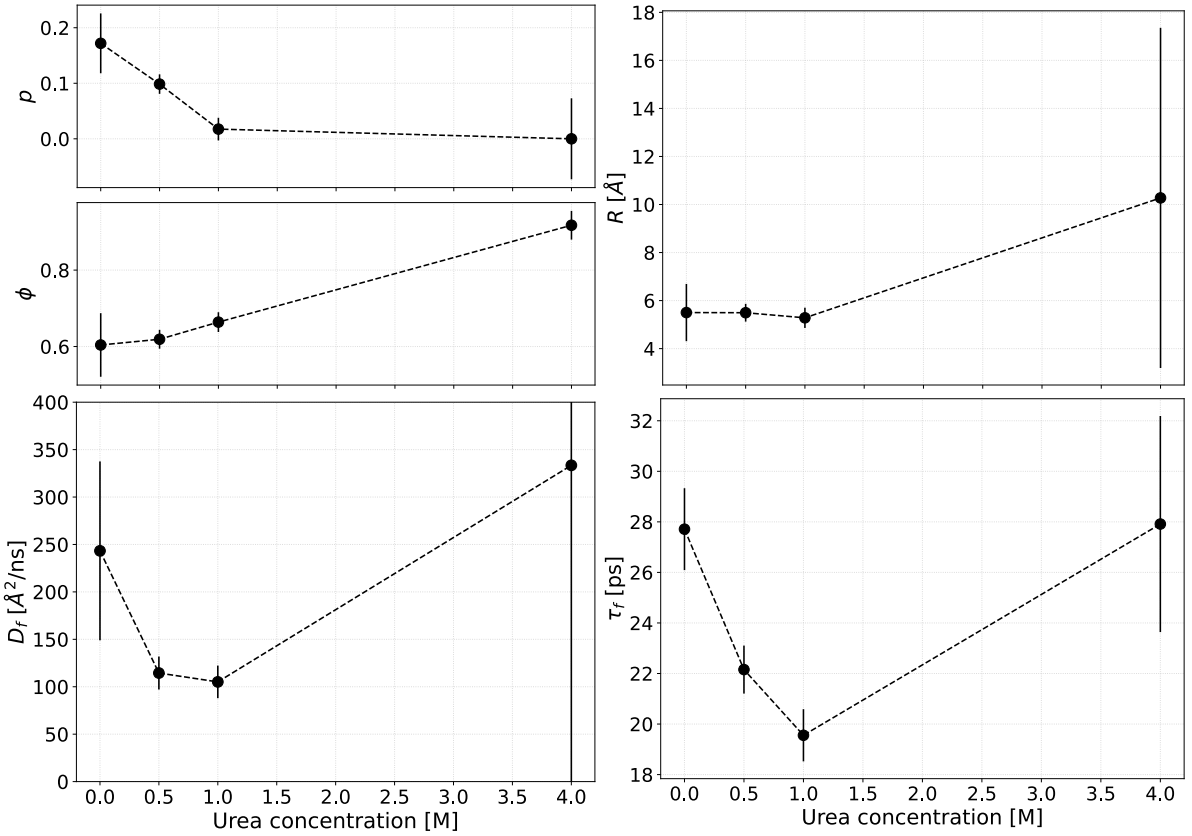

Figure 8.7. Dependence of the fitted parameters describing the fast internal dynamics of β-casein on urea concentration. **Top left**: Immobile fraction p (upper) and methyl fraction Φ (lower). **Top right**: Confinement radius R extracted from the EISF fits. **Bottom left**: Effective diffusion coefficient D_f obtained from the Singwi-Sjölander model, Eq. 7.4. **Bottom right**: Corresponding residence time τ_f.

the urea series (Fig. 8.6, right). Fits of Eq. (8.5) point to possible increases in D_f and τ_f between 1 and 4 M, but the associated confidence intervals are broad and the parameters are strongly correlated, so different $(D_\mathrm{f}, \tau_\mathrm{f})$ pairs can reproduce an essentially unchanged $\Gamma(q)$ within our q window.

A note of caution is warranted. At high urea concentrations the overall incoherent baseline rises, making the separation between the fast term, solvent, and background increasingly delicate; this amplifies parameter uncertainties and strengthens correlations. Additional measurements with denser sampling between 1 and 4 M (where structural and slow-dynamics results place the crossover) and optimized contrast conditions would be required to determine whether the apparent jump at 4 M reflects a genuine change in the geometry of internal motions or residual limitations of the present decomposition.

8.3 Conclusions

The experiments presented in this chapter show that urea provides an effective route to dissociate β-casein micelles and to follow how both structure and dynamics evolve as the system approaches a monomer-dominated state. The structural data obtained by SANS indicate that the crossover takes place between 1 and 4 M urea, although the present sampling does not allow a precise determination of the onset. In this interval, micelles progressively lose their characteristic correlation peak, the apparent aggregation number decreases toward unity, and the effective particle size approaches $\sim$7 nm. This dimension is strikingly consistent with the radii of gyration reported by atomistic simulations of β-casein in urea, where single chains swell from their compact state in water ($R_g \sim 2$ nm) to extended conformations of 5-7 nm [121]. The agreement between experiment and simulation therefore supports a scenario in which urea not only dissociates micelles but also modifies the conformational state of the monomers. At the same time, the persistence of the low-q excess across the full concentration range, although with reduced magnitude and steeper slopes, suggests that large-scale density fluctuations survive the micelle-to-monomer transition.

The dynamical response observed by QENS mirrors this structural evolution. The slow component, which in the micellar state exhibits heterogeneous non-Fickian behavior, progressively transforms with increasing urea. By 4 M the linewidths follow a linear Dq^2 dependence, indicating homogeneous Fickian diffusion consistent with free monomers. At lower urea concentrations, however, the data remain ambiguous: in the 0-1 M range, the measurements cannot distinguish whether the system corresponds to a polydisperse population of shrinking micelles or to a coexistence of micelles and monomers. Both scenarios are compatible with the effective description provided by the Singwi-Sjölander model.

The fast internal contribution provides additional insight. Its characteristic timescale remains essentially unchanged across the full urea range, but the fraction of mobile sites increases and the effective confinement radius expands. These changes are consistent with a relaxation of local constraints as monomers swell in urea, in line with the picture emerging from simulations. Thus, while the internal motions appear robust to crowding and dissociation, their spatial extent is enlarged in the urea-expanded state.

An important limitation of this work is that a direct neutron study of monomeric β-casein in native buffer is not feasible because of the very low CMC of the protein (see

Chapter 4), which is far below the concentrations required for scattering experiments. As a consequence, it is not possible to determine experimentally whether urea preserves or perturbs the native monomeric state. The available evidence, however, points to the latter: simulations consistently report chain expansion in urea, and SANS detects monomer sizes consistent with these swollen conformations. In polymer terms, urea behaves as a good solvent for casein, acting not only as a dissociating agent but also as a denaturant of the disordered monomer.

In summary, the combined SANS and QENS analysis reveals how chemical dissociation bridges the micelle-to-monomer transition in β-casein. Urea disrupts micellar correlations, reduces the effective aggregation number, and drives the system toward expanded monomers whose size matches that predicted by simulations. Dynamically, the anomalous non-Fickian diffusion of assemblies gives way to Fickian motion of free chains, while internal motions retain their intrinsic timescales but explore a larger configurational space. Urea thus provides a practical means to access monomer dynamics of β-casein at concentrations compatible with neutron scattering, but with the important caveat that the monomers observed in this regime are swollen and not identical to those in native solution.

Chapter 9

Conclusions and perspectives

9.1 Summary and conclusions

β-casein is a well-established model system that has been extensively studied for decades from biochemical, biophysical, and technological perspectives. Its amphiphilic character, intrinsic disorder, and ability to form dynamic assemblies have made it a prototype for understanding protein self-assembly and stability. Yet, despite this long-standing interest, neutron-based studies have predominantly targeted its structure which is highly sensitive to pH, temperature, ionic strength, and denaturants. In contrast, systematic investigations of its dynamics in solution remain scarce and were constrained by the accessible dynamic window and q-range. Earlier work typically isolated either structural descriptors or selected internal motions, without the high-resolution, multiscale strategy now enabled by modern instrumentation. In particular, the dynamics within micellar assemblies, i.e., the motion of chains inside these supercrowded interiors, had remained largely unexplored. This thesis fills that gap by combining a comprehensive suite of neutron scattering techniques with complementary light scattering and molecular dynamic simulations to establish an integrated description of β-casein structure and dynamics across a wide range of length and time scales, and under controlled variations of concentration, temperature, and chemical environment. The simultaneous use of SANS, NSE, and NBS provides access to correlations from a few Ångströms to hundreds of nanometers and to motions spanning picoseconds to hundreds of nanoseconds. This multiscale and multimodal approach allows us to connect static structure, collective transport, and internal relaxation within a coherent physical framework.

At the mesoscale, SANS measurements reveal that β-casein forms soft, polydisperse assemblies already at low concentration. With increasing concentration and temperature, the assemblies become progressively more defined: the size distribution narrows, a correlation peak appears, and a clearer core-shell partition emerges, while polydispersity decreases. A pronounced low-q excess persists across conditions, evidencing large-scale inhomogeneities or cluster-like aggregates coexisting with the micelles. These observations point to a structural hierarchy in which compact micellar entities and mesoscale fluctuations can coexist and evolve continuously with concentration and temperature. Dynamic light scattering confirms this picture, resolving fast and slow diffusive modes that track the evolution of micelles and clusters, respectively, and linking structural compaction to a shift in spectral weight between them.

The collective dynamics probed by NSE connects directly to this static landscape. The q-dependent diffusion coefficient $D(q)$ exhibits de Gennes narrowing at the position of the SANS correlation peak, and the product $D(q)S(q)$ increases toward higher q, indicating a non-constant hydrodynamic function. These features are hallmarks of hydrodynamic coupling in crowded, soft colloidal systems and demonstrate that β-casein assemblies display collective dynamics consistent with interacting, deformable particles rather than rigid micelles. The NSE data thus close the loop between static structure and dynamic response, revealing how crowding and compaction modulate both.

Zooming in to microscopic scales, QENS provides unprecedented insight into the motion of protein chains within the assemblies. The slow component of the spectra deviates markedly from the linear q^2 dependence expected for classical Fickian diffusion. This deviation, which is absent in well-folded reference proteins such as BSA, manifests as an apparent Singwi-Sjölander "jump-diffusion" response but arises physically from dynamic heterogeneity within the dense micellar interior. The assemblies represent a supercrowded regime in which chain mobility varies over nanometric domains. Molecular dynamics simulations, processed through the same analysis pipeline, reproduce the same deviation observed experimentally and reveal a continuous yet spatially heterogeneous diffusion landscape. A numerical model incorporating a distribution of locally Fickian diffusion coefficients quantitatively reproduces the observed dependence of the linewidth on q, providing a physical explanation for the apparent non-Fickian response and establishing dynamic heterogeneity as its microscopic origin. At faster timescales, both experiments and simulations converge on a robust internal relaxation mode in the tens-of-picoseconds

range, with characteristic linewidths of ∼20-25 μeV. This relaxation remains essentially unchanged across concentration, aggregation state, and protein fold for the systems studied, pointing to a confined, intrinsic process in protein dynamics. The EISF and linewidth analysis indicate that this relaxation corresponds to localized fluctuations within nanometric confinement, reflecting the interplay of side-chain and backbone motions in the heterogeneous protein matrix.

The final step in this study explores the transition from aggregated to monomeric states using controlled chemical dissociation with urea. SANS reveals a smooth crossover between 1 M and 4 M urea, in which the correlation peak characteristic of micelles fades, the apparent aggregation number approaches unity, and the effective particle size converges to ∼7 nm, consistent with the radius of gyration predicted by atomistic simulations of expanded β-casein monomers in urea. Dynamically, the non-Fickian response characteristic of assemblies progressively evolves into homogeneous Fickian diffusion as monomers dominate, while the fast internal relaxation remains at comparable timescales but broadens spatially. This indicates that urea not only dissociates micelles but also expands and softens the monomeric chains, acting both as a dissociating agent and as a denaturant for the disordered protein. These results demonstrate that chemical perturbation provides a tunable route to traverse the full dynamic range from supercrowded assemblies to free, swollen monomers.

Taken together, this work establishes β-casein as a versatile model for intrinsically disordered proteins, bridging static and dynamic descriptions across scales. The integration of SANS, NSE, and NBS with complementary techniques has enabled a level of temporal and spatial resolution not previously achieved in systematic studies of this protein. Four conclusions emerge from this work:

1. **Structure and dynamics are inseparably linked in disordered assemblies.** The multiscale neutron experiments reveal that the static organization of β-casein, from soft micelles to large-scale inhomogeneities, directly determines its collective dynamics. Hydrodynamic coupling and de Gennes narrowing show that mesoscale relaxation is governed by the same correlations that define the structure, demonstrating that disordered assemblies behave as dynamically coherent, many-body systems rather than collections of independent particles.

2. **Dynamic heterogeneity is the microscopic origin of apparent anomalous diffusion.** Deviations from Fickian behavior in the global dynamics do not require invoking discrete jumps or structural discontinuities. Instead, they arise naturally from spatial variations in local mobility within the supercrowded micellar interior. By combining QENS, molecular simulations, and a heterogeneous-diffusivity model, this thesis identifies dynamic heterogeneity as the key physical mechanism underlying the deviation from Fickain diffusion.

3. **A confined fast relaxation constitutes a fundamental dynamical element of proteins.** Across concentrations, aggregation states, and protein folds, a robust tens-of-picoseconds relaxation persists with nearly constant linewidths. This resilience indicates that the fast component reflects an intrinsic confined process in protein dynamics-one that coexists with large-scale heterogeneity and provides a universal baseline of molecular flexibility.

4. **Chemical perturbation provides a tunable bridge between collective and monomeric regimes.** Controlled dissociation with urea links the non-Fickian dynamics of assemblies to the homogeneous diffusion of free monomers while revealing how denaturation expands local configurational space. This chemical pathway clarifies how external perturbations reshape both global transport and internal relaxation, offering a continuum between crowding, swelling, and disorder.

In sum, this work delivers a multiscale framework that connects neutron observables to microscopic motion in a disordered, self-assembling protein, clarifying how crowding, heterogeneity, and confinement co-produce hierarchical dynamics and opening avenues for broader applications to intrinsically disordered proteins and soft condensed matter.

9.2 Perspectives

The results presented in this thesis open several directions for future work, all aimed at extending the present multiscale framework toward more complex and biologically relevant conditions. Importantly, most of the perspectives outlined in the following are not merely conceptual proposals: the corresponding neutron experiments have already been carried out, but their detailed analysis and interpretation lie beyond the scope of this thesis. These datasets provide a natural continuation of this work and will enable a

deeper understanding of how disorder, crowding, and environmental perturbations govern the dynamics of β-casein and related intrinsically disordered proteins.

External crowding and cellular mimetics

While this thesis has focused on self-crowding arising from β-casein assemblies, preliminary experiments performed in the presence of deuterated cellular lysate as crowding agent reveal that external crowding can modify both structure and dynamics in subtle but measurable ways. Comparing self-crowded and externally crowded conditions will clarify whether the observed dynamic heterogeneity is an intrinsic feature of β-casein assemblies or a more general manifestation of disordered chains in dense environments. A systematic analysis of these measurements will provide a critical step toward bridging the gap between simplified *in vitro* models and realistic intracellular conditions.

Ionic effects and electrostatic modulation

A second line of investigation concerns the influence of ionic strength and multivalent cations such as Ca^{2+}. Preliminary QENS data in $CaCl_2$ suggest that charge screening and ion-mediated crosslinking profoundly affect β-casein aggregation, possibly stabilizing more compact or transiently cross-linked assemblies. Quantifying how the non-Fickian response evolves with increasing salt concentration will clarify whether dynamic heterogeneity originates primarily from steric crowding or also from electrostatic correlations. Complementary SANS measurements will further establish whether ionic crosslinking leads to structural anisotropy or to cluster formation.

Thermal response and reversibility

Exploring the temperature dependence of β-casein assemblies at elevated temperatures will address whether intrinsically disordered proteins exhibit transitions analogous to unfolding in well-folded systems. Preliminary neutron data indicate that heating alters both the structural organization and the dynamic hierarchy of β-casein aggregates, with partial recovery upon cooling. Determining whether these changes correspond to reversible compaction, irreversible aggregation, or enhanced chain fluctuations will provide valuable insight into the energetic landscape of disordered assemblies and their thermal stability.

Dynamics across the aggregation threshold

Elastic and inelastic fixed-window scans (EFWS/IFWS) performed as a function of concentration provide a complementary route to explore the onset of aggregation at much lower concentrations, down to ∼0.25 mg/mL, well below the critical micelle concentration. These measurements will allow us to monitor how dynamical signatures evolve as the system transitions from monomeric chains to incipient aggregates, linking microscopic mobility to the earliest stages of self-association. The combination of fixed-window scans and QENS thus offers a unique view of aggregation dynamics in regimes previously inaccessible to neutron spectroscopy.

Pressure effects and non-denaturing dissociation

A final avenue concerns the role of hydrostatic pressure as a means of modulating protein association. Preliminary SANS and NBS experiments under pressure suggest that compression may act as a non-denaturing dissociating agent, perturbing micellar organization while preserving native chain conformations. Comparing these results with the urea-induced dissociation studied in this thesis will help disentangle the structural and dynamic consequences of chemical versus physical perturbations, and may provide access to the dynamics of free monomers in near-native conditions.

Together, these perspectives represent the natural continuation of this work, extending its scope to external crowding, electrostatic modulation, thermal activation, aggregation onset, and pressure-induced dissociation. Their systematic analysis will not only test the generality of the central concepts established here: supercrowding, dynamic heterogeneity, and confined relaxation, but also move toward a more complete and realistic description of intrinsically disordered proteins under conditions approaching the cellular environment.

Résumé détaillé

Les protéines intrinsèquement désordonnées (IDPs) remettent en question le paradigme classique reliant structure et fonction. Dépourvues d'un repliement tridimensionnel stable, elles conservent une activité biologique remarquable grâce à leur flexibilité conformationnelle, leur aptitude à l'auto-assemblage et leur grande sensibilité aux conditions environnementales. Ces propriétés rendent leur étude particulièrement difficile : comprendre comment le désordre structurel et l'environnement gouvernent leur organisation et leur dynamique nécessite des outils expérimentaux capables de sonder simultanément plusieurs échelles de temps et d'espace.

Dans ce cadre, cette thèse emploie la β-caséine comme protéine modèle afin d'explorer, au moyen de techniques de diffusion de neutrons à haute résolution, la relation entre désordre, auto-organisation et dynamique moléculaire. Amphiphile et hautement soluble, la β-caséine forme spontanément des assemblages micellaires souples dont les propriétés dépendent fortement du pH, de la température, de la force ionique et de la présence de dénaturants tels que l'urée. Si sa structure statique a été largement étudiée, les études neutroniques de sa dynamique en solution restent limitées en résolution énergétique et en domaine de vecteur d'onde (q-range). L'objectif de ce travail est donc d'établir une description intégrée, reliant structure et dynamique sur un large spectre d'échelles et de conditions expérimentales.

Chapitre 2. Théorie de la diffusion des neutrons et dynamique dans la matière condensée.

Ce chapitre présente les concepts fondamentaux nécessaires à l'interprétation des expériences. Les principes de la diffusion cohérente et incohérente, la définition du facteur de structure dynamique $S(q, \omega)$ et les modèles de diffusion brownienne, fickienne et anormale y sont

introduits. Les bases physiques des trois techniques neutroniques utilisées dans la thèse : la spectroscopie de rétrodiffusion des neutrons (NBS), la spectroscopie à écho de spin (NSE) et la diffusion aux petits angles (SANS), sont décrites, ainsi que les échelles de temps et d'espace qu'elles explorent. Ce cadre théorique relie directement les observables neutroniques aux mouvements microscopiques des protéines.

Chapitre 3. Contexte biophysique : la β-caséine comme protéine désordonnée modèle.

Ce chapitre présente les propriétés biochimiques et biophysiques de la β-caséine, protéine amphiphile dont la partie C-terminale hydrophobe favorise la formation d'assemblages micellaires stables mais dynamiques. Après un état de l'art des études spectroscopiques et de diffusion, le chapitre souligne que si la structure de ces micelles a été largement caractérisée, leur dynamique interne reste mal comprise. Cette lacune justifie une approche systématique, combinant plusieurs techniques neutroniques à haute résolution pour relier organisation supramoléculaire et fluctuations moléculaires.

Chapitre 4. Matériaux et méthodes expérimentales.

Ce chapitre décrit la préparation des échantillons de β-caséine, les conditions de solvant, de température et de concentration, ainsi que les dispositifs expérimentaux employés sur les lignes de neutrons IN16B (spectroscopie de rétrodiffusion), IN15 (écho de spin) et D33 (diffusion aux petits angles) de l'Institut Laue-Langevin. Les procédures d'analyse des données SANS, NSE et NBS sont détaillées, ainsi que les mesures complémentaires de diffusion de la lumière (DLS) et les simulations de dynamique moléculaire utilisées pour interpréter les résultats.

Chapitre 5. Organisation structurale et dynamique collective des assemblages de β-caséine.

Les mesures SANS révèlent que la β-caséine forme des agrégats souples et polydisperses dès de faibles concentrations. Avec l'augmentation de la concentration et de la

température, les assemblages deviennent plus compacts, un pic de corrélation apparaît et la distribution de tailles se resserre. Un excès marqué à bas q indique la coexistence de fluctuations de densité à grande échelle et de micelles plus définies. Les expériences de DLS montrent deux modes de diffusion : un mode rapide associé aux micelles et un mode lent lié aux structures de plus grande taille. Les mesures NSE mettent en évidence un *narrowing* de De Gennes au niveau du pic de corrélation, indiquant un couplage hydrodynamique entre structure et dynamique. Ce chapitre établit ainsi la corrélation directe entre organisation statique et relaxation collective.

Chapitre 6. Diffusion non-fickienne apparente dans les assemblages de β-caséine.

Les mesures NBS montrent que la composante lente du spectre quasi-élastique (QENS) s'écarte nettement du comportement fickien classique attendu pour des particules diffusantes indépendantes. Cette déviation, absente pour la protéine bien repliée BSA utilisée comme référence, traduit une hétérogénéité dynamique au sein des micelles surpeuplées (« supercrowded »). Les simulations de dynamique moléculaire, analysées selon le même formalisme QENS, reproduisent cette anomalie et confirment que la diffusion est spatialement hétérogène. Un modèle numérique basé sur une distribution de coefficients de diffusion locaux rend compte quantitativement de la dépendance en q observée, établissant ainsi l'hétérogénéité dynamique comme origine microscopique de la diffusion non-fickienne apparente.

Chapitre 7. Dynamiques internes confinées et relaxation rapide.

Ce chapitre examine la composante rapide des spectres obtenus par NBS, associée aux mouvements internes localisés des protéines. L'analyse quasi-élastique (QENS) de cette composante, appuyée par les simulations, révèle un mode de relaxation robuste d'environ 25 picosecondes (20-25 µeV), présent quel que soit l'état de repliement, la concentration ou l'agrégation. Cette relaxation confinée semble constituer un élément fondamental de

la dynamique protéique, reflétant la flexibilité intrinsèque du squelette et des chaînes latérales dans un environnement hétérogène.

Chapitre 8. Effet de la dissociation chimique : transition micellaire-monomérique.

L'ajout d'urée permet de suivre la transition entre l'état agrégé et l'état monomérique de la β-caséine. Les mesures SANS montrent une disparition progressive du pic de corrélation entre 1 M et 4 M d'urée, tandis que la taille apparente des particules converge vers ∼7 nm, valeur cohérente avec le rayon de giration prédit pour les chaînes monomériques étendues. Les mesures NBS montrent que la diffusion globale passe d'un régime non-fickien hétérogène à une diffusion homogène de type monomérique, alors que la composante rapide conserve sa constante de temps mais explore un volume local plus large. L'urée agit donc à la fois comme agent de dissociation et comme dénaturant, permettant d'accéder à la dynamique de monomères « gonflés » à des concentrations compatibles avec les techniques neutroniques.

Chapitre 9. Conclusions et perspectives.

Les résultats obtenus établissent la β-caséine comme un système modèle polyvalent pour l'étude des protéines désordonnées. Ils démontrent (i) la corrélation intime entre structure et dynamique dans les assemblages désordonnés, (ii) le rôle fondamental de l'hétérogénéité dynamique comme origine microscopique de la diffusion anormale, (iii) l'existence d'un mode de relaxation interne confiné et robuste, et (iv) la possibilité de relier de façon continue les régimes collectifs et monomériques par perturbation chimique.
Les perspectives ouvertes par ce travail concernent l'analyse en cours d'expériences déjà réalisées : l'effet du crowding externe à l'aide de lysats cellulaires, l'influence des ions multivalents (Ca^{2+}) sur la structuration et la dynamique, la réponse thermique et la réversibilité des assemblages, l'étude de l'agrégation à très faibles concentrations, et enfin l'impact de la pression comme agent de dissociation non dénaturant. L'exploitation de ces ensembles de données prolongera le cadre multi-échelles établi ici et contribuera à une compréhension plus complète du comportement des protéines désordonnées dans des environnements proches de ceux du vivant.

Appendix A
Molecular dynamics simulation details

All-atom molecular dynamics (MD) simulations were performed at $T = 280$ K in explicit solvent using the GROMACS 2023 simulation package [122]. Interatomic interactions were described by the AMBER99SB-ILDN force field in combination with the TIP4P-D water model.

The system containing $N = 5$ β-casein chains was initiated from an aggregated conformation within a cubic simulation box of side length $L_{\mathrm{box}} \approx 18.6$ nm, obtained from a preliminary run at $T = 295$ K. The configuration was cooled to the target temperature of 280 K through simulated annealing over 1.4 ns, followed by a 500 ns production run in the NPT ensemble. To minimize artifacts from box-length fluctuations on dynamical observables, the results discussed in the main text correspond to a subsequent 500 ns trajectory in the NVT ensemble.

Initial configurations for systems with fewer chains ($N < 5$) were generated by selectively removing proteins from the $N = 5$ aggregate. Each system was placed in a cubic box with at least 2.5 nm clearance between the solute and the box walls, solvated with water, and neutralized by adding 8 Na^+ ions per protein molecule. After energy minimization, short NVT and NPT equilibration runs were carried out to stabilize the systems. NPT equilibration times were at least 150, 200, 300, and 400 ns for $N = 1$, 2, 3, and 4, respectively. Dynamic observables were subsequently extracted from NVT trajectories.

All bond lengths were constrained using the LINCS algorithm. The equations of motion were integrated with the Verlet leapfrog scheme and a time step of 2 fs. A cutoff of 1.2 nm was applied for short-range electrostatic and Lennard–Jones interactions, while

long-range electrostatics were treated using the particle–mesh Ewald (PME) method with fourth-order interpolation and a grid spacing of 0.16 nm. Solute and solvent were coupled separately to a velocity-rescaling thermostat at $T = 280$ K with a relaxation time of 0.1 ps. In NPT simulations, the pressure was maintained at 1 bar using the Parrinello–Rahman barostat with a relaxation time of 2 ps and an isothermal compressibility of 4.5×10^{-5} bar^{-1}. Pressure coupling was disabled during the NVT production runs. Trajectory processing and basic analyses were performed using built-in *gmx* modules in GROMACS. The BATS spectra were generated with the MDANSE software [123]. Visualization of the simulation snapshots was carried out with VMD [117], and custom Python scripts were used for data parsing, post-processing, and figure generation.

Appendix B
List of experiments at large-scale facilities

This appendix compiles all experiments at large-scale facilities in which the author participated during the PhD period. For clarity, the list is split into two parts: (**I**) experiments directly related to this thesis (including those reported in the manuscript and additional measurements), and (**II**) other experiments not directly connected to this thesis (group projects and follow-ups to earlier work). Entries within each part are ordered from oldest to most recent and include facility, instrument, proposal/experiment number, dates, DOI, and the author's role.

Part I: Experiments related to this thesis

1. Casein as a model intrinsically disordered protein: Impact of salt on the internal diffusive dynamics in solution

Facility ILL

Instrument IN16B

Exp./Prop. No. 9-13-1046

Dates 08 Apr – 12 Apr 2023

DOI 10.5291/ILL-DATA.9-13-1046

Role Co-proposer; experimenter

---

2. Structural and Diffusive Properties of Intrinsically Disordered Proteins in a Polydisperse Environment

Facility ILL

Instrument IN16B, D33

Exp./Prop. No. 8-04-953

Dates 26 May – 01 Jun and 08 Sept – 10 Sept 2023

DOI 10.5291/ILL-DATA.8-04-953

Role Main proposer; experimenter

---

3. Internal diffusive dynamics in solution on the ns-nm-scale of polymers during thermal and chemical induced network formation

Facility ILL

Instrument In16B

Exp./Prop. No. 9-13-1077

Dates 01 Jul – 03 Jul 2023

DOI 10.5291/ILL-DATA.9-13-1077

Role Main proposer; experimenter

---

4. Systematic investigation of the diffusive properties of macromolecules in bovine milk

Facility ILL

Instrument IN16B

Exp./Prop. No. INTER-588

Dates 25 Aug – 28 Aug 2023

DOI 10.5291/ILL-DATA.INTER-588

Role co-proposer; experimenter

---

5. Accessing the short-time diffusive properties of dilute protein solutions

Facility ILL

Instrument IN16B

Exp./Prop. No. 1-20-76

Dates 29 Sept – 01 Oct 2023

DOI 10.5291/ILL-DATA.1-20-76

Role Co-proposer; experimenter

---

6. Casein micelle formation as result of liquid-liquid phase separation in an intrinsically disordered protein solution

Facility ILL

Instrument IN15, WASP

Exp./Prop. No. 9-13-1076

Dates 31)Ct – 02 Nov and 03 Nov – 06 Nov 2023

DOI 10.5291/ILL-DATA.9-13-1076

Role Main proposer; experimenter

---

7. Pressure-induced changes of β-Casein micelle properties

Facility ILL

Instrument SAM,IN16B

Exp./Prop. No. 9-13-1152

Dates 30 Jun – 06 Jul 2025

DOI 10.5291/ILL-DATA.9-13-1152

Role Main proposer; experimenter

Part II: Other experiments (not directly related to this thesis)

1. Influence of antibody type, temperature and additives on the viscosity of monoclonal anti- body solutions

Facility ESRF

Instrument ID-02

Exp./Prop. No. MD-1368

Dates 02 Dec – 05 Dec 2022

DOI 10.15151/ESRF-ES-970991476

Role Experimenter

---

2. Tuning mechanical properties of spread polypeptide/surfactant films by specific interactions. Relationship with their structure and dynamics

Facility ILL

Instrument FIGARO

Exp./Prop. No. 9-12-668,726

Dates 02 Jul – 05 Jul 2023 and 17 May – 19 May 2024

DOI 10.5291/ILL-DATA.9-12-668

Role Experimenter

---

3. Structure and dynamics approaching the arrested states for different monoclonal antibodies with PEG

Facility ILL

Instrument IN16B, IN15

Exp./Prop. No. 8-04-936,951

Dates 7 Sept – 13 Sept 2023, 15 Sept – 18 Sept 2023

DOI 10.5291/ILL-DATA.8-04-936

Role Experimenter

---

4. Role of a non-ionic surfactant in the adsorption of different therapeutically relevant monoclonal antibodies on siliconized surfaces

Facility ILL

Instrument FIGARO

Exp./Prop. No. 8-04-978

Dates 14 Mar – 16 Mar 2024

DOI 10.5291/ILL-DATA.8-04-978

Role Co-proposer; experimenter

---

5. Diffusive and structural properties of BLG during fibril formation

Facility ILL

Instrument IN16B, SANS

Exp./Prop. No. 8-04-987

Dates 28 Jun – 02 Jul 2024

DOI 10.5291/ILL-DATA.8-04-978

Role Co-proposer; experimenter

Appendix C
Comparison of standard and 3D cross-correlation DLS

To exclude the possibility of multiple scattering, complementary measurements were performed using 3D cross-correlation DLS (3D DLS), which is designed to suppress the contribution of multiply scattered light. For comparison, standard DLS (2D DLS) measurements were carried out under the same conditions. In standard DLS, a single detector records the scattered intensity fluctuations, which can be affected by multiple scattering events. In contrast, 3D DLS employs two simultaneous scattering experiments at the same scattering vector and sample volume. By cross-correlating the signals from both detectors, the single-scattering contribution is reinforced while the multiple-scattering contributions are effectively suppressed. A known limitation is the reduced correlation intercept due to cross-talk between the beams; this can be mitigated by temporal modulation of the laser sources, at the cost of limiting the accessible short-time dynamics.

Figure C.1 shows intensity auto-correlation functions $g^{(2)}(\tau)$ for the most concentrated sample studied (β-casein, 100 mg/mL) across scattering angles from 40° to 140°. This concentration was selected because it is the most susceptible to multiple scattering and thus represents the worst-case scenario. In both cases, the correlation functions were normalized to facilitate comparison. The results obtained for all other concentrations were essentially indistinguishable.

The only noticeable difference appears at very short correlation times, where no data are available from the 3D setup due to instrumental time-resolution limits.

Taking this into account, Figure C.2 compares the fitting parameters extracted from both techniques using Eq. 5.3. The close agreement between the two sets of parameters

confirms that multiple scattering does not contribute significantly, even at the highest concentration studied.

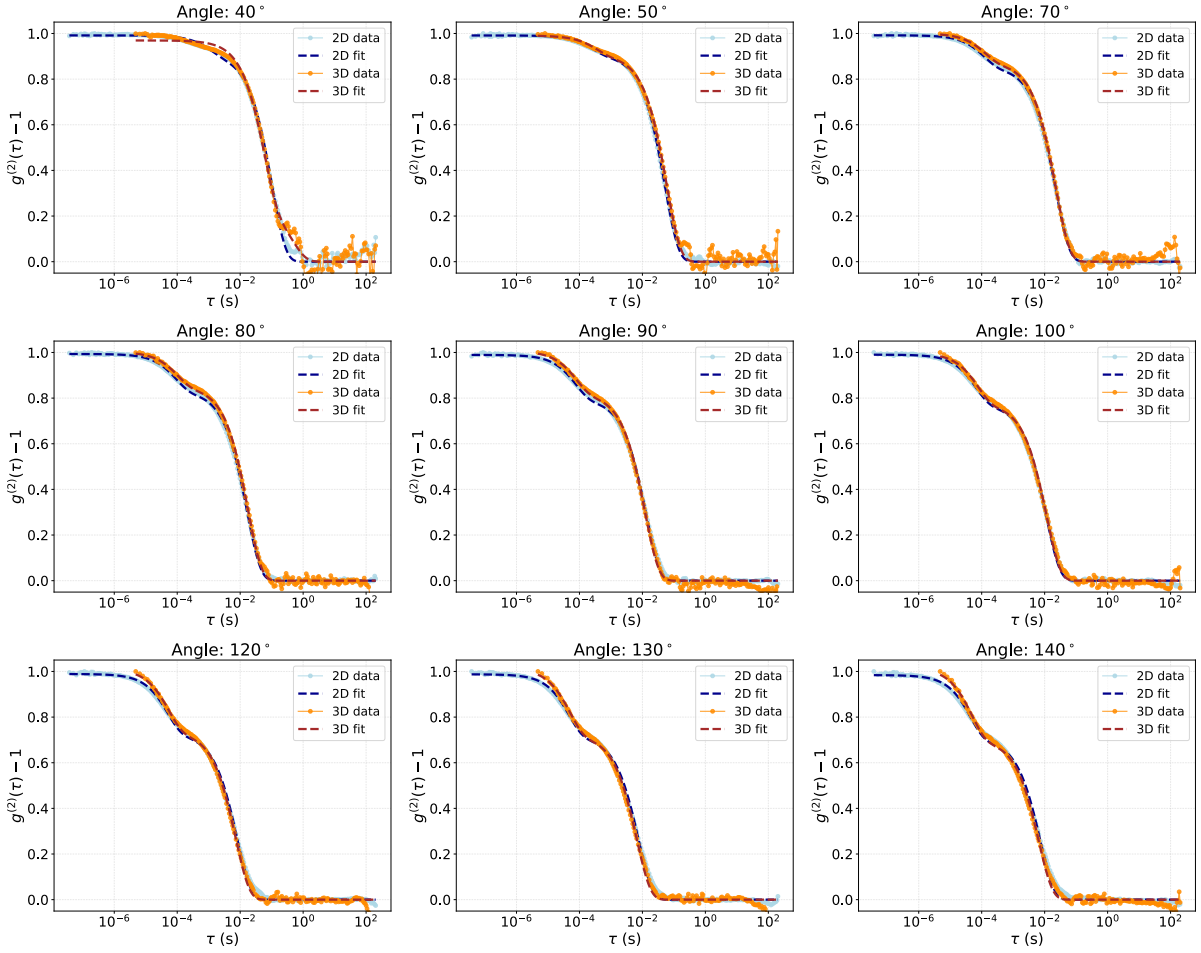

Figure C.1. Normalized intensity auto-correlation functions for β-casein at 100 mg/mL across scattering angles from 40° to 140°, measured using standard DLS (blue) and 3D cross-correlation DLS (red).

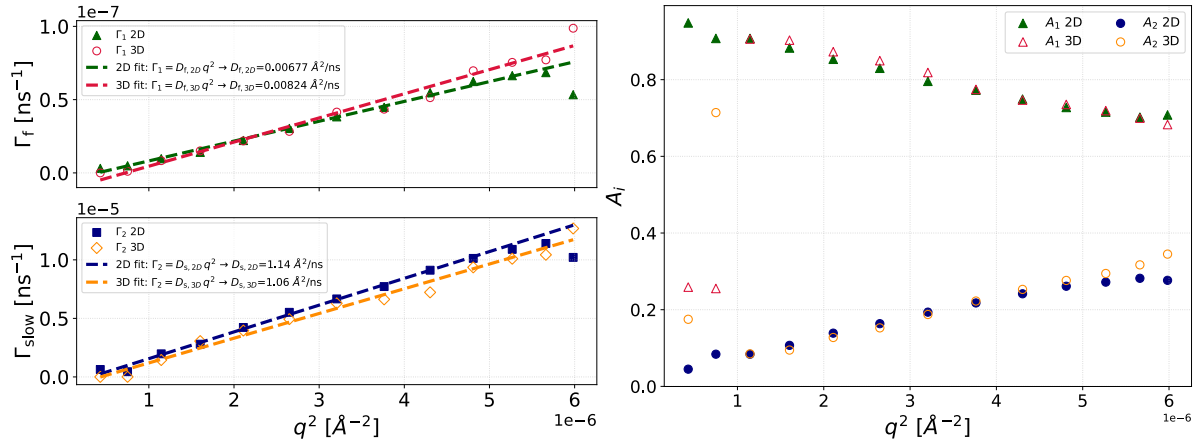

Figure C.2. Fit parameters for β-casein at 100 mg/mL obtained using standard DLS and 3D cross-correlation DLS. **Left**: Amplitudes A_1 and A_2. **Right**: Relaxation rates Γ_1 and Γ_2, fitted to the relation $\Gamma_i = 2D_i q^2$ to extract the diffusion coefficients D_i shown in the figure.

Appendix D
Single- vs. double-exponential fitting of DLS correlation functions

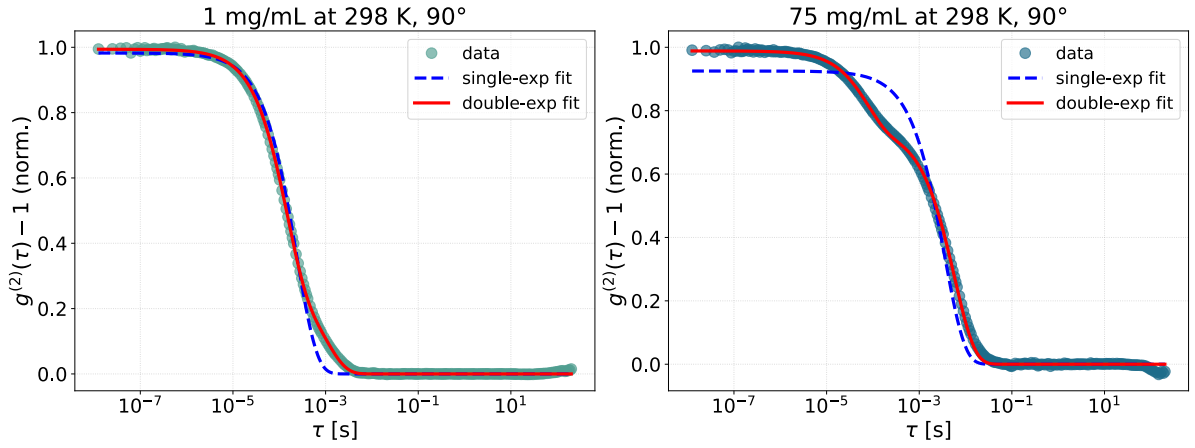

Figure D.1. Representative intensity correlation functions $g^{(2)}(\tau)$ for dilute (left) and concentrated (right) samples, with single- and double-exponential fits.

Figure D.1 shows representative intensity correlation functions $g^{(2)}(\tau)$ for two limiting concentrations: the left panel corresponds to a dilute sample (1 mg/mL), while the right panel corresponds to a concentrated sample (75 mg/mL). In both cases, the experimental data are fitted with both a single-exponential model and the double-exponential expression introduced in the main text (Eq. 5.3).

The single-exponential model is given by

$$g^{(2)}(\tau) - 1 = A \exp(-2\Gamma\tau), \tag{D.1}$$

while the double-exponential model is described by

$$g^{(2)}(\tau) - 1 = A_1 \exp(-2\Gamma_{\text{fast}}\tau) + A_2 \exp(-2\Gamma_{\text{slow}}\tau). \tag{D.2}$$

For the dilute sample (left, 1 mg/mL), the slow decay is less evident, and the single-exponential fit already provides a reasonable description of the initial relaxation. However, it systematically fails to reproduce the final part of the decay, which is captured more accurately by the double-exponential model. For the concentrated sample (right, 75 mg/mL), both relaxation steps are clearly resolved, and the double-exponential fit describes the data significantly better than the single-exponential one.

These examples illustrate that, although the improvement may appear less dramatic at low concentrations, two exponential terms are consistently required to properly describe the correlation functions across the entire concentration series.

Appendix E
Concentration and temperature dependencies of $S(q)$, $D(q)$, and $D(q)S(q)$

Figure E.1 summarizes the concentration and temperature dependencies of the structure factor, $S(q)$, the apparent diffusion coefficiento from NSE, $D(q)$ and the product $S(q)D(q)$. Overall trends are modest and do not alter the q-shape: increasing concentration from 75 to 100 mg/mL yields an almost uniform downward shift of $D(q)$ across q, while heating primarily rescales the overall rate. The minimum in $D(q)$ is less pronounced at 100 mg/mL, whereas $D(q)S(q)$ preserves its near-linear increase with q, consistent with de Gennes narrowing and a non-constant hydrodynamic response.

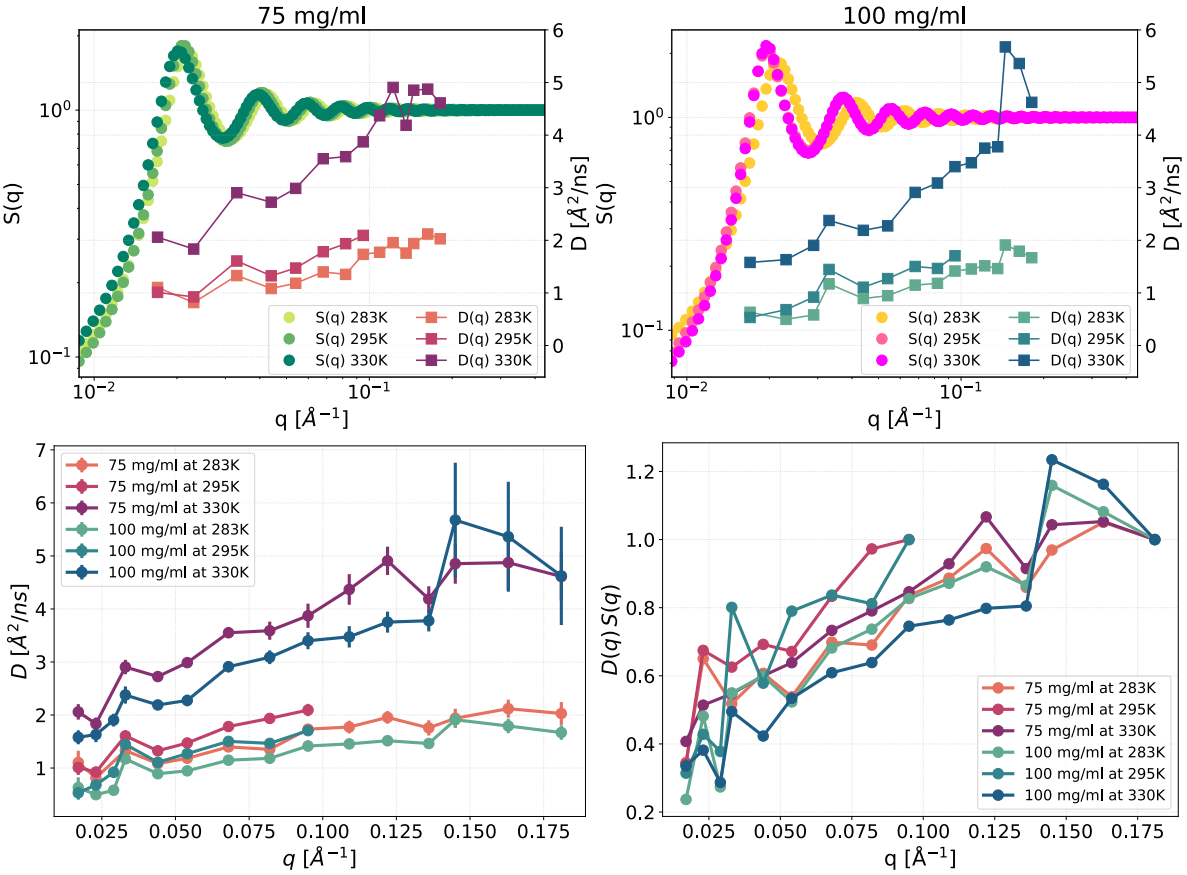

Figure E.1. **Top left**: $S(q)$ and $D(q)$ for 75 mg/mL; **top right**: the same for 100 mg/mL. **Bottom left**: $D(q)$ for both concentrations; **bottom right**: $D(q)S(q)$ for both concentrations. All panels show results at 283, 295, and 330 K.

Appendix F
Two-component fits with global Fickian diffusion contributions

To test whether separate populations of monomers (m) and micelles (a) could be distinguished, we attempted a two-component fit including two global translational contributions, both constrained to follow Fickian behavior ($\gamma = Dq^2$), together with a single internal relaxation common to both species.

These fits were carried out globally in order to reduce the number of free parameters and impose physically motivated constraints. A purely per-q analysis with three independent Lorentzian contributions leads to an excessive number of free parameters, resulting in unstable fits. In addition, two of the extracted linewidths do not display a clear q-dependence, which makes their physical interpretation highly ambiguous. By contrast, the global model forces both translational contributions to follow a Fickian q^2-dependence and assumes a common internal relaxation, thereby providing a more constrained framework. In this model, the dynamic structure factor is expressed as

$$S(q,\omega) = \mathcal{R} \otimes \Big\{ \beta(q) S_{\text{sample}}(q,\omega) + \beta_{D_2O}(q) \mathcal{L}(\gamma_{D_2O}(q),\omega) + \mathcal{D}_{Dirac}(q) \Big\} + B, \tag{F.1}$$

with the sample contribution

$$S_{\text{sample}}(q,\omega) = \Big[\phi_a \mathcal{L}(\gamma_a(q),\omega) + (1-\phi_a) \mathcal{L}(\gamma_m(q),\omega) \Big] \otimes \Big[A_0(q)\delta(\omega) + (1-A_0(q)) \mathcal{L}(\Gamma(q),\omega) \Big]. \tag{F.2}$$

The explicit form reads

$$\begin{aligned} S(q,\omega) =& \mathcal{R} \otimes \Big\{ \beta(q) \Big[\phi_a(q) A_0(q) \mathcal{L}(D_a q^2, \omega) + (1-\phi_a(q)) A_0(q) \mathcal{L}(D_m q^2, \omega) \Big] \\ &+ \phi_a(q)(1-A_0(q)) \mathcal{L}(D_a q^2 + \Gamma(q), \omega) + (1-\phi_a(q))(1-A_0(q)) \mathcal{L}(D_m q^2 + \Gamma(q), \omega) \\ &+ \beta_{D_2O}(q) \mathcal{L}(\gamma_{D_2O}(q), \omega) + \mathcal{D}_{Dirac}(q) \Big\} + B. \end{aligned} \tag{D.3}$$

Fitting parameters

Global: $\phi_a(q)$ (micelle volume fraction), D_a (micelle diffusion coefficient), D_m (monomer diffusion coefficient).
Per-q: $\beta(q)$, $A_0(q)$ (EISF), $\Gamma(q)$.
Fixed: $\beta_{D_2O}(q) = \phi_{\text{solvent}} A_{D_2O}(q)$, $\gamma_{D_2O}(q)$, $\mathcal{D}_{Dirac}(q)$, $\langle B \rangle$.

The internal relaxation rate $\Gamma(q)$ was parametrized as

$$\Gamma(q) = \frac{D_{int} q^2}{1 + D_{int} \tau q^2}, \tag{D.4}$$

with D_{int} the internal diffusion coefficient and τ the residence time.

$\phi_a(q)$	D_a (Å^2/ns)	D_m (Å^2/ns)	D_{int} (Å^2/ns)	τ (ns)	$\langle B \rangle$
0.952	1.71	8354	59.2	0.017	2.95×10^{-5}

Table F.1. Representative results from the two-component global fit.

Despite the additional constraints, the extracted parameters remain not physically meaningful: the fitted monomer diffusion coefficients are unrealistically large, while the micelle volume fraction approaches unity, implying that essentially only one dynamic process is present. This confirms that the system dynamics are better described by a single effective translational contribution rather than separate monomer and micelle populations.

Appendix G
Alternative reconstruction of $P(D)$ by direct averaging of synthetic distributions

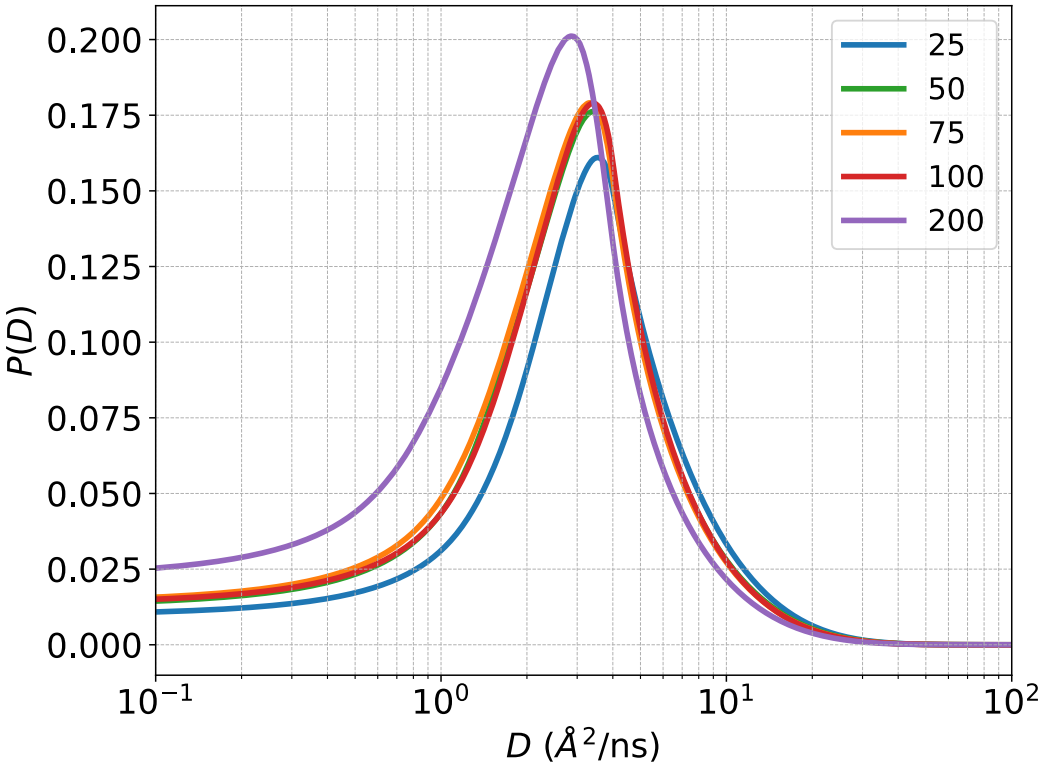

Figure G.1. Reconstructed diffusion coefficient distributions $P(D)$ obtained by directly averaging the synthetic curves selected within the experimental confidence regions.

As an alternative to the parametric reconstruction of $P(D)$ described in the main text, we also performed a direct averaging of the synthetic distributions. For each experimental data point, all synthetic $P(D)$ curves corresponding to diffusion coefficients D and residence times τ within the experimental confidence intervals were selected and averaged pointwise.

Figure G.1 shows representative results of this approach. The directly averaged distributions yield mean, standard deviation, and peak positions that are in close agreement with those obtained from the parametric method. This confirms that both approaches capture the same essential features of the underlying distribution, while the parametric representation has the advantage of offering a compact and interpretable form for comparison across experimental conditions.

Appendix H
Radius of gyration distributions of β-casein in water and urea

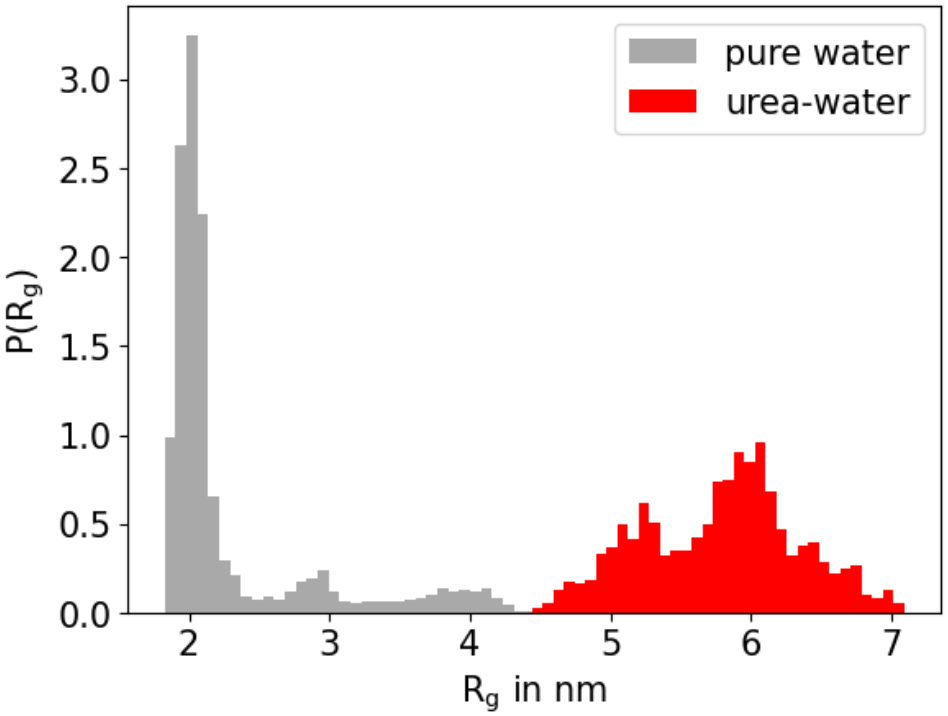

Figure H.1. Probability distribution $P(R_g)$ for a single β-casein chain from MD simulations in pure water (gray) and in 8 M urea (red). In water, the distribution peaks at $R_g \approx 2$ nm and vanishes above 4 nm, whereas in urea the chain expands, with a maximum near $R_g \approx 6$ nm and a range up to ~ 7 nm. Figure from [121]

Figure H.1 displays the probability distribution of the radius of gyration (R_g) obtained from molecular dynamics simulations of single β-casein chains in pure H_2O and in 6 M

urea. The distributions clearly show that the chain adopts a relatively compact conformation in water, with a pronounced maximum around $R_g \approx 2$ nm and an upper limit near 4 nm. In contrast, in urea the conformational ensemble shifts toward significantly larger sizes, spanning roughly 4.5–7 nm, with the most probable value near $R_g \approx 6$ nm. These results support the interpretation that urea not only disrupts casein micelles but also induces an expansion of the disordered monomeric chains.

Acknowledgements

When I was finishing my degree, I was quite sure that I did not want to continue in science. Everything changed during my first stay in Grenoble. Working in such an inspiring place as the ILL, surrounded by outstanding science, kind and interesting people, and living in a city I fell in love with from the very first day, made me decide to pursue a PhD.

First and foremost, my deepest gratitude goes to my main supervisor, Tilo. Without you, none of this would have been possible. Thank you for trusting me from day one, for your dedication, patience, and constant support. Thank you for always being present and helping me through every problem—even when it meant spending hours staring at Python code. Thank you for giving me the freedom to propose and develop my own ideas, and for trusting my judgment in so many decisions. I have learned an incredible amount from you.

I would also like to thank Jean-Louis for the many meetings in which you guided me through models, for always asking the right questions, and for the tremendous effort you put into reading and commenting on this thesis.

Among my supervisors, I also want to thank Frank. Even if not officially my supervisor, you always found the time and energy to guide me whenever I needed it. Thank you for believing in me and in "my talent," even when I could not see it myself. I also appreciate that you included me in the activities of the Tübingen group, like Oberjoch, and to everyone in the group for making me feel like one of them. In the end, that "venceremos" truly became a "vencimos."

I am also deeply grateful to the entire IDPXN collaboration.

Saikat, thank you for the enormous effort you put into the simulations. It has truly been a pleasure to work side by side with you over these past three years, trying to bridge experiments and simulations. I have learned a lot from our discussions, our shared frustrations, and our victories.

Tatiana, thank you for always listening so carefully. You always seemed to have the right words at the right time, and talking to you gave me confidence when I needed it most.
Anna, we have worked closely together throughout a large part of my PhD, and your help and perspective have truly been invaluable. A significant part of this success is thanks to you. You were there for every experiment and every trip, sharing both the hard work and the excitement along the way. You have not only been a wonderful colleague, but also a dear friend.
Maja, thank you for putting so much passion into everything you do. Thank you as well for letting me be part of your bachelor's thesis project and for giving me the chance to introduce you to the "magnificent" DLS.
Ilaria, thank you for your constant support, both professionally and personally. You have always been there for me, and you have been one of my greatest sources of strength during the difficult moments. You have always understood me, reassured me, and helped me find perspective when I needed it most. In many ways, you have been like a big sister in science to me, and I deeply admire you. Above all, you are a very dear friend. I feel incredibly lucky to have someone like you in my life.
Christian, I have learned so much from you throughout these years. Thank you especially for being present at each and every experiment, for your ideas, and for your remarkable ability to solve complicated problems during the beamtimes.
Felix, thank you for your insightful suggestions and advice, for being such a great source of knowledge, and for welcoming us to Lund when all the DLS instruments in Grenoble were out of service. Your support meant a lot to me.
I would also like to thank Lund University for giving us that opportunity, and all the professors and technicians who helped us during our stay.
Additionally, I am grateful to all the institutions that supported this work, including the Institut Laue-Langevin, Université Grenoble Alpes, and the Institute for Applied Physics of the University of Tübingen, as well as to the Deutsche Forschungsgemeinschaft (DFG) and the Agence Nationale de la Recherche (ANR) for their financial support through the German-French collaborative grant IDPXN (ANR-21-CE06-0047 / DFG SCHR700/42-1).
I am also deeply grateful to all the people at the Institut Laue-Langevin who have been essential for the development of my thesis, through their help in experiments, discussions, or simply by creating such a welcoming and inspiring work environment. Special thanks to Olga Matsarskaia, Ingo Hoffmann, Nicolas Martin, Lorenzo Metilli, Sylvain Prevost,

Martin Boehm, Laurence Tellier, Jérôme Rimet, Bela Farago, Martina Sandroni, Leonardo Chiappisi, Sandrine Verdon, and all the technicians for their support and patience. I would also like to acknowledge the cleaning staff and the cafeteria team, whose kindness and friendliness make every day at the ILL more enjoyable, and to Christine Andant, whose French lessons were always fun and friendly. Finally, thank you to everyone I have had the chance to discuss science with, your insights and encouragement have been invaluable. The collaborative and positive atmosphere at the ILL has made this journey truly special.
I would like to thank the members of my thesis committee, Marc Jamin and Marie Plazanet, for taking the time each year to review my work and for their thoughtful advice, encouragement, and genuine interest, which have been very useful in guiding the direction of my thesis.
I sincerely thank the jury members and reviewers for accepting to evaluate this thesis. I am truly grateful for your time, careful reading, and valuable feedback. It is an honor to have you as part of this milestone.
Three years is a long time and I have never felt alone. Many people who have become good friends shared part of this experience with me and made it even more special. I want to thank all my fellow PhD students who welcomed me at the beginning and became great friends: Matteo, Riccardo, Chakib, Kamal, Beatrice, Tong, Brigida, Lucas, Fernanda, Esther, and Anant. Thank you for all the fun discussions during lunch breaks and all the adventures we shared together.
Matte, we have shared a large part of our journey at the ILL from the very first day we started together, walking side by side through so many stages of it. Becoming roommates was the icing on the cake and made everything even more special. Thank you for teaching me how to play cards, for all the Italian recipes, both successful and disastrous, and for the long, honest conversations in confidence. You mean a lot to me, and I am truly grateful for our friendship.
Esther, mi primer recuerdo contigo es bailando durante horas en aquella primera barbacoa, como si fuesemos amigas de toda la vida. En muy poco tiempo te convertiste en una de las personas en las que más he confiado. Nos entendemos incluso sin hablar, y hemos pasado horas de “terapia” juntas, escuchándonos y compartiendo todo. No sé qué habría hecho sin ti durante ese tiempo. Eres una persona muy especial para mí, aunque a veces no sepa encontrar las palabras exactas para explicarlo. Te quiero mucho y te estoy profundamente agradecida.

Lucas, we connected like magnets through our love for climbing, but what I value most about you is how kind and caring you are, always ready to help, listen, and understand. Your friendship is a treasure that I hold dear, and I am truly grateful for your presence, encouragement, and all the adventures we have shared over these years, even though this is just the beginning. It is very hard to describe how important you have been and are, but I know you know!

I am also grateful to all the people with whom I have had the pleasure of sharing an office during this period for making every day enjoyable, full of laughter, and for inspiring me: Rasmus, Anna, Ronja, Lluís, Laura, Linn and Maja.

Aliki, your presence in the office during the final stage of my PhD was truly comforting. Thank you for listening to my constant complaints, for supplying me with snacks, and for teaching me some Greek. Your support and humor made the last months so much brighter. Ευχαριστώ πολύ.

I would also like to acknowledge friends who joined later or were part of my PhD for a shorter period, but whose presence I am equally thankful for: Finn, Theresa, Roody, Pelayo, Jason, Bettina, Francesca, María Val, Kirstin, Elliot, María, Elena, Xaver and Serena.

Roody, Rodolfo, thank you for spreading joy wherever you go. Your stay was short but intense. Thank you for the moments we shared and for all your good vibes.

Finalmente, quiero agradecer al grupo de españoles (y no tan españoles) que se convirtieron en mi "casa" durante la parte final de mi doctorado: Patri, Paula, Lorenzo, Pablo, Javi, Kenny, Harol, Samuel, Clément y Borja.

Javi, gracias por acompañarme en mis primeros contactos con la investigación, contagiarme tu entusiasmo por esta profesión y guiarme durante mis prácticas y mi tesis de máster. Eres un gran ejemplo a seguir.

Patri, gracias por los coffee breaks más intensos de mi vida, por compartir frustraciones y por no dejar nunca de reír. Me ha encantado compartir comidas, cenas, días de esquí y hasta maratones de Shrek contigo. Tu alegría es contagiosa y me hace muy feliz tenerte en mi vida.

Beyond the lab and the office, I have been lucky to share these years with wonderful people outside work. My roommates, close friends, and climbing buddies made this journey brighter, more fun, and full of unforgettable moments.

Belén, cualquier agradecimiento hacia ti se queda corto. Gracias, gracias y mil gracias por todas las aventuras, comidas, panes, sesiones de fisio, viajes, rando, carreras y un largo etcétera. Vivir contigo ha sido una de las mejores decisiones que tomé al venir a Grenoble. No existen palabras para describir lo importante que eres para mí y lo bien que me haces sentir. Este ha sido solo el principio de una larga y hermosa amistad. Te quiero mucho.

Lucía, el último elemento del trío perfecto, las capuchinas. Aunque te quedaste menos tiempo del que me hubiese gustado, agradezco muchísimo todo lo que compartimos. Gracias por hacernos un poco de mami, por cuidarnos y por tu cariño. Has sido una gran fuente de inspiración para mí, y tus ánimos y palabras siempre me han empujado hacia adelante.

Marta S, gracias por ser la persona tan auténtica y transparente que eres. Gracias por todas las aventuras y viajes que hemos compartido, por los días de yoga o pilates, las randos, esquí, y por estar siempre dispuesta a escuchar y ayudar. Todo es mil veces más divertido cuando estás tú.

Marta C, aunque llegaste al final y de manera inesperada, te convertiste rápidamente en alguien imprescindible, como si nos conociéramos de toda la vida. Gracias por todos los viajes, las largas conversaciones y las risas que compartimos.

Julián, te colaste en mi vida casi sin querer y menos mal que te quedaste! Gracias por tener una manera tan única de ver la vida, por perseguir y luchar por tus sueños con tanta dedicación, por tener un amor tan puro por la montaña, y por acompañarme, escucharme y verme. Has sido y eres una gran inspiración para mí.

Guillaume, my very first friend in this city. Thank you so much for including me in your crazy adventures, for sharing so much with me, and for trying to learn to say my name in Spanish, you almost got it! In the end, you are always right when you tell me “you will manage,” even if I don’t believe it at the time. Thank you for trusting me.

Géraldine, thank you for being such a kind, caring, and thoughtful person. Climbing with you is a true pleasure, but you have become so much more than a great belayer and climber, you are a wonderful friend. Thank you for always being there, for looking out for me, for caring so much, and for sharing so much with me.

Por supuesto que no me puedo olvidar de mis amigos de siempre, y de aquellos que, aunque no lo sean desde siempre, se sienten como si lo fuesen: Inma, Ginés, Alex, Josan

y Mario. Gracias por vuestro apoyo, por hacer que cada visita a España se sintiera como si nunca me hubiese ido, y por encontrar el tiempo para venir a verme.

I want to express my deepest gratitude to Laurent. You have been one of my greatest pillars throughout these years. Thank you for all the trips we've shared, for always being there on the other side of the rope or leading the way on the bike, and for introducing me to the guys, who have also become such an important part of my life. It has been a gift to share so much with you. I am endlessly grateful for your patience, your humor, your way of making even the heaviest moments feel lighter, and for your constant, steady presence. I truly could not have done this without you.

Finalmente, quiero agradecer a toda mi familia por apoyarme en todas las decisiones y por creer en mí de manera incondicional. Mamá, gracias por tu infinita paciencia, por tus cuidados, tu apoyo y por confiar tanto en mí. Gracias por aguantar todos mis cambios de humor, por escucharme cada día, incluso cuando a veces había tanto ruido al otro lado del teléfono, por compartir tu vida conmigo y hacerme partícipe de ella aun estando a más de mil kilómetros. No existen suficientes palabras de agradecimiento para ti.

A mi hermano, Pedro, gracias por estar siempre ahí y por tu apoyo constante. Por ser un modelo a seguir y un referente para mí desde siempre. Gracias por acompañarme tantas veces al aeropuerto y por estar siempre presente en los momentos importantes. Te admiro más de lo que a veces expreso y te estoy profundamente agradecida.

Y no puedo dejar de agradecer a mi perro Kito, por su amor incondicional, por su alegría infinita y por recordarme siempre lo importante que es volver a casa.

This thesis is not only the result of years of work, but also of all the people, experiences, and moments that have shaped me along the way.

Bibliography

[1] V. N. Uversky, "Introduction to intrinsically disordered proteins (IDPs)," *Chemical Reviews* **114** no. 13, (July, 2014) 6557–6560.

[2] C. J. Oldfield and A. K. Dunker, "Intrinsically disordered proteins and intrinsically disordered protein regions," *Annual Review of Biochemistry* **83** no. 1, (June, 2014) 553–584.

[3] C. K. Fisher and C. M. Stultz, "Constructing ensembles for intrinsically disordered proteins," *Current Opinion in Structural Biology* **21** no. 3, (June, 2011) 426–431.

[4] R. Trivedi and H. A. Nagarajaram, "Intrinsically disordered proteins: An overview," *International Journal of Molecular Sciences* **23** no. 22, (Nov., 2022) 14050.

[5] S. W. Lovesey, *Theory of Neutron Scattering from Condensed Matter*. Clarendon Press, Oxford, UK, 1984.

[6] G. L. Squires, *Introduction to the Theory of Thermal Neutron Scattering*. Courier Corporation, 1996.

[7] D. L. Price and F. Fernandez-Alonso, *Neutron Scattering–Fundamentals: Chapter 1. An Introduction to Neutron Scattering*, vol. 44. Elsevier Inc. Chapters, 2013.

[8] M. Bée, *Quasielastic Neutron Scattering*. CRC Press, Bristol (UK), 1988.

[9] L. Van Hove, "Correlations in space and time and born approximation scattering in systems of interacting particles," *Physical Review* **95** no. 1, (July, 1954) 249–262.

[10] T. Springer and R. Lechner, "Diffusion in condensed matter," in *Diffusion in Condensed Matter*. Springer-Verlag, Berlin/Heidelberg, 2005.

[11] J. K. Dhont, *An introduction to dynamics of colloids*, vol. 2. Elsevier, 1996.

[12] G. Nägele, *The physics of colloidal soft matter*. Centre of Excellence for Advanced Materials and Structures Warsaw, 2004.

[13] R. Zwanzig, *Nonequilibrium statistical mechanics*. Oxford university press, 2001.

[14] R. Metzler and J. Klafter, "The random walk's guide to anomalous diffusion: a fractional dynamics approach," *Physics Reports* **339** no. 1, (Dec., 2000) 1–77.

[15] C. T. Chudley and R. J. Elliott, "Neutron scattering from a liquid on a jump diffusion model," *Proceedings of the Physical Society* **77** no. 2, (Feb., 1961) 353–361.

[16] P. L. Hall and D. Ross, "Incoherent neutron scattering functions for random jump diffusion in bounded and infinite media," *Molecular Physics* **42** no. 3, (Feb., 1981) 673–682.

[17] K. S. Singwi and A. Sjölander, "Diffusive motions in water and cold neutron scattering," *Physical Review* **119** no. 3, (Aug., 1960) 863–871.

[18] I. Mosca, *Microscopic Dynamic Properties of Monoclonal Antibodies in Solution Studied by Neutron Scattering*. Phd thesis, Institute of Applied Physics, University of Tübingen, Tübingen, Germany, 2025.

[19] A. J. Banchio and G. Nägele, "Short-time transport properties in dense suspensions: From neutral to charge-stabilized colloidal spheres," *The Journal of Chemical Physics* **128** no. 10, (Mar., 2008) .

[20] M. Grimaldo, F. Roosen-Runge, F. Zhang, F. Schreiber, and T. Seydel, "Dynamics of proteins in solution," *Quarterly Reviews of Biophysics* **52** (2019) .

[21] H. Hervet, A. Dianoux, R. Lechner, and F. Volino, "Neutron scattering study of methyl group rotation in solid para-azoxyanisole (PAA)," *Journal de Physique* **37** no. 5, (1976) 587–594.

[22] M. Krutyeva, J. Martin, A. Arbe, J. Colmenero, C. Mijangos, G. J. Schneider, T. Unruh, Y. Su, and D. Richter, "Neutron scattering study of the dynamics of a

polymer melt under nanoscopic confinement," *The Journal of Chemical Physics* **131** no. 17, (Nov., 2009) .

[23] S. Mitra, R. Mukhopadhyay, and K. Venu, "Molecular motions in liquid crystal BBBA (4o.4): QENS study," *Chemical Physics* **261** no. 1–2, (Nov., 2000) 149–156.

[24] F. Roosen-Runge, M. Hennig, F. Zhang, R. M. J. Jacobs, M. Sztucki, H. Schober, T. Seydel, and F. Schreiber, "Protein self-diffusion in crowded solutions," *Proceedings of the National Academy of Sciences* **108** no. 29, (July, 2011) 11815–11820.

[25] S. Peggs, "ESS Technical Design Report," tech. rep., 2013.

[26] A. Triolo, V. Arrighi, R. Triolo, S. Passerini, M. Mastragostino, R. Lechner, R. Ferguson, O. Borodin, and G. Smith, "Dynamic heterogeneity in polymer electrolytes. comparison between QENS data and MD simulations," *Physica B: Condensed Matter* **301** no. 1–2, (July, 2001) 163–167.

[27] M. Kruteva, "Dynamics studied by quasielastic neutron scattering (QENS)," *Adsorption* **27** no. 5, (Feb., 2021) 875–889.

[28] V. K. Sharma, S. Mitra, and R. Mukhopadhyay, "Dynamic landscape in self-assembled surfactant aggregates," *Langmuir* **35** no. 44, (Feb., 2019) 14151–14172.

[29] V. G. Sakai and A. Arbe, "Quasielastic neutron scattering in soft matter," *Current Opinion in Colloid and Interface Science* **14** no. 6, (Dec., 2009) 381–390.

[30] M. Bée, "A physical insight into the elastic incoherent structure factor," *Physica B: Condensed Matter* **182** no. 4, (Dec., 1992) 323–336.

[31] F. Volino and A. Dianoux, "Neutron incoherent scattering law for diffusion in a potential of spherical symmetry: general formalism and application to diffusion inside a sphere," *Molecular Physics* **41** no. 2, (Oct., 1980) 271–279.

[32] Q. Berrod, K. Lagrené, J. Ollivier, and J.-M. Zanotti, "Inelastic and quasi-elastic neutron scattering. application to soft-matter," *EPJ Web of Conferences* **188** (2018) 05001.

[33] M. Appel, B. Frick, and A. Magerl, "A flexible high speed pulse chopper system for an inverted neutron time-of-flight option on backscattering spectrometers," *Scientific Reports* **8** no. 1, (Sept., 2018) .

[34] L. Fine, *Hydride-ion transport mechanisms in oxyhydrides and nitride-hydrydes: a neutron spectroscopy and computational approach*. Phd thesis, Chalmers University of Technology, 2025.

[35] R. Lowde, "The principles of mechanical neutron-velocity selection," *Journal of Nuclear Energy. Part A. Reactor Science* **11** no. 2–4, (Feb., 1960) 69–80.

[36] M. Hennig, *Dynamics of Globular Proteins in Crowded Electrolyte Solutions. Studied by Neutron Scattering*. Phd thesis, Universität Tübingen, Tübingen, Germany, 2011.

[37] L. Austin, R. Kumar, B. Kousar, C. Lampadaris, and M. M. Lucas, "SAXS and WAXS measurements of PET," tech. rep., 2018.

[38] G. J. Griffiths, L. Dubrez, C. P. Morgan, N. A. Jones, J. Whitehouse, B. M. Corfe, C. Dive, and J. A. Hickman, "Cell damage-induced conformational changes of the pro-apoptotic protein bak in vivo precede the onset of apoptosis," *The Journal of Cell Biology* **144** no. 5, (Mar., 1999) 903–914.

[39] G. B. Benedek, "Cataract as a protein condensation disease: the proctor lecture." *Investigative ophthalmology & visual science* **38** no. 10, (1997) 1911–1921.

[40] C. A. Ross and M. A. Poirier, "Protein aggregation and neurodegenerative disease," *Nature Medicine* **10** no. S7, (July, 2004) S10–S17.

[41] J. D. Gunton, *Protein condensation: Kinetic pathways to crystallization and disease*. 2007.

[42] K. A. Henzler-Wildman, M. Lei, V. Thai, S. J. Kerns, M. Karplus, and D. Kern, "A hierarchy of timescales in protein dynamics is linked to enzyme catalysis," *Nature* **450** no. 7171, (Nov., 2007) 913–916.

[43] S. Khodadadi and A. P. Sokolov, "Atomistic details of protein dynamics and the role of hydration water," *Biochimica et Biophysica Acta (BBA) - General Subjects* **1861** no. 1, (Jan., 2017) 3546–3552.

[44] R. Ellis, "Macromolecular crowding: an important but neglected aspect of the intracellular environment," *Current Opinion in Structural Biology* **11** no. 1, (Feb., 2001) 114–119.

[45] M. Grimaldo, F. Roosen-Runge, F. Zhang, T. Seydel, and F. Schreiber, "Diffusion and dynamics of γ-globulin in crowded aqueous solutions," *The Journal of Physical Chemistry B* **118** no. 25, (June, 2014) 7203–7209.

[46] A. S. Verkman, "Solute and macromolecule diffusion in cellular aqueous compartments," *Trends in Biochemical Sciences* **27** no. 1, (Jan., 2002) 27–33.

[47] J. Pérez, J.-M. Zanotti, and D. Durand, "Evolution of the internal dynamics of two globular proteins from dry powder to solution," *Biophysical Journal* **77** no. 1, (July, 1999) 454–469.

[48] G. Zaccai, "Proteins as nano-machines: dynamics function relations studied by neutron scattering," *Journal of Physics: Condensed Matter* **15** no. 18, (Apr., 2003) S1673–S1682.

[49] M. Marconi, E. Cornicchi, G. Onori, and A. Paciaroni, "Comparative study of protein dynamics in hydrated powders and in solutions: A neutron scattering investigation," *Chemical Physics* **345** no. 2–3, (Apr., 2008) 224–229.

[50] A. M. Stadler, F. Demmel, J. Ollivier, and T. Seydel, "Picosecond to nanosecond dynamics provide a source of conformational entropy for protein folding," *Physical Chemistry Chemical Physics* **18** no. 31, (2016) 21527–21538.

[51] F. Gabel, D. Bicout, U. Lehnert, M. Tehei, M. Weik, and G. Zaccai, "Protein dynamics studied by neutron scattering," *Quarterly Reviews of Biophysics* **35** no. 4, (Nov., 2002) 327–367.

[52] P. E. Wright and H. Dyson, "Intrinsically unstructured proteins: re-assessing the protein structure-function paradigm," *Journal of Molecular Biology* **293** no. 2, (Oct., 1999) 321–331.

[53] V. N. Uversky and A. K. Dunker, "Understanding protein non-folding," *Biochimica et Biophysica Acta (BBA) - Proteins and Proteomics* **1804** no. 6, (June, 2010) 1231–1264.

[54] A. K. Dunker, M. M. Babu, E. Barbar, M. Blackledge, S. E. Bondos, Z. Dosztányi, H. J. Dyson, J. Forman-Kay, M. Fuxreiter, J. Gsponer, K.-H. Han, D. T. Jones, S. Longhi, S. J. Metallo, K. Nishikawa, R. Nussinov, Z. Obradovic, R. V. Pappu, B. Rost, P. Selenko, V. Subramaniam, J. L. Sussman, P. Tompa, and V. N. Uversky, "What's in a name? why these proteins are intrinsically disordered," *Intrinsically Disordered Proteins* **1** no. 1, (Jan., 2013) e24157.

[55] J. D. Hunter, "Matplotlib: A 2d graphics environment," *Computing in Science & Engineering* **9** no. 3, (2007) 90–95.

[56] V. N. Uversky, J. R. Gillespie, and A. L. Fink, "Why are natively unfolded proteins unstructured under physiologic conditions?" *Proteins: Structure, Function, and Genetics* **41** no. 3, (2000) 415–427.

[57] P. Romero, Z. Obradovic, X. Li, E. C. Garner, C. J. Brown, and A. K. Dunker, "Sequence complexity of disordered protein," *Proteins: Structure, Function, and Genetics* **42** no. 1, (2000) 38–48.

[58] P. E. Wright and H. J. Dyson, "Intrinsically disordered proteins in cellular signalling and regulation," *Nature Reviews Molecular Cell Biology* **16** no. 1, (Dec., 2014) 18–29.

[59] E. Karlsson, C. Paissoni, A. M. Erkelens, Z. A. Tehranizadeh, F. A. Sorgenfrei, E. Andersson, W. Ye, C. Camilloni, and P. Jemth, "Mapping the transition state for a binding reaction between ancient intrinsically disordered proteins," *Journal of Biological Chemistry* **295** no. 51, (Dec., 2020) 17698–17712.

[60] A. De Simone, C. Kitchen, A. H. Kwan, M. Sunde, C. M. Dobson, and D. Frenkel, "Intrinsic disorder modulates protein self-assembly and aggregation," *Proceedings of the National Academy of Sciences* **109** no. 18, (Apr., 2012) 6951–6956.

[61] F. Scollo and C. La Rosa, "Amyloidogenic intrinsically disordered proteins: New insights into their self-assembly and their interaction with membranes," *Life* **10** no. 8, (Aug., 2020) 144.

[62] R. van der Lee, M. Buljan, B. Lang, R. J. Weatheritt, G. W. Daughdrill, A. K. Dunker, M. Fuxreiter, J. Gough, J. Gsponer, D. T. Jones, P. M. Kim, R. W.

Kriwacki, C. J. Oldfield, R. V. Pappu, P. Tompa, V. N. Uversky, P. E. Wright, and M. M. Babu, "Classification of intrinsically disordered regions and proteins," *Chemical Reviews* **114** no. 13, (Apr., 2014) 6589–6631.

[63] M. Goedert, "Alzheimer's and parkinson's diseases: The prion concept in relation to assembled Aβ, tau, and α-synuclein," *Science* **349** no. 6248, (Aug., 2015) .

[64] M. R. Cookson, "α-synuclein and neuronal cell death," *Molecular Neurodegeneration* **4** no. 1, (2009) 9.

[65] W. M. Babinchak, R. Haider, B. K. Dumm, P. Sarkar, K. Surewicz, J.-K. Choi, and W. K. Surewicz, "The role of liquid–liquid phase separation in aggregation of the TDP-43 low-complexity domain," *Journal of Biological Chemistry* **294** no. 16, (Apr., 2019) 6306–6317.

[66] L. G. Schrag, X. Liu, I. Thevarajan, O. Prakash, M. Zolkiewski, and J. Chen, "Cancer-associated mutations perturb the disordered ensemble and interactions of the intrinsically disordered p53 transactivation domain," *Journal of Molecular Biology* **433** no. 15, (July, 2021) 167048.

[67] E. Leclerc and P. Calmettes, "Interactions in micellar solutions of β-casein," *Physical Review Letters* **78** no. 1, (Jan., 1997) 150–153.

[68] M. Li, M. A. Auty, S. V. Crowley, A. L. Kelly, J. A. O'Mahony, and A. Brodkorb, "Self-association of bovine β-casein as influenced by calcium chloride, buffer type and temperature," *Food Hydrocolloids* **88** (Mar., 2019) 190–198.

[69] C. Cragnell, J. Choi, M. Segad, S. Lee, L. Nilsson, and M. Skepö, "Bovine β-casein has a polydisperse distribution of equilibrium micelles," *Food Hydrocolloids* **70** (Sept., 2017) 65–68.

[70] M. Noelken and M. Reibstein, "Conformation of β-casein b," *Archives of Biochemistry and Biophysics* **123** no. 2, (Feb., 1968) 397–402.

[71] L. Creamer, T. Richardson, and D. Parry, "Secondary structure of bovine α_{S1}- and β-casein in solution," *Archives of Biochemistry and Biophysics* **211** no. 2, (Oct., 1981) 689–696.

[72] P. X. Qi, E. D. Wickham, and H. M. Farrell, "Thermal and alkaline denaturation of bovine β-casein," *The Protein Journal* **23** no. 6, (Aug., 2004) 389–402.

[73] S. Chakraborty, T. I. Morozova, and J.-L. Barrat, "Intrinsically disordered proteins can behave as different polymers across their conformational ensemble," *The Journal of Physical Chemistry B* **129** no. 9, (Feb., 2025) 2359–2369.

[74] G. P. Berry and L. K. Creamer, "Association of bovine β-casein. importance of the C-terminal region," *Biochemistry* **14** no. 16, (Aug., 1975) 3542–3545.

[75] T. Huppertz, P. Fox, and A. Kelly, *The caseins: Structure, stability, and functionality*, p. 49–92. Elsevier, 2018. Proteins in Food Processing.

[76] E. Bahraminejad, D. Paliwal, M. Sunde, C. Holt, J. A. Carver, and D. C. Thorn, "Amyloid fibril formation by α_{S1}- and β-casein implies that fibril formation is a general property of casein proteins," *Biochimica et Biophysica Acta (BBA) - Proteins and Proteomics* **1870** no. 11–12, (Nov., 2022) 140854.

[77] C. Holt, *Structure and Stability of Bovine Casein Micelles*, p. 63–151. Elsevier, 1992. Advances in Protein Chemistry Volume 43.

[78] A. Thurn, W. Burchard, and R. Niki, "Structure of casein micelles I. small angle neutron scattering and light scattering fromβ- andκ-casein," *Colloid and Polymer Science* **265** no. 8, (Aug., 1987) 653–666.

[79] K. Kajiwara, R. Niki, H. Urakawa, Y. Hiragi, N. Donkai, and M. Nagura, "Micellar structure of β-casein observed by small-angle X-ray scattering," *Biochimica et Biophysica Acta (BBA) - Protein Structure and Molecular Enzymology* **955** no. 2, (July, 1988) 128–134.

[80] E. Leclerc and P. Calmettes, "Structure of β-casein micelles," *Physica B: Condensed Matter* **241–243** (Dec., 1997) 1141–1143.

[81] C. de Kruif and V. Grinberg, "Micellisation of β-casein," *Colloids and Surfaces A: Physicochemical and Engineering Aspects* **210** no. 2–3, (Nov., 2002) 183–190.

[82] C. Moitzi, I. Portnaya, O. Glatter, O. Ramon, and D. Danino, "Effect of temperature on self-assembly of bovine β-casein above and below isoelectric pH.

structural analysis by cryogenic-transmission electron microscopy and small-angle x-ray scattering," *Langmuir* **24** no. 7, (Mar., 2008) 3020–3029.

[83] A. Aschi, P. Calmettes, M. Daoud, R. Douillard, and A. Gharbi, "Micelle formation in β-casein solutions," *Polymer* **50** no. 25, (Nov., 2009) 6024–6031.

[84] J. O'Connell, V. Grinberg, and C. de Kruif, "Association behavior of β-casein," *Journal of Colloid and Interface Science* **258** no. 1, (Feb., 2003) 33–39.

[85] A. M. Gaspar, M.-S. Appavou, S. Busch, T. Unruh, and W. Doster, "Dynamics of well-folded and natively disordered proteins in solution: a time-of-flight neutron scattering study," *European Biophysics Journal* **37** no. 5, (Jan., 2008) 573–582.

[86] G. K. Dhindsa, M. Tyagi, and X.-q. Chu, "Temperature-dependent dynamics of dry and hydrated β-casein studied by quasielastic neutron scattering," *The Journal of Physical Chemistry B* **118** no. 37, (Sept., 2014) 10821–10829.

[87] S. Perticaroli, J. D. Nickels, G. Ehlers, E. Mamontov, and A. P. Sokolov, "Dynamics and rigidity in an intrinsically disordered protein, β-casein," *The Journal of Physical Chemistry B* **118** no. 26, (June, 2014) 7317–7326.

[88] H. Nakagawa, M.-S. Appavou, J. Wuttke, M. Zamponi, O. Holderer, T. E. Schrader, D. Richter, and W. Doster, "Nanosecond structural dynamics of intrinsically disordered β-casein micelles by neutron spectroscopy," *Biophysical Journal* **120** no. 23, (Dec., 2021) 5408–5420.

[89] P. Müller-Buschbaum, R. Gebhardt, S. Roth, E. Metwalli, and W. Doster, "Effect of calcium concentration on the structure of casein micelles in thin films," *Biophysical Journal* **93** no. 3, (Aug., 2007) 960–968.

[90] A. Post, B. Arnold, J. Weiss, and J. Hinrichs, "Effect of temperature and ph on the solubility of caseins: Environmental influences on the dissociation of α_s- and β-casein," *Journal of Dairy Science* **95** no. 4, (Apr., 2012) 1603–1616.

[91] R. Zangi, R. Zhou, and B. J. Berne, "Urea's action on hydrophobic interactions," *Journal of the American Chemical Society* **131** no. 4, (Jan., 2009) 1535–1541.

[92] B. J. Bennion and V. Daggett, "The molecular basis for the chemical denaturation of proteins by urea," *Proceedings of the National Academy of Sciences* **100** no. 9, (Apr., 2003) 5142–5147.

[93] B. Frick, E. Mamontov, L. v. Eijck, and T. Seydel, "Recent backscattering instrument developments at the ILL and SNS," *Zeitschrift für Physikalische Chemie* **224** no. 1–2, (Feb., 2010) 33–60.

[94] C. Beck, M. Appel, M. Grimaldo, F. Roosen-Runge, F. Zhang, B. Frick, F. Schreiber, and T. Seydel, "Neutron spectroscopy on protein solutions employing backscattering with an increased energy range," *Physica B: Condensed Matter* **562** (June, 2019) 31–35.

[95] O. Arnold, J. Bilheux, J. Borreguero, A. Buts, S. Campbell, L. Chapon, M. Doucet, N. Draper, R. Ferraz Leal, M. Gigg, V. Lynch, A. Markvardsen, D. Mikkelson, R. Mikkelson, R. Miller, K. Palmen, P. Parker, G. Passos, T. Perring, P. Peterson, S. Ren, M. Reuter, A. Savici, J. Taylor, R. Taylor, R. Tolchenov, W. Zhou, and J. Zikovsky, "Mantid—Data analysis and visualization package for neutron scattering and μSR experiments," *Nuclear Instruments and Methods in Physics Research Section A: Accelerators, Spectrometers, Detectors and Associated Equipment* **764** (Nov., 2014) 156–166.

[96] B. Farago, P. Falus, I. Hoffmann, M. Gradzielski, F. Thomas, and C. Gomez, "The IN15 upgrade," *Neutron News* **26** no. 3, (July, 2015) 15–17.

[97] B. Farago, "Recent neutron spin-echo developments at the ILL (IN11 and IN15)," *Physica B: Condensed Matter* **267–268** (June, 1999) 270–276.

[98] P. Schleger, B. Alefeld, J. Barthelemy, G. Ehlers, B. Farago, P. Giraud, C. Hayes, A. Kollmar, C. Lartigue, F. Mezei, and D. Richter, "The long-wavelength neutron spin-echo spectrometer IN15 at the Institut Laue-Langevin," *Physica B: Condensed Matter* **241–243** (Dec., 1997) 164–165.

[99] S. R. Kline, "Reduction and analysis of SANS and USANS data using IGOR Pro," *Journal of Applied Crystallography* **39** no. 6, (Nov., 2006) 895–900.

[100] D. I. Svergun, M. H. J. Koch, P. A. Timmins, and R. P. May, *Small angle X-ray and neutron scattering from solutions of biological macromolecules*. International

Union of Crystallography Texts on Crystallography. Oxford University Press, London, England, Aug., 2013.

[101] J. Teixeira, "Small-angle scattering by fractal systems," *Journal of Applied Crystallography* **21** no. 6, (Dec., 1988) 781–785.

[102] P. De Gennes, "Liquid dynamics and inelastic scattering of neutrons," *Physica* **25** no. 7–12, (Jan., 1959) 825–839.

[103] I. Hoffmann, P. Heunemann, B. Farago, I. Grillo, O. Holderer, M. Päch, and M. Gradzielski, "Structure and dynamics of nanoemulsions: Insights from combining dynamic and static neutron scattering," *Physical Review E* **86** no. 6, (Dec., 2012) .

[104] M. Jasnin, M. Moulin, M. Haertlein, G. Zaccai, and M. Tehei, "In vivo measurement of internal and global macromolecular motions in escherichia coli," *Biophysical Journal* **95** no. 2, (July, 2008) 857–864.

[105] S. Busch, W. Doster, S. Longeville, V. G. Sakai, T. Unruh, and F.-N. H. Maier-Leibnitz, "Microscopic protein diffusion at high concentration," *MRS Bulletin* (2006) 116–117.

[106] B. Caviglia, S. Timr, M. Guiral, M.-T. Giudici-Orticoni, T. Seydel, C. Beck, J. Peters, F. Sterpone, and A. Paciaroni, "Cytoplasmic fluidity and the cold life: Proteome stability is decoupled from viability in psychrophiles,".

[107] D. Andersson, C. Svanberg, J. Swenson, W. Howells, and L. Börjesson, "Diffusive dynamics in polymer gel electrolytes investigated by quasi-elastic neutron scattering," *Physica B: Condensed Matter* **301** no. 1–2, (July, 2001) 44–48.

[108] T. Rinesh, H. Srinivasan, V. K. Sharma, V. G. Sakai, and S. Mitra, "Role of molecular structure in defining the dynamical landscape of deep eutectic solvents," *The Journal of Chemical Physics* **162** no. 24, (June, 2025) .

[109] F. Ameseder, A. Radulescu, M. Khaneft, W. Lohstroh, and A. M. Stadler, "Homogeneous and heterogeneous dynamics in native and denatured bovine serum albumin," *Physical Chemistry Chemical Physics* **20** no. 7, (2018) 5128–5139.

[110] O. Matsarskaia, L. Bühl, C. Beck, M. Grimaldo, R. Schweins, F. Zhang, T. Seydel, F. Schreiber, and F. Roosen-Runge, "Evolution of the structure and dynamics of bovine serum albumin induced by thermal denaturation," *Physical Chemistry Chemical Physics* **22** no. 33, (2020) 18507–18517.

[111] M. Grimaldo, F. Roosen-Runge, M. Hennig, F. Zanini, F. Zhang, N. Jalarvo, M. Zamponi, F. Schreiber, and T. Seydel, "Hierarchical molecular dynamics of bovine serum albumin in concentrated aqueous solution below and above thermal denaturation," *Physical Chemistry Chemical Physics* **17** no. 6, (2015) 4645–4655.

[112] M. Grimaldo, H. Lopez, C. Beck, F. Roosen-Runge, M. Moulin, J. M. Devos, V. Laux, M. Härtlein, S. Da Vela, R. Schweins, A. Mariani, F. Zhang, J.-L. Barrat, M. Oettel, V. T. Forsyth, T. Seydel, and F. Schreiber, "Protein short-time diffusion in a naturally crowded environment," *The Journal of Physical Chemistry Letters* **10** no. 8, (Mar., 2019) 1709–1715.

[113] S. Perticaroli, G. Ehlers, C. B. Stanley, E. Mamontov, H. O'Neill, Q. Zhang, X. Cheng, D. A. A. Myles, J. Katsaras, and J. D. Nickels, "Description of hydration water in protein (green fluorescent protein) solution," *Journal of the American Chemical Society* **139** no. 3, (Nov., 2016) 1098–1105.

[114] B. Jachimska, M. Wasilewska, and Z. Adamczyk, "Characterization of globular protein solutions by dynamic light scattering, electrophoretic mobility, and viscosity measurements," *Langmuir* **24** no. 13, (May, 2008) 6866–6872.

[115] G. K. Batchelor, "Brownian diffusion of particles with hydrodynamic interaction," *Journal of Fluid Mechanics* **74** no. 1, (Mar., 1976) 1–29.

[116] C. Beck, M. Grimaldo, H. Lopez, S. Da Vela, B. Sohmen, F. Zhang, M. Oettel, J.-L. Barrat, F. Roosen-Runge, F. Schreiber, and T. Seydel, "Short-time transport properties of bidisperse suspensions of immunoglobulins and serum albumins consistent with a colloid physics picture," *The Journal of Physical Chemistry B* **126** no. 38, (Sept., 2022) 7400–7408.

[117] W. Humphrey, A. Dalke, and K. Schulten, "VMD – Visual Molecular Dynamics," *Journal of Molecular Graphics* **14** (1996) 33–38.

[118] K. Pounot, H. Chaaban, V. Foderà, G. Schirò, M. Weik, and T. Seydel, "Tracking internal and global diffusive dynamics during protein aggregation by high-resolution neutron spectroscopy," *The Journal of Physical Chemistry Letters* **11** no. 15, (July, 2020) 6299–6304.

[119] S. Fujiwara, K. Araki, T. Matsuo, H. Yagi, T. Yamada, K. Shibata, and H. Mochizuki, "Dynamical behavior of human α-synuclein studied by quasielastic neutron scattering," *PLOS ONE* **11** no. 4, (Apr., 2016) e0151447.

[120] S. Fujiwara, "Dynamical behavior of disordered regions in disease-related proteins revealed by quasielastic neutron scattering," *Medicina* **58** no. 6, (June, 2022) 795.

[121] A. C. Grundel, "Structure and dynamics of intrinsiclly disordered proteins: A combined scattering, simulation and regularization approach," 2025. Master thesis, University of Heidelberg.

[122] M. Abraham, A. Alekseenko, C. Bergh, C. Blau, E. Briand, M. Doijade, S. Fleischmann, V. Gapsys, Gaurav Garg, S. Gorelov, G. Gouaillardet, A. Gray, M. Eric Irrgang, F. Jalalypour, J. Jordan, C. Junghans, Prashanth Kanduri, S. Keller, C. Kutzner, J. A. Lemkul, M. Lundborg, P. Merz, V. Miletić, D. Morozov, S. Páll, R. Schulz, M. Shirts, A. Shvetsov, B. Soproni, D. Van Der Spoel, P. Turner, C. Uphoff, A. Villa, S. Wingbermühle, A. Zhmurov, P. Bauer, B. Hess, and E. Lindahl, "GROMACS 2023 manual,". `https://zenodo.org/record/7588711`.

[123] G. Goret, B. Aoun, and E. Pellegrini, "MDANSE: An interactive analysis environment for molecular dynamics simulations," *Journal of Chemical Information and Modeling* **57** no. 1, (Jan., 2017) 1–5.